Technical University of Denmark

DTU

Alternative deNOx catalysts and technologies

Due-Hansen, Johannes; Fehrmann, Rasmus; Riisager, Anders

Publication date:
2010

Document Version
Publisher's PDF, also known as Version of record

Link back to DTU Orbit

Citation (APA):
Due-Hansen, J., Fehrmann, R., & Riisager, A. (2010). Alternative deNOx catalysts and technologies. Kgs. Lyngby, Denmark: Technical University of Denmark (DTU).

DTU Library
Technical Information Center of Denmark

Alternative

deNO$_x$ catalysts and technologies

Johannes Due-Hansen

Ph.D. Thesis

Department of Chemistry
Centre for Catalysis and Sustainable Chemistry
Technical University of Denmark
Lyngby 2800, Denmark
June, 2010

A section in *Zirconia-based catalyst systems* (section 3.2), regarding enhanced acidification of the sulfated zirconia originally presented here, cannot currently be made freely available due to a concurrent patent application. The material has thus been removed from this version.

Cover illustrations

The produced monoliths of V$_2$O$_5$−WO$_3$−TiO$_2$ stabilized with 50 wt% sepiolite.

Cover artwork by Johannes Due-Hansen.

Preface and acknowledgments

This thesis has been submitted in candidacy for the Ph.D. degree in chemistry at the Technical University of Denmark (DTU). The majority of the work summarized herein was carried out at the Department of Chemistry, from June 2007 to May 2010 under the joint supervision of Assoc. Prof. Anders Riisager and Prof. Rasmus Fehrmann. This project is financed through a Ph.D.-scholarship from DTU, Energinet.dk, DONG, Vattenfall and Haldor Topsøe.

During March and April 2009, I worked with the group of Pedro Ávilla at Instituto de Catálisis y Petrolequimica, Consejo Superior de Investigaciones Científicas (ICP-CSIC), Campus de Universidad Autonoma de Madrid in Spain.

First and foremost, I would like to thank my two supervisors for many fruitful discussions and suggestions during the project and for a constant source of inspiration.

I would further like to thank Steffen Buus Kristensen and Siva Sankar Reddy Putluru (DTU Chemistry) for a productive lab-collaboration and many interesting catalysis discussions, Olivier Nguyen van Buu (DTU Chemistry) for lending me his vast expertise in organic synthesis, and Kenny Ståhl (DTU Chemistry) for his help and inspiration with X-ray diffraction and Rietveld refinement. Warm thanks to Soghomon Boghosian (FORTH/ICE-HT and University of Patras, Greece), Rolf W. Berg (DTU Chemistry), Bodil Holten (DTU Chemistry), and Berit Wenzell (DTU-CEN) for an always enjoyable collaboration. Special Thanks to Pedro Ávila and Søren Birk Rasmussen (ICP-CSIC) for many inspiring ideas and an exciting collaboration from which I have learned a lot. Furthermore, I am indebted to Julie Skotte for assistance with Adobe Photoshop and Illustrator issues, as well as moral support.

I am grateful to the Travel Foundation of The Danish Chemical Society, the foundation of Fabrikant P.A. Fisker, the Idella foundation and Berg, Nielsens scholarship, for financial support for the external stay.

I have been very fortunate to have some dedicated students, Selcuk Mert, Søren Heintz and Thorey Anna Grétarsdóttir, with whom I have collaborated on various projects throughout the project period.

Finally I would like to thank all the people at the department and at the Centre for Catalysis and Sustainable Chemistry (CSC) for advice, feedback, co-work, and an always enjoyable atmosphere which has made the past three years memorable.

———————————

Johannes Due-Hansen

Lyngby, July 26, 2010

Abstract

The present thesis entitled *Alternative deNO$_x$ Catalysts and technologies* revolves around the topic of removal of nitrogen oxides. Nitrogen oxides, NO$_x$, are unwanted byproducts formed during combustion (e.g. in engines or power plants). If emitted to the atmosphere, they are involved in the formation of acid rain and photochemical smog. Some basic concepts and reactions regarding the formation and removal of NO$_x$ are presented in chapter 1 and 2.

Two approaches are undertaken in the present work to reduce the emission of NO$_x$: by means of catalytic removal, and by NO absorption in ionic liquids.

The commercial catalyst used for the selective catalytic reduction (SCR) of nitrogen oxides exhibits high activity and selectivity towards N$_2$. However, the vanadia-titania-based catalyst used is very sensitive to deactivation by alkali-species (primarily potassium), which are typically present in high amounts in the flue gas when biomass is combusted. By co-firing with large amounts of CO$_2$-neutral straw or wood (to meet stringent CO$_2$ emission legislation), the lifetime of the traditional SCR catalyst is thus significantly reduced due to the presence of deactivating species originating from the fuel. To develop a catalyst less susceptible to the poisons present in the flue gas, a number of catalysts have been synthesized and tested in the present work, all based on commercially available supports. A highly acidic support consisting of sulfated zirconia was chosen based on preliminary studies. A number of different active species distributed on the support were investigated, such as iron, copper and vanadium oxides. However, based on the catalysts performance in the SCR reaction and their resistances towards potassium, the most promising candidate of the formulations studied was the vanadia-loaded catalyst, i.e. V$_2$O$_5$-SO$_4^{2-}$-ZrO$_2$. This work, together with an introduction to the catalytic removal of NO$_x$, are described in chapter 3.

The remainder of the first part is concerned with the catalytic NO$_x$ removal (chapter 4) and it addresses the upscaling of the best catalyst candidate. The catalyst was mixed with the natural binding clay (sepiolite) to upscale the selected catalyst to the monolithic level, suitable for installation in gas stream with high flows, e.g. a flue gas duct of a power plant. A series of catalyst pellets with increasing levels of sepiolite were produced to evaluate the optimum mixing ratio. Based on these results, a monolith containing V$_2$O$_5$-SO$_4^{2-}$-ZrO$_2$ in 25 wt% sepiolite was produced, and evaluated with respect to the influence of space velocity, reaction temperature, and NH$_3$/NO feed ratio on the NO reduction efficiency.

The last part of this thesis deals with the non-catalytic sorption of NO$_x$ in ionic liquids, collected in chapter 5. Since no previous studies of the absorption of NO in ionic liquids have been reported, a preliminary study was conducted to identify suitable solvents. Two result-

ing imidazolium-based candidates, namely [BMIM]OAc and [BMIM]OTf, were selected due to their impressively high sorption capacities. Both solvents examined here revealed solubilities about twofold higher than those previously reported for e.g. CO_2-capture in ionic liquids. Especially the [BMIM]OAc demonstrated extraordinary absorption capabilities, being able to retain around four NO molecules per molecule ionic liquid. However, [BMIM]OTf exhibited promising behavior due to its reversible absorption/desorption properties. This in principle allows recycling of the ionic liquid as well as harvesting the NO. The accumulated NO could hereby be used in e.g. the synthesis of nitric acid allowing production of value-added chemicals from waste flue gas effluent. Although additional understanding of the mechanisms of the presented system is required, the perspective of a selective NO stripping technology is a very interesting alternative to the catalytic removal of NO from industrial flue gases.

Dansk resumé

Foreliggende afhandling med titlen *Alternative deNO$_x$-katalysatorer og -teknologier* omhandler fjernelse af nitrogen oxider fra røggasser. Nitrogen oxider, NO$_x$, er uønskede biprodukter dannet under forbrænding, f.eks. i motorer eller kraftværker. Ved udledning til atmosfæren er de medvirkende til dannelsen af syreregn og fotokemisk smog. Nogle grundlæggende koncepter og reaktioner vedrørende dannelsen og fjernelsen af NO$_x$ er beskrevet i kapitel 1 og 2.

To forskellige metoder til at reducere emissionen af NO$_x$ bliver undersøgt i denne afhandling: katalytisk fjernelse samt absorption i ioniske væsker.

Den kommercielle katalysator som idag primært bliver brugt i den selektive katalytiske reduktion (SCR) af nitrogen oxider udviser høj katalytisk aktivitet og selektivitet for omdannelse til N$_2$. Men denne vanadia-titania baserede katalysator er meget følsom overfor deaktiverende alkali metal specier (primært kalium), som typisk er tilstede i høje koncentrationer i røggassen når biomasse afbrændes. Afbrænding af store mængder CO$_2$-neutralt træ eller halm (for at imødekomme stringente CO$_2$ emissionskrav) vil derfor reducere levetiden af den traditionelle SCR katalysator betydeligt pga. tilstedeværelsen af deaktiverede specier fra brændslet. For at udvikle en katalysator, der er mindre følsom overfor forgiftende stoffer i røggassen, er en række katalysatorer blevet fremstillet og testet, alle baseret på kommercielt tilgængelige bærematerialer. En særdeles sur bærer bestående af sulfatiseret zirkonia blev udvalgt, baseret på indledende studier. En række forskellige aktive metaller fordelt på bæreren blev undersøgt, såsom oxiderne af jern, kobber og vanadium. Baseret på katalysatorernes virkningsgrad i SCR reaktionen og deres modstandsdygtighed overfor kalium, var den vanadium-baserede katalysator (V$_2$O$_5$-SO$_4^{2-}$-ZrO$_2$) den mest lovende kandidat. Dette arbejde, sammen med en introduktion til den katalytiske fjernelse af NO$_x$, er beskrevet i kapitel 3.

Resten af første del (kapitel 4), som omhandler den katalytiske fjernelse af NO$_x$, håndterer opskaleringen af den mest lovende katalysator, V$_2$O$_5$-SO$_4^{2-}$-ZrO$_2$. Katalysatoren blev sammenblandet med en naturlig lerbinder (sepiolit) for at opskalere den valgte katalysator til monolit niveau, som er egnet til at indsættelse i gasstrømme med høje hastigheder f.eks. i en røggaskanal på et kraftværk. En serie af katalysator-ekstrudater med stigende indhold af sepiolit blev fremstillet for at evaluere det optimale sammenblandings forhold. På baggrund af disse resultater, blev en monolit indeholdende V$_2$O$_5$-SO$_4^{2-}$-ZrO$_2$ i 25 wt% sepiolit fremstillet og indflydelsen af hhv. gas hastighed, reaktions temperatur, NH$_3$/NO forholdet i fødegassen, og NO reduktions effektivitet, blev undersøgt.

Sidste del af denne afhandling (kapitel 5) beskæftiger sig med den ikke-katalytiske sorption (absorption/desorption) af NO$_x$ i ioniske væsker. Da absorption af NO$_x$ i ioniske væsker ikke

tidligere har været beskrevet i litteraturen, blev der udført et indledende studie for at identificere egnede solventer. To imidazolium-baserede kandidater ([BMIM]OAc og [BMIM]OTf) blev herved udvalgt på baggrund af deres imponerende høje sorptions kapaciteter. Begge solventer, som blev undersøgt, udviste NO-opløseligheder omkring dobbelt så høje som dem rapportet for f.eks. CO_2 indfangning i ioniske væsker. Specielt [BMIM]OAc udviste ekstraordinære absorptions kapaciteter, og var i stand til at fiksere fire NO molekyler per molekyle ionisk væske. Omvendt, så udviste [BMIM]OTf lovende opførsel pga. dens reversible egenskaber. Dette vil i princippet tillade genbrug af den ionisk væske samt opkoncentrering af NO. Den akkumulerede NO kunne herved blive udnyttet til f.eks. fremstillingen af salpetersyre, hvorved et affaldsprodukt fra gassen bliver værdiskabende. Selvom en yderligere forståelse af mekanismerne i det omtalte system er nødvendig, så er perspektivet for en teknologi der selektivt kan isolere NO meget lovende som alternativ til den katalytiske fjernelse af NO fra industrielle røggasser.

Table of Contents

Chapter 1

Basic concepts

The work embedded in this thesis is the continuation of a long tradition of continuous optimizing and development of the methods for removal of nitrogen oxides. To ensure a common denominator, some basic terms are examined in the following sections.

1.1 NO$_x$ sources

Nitrogen oxides, NO$_x$, are among the most troublesome atmospheric pollutants and represents a major environmental problem, being partly responsible for the depletion of ozone (see reaction R-1.1), acid rain and town smog[1].

$$NO + O_3 \xrightarrow{h\nu} NO_2 + O_2 \qquad \Delta H^o_{298K} = -201 \text{ kJ/mol} \qquad \text{(R-1.1)}$$
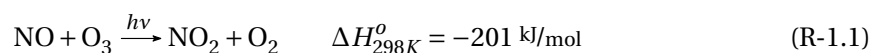
NO$_x$ is not only produced in all combustion processes involving fossil- and bio-fuels, but also in lightning, microbiological denitrification processes in the soil, and by volcanic activity. However, the man-made NO$_x$ from combustion processes contribute to almost three-quarters of the total amount of NO$_x$ emitted into the atmosphere[2,3]. Fig. 1.1 depicts the NO$_x$-contribution from different sources in the US and Europe.
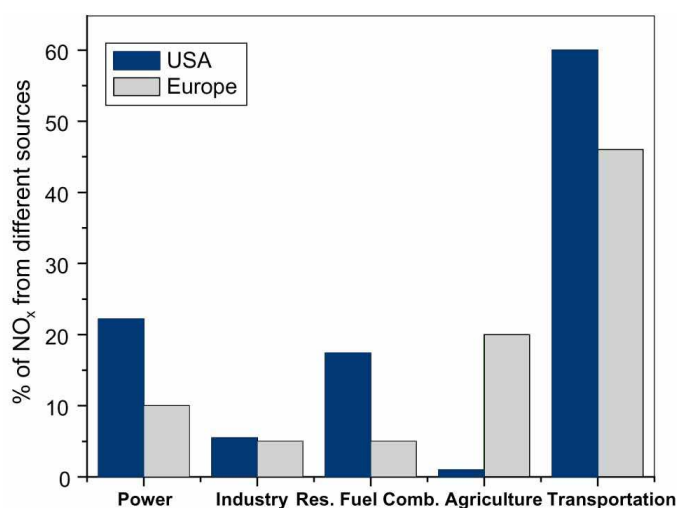
Fig. 1.1: Emission of NO$_x$ by source category in USA and Europe (based on data from 1993 and 2006). Adapted from [4]

The term 'NO$_x$' covers all the seven known oxides of nitrogen, NO, NO$_2$, NO$_3$, N$_2$O, N$_2$O$_3$, N$_2$O$_4$ and N$_2$O$_5$. However, the resulting gas from a combustion is predominantly the oxides NO and NO$_2$, with nitric oxide representing 90-95% of the total NO$_x$[3,5,6].

1.2 Catalysis

Nowadays, catalysis is a fundamental part of modern chemistry.

A catalyst is defined as a substance that increases the rate of reaction without modifying the overall standard Gibbs energy change of the reaction, i.e. a catalyst does not affect the position of the chemical equilibrium[7]. The concept of catalysis was established by Ostwald, but was coined by Berzelius as early as 1836[8]. Catalysis is of major significance to our society as we rely on catalytic reactions in almost every part of the chemical industry - more than 90% of the processes in the chemical manufacturing utilize catalysts in some form[9].

Catalysis can be subcategorized as homogeneous, in which reactants and catalyst are in the same phase, and heterogeneous catalysis, in which the reaction occurs at or near an interface between phases. However, in this study only heterogeneous catalysis is examined.

Chapter 2

Nitrogen oxides - a mechanistic approach

Before embarking upon the catalytic removal of the undesired NO_x, it is worthwhile looking into the fundamentals of the reactions taking place. This chapter is subdivided into sections dealing with the reactions regarding the formation and removal of NO_x.

The calculations of thermodynamic reaction parameters employed in this chapter, such as ΔH^o and ΔS^o, are all based on the standard values of the CRC Handbook of Chemistry and Physics [10]. An overview of the reactions and calculated thermodynamic entities are collated in the appendix tables: Tab. B.1 and B.2 (page 97).

2.1 Formation

Already in 1988 Bosch and Janssen [3] categorized the formed NO_x into three types, all formed during the combustion process. The first category, *thermal NO_x*, is responsible for the majority of the nitrogen oxides formed during combustion and is formed by oxidation of the atmospheric nitrogen at very high temperatures via the overall reaction:

$$N_2 + O_2 \longrightarrow 2\,NO, \qquad \Delta H^o_{298K} = -183 \text{ kJ/mol} \tag{R-2.1}$$
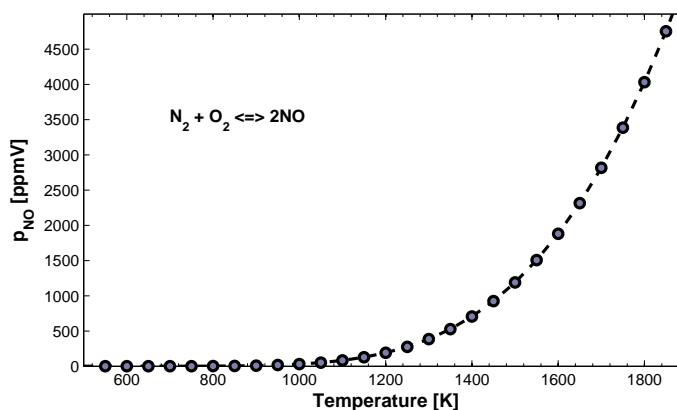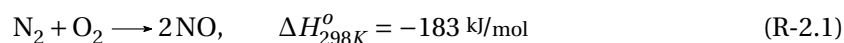
Fig. 2.1: Theoretical equilibrium concentration of NO in air under the assumption that ΔH^o_{298K} and ΔS^o_{298K} are temperature-independent

Reaction R-2.1 is very unfavored thermodynamically at ambient temperatures, and only allows formation of a few hundreds ppm of NO at temperatures of 1300 K, but the NO evolution at higher temperatures is considerable, as illustrated in Fig. 2.1, since flame combustion temperatures in excess of 1700 K can occur [11]. Reaction R-2.1 can be catalyzed by materials

(e.g. particles from the fuel) in contact with the flame during the combustion, some endorsing the formation of NO, others inhibiting. This is highly relevant for fluidized bed solid combustors, as reported by Olofsson et al.[12]. Efforts have been made to minimize the amount of thermal NO_x by combustion control, achieved by e.g. redesign of the combustor itself or low NO_x-burners, where the combustions peak temperature are smoothed by partial premixing[13].

The second, and more complex, category of NO_x is called *prompt NO_x*, which involves the reaction of molecular nitrogen with organic hydrocarbon fragments to yield intermediate products, such as HCN, which subsequently is oxidized to NO. The reaction occurs at 1500 K or above and is responsible for the formation of NO in the range of tens of ppm[14], and due to the high temperature, the reverse reaction of reaction R-2.1, i.e. the decomposition of NO, does not take place. Furthermore, at lower temperatures NO can react with oxygen to form NO_2 (reaction R-2.2) or N_2O (reaction R-2.3).

$$2\,NO + O_2 \longrightarrow 2\,NO_2, \qquad \Delta H^o_{298K} = -116 \text{ kJ/mol} \qquad \text{(R-2.2)}$$
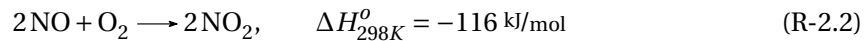
Reaction R-2.2 is shifted to the left at high temperatures due to its exothermic character, whereby only NO is formed during combustion. The equilibrium temperature for the reaction, where the Gibbs free energy is zero, can be calculated:

$$\Delta G^o = \Delta H^o - T\Delta S^o \Rightarrow$$
$$0 = \Delta H^o - T\Delta S^o \Leftrightarrow$$
$$T_{\Delta G^o=0} = \frac{\Delta H^o}{\Delta S^o} = \frac{-116200 \text{ J/mol}}{-146.6 \text{ J/mol·K}} = 793 \text{ K} \qquad \text{(2.1)}$$

Consequently, NO_2 is practically completely decomposed to NO and O_2 at temperatures above 800 K. Although the enthalpy and entropy values utilized in the calculation only holds valid at 298 K and 1 bar, the result comply well with other reported findings for this reaction[1,11,14]. When air is present, the equilibrium of the NO oxidation (reaction R-2.2) is shifted to the right. However, the reaction is slow and as a result of this, most of the NO_x is essentially composed of NO[14].

The prompt NO can also form N_2O via reaction R-2.3.

$$2\,NO \longrightarrow N_2O + \tfrac{1}{2}O_2, \qquad \Delta H^o_{298K} = -101 \text{ kJ/mol} \qquad \text{(R-2.3)}$$
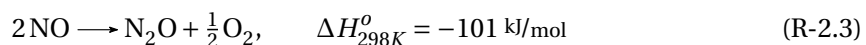
This reaction can be mediated by dimeric species of NO, such as N_2O_2 [5], and is only favored at low temperatures[11]. Thus, during combustion at high temperatures the reverse reaction can take place, whereby N_2O can be intermediate in the formation of NO. However, N_2O can also be (but not necessarily) intermediate in the formation of NO at low temperatures via reaction R-2.4.

$$2\,N_2O \longrightarrow 2\,NO + N_2, \qquad \Delta H^o_{298K} = 19 \text{ kJ/mol} \qquad \text{(R-2.4)}$$
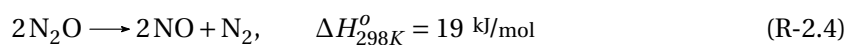
The third category of NO_x is called *fuel NO_x* and is formed by oxidation of nitrogen in the fuel. Substantial amounts of fuel nitrogen is present in coal and heavy oils as well as in biomass, such as wood[14]. In contrast to the temperature controlled thermal NO_x, fuel NO_x is relatively

independent of temperatures at normal combustion temperatures [4]. On the other hand it is strongly influenced by reactor design [14], but can be moderated by use of e.g. staged burning or reburning [15].

2.1.1 Ammonia oxidation

Another source to NO_x, which is highly relevant for the selective catalytic reduction reaction where NH_3 or urea (decomposes to equimolar amount of ammonia and isocyanic acid, HNCO) is used as reductant in the presence of oxygen, is the reaction of ammonia with oxygen, and can take place through the following ways:

$$4\,NH_3 + 3\,O_2 \longrightarrow 2\,N_2 + 6\,H_2O, \qquad \Delta H^o_{298K} = -1267 \text{ kJ/mol} \qquad \text{(R-2.5)}$$

$$4\,NH_3 + 4\,O_2 \longrightarrow 2\,N_2O + 6\,H_2O, \qquad \Delta H^o_{298K} = -1104 \text{ kJ/mol} \qquad \text{(R-2.6)}$$

$$4\,NH_3 + 5\,O_2 \longrightarrow 4\,NO + 6\,H_2O, \qquad \Delta H^o_{298K} = -902 \text{ kJ/mol} \qquad \text{(R-2.7)}$$

$$4\,NH_3 + 6\,O_2 \longrightarrow 2\,N_2O_3 + 6\,H_2O, \qquad \Delta H^o_{298K} = -1094 \text{ kJ/mol} \qquad \text{(R-2.8)}$$

$$4\,NH_3 + 7\,O_2 \longrightarrow 4\,NO_2 + 3\,H_2O, \qquad \Delta H^o_{298K} = -1134 \text{ kJ/mol} \qquad \text{(R-2.9)}$$
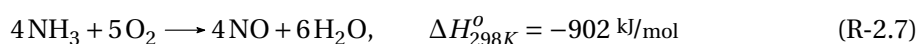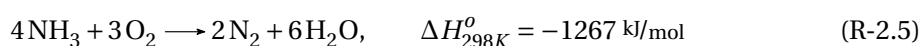
These unwanted secondary reactions to the SCR reaction can occur as a result of the presence of oxygen, the temperature, the catalyst nature and the ratio of NO/NH_3 [1,5,16,17].

Reaction R-2.5 to R-2.9 are all displayed with four stoichiometric ammonia as reactants even though e.g. reaction R-2.6 strictly speaking only should contain half the amount of molecules. This is done for easy comparison of the resulting enthalpies. Furthermore, note that increasing the partial pressure of oxygen leads to a corresponding increase in the oxidation number of the resulting nitrogen species.

All the oxidations of ammonia shown above are fully accepted thermodynamically (ΔG^o_{298K} < 0), although the oxidation to N_2 is most favored in enthalpy. Reaction R-2.5 is the so-called selective catalytic oxidation (SCO) of ammonia and is interesting because it in principle allows abatement of excess ammonia (ammonia slip) from the NH_3-SCR process. Several active SCR catalysts also perform well in SCO, although at slightly higher temperatures [5]. The oxidation of ammonia to NO in reaction R-2.7 is applied industrially in the synthesis of HNO_3 using Pt as the catalyst, although several transition metals can catalyze the reaction [5,17,18].

Due to the higher thermodynamic stability of N_2 with respect to NO and N_2O, reaction R-2.5 is in general favored at lower temperature compared to reaction R-2.6 and R-2.7, whereas the opposite holds true at higher temperatures.

Even though nitrogen trioxide formed in reaction R-2.8 only exist in its pure form below the melting point at -101°C [10], it disproportionates at higher temperatures according to reaction R-2.10.

$$N_2O_3 \rightleftharpoons NO + NO_2, \qquad \Delta H^o_{298K} = 38 \text{ kJ/mol} \qquad \text{(R-2.10)}$$
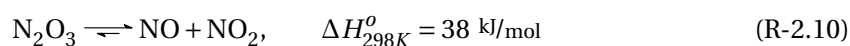
At ambient conditions the reaction is shifted to the right (K_{298K} = 3 bar), and equilibrium is quickly settled [19].

Formation of NO_2 in reaction R-2.9 does generally not compose a problem in correlation with the SCR reaction, other than the removal of ammonia (accounting for a non-stoichiometric conversion of NO and NH_3 in the SCR reaction), since the formed nitrogen dioxide can participate in an 'improved' SCR process in concert with NO and ammonia, the so-called *fast SCR*. This aspect is further treated in the following section.

2.2 Removal

The most simple way to remove NO is in principle by its decomposition reaction, i.e. the reverse of reaction R-2.1.

$$NO \longrightarrow \tfrac{1}{2}N_2 + \tfrac{1}{2}O_2, \qquad \Delta H^o_{298K} = -91 \text{ kJ/mol} \qquad \text{(R-2.11)}$$
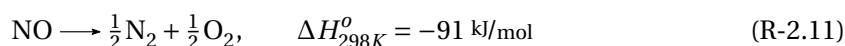
The simple NO decomposition is thermodynamically favored at lower temperatures (cf. Fig. 2.1) but does not occur spontaneously due to slow kinetics. Many efforts have been made to catalyze the reaction, and several materials have been found (e.g. iron or copper oxides supported on ZSM-5), but a suitable catalyst which is active and resistant enough are yet to be found [1,5,20–23]. Consequently, to reduce NO to N_2 selectively at sufficiently low temperatures, a catalyst must be applied. Although the specific type of catalyst may vary, the reduction of NO can efficiently be accomplished by a range of different reductants:

$$NO + H_2 \longrightarrow \tfrac{1}{2}N_2 + H_2O, \qquad \Delta H^o_{298K} = -333 \text{ kJ/mol} \qquad \text{(R-2.12)}$$

$$NO + CO \longrightarrow \tfrac{1}{2}N_2 + CO_2, \qquad \Delta H^o_{298K} = -374 \text{ kJ/mol} \qquad \text{(R-2.13)}$$

$$NO + CH_4 + \tfrac{3}{2}O_2 \longrightarrow \tfrac{1}{2}N_2 + CO_2 + 2H_2O, \qquad \Delta H^o_{298K} = -894 \text{ kJ/mol} \qquad \text{(R-2.14)}$$

$$4NO + 4NH_3 + O_2 \longrightarrow 4N_2 + 6H_2O, \qquad \Delta H^o_{298K} = -1632 \text{ kJ/mol} \qquad \text{(R-2.15)}$$
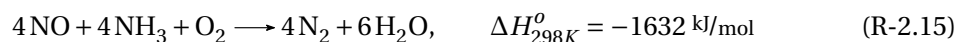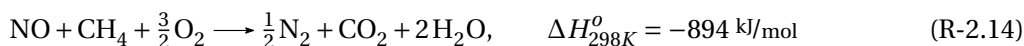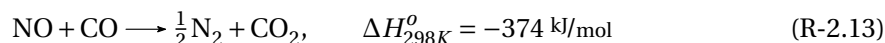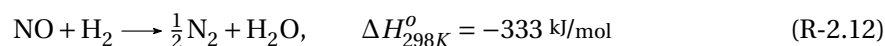
Comparing the above reactions with the direct NO decomposition in reaction R-2.11, an overall decrease in enthalpy is generally observed when applying a reductant, i.e. an increase in the exothermic character of the reactions. A corresponding trend is also observed in the Gibbs free energy change of the reduction reactions, which is collated in Tab. 2.1. With the decrease in Gibbs free energy change using H_2, CO , CH_4, and NH_3 as reductants, respectively, the corresponding equilibrium of the reactions is shifted further to the right, also compared with the Gibbs free energy change of the direct NO decomposition in reaction R-2.11 of $\Delta G^o_{298K} = -88$ kJ/mol.

Use of hydrogen as the reducing agent to remove NO (reaction R-2.12) is only applicable under anaerobic conditions, which is not the case with the SCR process. Reaction R-2.13 is used in reducing conditions. The reaction is exploited in the catalytic converters of cars, the so-called three-way catalyst [5]. The use of hydrocarbons, such as methane (reaction R-2.14), can constitute a suitable alternative to the traditional ammonia, which today is used in large stationary plants working in excess oxygen. However, the so-called HC-SCR is still not available for stationary plants on a commercial basis [14].

$$6NO + 4NH_3 \longrightarrow 5N_2 + 6H_2O, \qquad \Delta H^o_{298K} = -1815 \text{ kJ/mol} \qquad \text{(R-2.16)}$$
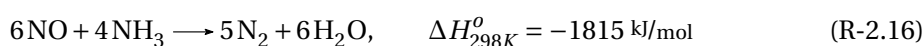
Tab. 2.1: Thermodynamic entities of the NO removal with different reductants

Reaction no.	Reductant	ΔH^o_{298K}	ΔS^o_{298K}	ΔG^o_{298K}	Eq. const., K_{298K}	
		[kJ/mol]	[J/mol K]	[kJ/mol]		
(R-2.12)	H_2	-333	-127	-295	$5.3 \cdot 10^{51}$	$bar^{-1/2}$
(R-2.13)	CO	-374	-99	-345	$2.6 \cdot 10^{60}$	$bar^{-1/2}$
(R-2.14)	CH_4	-894	-158	-847	$2.2 \cdot 10^{148}$	bar^0
(R-2.15)	NH_3	-1632	-340	-1531	$1.6 \cdot 10^{268}$	bar^1

Even though NO can be reduced with NH_3 based on the exothermic reaction R-2.16, the SCR process is usually performed with ammonia in the presence of oxygen, yielding reaction R-2.15, which has a substantial thermodynamic drive to the right (cf. Tab. 2.1). Furthermore, reaction R-2.16 is also performing much slower than the standard SCR reaction on vanadia-based catalysts (R-2.15), and therefore not relevant under lean (oxygen-containing) conditions[24].

If NO_2 is present in the gas, equimolar amounts of NO and NO_2 will react in a manner much faster than the standard SCR reaction (on a traditional vanadia-based catalyst)[25,26], the so-called *fast SCR* reaction:

$$2\,NO + 2\,NO_2 + 4\,NH_3 \longrightarrow 4\,N_2 + 6\,H_2O, \qquad \Delta H^o_{298K} = -1516 \; kJ/mol \tag{R-2.17}$$

NO_2 can be produced by introducing e.g. a platinum oxidation catalyst upstream of the SCR catalyst. However, if the NO_2 concentration downstream of the oxidation catalyst surpasses 50%, which can be removed via reaction R-2.17[24,26], excessive NO_2 can only react with ammonia.

$$6\,NO_2 + 8\,NH_3 \longrightarrow 7\,N_2 + 12\,H_2O \qquad \Delta H^o_{298K} = -2734 \; kJ/mol \tag{R-2.18}$$

However, reaction R-2.18 is slower than the standard SCR reaction[26], but may promote formation of other side products, such as N_2O, all ultimately decreasing the N_2-selectivity of the SCR reaction. The formation of the byproduct N_2O depends on the reaction temperature. At intermediate temperatures (~200-350°C) NO_2 will react with ammonia in the absence or presence of oxygen in the following manner:

$$8\,NO_2 + 6\,NH_3 \longrightarrow N_2O + 9\,H_2O, \qquad \Delta H^o_{298K} = -1595 \; kJ/mol \tag{R-2.19}$$

$$4\,NO_2 + 4\,NH_3 + O_2 \longrightarrow 4\,N_2O + 6\,H_2O, \qquad \Delta H^o_{298K} = -1074 \; kJ/mol \tag{R-2.20}$$
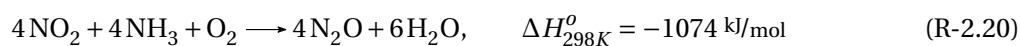
At high temperatures (>350°C) the thermodynamic equilibrium in reaction R-2.2 (Page 16) will settle at low space velocity, forming NO[26].

Chapter 3

Catalytic removal of NO$_x$

Introduction

Nitrogen oxides belong to a class of troublesome pollutants and also have substantial damaging effects on the environment. NO$_x$ is also involved in the formation of photochemical smog and acid rain, which is perturbing the ecosystem.

Nitrogen oxides plays an important role in the photochemistry involving ozone. NO$_x$ contributes to the depletion of stratospheric (located above the troposphere) ozone. The photochemical destruction of ozone is catalyzed by NO via the reactions [4]:

$$NO + O_3 \xrightarrow{h\nu} NO_2 + O_2 \qquad \text{(R-3.1)}$$

$$NO_2 + O \longrightarrow NO + O_2 \qquad \text{(R-3.2)}$$

Great efforts have been applied to reduce the emission of these pollutants through available technologies or by developing new methods [1,5]. Different catalytic abatement technologies have in particular been applied to both mobile sources [4,27–29] and stationary sources [30]. However, the focus here will be on catalysis for stationary applications, which will be described below along with a general introduction to catalysts for the selective catalytic reduction (SCR) in section 3.1.1. Finally, the results obtained during this work are presented in section 3.2.

3.1.1 SCR catalysts

The direct decomposition of NO into N$_2$ and O$_2$ (reaction R-2.11) does not occur selectively at reasonable temperatures without an appropriate catalyst, as discussed in Chapter 2. Although the NO$_x$ can be removed without the use of catalyst, such as in the so-called selective non-catalytic reduction (SNCR) which takes place at high temperatures between 850 to 1100°C [31], there are certain challenges with the SNCR process. The SNCR process can achieve the same efficiency in the NO$_x$ removal as in SCR, but practical constraints (longer residence time, narrow temperature window) limits the overall flexibility of the process [4,15]. However, when utilizing a catalyst, the temperature window can be decreased to around 200-650°C, while still maintaining a high conversion of NO$_x$ [30,31]. The SCR process was invented and patented in the US in 1959 [32] and has since the 1970s been used commercially on a worldwide basis (primarily in Japan and Europe, but the technology is developing in the USA and Asia [30]) to meet the legally proscribed NO$_x$ emission limits from stationary sources [5,6].

Ammonia has a key role in both the SCR and SNCR processes, due to the ability of ammonia to react with NO$_x$ to selectively form N$_2$, instead of being oxidized further by oxygen to N$_2$O as

other reactants (CO or hydrocarbons) would do [6,30].

The fact that roughly 80% of the stationary plants in Europe are removing NO$_x$ by use of the SCR process illustrates the size and importance of the technology [14]. However, there are still challenges that need to be addressed regarding the existing commercial catalyst, and further development is always possible in terms of improved efficiency, selectivity, and resistance to deactivation.

3.1.1.1   Commercial catalysts

In general, three types of catalyst systems have been developed for commercial SCR: noble metals, metal oxides, and zeolites [5,30].

The noble metals, developed in the 1970s, were very active in the selective reduction of NO$_x$. Unfortunately, they were also active in the oxidation of ammonia, and were soon succeeded by metal oxide catalysts [30].

Of the many catalyst combinations investigated, those based on vanadia supported titania promoted with tungsta (WO_3) or molybdena (MoO_3) were found to possess genuine advantages in NO reduction and SO$_2$ oxidation [30]. Today, after three decades of studies and industrial application, the most widespread commercial SCR catalyst is based on V_2O_5/TiO_2 formulations, such as $V_2O_5-WO_3/TiO_2$ and $V_2O_5-MoO_3/TiO_2$. The present catalysts are constituted of TiO_2 anatase supports with a monolayer surface coverage of V_2O_5 and WO_3 (or MoO_3), deposited by impregnation. The surface area of the catalysts is around 50-100 $^{m^2}$/g, with a V_2O_5 content of 0.5-3 wt% and WO_3 or MoO_3 loading of 5-10 wt%. Vanadia, especially as bulk, is responsible for the undesired oxidation of SO$_2$, and the vanadia content is thus generally kept low in the presence of high SO$_2$ concentrations [14,30]. Monolayer catalysts are more efficient than bulk V_2O_5 and utilizing TiO_2 anatase as support material relies on the fact that TiO_2 is only weakly and reversibly sulfated in presence of SO$_2$ and oxygen [33]. Furthermore, TiO_2-supported V_2O_5 possesses high acid site density and the vanadia is more readily distributed on the surface of TiO_2 anatase than on SnO_2 and ZrO_2 (only monoclinic zirconia tested) [30,34,35].

Commercial SCR catalysts are typically shaped in form of honeycomb monoliths, plates and coated metal monoliths with parallel channels. This gives several advantages over i.e. a packed bed: lower pressure drop, higher attrition resistance and lower tendency to plugging of fly ash [1].

Since Iwamoto et al. and Held et al. independently discovered in the 1990s that selective reduction of NO$_x$ takes place over a Cu-ZSM-5 catalyst [36] (and references herein), the SCR by hydrocarbons have been studied intensely. An unique feature of zeolite catalysts for SCR is that NO first has to be oxidized to NO$_2$, which is the rate-determining step of the reaction. The actual reaction taking place over zeolites is therefore the fast SCR reaction (reaction R-2.17). The NO$_2$ is produced on the metal centers (i.e. iron) of metal-exchanged zeolites, but the SCR reaction takes place in the zeolite framework. Zeolites on the acid form with transition metal centers present rather high SCR activity at high temperatures. However, their durability under hydrothermal conditions is still a challenge. Deactivation at temperatures above 500°C is always observed, where sintering of metal centers and dealumination initiates with resulting loss of surface area

and Brønsted acidity (cf. Tab. 3.1). Although vanadia-based catalysts have been introduced to diesel vehicles, zeolites do not have similar problems with SO_2 to SO_3 oxidation, low selectivity at higher temperature and the volatilization of the toxic vanadium species above 650°C [23,30] (and references therein). Even though zeolites exhibit high activity in the SCR process, they are primarily being developed for the automotive industry due to the higher cost of zeolites than conventional catalyst supports, such as TiO_2.

Tab. 3.1: General Brønsted/Lewis acid/base properties

	Acid	Base
Brønsted	Proton donor	Proton acceptor
Lewis	Electron acceptor	Electron donor

3.1.1.2 Vanadium-based catalysts

The properties of the TiO_2-supported V_2O_5 catalyst promoted with WO_3 (or MoO_3) have been extensively studied by numerous laboratories since its discovery as an active SCR catalyst several decades ago. The catalytic properties of the supported vanadium catalysts are evidently strongly affected by the vanadia loading, preparation method, and type of support and promoter. The type of metal oxide species present on the support surface is determined by the content of vanadium. At low loadings the isolated and monomeric VO_x species predominate, which, with increasing loading, will react to form dimeric and polymeric species until monolayer coverage is reached, illustrated in Fig. 3.1. The crystalline phase of V_2O_5 will dominate on the surface above monolayer coverage [37].
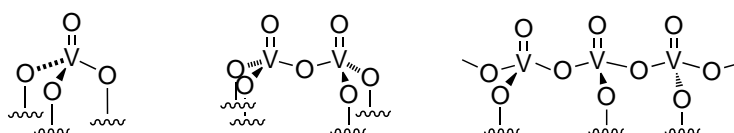
Fig. 3.1: Schematic figure of dispersed surface vanadates in their dehydrated form. Vanadia loading increasing from left to right

Although there have been significant contributions to the understanding of the SCR process over vanadium-based catalysts, an exhaustive elucidation of the mechanism has not yet been achieved.

It is widely accepted that both the titania support and V_2O_5 contain Lewis acidity, and that Lewis sites on vanadia under adsorption of H_2O can be converted into Brønsted acid sites [38,39], as depicted in Fig. 3.2. The ammonia species adsorbed on vanadia/titania-based catalysts therefore show two forms: coordinated NH_3 on the Lewis acid site and ammonium (NH_4^+) on the Brønsted acid site (Fig. 3.3). In accordance, two types of mechanisms are suggested, Lewis-NH_3-based and Brønsted-NH_4^+-based mechanisms.

Even though one of the first reaction schemes proposed for the SCR reaction was based on a Langmuir-Hinshelwood mechanism [40], there is a today general consensus that the SCR re-
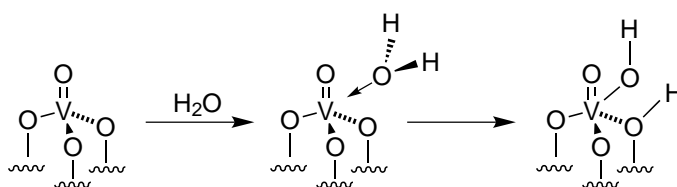
Fig. 3.2: Generation of Brønsted acid sites from Lewis acid site (surface vanadyl center). Adapted from Busca et al. [5]. However, the vanadium specie formed is here over coordinated, which should have resulted in cleavage of the weakest bond: the V-O-support bond

Lewis-bonded NH$_3$ Brønsted-bonded NH$_4^+$
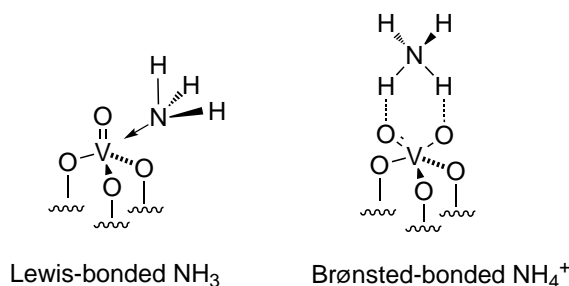
Fig. 3.3: Proposed structures for ammonia adsorbed on titania supported V$_2$O$_5$. Adapted from Busca et al. [5]

action occurs via an Eley-Rideal type mechanism, in which ammonia is first adsorbed on the vanadium-based catalyst, followed by activation with gas-phase NO [5,41–52]. Different proposals have been suggested for the adsorption mode of ammonia, which is still not fully elucidated. Inomata et al. [41,42] suggested that ammonia is first adsorbed at a Brønsted V^{5+}-OH site adjacent to a V^{5+}=O site. With isotopic labeling studies, Janssen et al. [43,44] suggested a dual site mechanism with V^{5+}=O as the easy reducible active species. According to the mechanism, ammonia is adsorbed on a V=O site as V−ONH$_2$ by reduction of the neighboring V=O site to V-OH. Ozkan et al. [49,50] applied isotopic labeling of ^{18}O$_2$, ^{15}NH$_3$, ^{15}NO, and ^{15}N^{18}O to suggest that ammonia adsorbs on Brønsted pairs of V-OH, forming ammonium ion species (cf. Fig. 3.3, right). Topsøe et al. [45–47] and Gasior et al. [48] proposed that predominantly Brønsted acid sites (V-OH) were responsible for the ammonia adsorption and subsequent formation of an activated complex in concert with an adjacent vanadyl group. The mechanism they suggested (reproduced in Fig. 3.4) is a perfected version of that proposed by Inomata et al. [42]. Density functional theory (DFT) performed on V$_2$O$_5$ show that ammonia interacts with Brønsted acid sites, and together with NO reacts to form the intermediate NH$_3$NHO, which undergoes a series of hydrogen-transfer steps on the vanadia cluster to form adsorbed NH$_2$NO species that decomposes to N$_2$ and H$_2$O and a reduced vanadium oxide cluster [53,54]. In contrast, Ramis et al. suggested that the presence of Brønsted acid sites is not a prerequisite for the SCR reaction to occur [38,51,52]. Based on FTIR studies, the authors propose that ammonia is adsorbed on Lewis acid sites and is activated to from adsorbed amide NH$_2$ species, which then can react with gaseous NO to give an intermediate nitrosamide (NH$_2$NO) that is known to decompose into N$_2$ and H$_2$O. The authors investigated the spectra region where ammonia is coordinated (1300–1100 cm^{-1}), a region which Topsøe et al. did not include in their publications, even though Lewis coordinated NH$_3$ show
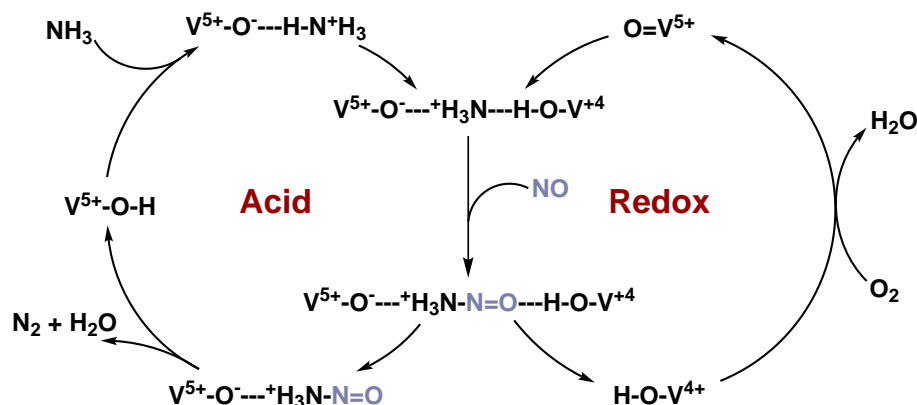
Fig. 3.4: Catalytic cycle of the SCR reaction on vanadia/titania in the presence of O_2, proposed by Topsøe et al. [45,46]

a significant band in this spectral range. Recent DFT calculations performed by Soyer et al. [53] on a $V_2O_9H_8$ cluster have, however, showed that Lewis acidic adsorption of ammonia is highly unfavorable.

Even though the *Brønsted-NH$_4^+$* mechanism has gained the major support in the literature, it should be noted that it is still a hypothesis and lacks solid experimental evidence under *in situ* conditions. It can thus not be ruled out that the SCR reaction on vanadia/titania (dependent on the reaction conditions) proceeds through several mechanisms involving both types of acid sites.

3.1.1.3 Role of promoter and support material

As already mentioned, the commercial SCR catalyst is based on vanadia/titania formulations, such as $V_2O_5-WO_3/TiO_2$ and $V_2O_5-MoO_3/TiO_2$. According to Chen and Yang[55] (and references herein), the advantages of adding WO_3 to the catalyst as promoter are numerous: stabilization of the metastable anatase phase of TiO_2; broadening the operating temperature window; increase of the surface acidity; decrease of the ammonia oxidation activity; decrease of the activity for SO_2 oxidation; and improved resistance towards alkali poisoning. DFT has been performed on the $V_2O_5-WO_3$ system, where it was suggested that addition of tungsten oxide lead to enhanced probability of the dissociation of water molecules, thereby forming more Brønsted acid sites[56]. Lietti et al.[57] performed a comparative study of $V_2O_5-WO_3/TiO_2$ and $V_2O_5-MoO_3/TiO_2$ catalysts in the SCR reaction, and found that although MoO_3-based catalysts are more active they are also less N_2-selective than the corresponding WO_3-based catalysts. However, both 'additives' acts as structural promoters, by preventing the sintering of the TiO_2 matrix.

Sulfate has also been applied as promoter for the SCR catalyst, and is suggested to have a promoting effect on the SCR activity due to significant increase in Brønsted acidity (if water is present. The surface sulfate species on the catalyst can originate from impregnation or treatment with i.e. H_2SO_4 or $(NH_4)_2SO_4$ solutions, or from the gaseous SO_2 if present in flue gas[5]. The surface acidity of the sulfate-promoted catalysts is even higher than the correspond-

ing WO$_3$-promoted catalysts [38,55,58]. Sulfate (like WO$_3$) was shown to have an inhibiting effect on the phase transformation from TiO$_2$ anatase to rutile [59], and to increase the number and strength of surface acid sites [60,61]. However, TiO$_2$ is only weakly and reversibly sulfated at normal SCR conditions due to the low sulfate stability on the titania surface. If WO$_3$ or MoO$_3$ is present on the surface, they will compete and displace SO$_3$ on the basic sites of titania, consequently limiting the sulfate absorbed from gaseous oxidized SO$_2$ [5]. On the other hand, sulfation of ZrO$_2$ or Al$_2$O$_3$ is more favorable with regard to sulfate stability. Titania-based catalysts are therefore only partially surface-sulfated during SCR operation in the presence of SO$_2$ [5,30,59,62].

Hamada et al. [63] were the first to report of SCR active sulfated metal oxides (TiO$_2$, Al$_2$O$_3$, ZrO$_2$, Fe$_2$O$_3$). The most promising catalysts of this type have been shown to consist of transitions metals supported on ZrO$_2$ or SO$_4^{2-}$/ZrO$_2$ for the SCR of NO with NH$_3$ [64] and with hydrocarbons [64–66]. Sulfated zirconia was first reported by Hino and Arata [67] to possess unusually high acidic properties, and was suggested to be a so-called solid superacid. A superacid is a medium having an acidity higher than 100 wt% H$_2$SO$_4$ [7], such as HF or HSO$_3$F. Superacidity can also be expressed with the Hammet scale, H$_0 \leq$ -11.93 [68], although some authors disagree on whether sulfated zirconia is in fact a solid superacid [69] (and references herein). However, a general issue regarding the characterization of sulfate-doped samples is that the acidic and catalytic properties depend on a large number of preparative variables, such as; calcination temperature; sulfate content; concentration of sulfate solution; sulfate precursor; crystal phase; surface area and sample activation [70–73]. The most abundant use of this type of solid acids has been for alkane isomerization reactions, but a review on the wide range of reactions that sulfated zirconia can catalyze have been collected by Yamaguchi et al. [74] and Jin et al. [75].
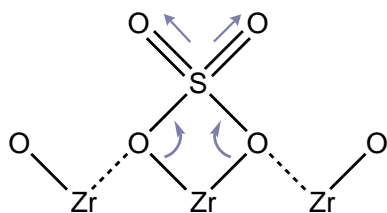
Fig. 3.5: Proposed Lewis acidic site structure of sulfated zirconia. Reproduced from Yamaguchi [74]
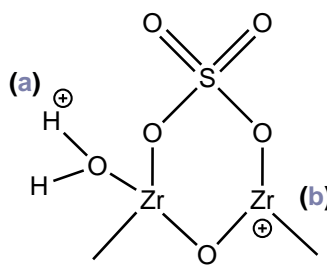
Fig. 3.6: Proposed structure where both Brønsted (a) and Lewis acid sites (b) are present. Reproduced from Arata and Hino [76]

Although there is a generally consensus that the presence of sulfate species with covalent S=O bonds are necessary to achieve superacidity [76] (and references herein), the exact nature of the acidic sites remains unknown [71]. Dunn et al. [77] report that the sulfated species present on TiO$_2$, ZrO$_2$, and Al$_2$O$_3$, with similar vanadia loading, all have identical molecular structures, i.e. (M−O)$_3$=S. Morterra et al. [70] reported that the monoclinic phase of ZrO$_2$ is not active in the isomerization of butane. Thus, the sulfate acid site formation is weaker on phases of zirconia other than the tetragonal. This has been confirmed recently by DFT calculations, where it was found that the affinity for SO$_3$ absorption on t-ZrO$_2$ was significantly larger than on the cor-

responding cubic and monoclinic crystal configurations, due to stabilization by abstraction of oxygen atom from the tetragonal phase[78] (knowing this can be an useful indicator of the crystal phase of zirconia in acid-catalyzed studies where the ZrO_2-phase is not reported, e.g. in[79]). Jin et al.[75] suggested that the acid centers are Lewis sites, and associated with the metal cation. The strength of this Lewis site is enhanced by the strong ability of the sulfur complex to absorb the electrons as outlined in Fig. 3.5. Others suggest the simultaneous presence of Brønsted and Lewis acid sites at hydrated conditions[76,80], depicted in Fig. 3.6. However, the Brønsted acid sites are readily interconverted to Lewis sited by evacuation at temperatures above 150°C[71].

Even though sulfated zirconia show stronger acidic sites than tungstated zirconia[72,79], sulfate species have been shown desorb from the surface during thermal treatment, above ca. 700°C[71,72]. Therefore, in terms of thermally stability, WO_3/ZrO_2 can be suggested as an alternative solid acid catalyst. Sohn and Park[81] found that a tungstate concentrations of 20 wt% on zirconia, resulted in maximum surface area and acidity. Surface coverage, n_s, can be calculated with expression 3.1, where N_A is Avogadro's number, S_{BET} the surface area, and c_W the metal loading [g/g].

$$n_s = \frac{c_W N_A}{M_W S_{BET} \cdot 10^{18} \text{ nm}^2/\text{m}^2} \Rightarrow \frac{\frac{0.159 \text{ gW/g}}{183.84 \text{ g/mol}} \cdot 6.022 \cdot 10^{23} \text{ mol}^{-1}}{155 \text{ m}^2/\text{g} \cdot 10^{18} \text{ nm}^2/\text{m}^2} = 3.35 \text{ WO}_x/\text{nm}^2 \qquad (3.1)$$

Assuming surface area of $155 \text{ m}^2/\text{g}$, the surface coverage of 20 wt% WO_3/ZrO_2 can be calculated to $3.4 \text{ W}/\text{nm}^2$, which according to Wachs measurements of monolayer coverage outlined in Tab. 3.2, corresponds to submonolayer coverage. However, Zhou et al.[82] have reported polytungstate cluster formation at loadings below monolayer coverage, already at $2.9 \text{ W}/\text{nm}^2$. Thus, the reported two-dimensional polytungstated species which has been suggested to be important for generation of strong acid sites[83], could possibly be formed below monolayer coverage.

Tab. 3.2: Monolayer surface coverages of supported metal oxides (atoms/nm²) obtained by Raman and IR studies. Adapted from Wachs[84] (and references herein)

	Al_2O_3	TiO_2	ZrO_2	SiO_2
V	7.3	7.9	6.8	0.7
W	4.0	4.2	4.0	0.1
Mo	4.6	4.6	4.3	0.3

Naturally, the dispersion and surface species strongly depend on the nature of the support, as can be envisaged in Tab. 3.2. For example, distributing vanadia on the surface of SiO_2 results in formation of polycrystalline V_2O_5 already at very low loadings, whereas on Al_2O_3, TiO_2, and ZrO_2 much more vanadia (almost an order of magnitude) can be added to the support before crystalline V_2O_5 is formed. The low surface coverage of metal oxides on silica are due to the lower reactivity and density of surface hydroxyls compared to the other metal oxides[84]. A comparative study of the surface acidity of various promoted metal oxides was performed by Niwa et al.[79]. The authors found that for the metal oxides studied (SnO_2, ZrO_2, TiO_2, and Al_2O_3) strong acidity is obtained following the sequence, $SO_4^{2-} > WO_3 > MoO_3 > V_2O_5$. Dunn et al.[33]

performed a comparative study of the SO_2 oxidation activity ability of 1 wt% loaded V_2O_5 catalysts, and found the following trend: $V_2O_5/CeO_2 > V_2O_5/ZrO_2 > V_2O_5/TiO_2 > V_2O_5/Al_2O_3 > V_2O_5/SiO_2$.

Finally, even though tungsta-promoted titania has traditionally been used as a commercial SCR catalyst, other catalyst combinations options exist that can be tuned depending on the operational requirements, e.g. temperature of operation, SO_2 or deactivating species in flue gas.

3.1.2 Catalyst deactivation

The mechanism of catalyst deactivation can be subdivided into three classes: poisoning, coking and sintering. Other types of deactivation include masking, volatilization of active elements, erosion and attrition[85]. Throughout the thesis, the primary area of focus will be on the chemical deactivation by poisoning.

3.1.2.1 Inorganics in coal and biomass

Naturally, the SCR catalyst is exposed to many different gaseous species, depending on the type of fuel combusted in the power plant. Natural gas comprise a relatively clean combustion gas, whereas combustion of e.g. municipal waste or straw often contain species that can lead to possible deactivating of traditional vanadia-titania-based SCR catalysts. The composition of various species of both fuel and ash associated with commercial or pilot plants currently combusting or co-combusting biomass have recently been reported[86–88]. All studies show a significant increase in the quantity of alkali and alkaline-earth elements (K, Na, Mg, Ca), phosphorous and chlorine in the biomass-based fuels compared to coal. The quantity of potassium and chlorine

Tab. 3.3: Fuel composition. Moisture, volatiles and ash-concentration are given on a wet basis, all other elements on dry basis. Adapted from Zheng et al.[87]

	COPRIB[†]	SAKLEI[‡]	Lignite	Straw
	[wt%]			
Moisture	2.00	2.00	2.00	6.70
Volatiles	39.53	24.07	51.85	68.76
Ash	5.00	14.49	5.28	7.37
C	76.14	71.51	62.70	44.80
O	11.59	6.55	-	-
N	1.41	1.75	0.71	1.10
S	0.81	0.63	0.40	0.20
Cl	0.01	0.01	0.05	0.73
P	0.004	0.11	0.02	0.14
Ca	0.06	0.93	1.17	0.42
Mg	0.03	0.16	0.19	0.10
Na	0.01	0.02	0.01	0.02
K	0.07	0.08	0.01	1.90

[†] Columbia high volatile bituminous coal
[‡] South Africa medium volatile bituminous coal

in the straw can be more than an order of magnitude higher than that of coal (cf. Tab. 3.3). Especially the high content of potassium in e.g. wood and straw is of concern, which will be further

discussed in section 3.1.2.2. On the other hand, the sulfur content in biomass is typically lower in biomass than in coal. Zheng et al.[87] showed a clear relationship between sulfur in fuel and SO_2 emission. Thus, by firing or co-firing with biomass a reduction of SO_2 in the flue gas is expected.

There are several practical concerns when these constituents enter the boiler in higher concentrations: high-temperature corrosion due to chlorine; accelerated slagging; and fouling[88]. A major problem regarding the application of SCR catalysts has been their deactivation by different components in the flue gas. This issue is addressed in the following.

3.1.2.2 Effect of alkali on vanadia-based catalysts

Alkali metals were identified early as poisons for vanadia-titania-based SCR catalysts by Chen and Yang[89], where they found that the strength of the poison is related to the increase of basicity. Since then, the effect of alkali species on the vanadia-based catalyst have been reported by several groups[55,72,85,86,88,90–98]. Although the alkali-vanadium system has been intensively studied, the exact role of the dopants on the supported vanadium oxide at the molecular level are still a subject of discussion. Most authors agree that potassium is severely deactivating the traditional $V_2O_5-WO_3-TiO_2$ catalyst, although tungsta is partially inhibiting the deactivating effect[55,85,86,90–92,94,95,98,99]. Numerous TPD and spectroscopic studies show that the deactivating nature of potassium is clearly connected with a reduction of the V_2O_5 Brønsted acid sites of the catalyst[90–92,98,99]. However, only a limited number of studies have been performed on WO_3-containing catalysts[85,91,92,94,95,98]. Loss of Brønsted acid sites, as discussed in section 3.1.1.2, would reduce catalyst activity severely, since they are vital for the SCR reaction to occur.

The deactivating effect of potassium on an industrial reference catalyst with the formulation 3 wt% $V_2O_5-WO_3-TiO_2$ is illustrated in Fig. 3.7, where an increasing degree of potassium is deposited on the catalyst. Although a high SCR activity (expressed by the first order rate constant) is obtained for the fresh catalyst, the impact of potassium is significant, almost completely deactivating the catalyst at K/V ratio of 0.3 mol/mol. Experimental details regarding catalyst extraction from the commercial monolith is described in section A.2.1 (page 89).
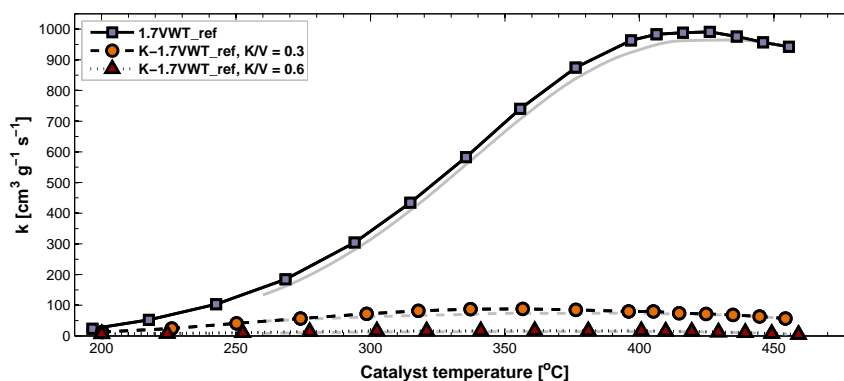

Fig. 3.7: SCR performance of commercial 1.7VWT_HT catalyst with increasing potassium loading.

Theoretical studies regarding the adsorption of potassium on the pure surface of TiO_2 ru-

tile [100,101] were initially performed, but recent theoretical DFT studies have addressed the alkali-vanadia system [72,99,102–104]. Zheng et al. [105] suggested an early mechanism, based on a substitution reaction on the Brønsted site, whereby the reactive site is blocked by potassium:

$$-V-OH \xrightarrow[-HCl]{KCl} -V-O-K \qquad\qquad \text{(R-3.3)}$$

This mechanism require an equimolar ratio of vanadium and potassium to completely deactivate the catalyst. Although the model provides a very intuitive understanding of the deactivation, several groups report of almost complete loss of catalyst activity already at K/V ≈ 0.5 (mol/mol) [85,89,93,94] (see also Fig. 3.7), which suggests that potassium blocks multiple active sites. Recent DFT studies suggest mechanisms in better agreement with experimental findings. Witko et al. [102] and Nicosia et al. [99] both studied the addition of one alkali atom to clusters of $V_{10}O_{31}H_{12}$ and $V_6O_{20}H_{10}$, respectively, which in practice would resemble crystalline V_2O_5. Based on their findings, they suggested that the deactivating agent preferentially occupy hole sites between four V_2O_5 centers, thereby inhibiting both Brønsted and V^{5+}=O sites. Calatayud and Minot [103] used smaller V_2O_5 clusters, but added the substrate titania anatase to the model. With a K/V concentration of 0.5, they suggested that potassium is interacting with the oxygens of two neighboring vanadia units (bridging V-O-Ti and terminal V=O) and the support, as shown in Fig. 3.8.
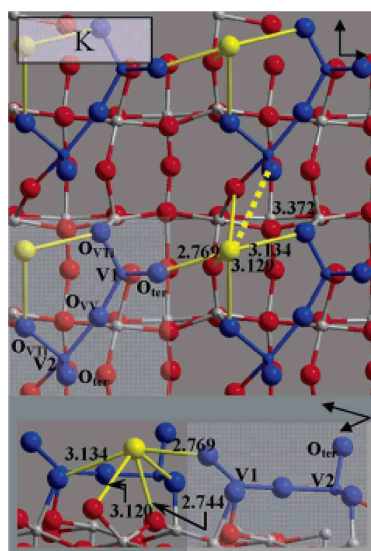
Fig. 3.8: Suggested structure for coordination of potassium to several vanadia and titania sites. Yellow: K, blue: V_2O_5, Red: oxygen, Gray: Ti [103]
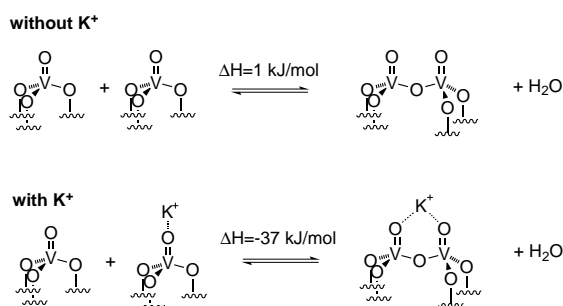
Fig. 3.9: Previously proposed potassium-induced dimerization model [72]

All the proposed models of the alkali doping of vanadia can explain the observed elongation of the V=O bond, readily observed in Raman spectroscopy, and a reduction in the reducibility of the K-doped catalyst compared to the fresh catalyst [72,91,104,106,107]. Lewandowska et al. [104], Kiwi-Minsker et al. [106], and Calatayud et al. [103] report that alkali doping would counteract the polymerization of vanadia-units by stabilization of the vanadium cluster. Furthermore, Kiwi-Minsker et al. reported of the disappearance of monomeric vanadium species upon potassium

doping, which fit well with the findings suggested in Fig. 3.9. This suggests that potassium is also involved in the reaction and cleavage of bridging V-O-V bonds.

The apparent disagreements between the reactivity of different vanadium-based clusters reported in the theoretical literature was recently addressed by Calatayud et al. [108]. Based on periodic calculation of V_2O_5 compounds as gas-phase clusters, single crystals and supported on titania, they report significant differences in reactivity dependent on the choice of model cluster. This issue can be extrapolated to the conflicting reports in the literature of how alkali atoms could bind to the active sites. The nature of potassium coordination to the active sites of the vanadium catalyst would strongly depend on the vanadium oxide cluster model for the DFT calculation. Hence, a study of the alkali coordination on molecule models with various vanadia loadings, promoted with e.g. sulfate, tungsta, supported on substrate is strongly required.

3.1.2.3 Deactivation overview

The content of possible poisons in the fuel for e.g. municipal solid waste (MSW) or biomass incineration can vary significantly. Many parameters besides the fuel composition influence the activity of the SCR catalyst e.g. particle size of poison in flue gas; placement of catalyst in high- or low-dust positions; temperature of operation; scrubbing etc. Hence, it is feasible to evaluate the potential deactivation of the catalyst in a comparable way for the different fuel types, which is attempted in table 3.4, where the impact on the traditional SCR catalyst for different fuel types, based on the fuel composition is collected.

Tab. 3.4: Estimation of the degree of deactivation (χ) of the traditional vanadia-based SCR catalyst based on fuel composition (dry basis). $\chi = 5$: Severe deactivation, $\chi = 1$: Negligible effect

	MSW			Wood			Forrest Residues			Straw			Coal		
	χ	wt%	Ref	χ	wt%	Ref	χ	wt%	Ref	χ	wt%	Ref	χ	wt%	Ref
Na	1–2	0.2	[109]	1	0.02–0.1	[85]	1–2	0.01–0.05	[86]	1–2	0.05–0.3	[85]	1–2	0.02	[110]
S	1–2	0.2	[111]	1	0.05–0.1	[85]	2	0.02–0.05	[86]	1	0.1–0.2	[85]	2–3	1–2.2	[110]
Cl	2–3	0.62–0.9	[109,111]	1	0.02–0.1	[85]	1–2	0.01–0.03	[86]	2–3	0.1–1.1	[85]	1–2	0.02–0.25	[110]
K	1–2	0.2	[109]	1–3	0.05–0.4	[85]	2	0.1–0.2	[86]	4–5	0.2–1.9	[85]	1	0.06–0.07	[110]
Zn	2	0.09–0.16	[109,111]	2–3	0.015	[112]	1–2	1.5 ppb†	[113]	1–2	< 0.01	[112]	2	0.06	[111]
Pb	1–2	0.01–0.04	[109,111]	1–2	< 0.01	[112]	1	0.05 ppb†	[113]	1	< 0.01	[112]	1–2	< 0.01	[111]

† Measured in flue gas, particle diameter <1µm

Considering the incineration of biomass, it can be concluded from table 3.4 that alkali, especially potassium, has to be considered as potential poison for the traditional SCR catalyst when significant amounts of straw is burned.

3.1.2.4 Alkali-resistant SCR catalyst

Although tungsta is added to the $V_2O_5-TiO_2$ formulation to decrease the poisoning effect of alkali, the traditional catalyst is still far from being resistant to deactivating agents typically found in the flue gas of biomass, confirmed by several full-scale experiments with the $V_2O_5-WO_3-TiO_2$ catalyst [85,88,95,110]. As concluded in previous sections, the basic potassium is blocking the Brønsted V_2O_5 acidic sites of the working SCR catalyst, as schematically illustrated in Fig. 3.10.

Several approaches can be applied to design a SCR catalyst more resistant to alkali. One
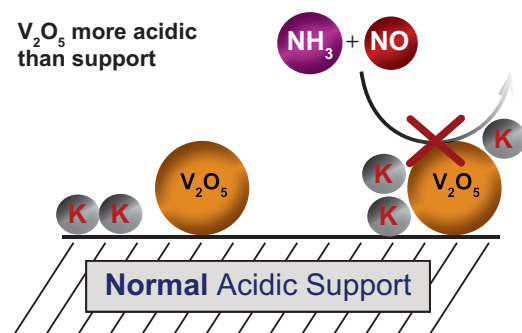
Fig. 3.10: Schematic view of alkali-deactivated catalyst, where the acidic V$_2$O$_5$ is attracting the deactivating basic potassium
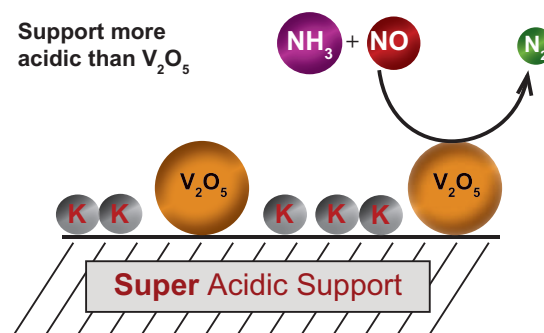
Fig. 3.11: Illustration of alkali-resistant SCR catalyst, where the relatively more acidic support is hosting incident potassium, leaving vanadia sites vacant and active

procedure is to increase the acidity of the substrate, which would have a stronger interaction with potassium than the active vanadia sites, which is illustrated in Fig. 3.11. As suggested in section 3.1.1.3, sulfated zirconia possesses very strong acidity, and is thus a suitable candidate, alongside tungstated zirconia. Another approach is based on substituting the active species of the catalyst. A crucial part of the mechanism is the Brønsted acid sites of vanadia, which is much more affected than the Lewis acid sites by potassium doping. Hence, by using metal oxides which mainly possess Lewis acidity, the catalyst could avoid deactivation by alkali. CuO and Fe$_2$O$_3$ are attractive under these conditions, since they are well known Lewis acids [51] and have also exhibited NH$_3$-SCR activity [1,5]. This approach method has already been applied by Kustov et al. [93,114]. However, only sulfated monoclinic ZrO$_2$ was investigated in the study, whereas the sulfated tetragonal zirconia contain much higher acidity (discussed in section 3.1.1.3). Tungstated zirconia has also previously been investigated in our group as a support material for vanadia loaded SCR catalysts with promising results [115]. Finally, as a more exotic

Fig. 3.12: Schematic NO removal by gas capture in solvent

non-catalytic method of NO removal, is by means of gas capture in ionic liquids as illustrated in Fig. 3.12. The technology has already been used for CO$_2$ (although some challenges are still to be overcome [116]) and SO$_2$ absorption, but has never been applied to the removal of NO. All three approaches will be explored in the following thesis.

3.2 Zirconia-based catalyst systems

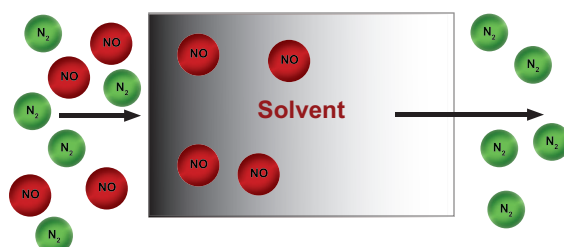This section is dedicated to the study of ternary SCR catalysts, consisting of metal oxide as active phase, sulfate as promoter and zirconia as support material. The sulfated zirconia is loaded with the oxides of vanadium, iron and copper.

3.2.1 Vanadium-based catalysts

Early in the study of zirconia-based catalysts, we found that a line of commercial zirconia-based samples from Saint-Gobain Norpro (NP) proved suitable as support material, competitive with the SCR activities of vanadia-loaded synthesized zirconia which was previously published [72]. Since the zirconia already was commercially available on extruded form (pellets), the exploitation of this material as possible SCR catalyst is a step closer to industrial relevance. Hence, the commercial zirconia is forming the frame for all the ternary catalysts synthesized in the following sections.

The initial selection of suitable support materials, was primarily based on the surface area and crystalline form. As earlier discussed (section 3.1.1.3), the monoclinic phase of ZrO_2 provides weak acid sites when sulfated, whereas the tetragonal form is responsible for the generation of strong acid sites [70,117]. Zirconia has three stable polymorphs: tetragonal ($t-ZrO_2$), monoclinic ($m-ZrO_2$), and cubic ($c-ZrO_2$), and the occurrence and transformation between the phases depend on doping and/or thermal treatment. The monoclinic phase is stable up to 1050°C, where it transforms into the tetragonal phase, which further changes into the cubic phase at 2400°C. The cubic phase of zirconia is stable up to the melting point at about 2700°C. Thus, tetragonal and cubic ZrO_2 are only metastable phases below 1050°C, where monoclinic is the thermodynamically preferred form. In the case of i.e. sulfate or tungstate promoted zirconia catalysts, the crystalline structures of the samples behave differently from that of pure ZrO_2. Amorphous zirconia has been reported to undergoes crystallization around 350-450°C [81,118], but when doping the matrix with e.g. a promoter, the phase transition temperature from amorphous to tetragonal zirconia is shifted to higher temperatures [72,76,81,115]. Zirconia is thus a grateful material to work with, because it can easily be stabilized in its tetragonal phase by e.g. a promoter, which hinders the phase transition to monoclinic.

3.2.1.1 ZrO$_2$ crystal phases

With XRD it is easy to identify the monoclinic phase of ZrO_2, whereas tetragonal and cubic zirconia can be difficult to distinguish between. However, by refining the XRD data with the Rietveld method (further description in Appendix A), it is possible to discriminate the abundance of the $c-ZrO_2$ from $t-ZrO_2$. In Fig. 3.13 is the diffraction patterns of the commercial supports depicted together with the difference curve from the Rietveld fit. If the Rietveld analysis results in a perfect fit, accounting the presence of all phases present, the difference curve would yield a straight line, located on the baseline.
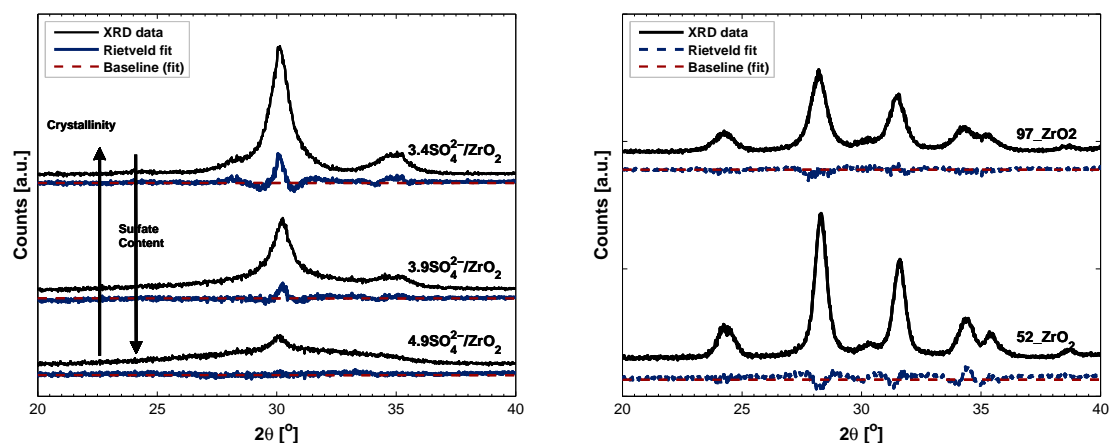
Fig. 3.13: Powder X-ray diffraction and Rietveld refinement of commercial zirconia-based supports from Saint-Gobain Norpro. Left: SO$_4^{2-}$/ZrO$_2$-based, right: ZrO$_2$-based

From the diffraction patterns in Fig 3.13 it is clear that the pure ZrO$_2$ samples primarily consist of monoclinic ZrO$_2$, whereas the samples containing sulfate mainly contain tetragonal and cubic ZrO$_2$. The numbers in the name of the pure zirconia samples correspond to their surface area (m^2/g), and in the sulfated samples they denote the loading of sulfate measured as SO$_3$ (wt%) (from here on, sulfate is abbreviated as *S*, and zirconia as *Z*). Through Rietveld refinement the phase distributions can be obtained, which is collected in Tab. 3.5. Although synthesis details for these commercial materials not can be obtained, a trend can be extracted regarding the concentration of sulfate versus the crystallinity, being inverse proportional. Assuming that the sulfated materials are calcined under similar conditions, the degree of crystallinity obtained agrees well with results from literature, where increasing the dopant would retard the temperature of crystallization [81].

Tab. 3.5: Properties of commercial zirconia samples. The phases (tetragonal, cubic and monoclinic) of zirconia are given as volumetric percent of the crystalline phase. Full TPD profile are shown in Fig. 3.15

Sample	BET Area	Crystallinity[†]	Phase distribution			Surface acidity	
			t−ZrO$_2$[‡]	c−ZrO$_2$[‡]	m−ZrO$_2$[‡]	Total*	<500°C
	[m^2/g]	[%]		[Vol%]			[μmol/g]
52Z_NP	52	75	3	0	97	372	372
97Z_NP	97	100	0	0	100	648	648
3.4SZ_NP	145	73	10	67	23	2004	896
3.9SZ_NP	130	60	5	36	59	2109	785
4.9SZ_NP	125	53	3	58	39	2351	910
1.7VWT						1324	930

[†] Calculated in software program Winprep
[‡] Phase distribution found through Rietveld refinement
* Total amount of desorbed NH$_3$ in temperature range 100-1000°C

The phase distribution of the three crystalline ZrO$_2$ configurations of the commercial samples are outlined in Tab. 3.5, where the two pure ZrO$_2$ samples consist almost entirely of monoclinic ZrO$_2$. The sulfated samples are all polymorph mixtures, comprising mostly of monoclinic

and cubic zirconia. Only 3.4SZ_NP holds significant amounts of the tetragonal phase, namely 10 vol%. However, the high content of c-ZrO_2 in the samples is slightly surprising when comparing with literature. The majority of XRD-studies on promoted zirconia report only of the monoclinic and tetragonal ZrO_2 phase, only using the strong (111) reflection around $30°$ 2θ of the latter phase, without mentioning the cubic phase[65,70,117–119]. Only a few distinguishes the phases[120,121]. On the other hand, differentiation between the two is not straight forward, and only few differences exist, as can be seen in Fig. 3.14, where the diffraction pattern from the three phases have been calculated. Only using the (111) reflection line would therefore not be enough
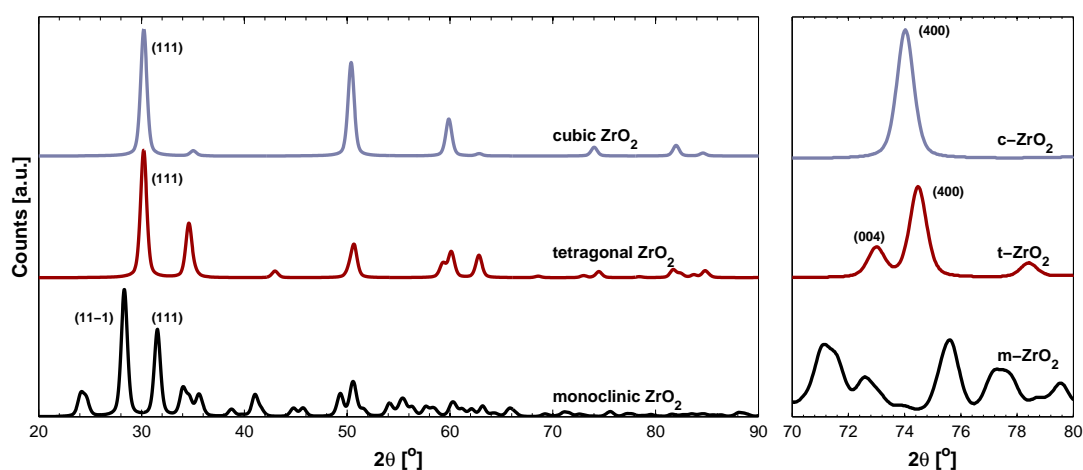
Fig. 3.14: Calculated diffraction patterns of the three phases of ZrO_2. The plots are for CuK$_{\alpha 1}$ X-rays. Unit cells of zirconia: **m-ZrO_2** (spacegroup P2$_1$/c), a = 5.107 Å, b = 5.174 Å, c = 5.332 Å, $\alpha = \gamma = 90°$, $\beta = 99°$; **t-ZrO_2** (spacegroup P4$_2$/nmc), a = b = 3.6 Å, c = 5.18 Å, $\alpha = \beta = \gamma = 90°$; **c-$ZrO_2$** (spacegroup Fm3m), a = b = c = 5.118 Å, $\alpha = \beta = \gamma = 90°$

to discriminate t-ZrO_2 from c-ZrO_2, which is located at almost the same angle. However, the relative intensity of the (111) reflection to the line of $\approx 35°$ 2θ or the (004) reflection at $73°$ 2θ can by used to identify the tetragonal phase.

3.2.1.2 Determination of surface acidity

The ammonia desorption profiles of the commercial samples are depicted in Fig. 3.15. The total amount of adsorbed ammonia, which is listed in Tab. 3.5, corresponds to molecular adsorbed ammonia or ammonium ions on Lewis or Brønsted acid sites, respectively. The relative strength of the acid sites are reflected by the temperature of maximum ammonia desorption, these are listed in the figure legend.

The broad nature of the low-temperature desorption peaks of sulfate zirconia in Fig. 3.15 can be attributed to a wide range of surface acid sites present with different acid strengths. However, categorizing the exact nature of the acid sites are not possible with NH_3-TPD alone, but a commonly used technique is infrared spectroscopy (IR) coupled with pyridine adsorption, where the lone pair of nitrogen in pyridine can coordinate to Lewis acid sites and react with Brønsted sites (forming the pyridinium ion), giving yield to different IR signals which can be used to

Fig. 3.15: NH$_3$-TPD profiles of the commercial supports and 3V$_2$O$_5$-10WO$_3$−TiO$_2$ reference catalyst. The amount of desorbed ammonia is listed in Tab. 3.5
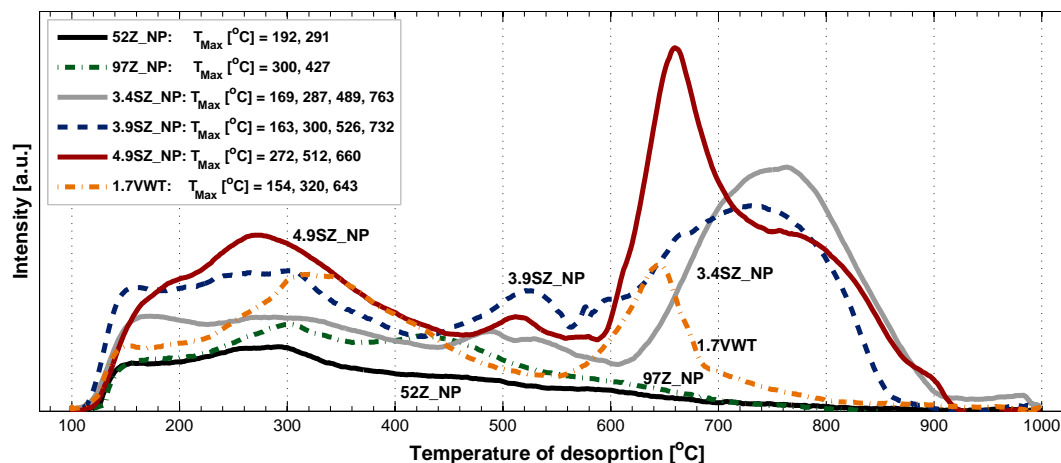
differentiate between the two acid sites. Barthos et al.[122] used combined TPD and frequency response (further description of method in [123]) on sulfated zirconia and determined a number of Lewis acid sites desorbing ammonia around 300-430°C and a peak around 470°C attributed as the Brønsted acid site.

The TPD curve for the supports 52Z_NP and 97Z_NP showed a bi- and tri-modal desorption profile with peaks at about 190, 300, and 427°C, whereas no desorption peaks are observed at higher temperatures. The overall acidity (listed in Tab. 3.5) of the two pure monoclinic ZrO$_2$ samples contain an order of magnitude less surface acidity compared to the sulfated ZrO$_2$. Only desorption peaks above 430°C are observed for sulfated zirconia, which tentatively can be attributed to the presence of Brønsted acid sites[122], which does not exist on the pure monoclinic ZrO$_2$. Moreover, the absence of any ammonia desorption peak of 1.7VWT around 430°C, suggests a low concentration of Brønsted acid sites on this type of catalyst.

At lower temperatures, roughly two types of acid sites can be identified on the sulfated samples, one around 165°C, which is likely to originate from very weakly bound or physisorbed ammonia, and one at around 270-300°C. A number of high-temperature peaks exist for the sulfated samples, the strongest at 660°C, 732°C, and 763°C for 1.7V-4.9SZ_NP, 1.7V-3.9SZ_NP, and 1.7V-3.4SZ_NP, respectively. The temperature of desorption from these strong acid sites are consistent with the findings of Barthos et al.[122], which detected ammonia desorption on sulfated zirconia at about 630°C, attributed to be of Lewis-acid nature. Besides the very low temperature desorption peaks observed around 165°C in Fig. 3.15, the Brønsted and Lewis acid site designation of Barthos et al. could tentatively be extrapolated to the results observed of the commercial sulfated ZrO$_2$. However, the NH$_3$-desorption peak of 3.9SZ_NP and 4.9SZ_NP from the apparent Brønsted acid site are located at a slightly higher temperature than they reported, namely above 500°C.

Ammonia that is strongly bound to the acid site is not likely to participate in the SCR reaction, which takes place at much lower temperatures, e.g. the vanadia-titania system oper-

ates around 350-400°C. Also, many authors using TPD for characterization of SCR catalysts used lower maximum temperature, e.g. 400°C[60] or 700°C[122], and Barthos et al.[122] and Katada et al.[124] reported of Brønsted acid sites on sulfated zirconia which releases ammonia below 500°C. Furthermore, the endothermic decomposition of sulfate on SO_4^{2-}/ZrO_2 have been found to take place at temperatures above 550°C[125,126], whereby the surface acidity could change during the TPD experiment. On the other hand, Khodayari et al.[60] suggests that ammonia may promote the decomposition of surface sulfate species during the TPD experiment. Therefore, only peaks with NH_3-desorption maxima below 500°C is reasonable to use for the determination of surface acidity relevant to SCR operation. Hence, the surface acidity collated in Tab. 3.5 are subdivided into total surface acidity and surface acidity below 500°C.

Haw et al.[127] postulates that the number of Brønsted acid sites on sulfated zirconia are moderate, consisting only of about 7% of the number of sulfur atoms on the basis of ^{15}N NMR of adsorbed pyridine-^{15}N. This was confirmed by Katada et al.[124], which found a slightly higher number of Brønsted acid sites, namely 12–18%, whereas Wachs and Weckhuysen[128] reported that around 5–10% of the surface vanadia species are surface Brønsted acid sites. Assuming that the peaks observed at 489–526°C of the sulfated zirconia supports are due to Brønsted acid sites. An integration of the peak area versus the total desorption area would then result in the fraction of Brønsted acid sites, where the number of Brønsted acid sites versus total acidity is in the range of 9–15%. Although this number is encumbered with some uncertainty, it is close to the observed in literature.

3.2.1.3 Catalytic activity

The commercial samples were impregnated with vanadyl (incipient wetness impregnation, IWI) corresponding to a vanadia loading of 3.0 wt% and calcined at 400°C for 2 hrs in air. Further synthesis description of the catalysts and the 3wt% V_2O_5-10wt% WO_3-TiO_2 (1.7VWT) reference catalyst is given in section A.2 (page 88). Experimental description of the SCR test rig, gas composition and first-order rate constant, k, are given in appendix, section A.3 (page 92).

The SCR activity of the vanadium-impregnated samples have been measured from room temperature to 550°C, presented in Fig. 3.16. The SCR activity of unpromoted 1.7V-97Z_NP reaches maximum conversion of NO around 500°C, only yielding a k-value around 170 $cm^3 g^{-1} s^{-1}$. 1.7V-52Z_NP yields even lower activities, and is therefore not shown here. In contrast, the sulfate-promoted catalysts render somewhat higher SCR activities, where the total activity follow the order 1.7V-4.9SZ_NP < 1.7V-3.9SZ_NP < 1.7V-3.4SZ_NP, with a concurrent decrease in temperature of maximum NO conversion. Thus, 1.7V-3.4SZ_NP present the highest SCR activity of the vanadium-loaded sulfated-zirconia catalysts at the lowest temperature, namely 430°C. In the absence of potassium, the reference catalyst 1.7VWT, based on the traditional vanadia-based catalyst, display a somewhat higher activity with a maximum at 400°C. However, the first order rate constant is here given on a weight basis of the catalyst (cf. section A.3), and the density of titania is somewhat lower than for zirconia (particle density for titania-based catalyst ≈ 0.2 g/ml, zirconia-based catalyst ≈ 0.5 g/ml). Since similar catalyst mass is used for the activity mea-

surements, the difference in density (catalyst volume) should be taken into consideration in the evaluation of catalyst performance.

The thermal deactivation is an issue for all the catalysts, where lower SCR activity is observed while cooling the catalyst down after treatment at 550°C, except for 1.7V-97Z_NP, which show reversible behavior. The low reversibility of the sulfate-type catalysts could be associated with thermal loss of sulfate species. Based on FTIR measurements at hydrated conditions, Kustov et al. [129] reported of a decrease in the intensity of the $\nu_{S=O}$-band at 500°C, and concluded that 25% of the sulfate groups on zirconia were eliminated due to thermal decomposition. On the other hand, the (sulfate free) reference catalyst also suffers from thermal deactivation, which suggests sintering of active centers. The solid-state diffusion of vanadia can be assessed with the so-called Tamman and Hüttig temperatures [130]. Based on the melting point (in Kelvin), it is possible to estimate the temperature where atoms become mobile and sintering can occur, based on the semi-empirical relation:

$$T_{Tamman} = 0.5T_{mp} \qquad \text{(bulk atoms becomes mobile)}$$
$$T_{Hüttig} = 0.3T_{mp} \qquad \text{(atoms at defects becomes mobile)} \qquad (3.2)$$

For V$_2$O$_5$ (T$_{mp}$ = 681°C [10]) the Tamman temperature, where bulk vanadia exhibit mobility, is obtained at 477°C. Although vanadia does not exist as bulk on the catalyst, but as monolayer with stronger vanadia-support interaction which would increase the actual Tamman temperature, some degree of sintering can not be avoided at 550°C.
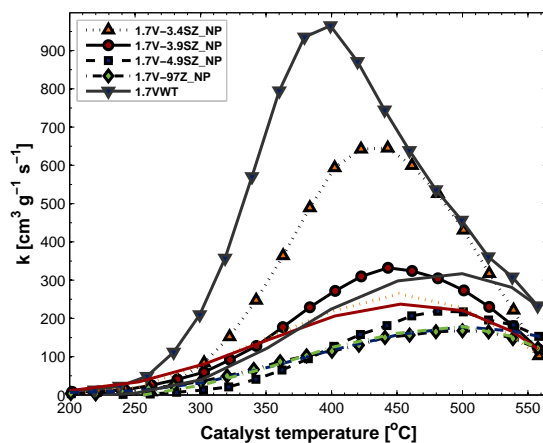
Fig. 3.16: SCR profile of various vanadia-loaded commercial supports and a 1.7VWT reference catalyst. Markers indicate SCR activity while heating, lines the activity while cooling from 550°C
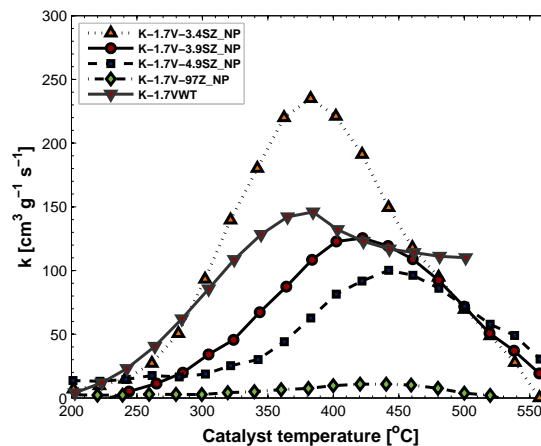
Fig. 3.17: SCR activity of various potassium-doped commercial supports and the reference catalyst, K/V = 0.4

Impregnation of the catalysts with potassium (K/V = 0.4) leads to a considerable decrease of their catalytic activity (Fig. 3.17). This deactivation is pronounced for all catalysts, but in the case of the unpromoted K-1.7V-97Z_NP, an almost complete deactivation observed. In the case of the potassium-doped reference catalyst, severe deactivation is also detected, whereas the sulfate-promoted samples still exhibit SCR activity, especially K-1.7V-3.4SZ_NP. Moreover, the addition

of potassium results in a shift of maximum catalytic activity towards lower temperatures compared with the corresponding catalyst. A possible explanation of such a shift in temperature is that potassium reduces the activity of the main SCR reaction while the rate of the competitive oxidation of ammonia remained constant or even increased.

The SCR activity at 360°C(which is close to the operating temperature of the traditional SCR catalyst) of the fresh and potassium-doped catalysts are listed in Tab. 3.6 for comparison. Based on the measured deactivations, it is clear that the binary vanadia-zirconia catalysts are very sensitive to potassium, which can be explained by the supports low surface acidity combined with the apparent absence of Brønsted acid sites and lack of tetragonal ZrO_2. Severe deactivation was also observed for the 1.7VWT catalyst, where loss of more than 80% of the original SCR activity is observed, whereas the catalysts based on sulfated zirconia are less affected by the potassium. Although 1.7V-4.9SZ_NP only deactivated 32%, the overall SCR activity of 1.7V-3.4SZ_NP is higher and still exhibit high resistance towards potassium. The 1.7V-3.4SZ_NP only deactivated 38%, more than a factor of two less deactivated than the vanadia-tungsta-titania catalyst.

Tab. 3.6: SCR activities at 360°C of fresh vanadium-loaded zirconia-based catalysts and the corresponding potassium-doped (K/V = 0.4)

	SCR activity		Deactivation[†]
	Fresh	K-doped	
	[cm^3/g s]		[%]
1.7V-3.4SZ_NP	347	215	38
1.7V-3.9SZ_NP	170	83	51
1.7V-4.9SZ_NP	63	42	32
1.7V-97Z_NP	86	7	93
1.7VWT	794	139	83

$$^† \text{Deactivation} = \frac{k_{fresh}^{360^oC} - k_{K-doped}^{360^oC}}{k_{fresh}^{360^oC}}$$

A rough indicator for high resistance toward the poisoning of the basic alkali can be found in the initial surface acidity of the supports. The un-promoted ZrO_2-based catalysts possess relatively low surface acidity (less than 650 μmol/g) and suffer from significant deactivation, as does the 1.7VWT reference catalyst (total surface acidity = 1324 μmol/g).

If we take into account that the catalytically active Brønsted acid sites consist of less than ca. 20% of all surface acid sites [124,127,128], it emphasize the vulnerability of the catalyst. Thus, even a small amount of alkali potentially can deactivate the majority of Brønsted sites, which are essential for the SCR reaction on vanadia catalysts.

3.2.1.4 Concise conclusion

Binary $V_2O_5-ZrO_2$ catalysts were shown to provide low catalytic activity and almost complete deactivation was observed upon alkali-doping due a combination of low surface acidity and/or high abundance of monoclinic ZrO_2 in the matrix.

The 3wt% V_2O_5-10wt% WO_3-TiO_2 reference catalyst also suffered from significant deacti-

vation, where less than 20% of the initial SCR activity was present after potassium doping (K/V = 0.4). The low overall surface acidity and apparent absence of Brønsted acid sites are likely contribute to a high sensitivity to the basic potassium.

The sulfated zirconia catalysts of commercial grade presented here contain high surface acidity, and especially 3.4SZ_NP contain the least fraction of monoclinic zirconia among the samples studies and the highest surface area. The corresponding vanadia-loaded catalyst exhibited much higher resistance toward potassium (only deactivating 38%) than the two titania-based reference catalysts. Utilization of sulfated zirconia as support material is thus a promising candidate for increasing the catalysts resistance when confronted with deactivating potassium in the flue gas.

3.2.2 Iron and copper mixed oxide catalysts

Studies similar to those reported previously for vanadium-based catalysts in section 3.1.1.2, have recently also been performed with other oxide catalysts with copper-[51,64,93,131,132] and iron-based catalysts[93,133,134]. Since the metal oxides of copper and iron mainly possess Lewis acidity[51] they belong to an interesting class of SCR catalysts in principle less sensitive to deactivation of the Brønsted acid sites. This was exploited by Kustov et al.[93,114] who studied the effect of potassium on vanadium, copper and iron oxides supported on sulfated zirconia (monoclinic), where a slight increase in alkali resistance was found using the metal oxides of copper and iron compared to vanadium. However, samples with less or no monoclinic phase of ZrO$_2$ were not investigated, and sulfation was performed after calcination of zirconia, which has been found to result in less acidic samples than sulfation of the hydroxide Zr(OH)$_2$[71]. Thus, in continuation of the study of copper and iron oxides on sulfated zirconia, a series of mixed Cu and Fe oxides supported on the best commercial sulfated zirconia support from previous section were investigated in the following.

The catalysts studied in this section consist of iron-copper mixed oxides in different molar ratio, with a constant total metal loading of 364 $^{\mu mol}$/$_g$ (similar loading as in [93]) and doped with potassium to K/M = 0.4. The optimal support, 3.4SZ_NP, were used in all catalysts. Further synthesis details are given in appendix A.2.2 (page 89).

3.2.2.1 Temperature programmed desorption

The TPD profiles of the iron-copper mixed oxide on sulfated zirconia are collected in Fig. 3.18. The fresh catalysts primarily consisting of copper oxide (i.e. samples with the iron mole fraction: X_{Fe} = 0.00–0.33) show roughly a tri-modal desorption profile and a shoulder around 260–290°C, whereas for the catalysts comprising mainly iron oxides (i.e. X_{Fe} = 0.50–1.00) only two major desorption peaks are observed and the shoulder is disappeared. The first major desorption peak can be attributed to acid sites generated by the copper and iron oxides, considering that only the small peak at 489°C was present on the TPD profile of 3.4SZ_NP. Moreover, as can be concluded from Tab. 3.7, a gradual shift in temperature of desorption is observed with the relative content of iron oxide in the samples. For the pure CuO-based catalyst (i.e. X_{Fe} = 0.00) the temperature of
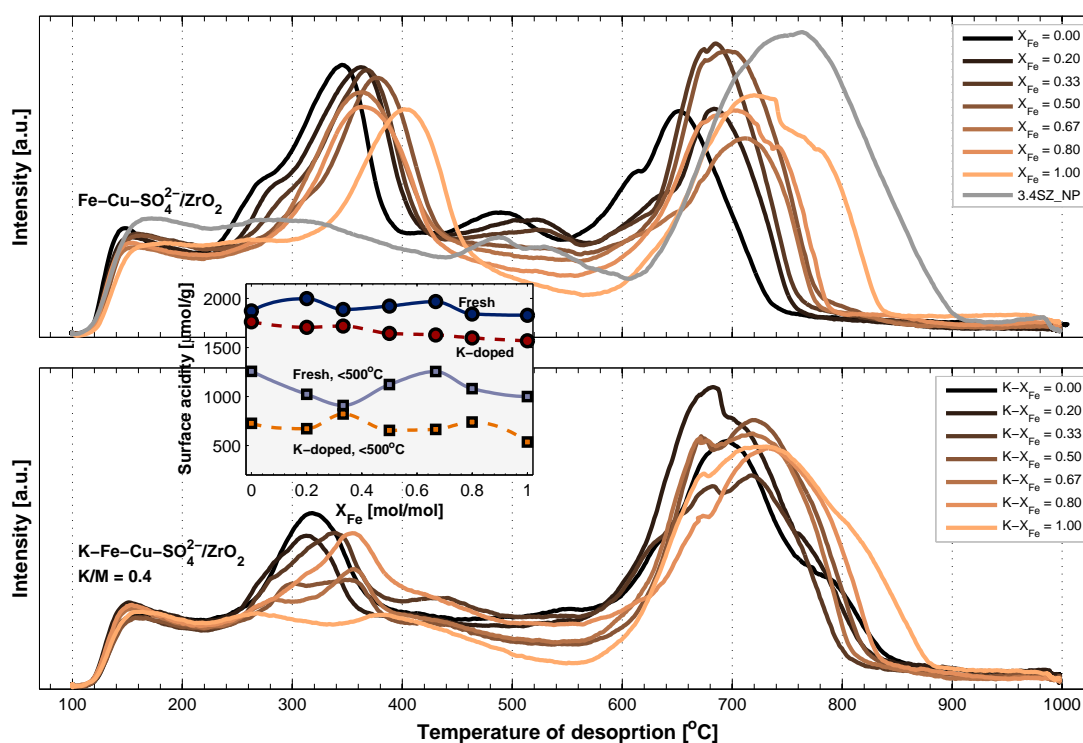
Fig. 3.18: NH_3-TPD profiles for fresh iron-copper oxides hybrid catalyst and the pure support material as reference (**top**) and the corresponding potassium-treated samples (**bottom**), same scale. Inset figure show the trends in the surface acidity of the Fe-Cu mixed oxide catalysts

maximum desorption below 600°C is located at 345°C, which is increasing slowly with the content of iron up until 402°C for X_{Fe} = 1.00, suggesting an increase in the strength of acid sites as iron oxide loading displaces copper oxide on the sulfated zirconia. The gradual displacement of CuO with Fe_2O_3 does almost not affect the overall acidity (cf. inset figure in Fig. 3.18). The disappearance of the minor peak around 490–520°C, combined with the small decrease in overall surface acidity when increasing the fraction of iron oxide, could be attributed to physical coverage of acid sites with Fe_2O_3 species. At X_{Fe} = 0, the CuO loading is 3.5 wt% with a corresponding surface density of 2.4 CuO/nm² (cf. Tab 3.7, and equation 3.1), whereas at X_{Fe} = 1, the equimolar concentration of Fe_2O_3 is 7.7 wt%, corresponding to a surface density of 5 FeOₓ/nm². Although monolayer capacity probably is not reached for either of the pure metal oxide catalysts [84], the coverage of iron species is higher, covering or weakening the acid sites of sulfated zirconia.

For all the catalysts, the addition of potassium results in a significant reduction in total acidity, in agreement with previous observations [72,93]. Especially the amount of ammonia desorbed at low-temperature peaks around 340–400°C is reduced considerably, whereas the peaks observed at temperatures above 650°C does not seem to have changed upon treatment with alkali. This could suggest that the unaffected desorption peak originates from decomposing sulfate. Furthermore, it should be noticed that the desorption-peak around 340–400°C is shifted towards lower temperatures for the K-treated samples, whereby the acid sites and ammonia adsorption are weakened, presumably due to electron donation from the basic potassium oxide, previously discussed in section 3.1.2.2. An interesting behavior in the surface acidity of the K-

Tab. 3.7: Characteristics of fresh and potassium-treated Fe-Cu mixed oxide catalysts: surface area, surface acidity, and temperature of NH$_3$-desorption during TPD

X_{Fe}	BET surface area		Total surface acidity		Major TPD peaks <600°C			
	Fresh	K-doped	Fresh	K-doped	Fresh		K-doped	
	[m^2/g]		[µmol/g]		[°C]		[°C]	
0.00	127	132	1873	1763	345	489	317	
0.20			1999	1706	362	522	313	
0.33			1888	1719	367	521	339	427
0.50			1923	1643	377		348	420
0.67			1969	1628	364		356	
0.80			1842	1598	365		354	
1.00	115	128	1829	1568	402		380	

doped compared to the fresh catalysts is the trend in overall acidity (cf. inset figure in Fig 3.18). Linear fitting of the total surface acidity versus iron mole fraction of the fresh series, reveals an almost constant slope, corresponding to a difference between the pure CuO-based and Fe$_2$O$_3$-based catalysts of on 75 µmol/g, whereas the overall decline of the K-treated catalysts show a difference of around 200 µmol/g. In other words, copper oxide catalysts maintain the surface acidity better upon potassium doping than catalysts consisting mainly of iron oxide.

3.2.2.2 Catalytic activity

The activity of the Fe-Cu oxide catalysts in the catalytic removal of NO were measured in the temperature range of 25–500°C, presented in Fig. 3.19. Here, the catalysts based solely on CuO (on sulfated zirconia) is denoted X_{Fe} = 0.00, whereas the iron-based catalyst without any copper oxide is denoted X_{Fe} = 1.00. In general, the temperature of maximum activity is shifted from 400°C for the reference catalyst to around 460°C for the hybrid catalysts, along with a decrease in maximum activity. All the fresh catalysts roughly possess similar SCR activity up to around 440°C, at which point the SCR activity is decreasing rapidly for catalysts comprising mainly copper oxide (X_{Fe} = 0.00–0.67), whereas the two samples with highest content of iron oxide maintain, or even increase, their high-temperature activity. The shift of the catalytic activity towards higher temperatures for the catalysts with most iron oxide, agrees well with the increase of the overall strength of the acid sites with iron content, as reflected by TPD measurements. The different behavior in the high-temperature region, where sudden loss of activity on the catalysts with most copper oxide, could be a result of thermal deactivation. The Tamman temperature of CuO is 477°C (T$_{mp}^{CuO}$ = 1227°C[10]), whereas for Fe$_2$O$_3$ it is 633°C (T$_{mp}^{Fe2O3}$ = 1539°C[10]). However, the catalytic activity upon stepwise cooling from 500°C (only shown in figure for the pure iron- or copper-based catalyst) of the fresh and K-doped samples, reveal almost complete reversibility of copper-based catalysts, whereas the iron-based catalysts exhibit some degree of deactivation after treatment at 500°C. Thus, the copper-based catalyst are not thermally deactivated at the highest temperatures, and the reversibility suggests that competing reactions to SCR are dominating at higher temperatures. In contrast, the high coverage of Fe$_2$O$_3$-species (5
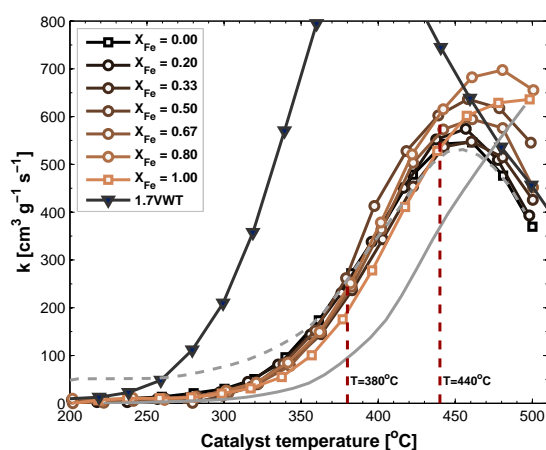
Fig. 3.19: SCR activity profile of fresh Fe-Cu mixed oxide catalysts supported on 3.4SZ_NP. The activity when cooling from 500°C for X_{Fe} = 0.00 and 1.00 is indicated by gray lines, dotted is CuO-based, and solid Fe_2O_3-based catalyst
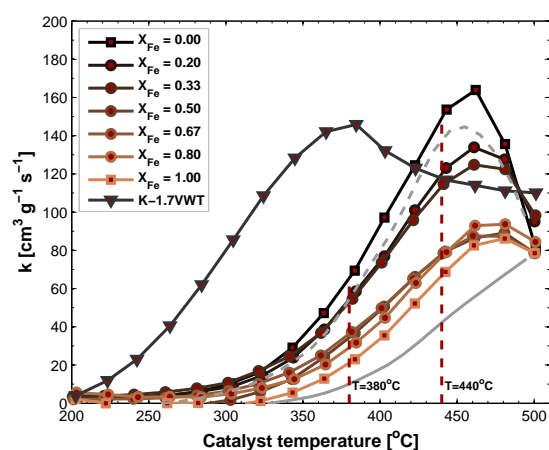
Fig. 3.20: Temperature dependency of the SCR activity of K-treated Fe-Cu mixed oxide catalysts. K/M = 0.4. Dotted gray line is CuO-based, solid Fe_2O_3-based catalyst

FeO_x/nm^2) compared to CuO, could promote sintering of active centers in close vicinity.

The SCR activity of the Fe-Cu catalysts after impregnation of potassium are shown in Fig. 3.20, where a significant reduction in activity are observed for all catalysts, especially for the hybrid catalysts with highest concentration of iron oxide. However, catalysts comprising primarily copper oxide, namely X_{Fe} = 0.00–0.33, seem less deactivated.

To obtain a more clear trend in the performance of the Fe-Cu series supported on sulfated zirconia, the activities of the fresh and K-doped catalysts at two selected temperatures are compared and presented in Fig. 3.21. Based on the interpolated activities[1] at 380 and 440°C, the activity of the fresh Fe-Cu mixed oxide catalyst at these temperatures is almost constant, regardless of composition, although catalysts containing most iron oxide exhibit slightly higher activity at 440°C. However, a different trend is observed when the catalysts have been deactivated with potassium, where it is clear that predominantly the copper oxide-containing catalysts (X_{Fe} = 0.00-0.50) exhibit higher activity than the corresponding iron-samples.

The degree of deactivation through the series, based on the interpolated values, are depicted in Fig. 3.21 (right). Here, the catalysts with pure CuO as active component, or a high relative content of copper oxides, display somewhat better alkali resistance than catalysts with increasing content of iron oxide. Compared to the $V_2O_5-WO_3-TiO_2$ reference catalyst, which deactivated 83% at 360°C (cf. Tab. 3.6), slightly lower activity loss is observed for the $CuO-SO_4^{2-}-ZrO_2$ (X_{Fe} = 0.00), deactivating around 75%, whereas the $Fe_2O_3-SO_4^{2-}-ZrO_2$ is loosing almost all SCR activity, around 90%.

For the potassium-treated catalysts, a similar decreasing trend is observed in surface acidity as well as in SCR activity with increasing iron-oxide content (i.e. inset figure in Fig. 3.18 and Fig. 3.21), suggesting a relationship. Based on TPD observations, the basic potassium is

---

[1] The temperature obtained during experiment deviate slightly from set-point, and to obtain comparable values the activities are linear interpolated
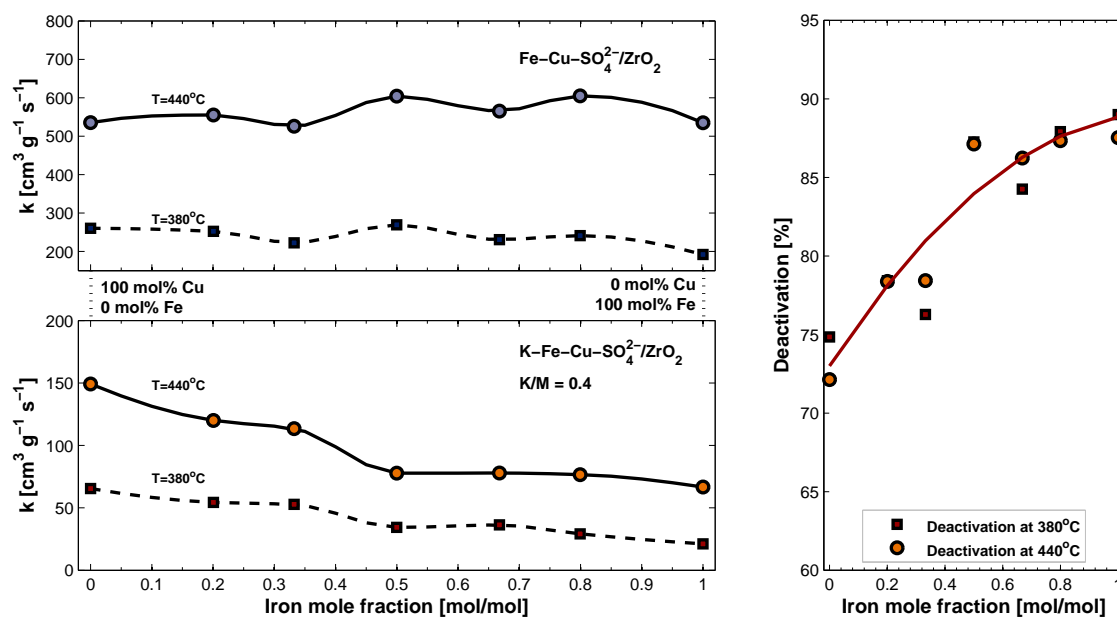
Fig. 3.21: Left: interpolated SCR activities of Fe-Cu 'alloy' catalysts at 380°C and 440°C versus iron loading for fresh hybrid catalyst and corresponding K-doped samples. Total metal loading 364 µmol/g, equivalent of 3.5 wt% CuO loading. **Right**: loss of SCR activity versus Fe-Cu oxide composition at 380°C and 440°C

deactivating a higher number of acidic sites on iron-based catalysts than on copper-based. On the pure Fe$_2$O$_3$-based catalyst, the potassium treatment resulted in complete removal of the the TPD peak at 402°C on the fresh catalyst. This indicates that potassium is attacking the lewis sites generated by iron oxides or because of the high surface coverage of iron-oxides, whereby sulfate-generated acid sites are weakened or covered by iron-oxides, unable to effectively host the incident potassium. Furthermore, the presence of the stronger acid site (TPD peak at 489°C for X$_{Fe}$ = 0.00), introduced by sulfated zirconia, is likely to appear as a more attractive site for potassium than relatively weaker sites, such as the Lewis sites of the active catalyst.

Finally, only linear behavior were observed in the TPD experiments and SCR activity measurements of the iron-copper mixed oxide series as a function of the molar Cu-Fe content, suggesting that no predominant metal alloys are formed on the catalysts or other symbiotic effects occur.

3.2.2.3 Concise conclusion

All the catalysts with equimolar copper and iron loadings, a mixture of 3.5 wt% CuO$-$SO$_4^{2-}-$ZrO$_2$ and 7.7 wt% Fe$_2$O$_3-$SO$_4^{2-}-$ZrO$_2$, display similar surface acidity, although iron oxides displaces the apparent Brønsted sites (490–520°C), originating from the sulfated zirconia support. Increasing the molar fraction of iron oxides in the catalysts, is accompanied by a strengthening of the low-temperature acid site, desorbing ammonia around 345–402°C, which is reflected by the corresponding higher SCR activity of high iron content catalysts (i.e. X$_{Fe}$ = 0.80–1.00) at elevated temperatures (<460°C).

SCR activities up until ca. 440°C are almost similar for all fresh catalysts. However, after K-doping it is evident that catalysts comprising mainly copper oxide (X$_{Fe}$ = 0.00–0.50) exhibit

higher resistance to potassium-poisoning, which were attributed to the presence of strong acid-sites of the sulfated zirconia. These sites were either covered or chemically weakened by the Fe_2O_3-species at higher iron mole fractions.

Although interesting trends were found in the Fe-Cu mixed oxide catalyst series, the 'best' catalyst, namely $CuO-SO_4^{2-}-ZrO_2$, deactivated around 70%, and were thus only marginally more resistant than the 1.7VWT reference catalyst which deactivated 83%.

3.2.3 Concluding remarks

The commercial sulfated zirconia 3.4SZ_NP was selected as support based on its low content of monoclinic ZrO_2, high crystallinity, acidity and surface area. Furthermore, loaded with V_2O_5, the initial activity in the catalytic removal of NO_x is lower than of the titania-based reference catalyst, 1.7VWT. However, when potassium is deposited ($K/V = 0.4$ mol/mol), the 1.7V-3.4SZ_NP catalyst exhibit twice better alkali resistance, only deactivating 38% at 360°C, whereas in the case of 1.7VWT, less than 20% of the original activity were left after K-doping. Unpromoted $V_2O_5-ZrO_2$ catalysts suffer from almost complete deactivation, stressing the significance of surface acidity enhancement, provided by sulfation of the zirconia. For comparison, SCR activities and deactivation due to K-doping of some selected catalysts investigated here, are collated in Tab. 3.8.

Tab. 3.8: Comparison of SCR activity at 360°C of the most promising catalysts based on sulfated zirconia (3.4SZ_NP) investigated

Catalyst	Fresh SCR activity	Deactivation[‡]
	$[cm^3 g^{-1} s^{-1}]$	[%]
1.7VWT	794	83
1.7V-3.4SZ_NP	347	38
2.8Cu-3.4SZ_NP[†]	260	75

[†] k-value at 380°C

[‡] Deactivation after doping, K/M 0.4, IWI

Using the alternative transition metal oxides of iron and copper, which mainly possesses Lewis acidity (in contrast to V_2O_5-based catalysts), show that Cu-based catalysts in general maintain their acid strength better upon K-doping compared to the iron-based catalysts, which is reflected by the corresponding higher resistance toward alkali poisoning in the SCR reaction.

The depositing of potassium on the catalysts leads to a significant decrease of their SCR activity, in concert with an observed shift in the maximum SCR activity to lower temperatures and a reduction in acid strength, probably due to electron donation from the basic potassium oxide. In general, vanadium-based catalysts supported on sulfated zirconia reveal maximum SCR activity at lower temperatures than that of the corresponding copper and iron-based catalysts. However, thermal deactivation is an issue for both iron- and vanadium-based catalysts, revealed by hysteresis in the temperature profile of the SCR activity. On the other hand, the copper-based catalysts investigated here, all exhibit extremely high reversibility, even after treatment at 500°C, making CuO-based catalysts more suitable for high-temperature exposure than e.g. vanadia-

based catalysts.
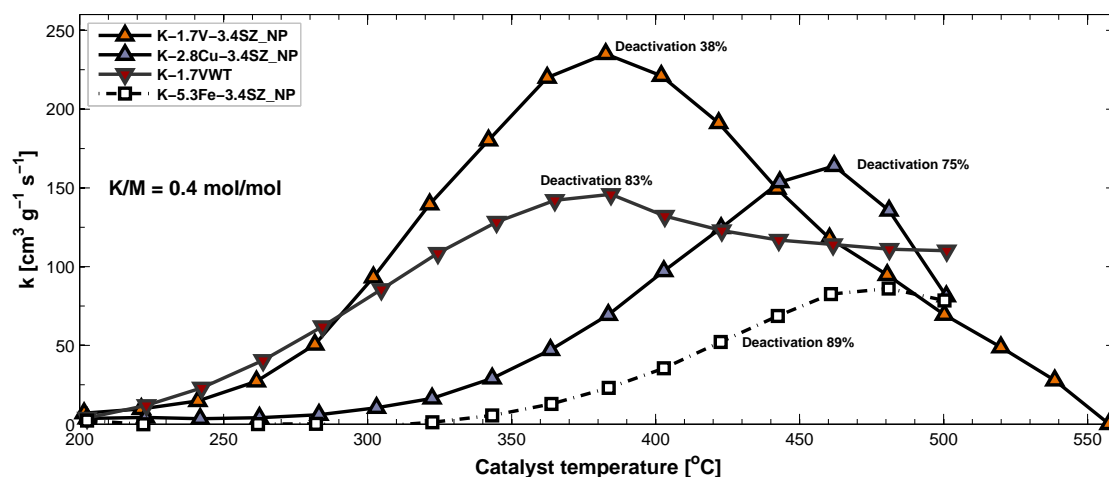
Fig. 3.22: Comparison of the SCR activity of some selected potassium-poisoned catalysts investigated

The effect of potassium-deposition on the catalytic SCR activity for some selected zirconia-based catalysts are collected in Fig. 3.22 for comparison. From the activity profiles it is clear that vanadium is the most promising active metal in terms of alkali-resistance, and low-temperature activity. It is noteworthy that the maximum in SCR activity of the K-doped V-based catalysts, as well as the titania-based reference catalyst, all are at the same temperature, ca. 380°C, whereas Fe- and Cu-based catalysts typically display maximum activity at higher temperatures. Since the operating catalyst typically performs around 350-400°C, the development of an alternative alkali-resistant catalyst operating within similar temperature range would expedite the implementation. Therefore, for industrial use, vanadium-based SCR catalysts seem to be the best candidate of the catalysts studied here. Following the identification of vanadium supported on sulfated zirconia as a suiting alkali-resistant catalysts, is the issue of upscaling. Until now, all the catalysts have been on particle form and tested at relatively low flows, which is unsuitable for the high flows used in e.g. power plants. Therefore, the next chapter is addressing the issue of catalyst upscaling.

ZrO$_2$-sepiolite composite catalysts

This chapter is dedicated to the upscaling of the best alkali-resistant catalyst found in chapter 3, namely V$_2$O$_5$ $-$ SO$_4^{2-}$ $-$ ZrO$_2$. For practical reasons, the previous investigations were done on small catalyst particles. However, utilizing such particles under industrial conditions, i.e. high flow and in the presence of fly ash, would quickly result in massive pressure drop and ash-plugging. Hence, the catalysts are shaped into monoliths to avoid these problems. The natural clay material, sepiolite, is used as a binder to shape the catalyst. An introduction of the properties of sepiolite is given below.

4.1 Introduction

The incorporation of sepiolite into the catalyst significantly enhances the mechanical properties of both the paste to be extruded and the final monolith, an important factor for its adaptation in industrial applications.

Although sepiolite has only once before been used as binding material for ZrO$_2$-based catalysts[135], the use of sepiolite in TiO$_2$-based catalysts is a well-known technology[136–140]. As can be extracted from the references on the subject, a considerable amount of the work done within the use of sepiolite as catalyst binder, are carried out at ICP-CSIC[1] in Madrid, Spain. There, I had the pleasure to visit the institute for a few months to learn the technology and produce some 'beta'-catalysts in collaboration with Pedro Ávila and Søren Birk Rasmussen.

Since almost all the extruded catalysts in this chapter are based on sepiolite, its structural and thermal properties are briefly highlighted here.

4.1.1 Sepiolite structure and thermal behavior

The sepiolite used as binder in this study, Mg$_8$(Si$_{12}$O$_{30}$(OH)$_4$)$\cdot$(H$_2$O)$_{12}$, is a natural hydrous magnesium silicate clay mineral, with fibrous morphology. Sepiolite has a layered structure with phyllosilicate modules composed of two layers of tetrahedral silicate that sandwich the octahedral MgO strip (Fig. 4.1). The ribbons are linked by inversion of the SiO$_4$ tetrahedra Si-O-Si bonds. This structure induces needle-like particle shapes, containing large channels with the dimensions 3.7 x 10.6 Å, running in parallel to the phyllosilicate ribbons[141]. In the hydrated form, these tunnels are occupied by zeolitic H$_2$O molecules.

The structure of sepiolite was first reported by Brauner and Preisinger[142], but because of its

---

[1]Instituto de Catálisis y Petroleoquímica, Consejo Superior de Investigaciones Científicas
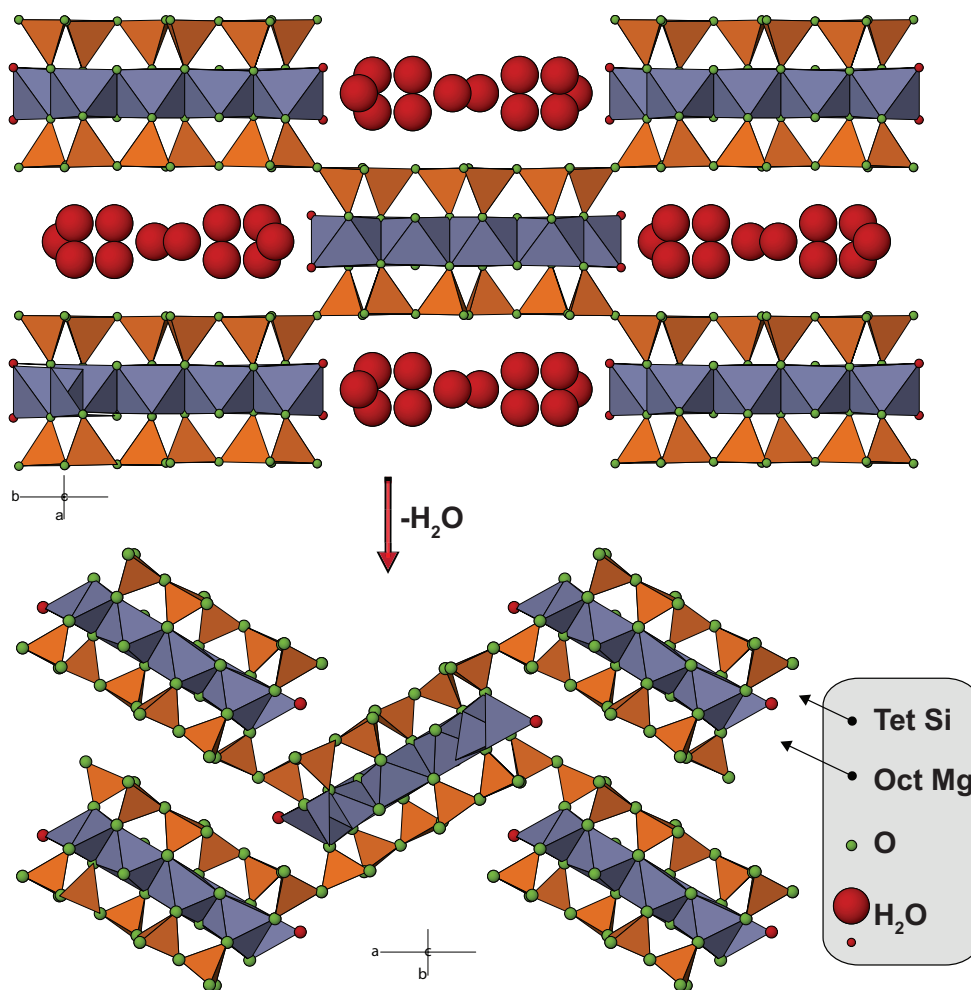
Fig. 4.1: Dehydration of sepiolite. **Top**: Sepiolite structure at ambient conditions with 8 zeolitic H_2O and four structural H_2O molecules per unit cell, $Mg_8(Si_{12}O_{30}(OH)_4)(OH_2)_4 \cdot (H_2O)_8$, viewed along the orthorhombic c-axis. Unit cell a = 13.405 Å, b = 27.016 Å, c = 5.2750 Å, $\alpha = \beta = \gamma = 90^o$. **Bottom**: Structure of the 'dehydrated' dihydrate form of sepiolite, $Mg_8(Si_{12}O_{30}(OH)_4) \cdot (H_2O)_2$ viewed down the monoclinic c axis. Unit cell a = 23.446 Å, b = 11.352 Å, c = 5.2782 Å, $\alpha = \gamma = 90^o$, $\beta = 89.06^o$. Crystallographic information file (CIF) obtained from [141]

poor crystallinity, resulting in low crystallographic resolution, some details regarding the structure were unanswered. However, recently the structure was resolved by synchrotron powder X-ray, with various degrees of hydration on a purified sepiolite by Post et al. [141]. They found that the hydrated form contain almost 16 H_2O molecules per unit cell, where the zeolitic water is distributed over four sites in the channels, and four as structural H_2O bound to the terminal Mg atoms in the ribbons. Applying vacuum to the hydrated structure at room temperature only removes about 10% of the zeolitic water, whereas heating to around 200°C results in loss of most zeolitic water, and until about 350°C, the dehydration of sepiolite is reversible, whereby zeolitic water quickly is replaced by humidity [141–143]. Around 380°C the sepiolite structure collapses under the loss of half of its structural water, causing the phyllosilicate ribbons to rotate around the linking Si-O-Si bond, reducing the cross sectional area of the channels and changing the structural symmetry from orthorhombic to monoclinic (Fig. 4.1, bottom). The last structural water is slowly removed by additional heating to about 600°C, obtaining the 'anhydrous' structure (OH

groups still present) [141].

The dehydration temperatures of the purified form of sepiolite suggested by Post et al. [141] do not agree well with those in the literature, mainly because the purity of natural sepiolite is rather low and depends on the origin. Frost et al. [144] compared the gravimetric decomposition profiles of sepiolite from Nevada, Nairobi and Spain, and found that the dehydration and dehydroxylation temperatures varied significantly. However, most authors agree that phase transition occurs below 500°C [141,142,144], which is the temperature often used for the calcination of sepiolite-titania composite catalysts [145].
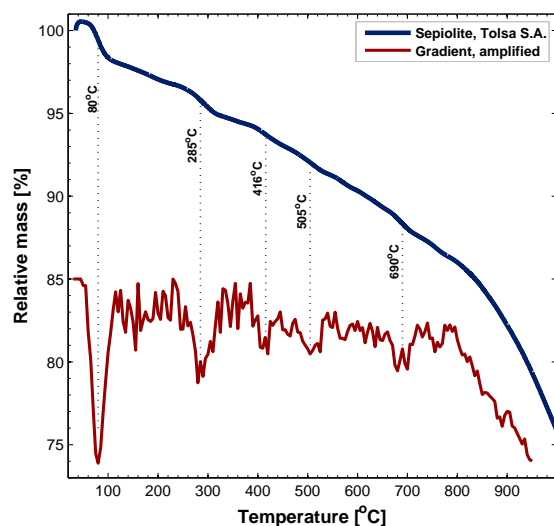

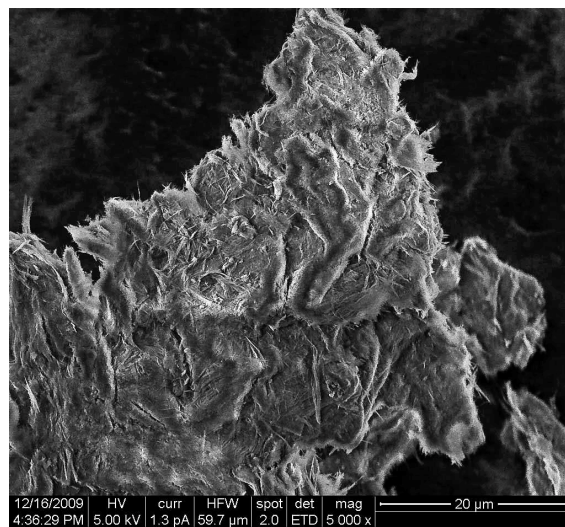**Fig. 4.2:** TGA profile of commercial Sepiolite from Tolsa S.A.

Fig. 4.3: SEM image of sepiolite, calcined at 500°C

To evaluate the thermal behavior of the sepiolite applied in this study, the TGA-DSC profile of the as-received clay was performed, the TGA result of this is presented in Fig. 4.2. However, due to its low purity (60%), the dehydration mass losses are significantly damped. To assist in the exact temperature-determination of the weight profile, the curve gradient is calculated and plotted, whereby roughly five steps of mass loss are obtained. The presence of other impurities can be confirmed by the relative molar weight between the hydrated and completely dehydrated sepiolite. The molar mass of $Mg_8(Si_{12}O_{30}(OH)_4)$ is 1080 g/mol and the hydrated $Mg_8(Si_{12}O_{30}(OH)_4) \cdot 12\,H_2O$ is 1295 g/mol, 17% higher. Therefore, upon complete dehydration of the sepiolite, the mass should decrease by a maximum of 83%, but the relative mass loss at 1000°C is 76%, suggesting simultaneous removal or decomposition of other contaminants, and clouding the assignment of dehydration steps of the sepiolite. However, based on the reported thermal behavior of sepiolite [141,144], the endothermic mass loss step observed at 416°C in Fig. 4.2 can tentatively be attributed to the phase transition to the monoclinic dihydrate form. It should be mentioned that the choice of the low purity sepiolite is not only for economic concern, the other clay-contaminants play an active role in providing rheological properties to the paste. The before mentioned fibrous character of sepiolite is clearly seen in the SEM micrograph, Fig. 4.3, of a pure extruded sepiolite after calcination.

4.1.2 Pore distribution

Details regarding the porosimetry of the sepiolite can be extracted with mercury intrusion porosimetry (MIP). In Fig. 4.4 the MIP profile is shown for the extruded and calcined sepiolite and reveals a small pore diameter of the pure sepiolite after extrusion, with both meso pores (2–50 nm) and 'small' macro pores (50–100 nm). However, it has previously been observed that
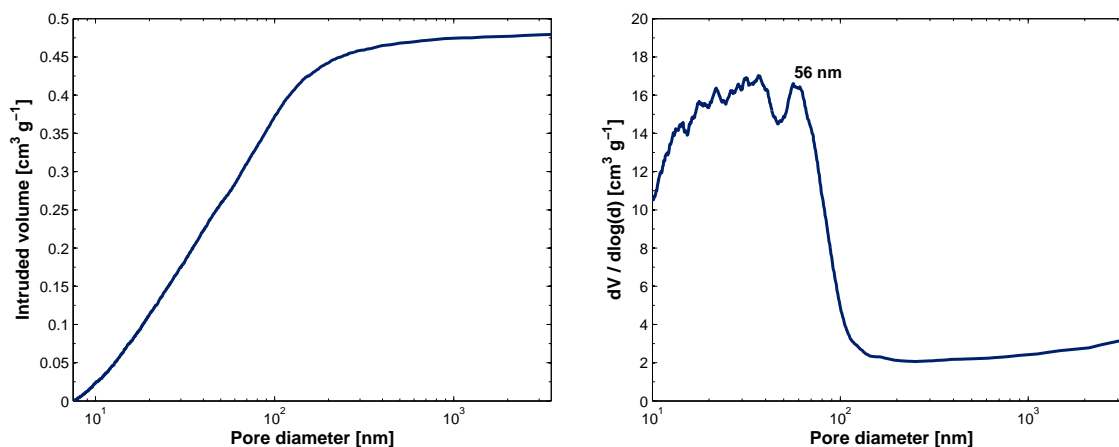

Fig. 4.4: Mercury intrusion profiles of extruded sepiolite, calcined at 500°C. Left: Cumulative pore volume curves; Right: Pore size distribution

composite zirconia and sepiolite retain some interparticular porosity even if diminished by the sepiolite component [140]. In other words, the pore sizes of the composite catalyst is a blend of pores originating from sulfated zirconia, containing interparticular porosity from the zirconia particles and meso and macro porosity from the sepiolite (cf. Fig. C.2).

In the following section, where sulfated zirconia were mixed into the matrix of sepiolite, the ratio of sulfated zirconia/sepiolite is studied, to find the optimal formulation.

4.2 Optimization of sepiolite content

A series of pelletized catalysts with mixed ratios of sepiolite and $V_2O_5-SO_4^{2-}-ZrO_2$ (VSZ) were synthesized for this study. Details regarding the synthesis of the catalysts are described in section A.2.3 (page 90). The catalysts were denoted by the mass fraction of sepiolite, ranging from 0/8 to 8/8, the latter being the pure sepiolite and 0/8 corresponds to $V_2O_5-SO_4^{2-}-ZrO_2$, which is on powder form due to the lack of binder. Some properties of the series are collected in Tab. 4.1, including the elemental analysis of the samples. Based on the content of sulfur, the sulfate concentration on 0/8 is 5.5 wt% (measured as SO$_3$), and therefore slightly higher than the 3.4 wt% on the commercial sulfated zirconia, 3.4SZ_NP. The high content of silicon in the 8/8, suggests the presence of impurities, expected considering the 60% purity of sepiolite.

High BET surface areas are obtained for all samples, which slowly decrease with the sepiolite content.

The SCR activities at 360°C as a function of sepiolite content are presented in Fig. 4.5. The

Tab. 4.1: Properties of $V_2O_5-SO_4^{2-}-ZrO_2$-sepiolite composite catalysts

Sample[†]	Sepiolite content	BET area	IEP*	Elemental analysis					Surface acidity		Major TPD peaks[‡]			
				m_{Mg}	m_S	m_{Si}	m_V	m_{Zr}	Total	<550°C	α	β	γ	δ
	[wt%]	[m²/g]	[pH]			[wt%]				[μmol/g]			[°C]	
0/8 Sep_VSZ	0	165	5.8	0.0	2.2	0.0	3.9	65.1	2131	1141	473		801	
1/8 Sep_VSZ	12.5	152	5.4	1.4	2.4	3.1	2.8	54.5	2495	1169	436		789	
2/8 Sep_VSZ	25	154	2.6	2.7	2.1	6.0	2.7	49.7	1897	894	451		795	
3/8 Sep_VSZ	37.7	153	-	4.3	1.9	9.4	2.4	43.4	2234	871	423		768	
4/8 Sep_VSZ	50	153	2.5	5.7	1.6	12.6	1.9	34.0	2066	715			789	
5/8 Sep_VSZ	62.5	149	-	7.1	1.4	1.4	1.5	26.9	1965	571		646	790	
6/8 Sep_VSZ	75	143	2.4	8.6	0.9	19.1	1.0	18.2	2140	594		642	791	901
7/8 Sep_VSZ	87.5	136	-	9.9	0.6	22.4	0.5	9.2	2146	563		651	793	943
8/8 Sep_VSZ	100	130	2.3	12.0	0.4	25.7	0.0	0.0	2255	562		661	797	

[†] Sample name correspond to weight fraction of sepiolite mixed with $V_2O_5-SO_4^{2-}-ZrO_2$
[‡] α, β, γ, and δ correspond to the desorption sites observed in Fig. 4.8
* Isoelectric point charge

sample on powder form, i.e. 0/8, were pressed at two tons and fractionated. However, since the sample was prepared slightly different than the extrudates (i.e. not extruded with sepiolite, but pressed and fractionated), the fresh activity is only written in the figure since direct comparison should not be done. As expected, the activity is declining as the fraction of $V_2O_5-SO_4^{2-}-ZrO_2$ de-
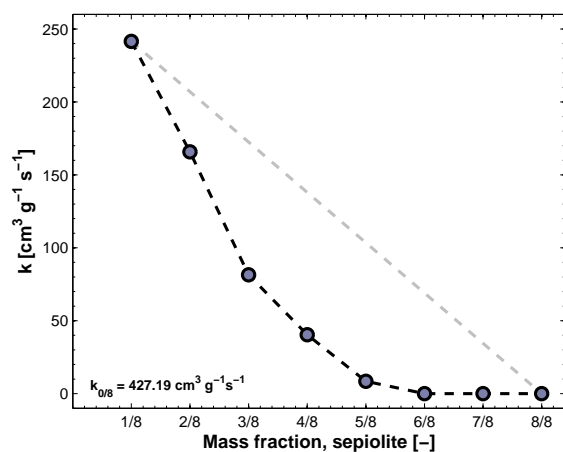
Fig. 4.5: SCR activity at 360°C of fractionated pellets (180-300 μm)
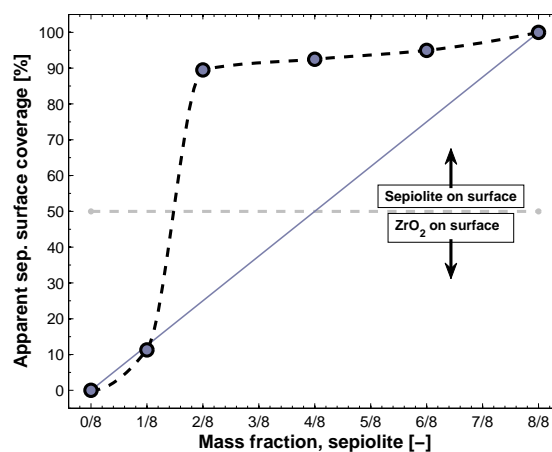
Fig. 4.6: Apparent surface coverage of sepiolite on the VSZ-sepiolite particle versus sepiolite content, based on Zeta potential measurements

creases. However, the drop in activity is higher than can be accounted for by the mere dilution of the active VO_x-species, which would ideally follow a linear dependence, as illustrated in the figure. The apparent discrepancy suggests that sepiolite (or an impurity in sepiolite) either chemically deactivates the active phase or physically blocks the access for the SCR gas molecules. However, the BET areas do not decrease substantially with increasing sepiolite content, ruling out that sepiolite is blocking the pores to the catalyst. The relative surface coverage of sepiolite

can be elucidated by measuring the zeta potential[2] as a function of pH of the composite cata-lysts suspended in water Thereby the isoelectric points (IEP) can be obtained, from which the molar surface coverage of sepiolite can be calculated [137], the results are shown in Fig. 4.6. The addition of sepiolite entail a dramatic decrease of VSZ at the surface, even by addition of small quantities of sepiolite. At 25 wt% loading, the VSZ particles are almost completely coated by the sepiolite, which might partly be responsible for the rapid decrease in catalytic activity. The cov-erage of the active particle by sepiolite was also previously observed for TiO$_2$-sepiolite mixtures, reported by Knapp et al. [137]. Avila et al. [146] suggested the kneading of the catalyst and sepiolite, and subsequent calcination causes 'delamination' of the sepiolite fibers in a manner where the catalyst particles were dispersed among the fibers, accounting for the coverage of VSZ particles, even at low loadings of sepiolite.

4.2.1 Structural characterization

The samples were further characterized with SEM (Fig 4.7), where the surface morphology of the 0/8 and 1/8 are almost similar, consisting of particles in the 5-10 µm size region. However, with
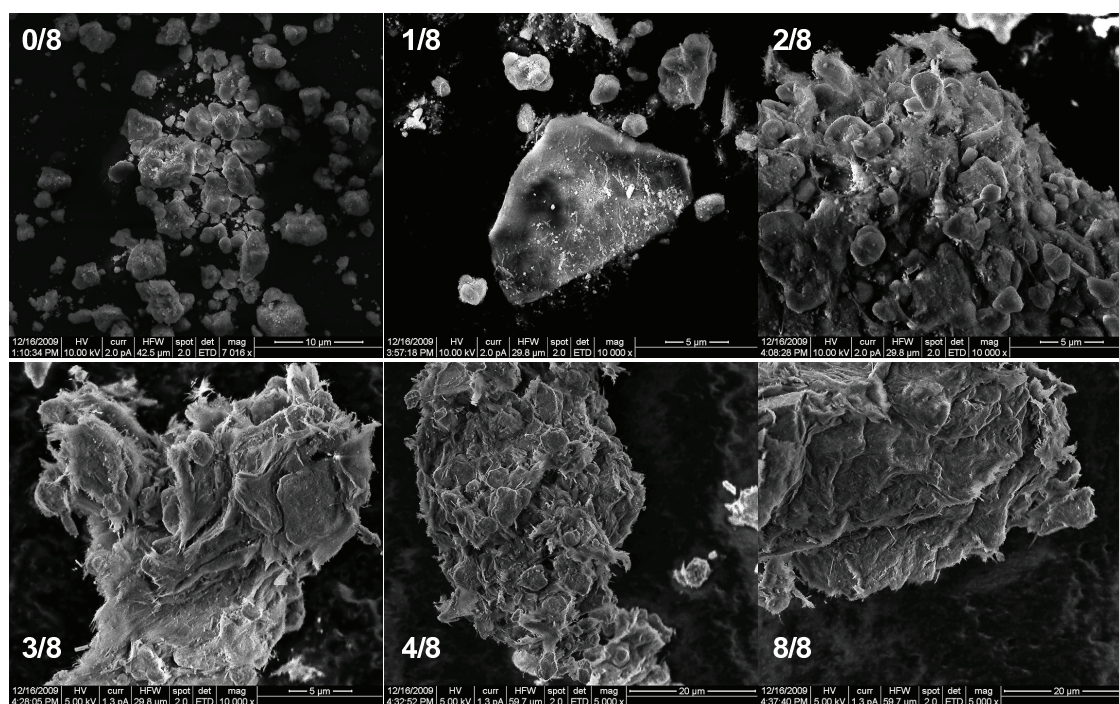
Fig. 4.7: SEM images of selected composite catalysts. The numbering refer to the mass fraction of sepiolite in the catalyst

increasing sepiolite content there is a sudden shift in particle appearance and size, reminiscent of particle bundles around 20-50 µm in diameter, thus confirming the sudden shift in surface coverage observed with zeta potential measurements. On the surface on the 2/8–4/8 samples, although it roughly resembles the morphology of the pure sepiolite, it is still possible to identify particles of VSZ linked to the surface, which emphasizes that the zeta potential measurements

---

[2]difference in potential between dispersed particle and medium

are based on an average interpolation between the two pure phases. Thus, the particles of zirconia are, more or less, enclosed into the sepiolite cluster at loadings surpassing ca. 12.5 wt%.

The surface acidity of the composite catalysts were measured with NH_3-TPD and depicted in Fig. 4.8, and reveal a number of different desorption sites, especially at high temperatures. Four distinct acid sites were denoted according to their acid strength: α, β, γ, and δ. The exact desorption temperatures are collected in Tab. 4.1. The samples consisting mostly of VSZ (i.e. 0/8–4/8) display a broad desorption profile around 150–400°C (similar to the profile observed previously for 3.4SZ_NP), whereas only the 0/8–1/8 samples contain an acid site desorbing ammonia around 435–475°C, corresponding to the α-acid site. The elimination of the α-acid site at sepiolite loadings above 25 wt%, suggest that the coverage of the VSZ-particles in sepiolite impede the acid site. The β-acid site is only present on samples containing more than 50% sepiolite, and can thus be attributed to a sepiolite acid site. All samples desorb ammonia around 790–800°C at the γ-site, but only mixtures of sepiolite and VSZ contain sites desorbing ammonia at the strongest δ-site, peaking for the 4/8 sample. The δ-site can thus be attributed to a composite acid site, probably formed at the sepiolite/VSZ interface.
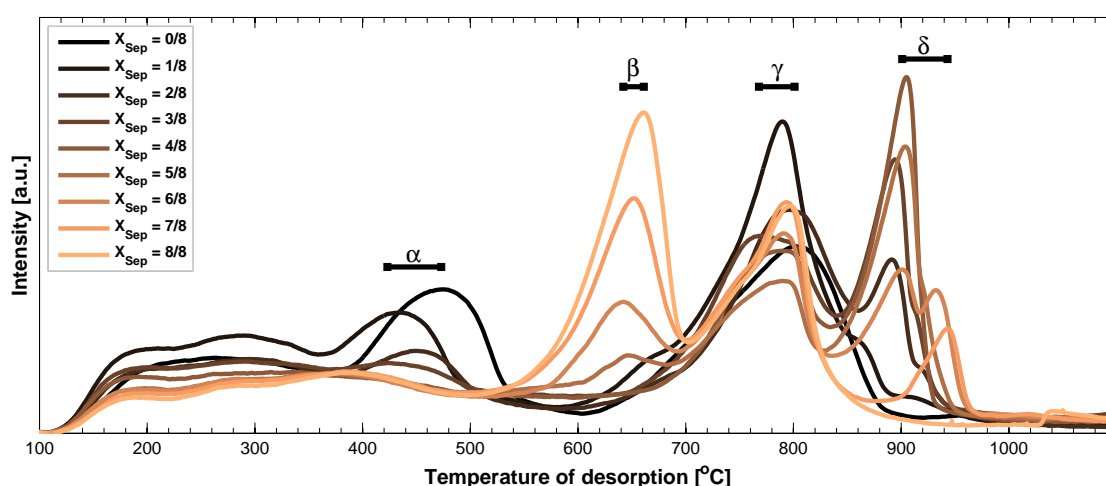
Fig. 4.8: NH_3-desorption profile for sepiolite-VSZ composite catalysts. Four desorption sites are observed in the high temperature region

Comparing the overall acidity of the series reveal almost identical total acidity across the series. However, for catalysis applications, the strongest sites of the active catalyst (i.e. γ and δ sites) are assumed to bind ammonia too strongly to participate in the SCR reaction. Therefore, only counting acid sites below ca. 550°C (cf. Tab. 4.1) is much more representative of the catalytic performance observed. The development in acidity, desorbing NH_3 below 550°C, with sepiolite content show a sharp decrease in acidity between the 1/8 and 2/8 sample, which can be explained by the sudden surface coverage of sepiolite, whereas at higher sepiolite loadings, a more moderate decline in acidity is observed as the sepiolite progressively covers the remaining VSZ particles.

The X-ray patterns of the calcined samples are presented in Fig. 4.9. The reflexes from the two phases resembling zirconia, cubic and tetragonal are located at 2θ 30.4°, sandwiched by the

two reflexes from the monoclinic ZrO$_2$ at 28.4° and 31.6°. Sepiolite only has few reflexes between 25 and 55°, but is acknowledged by the reflex at 39° 2θ. However, several reflexes besides those of sepiolite and zirconia exist. Catalysts with low content of sepiolite, reveal a trace of solid solutions of vanadium in zirconia. At intermediate sepiolite loadings, reflexes from CaSO$_4$ emerges, where Ca^{2+} from sepiolite react with sulfate from the sulfated zirconia. Samples consisting predominantly of sepiolite, reveal reflexes from CaCO$_3$, SiO$_2$, as well as diminutive reflexes, suggesting the presence of iron oxides, and silicates, verifying the high concentration of foreign compounds in the sepiolite. Electron spin resonance (EPR) spectroscopy performed on the samples (presented in Appendix C.1, Fig. C.1) also confirm the presence of Fe^{3+}-species in the sepiolite.
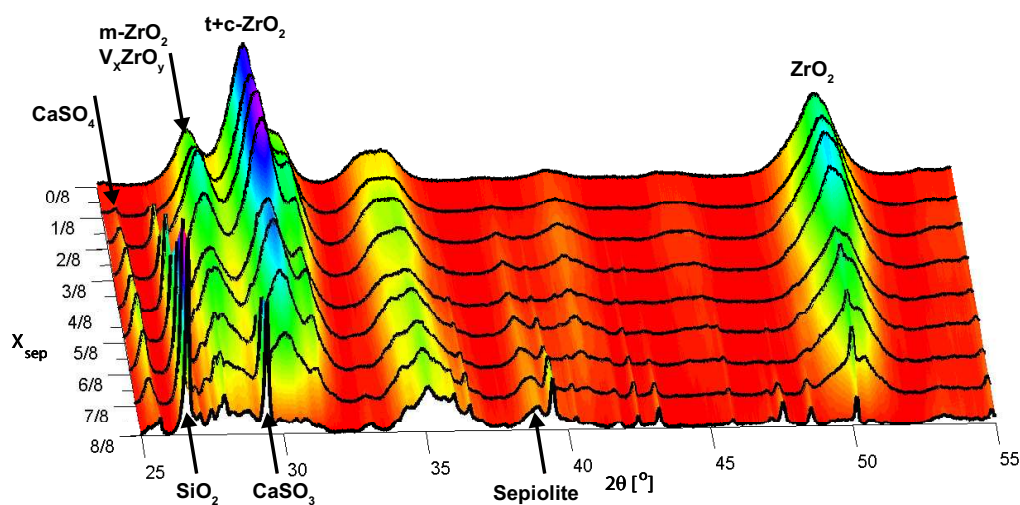

Fig. 4.9: XRD pattern of the sepiolite-VSZ series

To estimate the amount of the aforementioned phases present in the composite catalysts, Rietveld analysis has been performed on the series, the results of which are presented in Fig. 4.10. However, it must be noted that only the crystalline fraction can be observed in XRD, and the results obtained with Rietveld refinement are therefore not necessarily representative of these partially amorphous materials. With increasing sepiolite fraction, the concentration of crystalline m-ZrO$_2$ and c-ZrO$_2$ obtained through Rietveld refinement (Fig. 4.10), are gradually reduced in a linear manner, suggesting that the sepiolite to some degree inhibits formation of crystalline compounds by perturbing the matrix, resulting in amorphous species not detectable by XRD. The increasing fraction of sepiolite, represented by the hydrated and dehydrated conformations, only shows linear behavior for the dehydrated form of sepiolite, whereas the linearity of the hydrated sepiolite breaks off at sepiolite loadings above 50%, suggesting that the orthorombic structure is stabilized by the zirconia at low sepiolite loadings. The low concentration of dehydrated monoclinic sepiolite, could suggest that the zirconia-based particles perturb the dihydrate-structure of sepiolite, forming amorphous monoclinic sepiolite, not detected with XRD. This is supported by the structure of TiO$_2$-particles embedded within the fibers of sepiolite proposed by Ávila et al. [140,146]. Thereby, the actual concentration of the monoclinic structure of
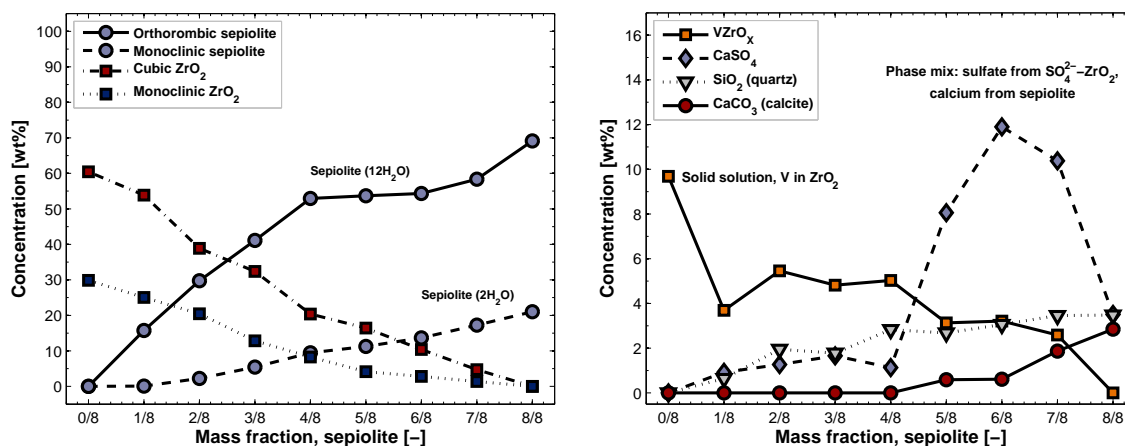
Fig. 4.10: Concentration of crystalline phases in the composite catalysts based on Rietveld refinement of the composite catalysts. **Left**: major phases present in the composite catalyst series, **Right**: minor phases present

sepiolite could be considerably higher than observed here.

The formation of $CaSO_4$ in composite samples consisting mostly of sepiolite, i.e. 5/8-7/8, constitute a rather large fraction of the total crystalline fraction, responsible for around 10 wt% (Fig. 4.10, right). A considerable amount of sulfate is therefore abstracted from the sulfated zirconia and diminishing its acidity, probably responsible for the enhanced decrease in SCR activity with sepiolite content observed in Fig. 4.5. The extraction of sulfate from zirconia, reducing its acidity, imply that additional sulfate should be added to the mixture during synthesis to compensate for this effect. This was attempted by impregnating the synthesis mixture of the 2/8 catalyst with additional ammonium sulphate. However, the effect on the SCR activity was negligible, although a small maximum was found, the results are shown in appendix C (Fig. C.4). Due to the insignificant impact on activity, optimization by means of additional sulfation were not pursued any further.

Based on the results obtained with MIP of the composite catalysts (shown in appendix, section C.1), the pore sizes of the catalysts can be extracted, and are presented in Fig. 4.11. Increasing the sepiolite content of the $V_2O_5-SO_4^{2-}-ZrO_2$/sepiolite composites has a marked effect on the observed pore volumes and macro pore diameter. By introducing 25 wt% of sepiolite the characteristic interparticular macro pore diameter decreased from 911 nm (0/8) to 320 nm, whereas the meso pore diameter remained almost constant throughout the series.

Finally, the physical strength of the pelletized catalysts were evaluated, the results from this are depicted in Fig. 4.12. As expected, the overall robustness of the pelletized catalysts increase with the sepiolite content. However, an abrupt increase in pellet strength were observed for the 2/8 sample, constituting a fair compromise between catalytic activity and physical strength. Furthermore, the coating effect of sepiolite at low loadings may provide some degree of shielding effect, enhancing the durability of the operating catalyst. This is further explored in the following section.
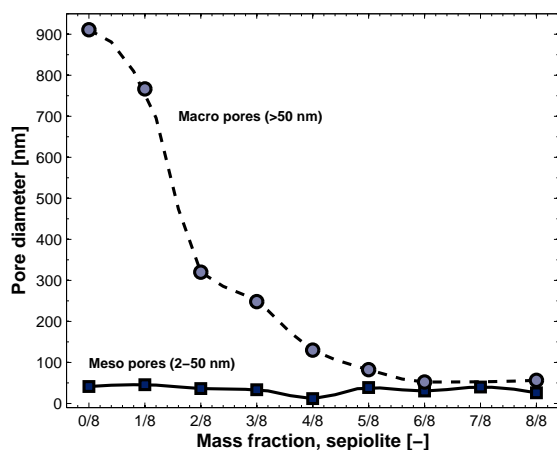
Fig. 4.11: Development in pore diameter of macro- and meso pores obtained from MIP with increasing sepiolite content
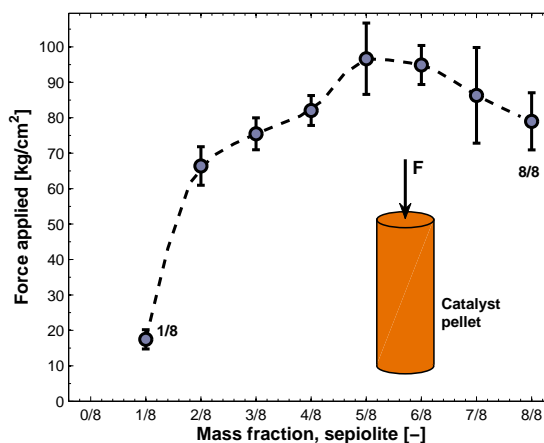

Fig. 4.12: Physical strength of produced pellets. Robustness measured by applying vertical force on identical sized pellets until breakage, as outlined in figure

4.2.2 Alkali-resistance of composite catalysts

The resistance toward potassium-poisoning of the composite catalysts were evaluated. Two methods of alkali-depositing were explored: incipient wetness impregnation (IWI) and hydrothermal treatment of the catalysts pellets submerged in fine particles of KCl as outlined in Fig. 4.13. The latter method, inspired by Zheng et al. [95], were performed to mimic the deactivation thought
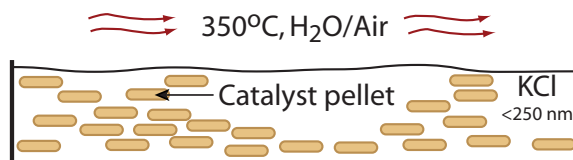
Fig. 4.13: Schematic illustration of the hydrothermal treatment of catalyst pellets

to occur through surface diffusion of alkali-species hitting the catalyst surface and migrating to the active sites of the SCR catalyst during operation [88]. An actual *in situ* deactivation would require catalyst exposure to aerosol alkali-particles, so this method is a crude simplification, but considerably easier to carry out.

The impact of potassium introduced via IWI and hydrothermal treatment in KCl under humid air at 350°C for 188 hrs (7.8 days) and 384 hrs (16 days) on the catalytic performance, are presented in Fig. 4.14 together with the 1.7VWT reference catalyst. Since a threshold of physical strength is required of the catalysts, only the 2/8, 4/8 and 6/8 composite catalysts were tested here. The catalytic activity of the 1.7VWT reference catalyst yielded considerably higher SCR activity than all of the composite catalysts 'diluted' with sepiolite, and the 6/8 catalyst with 75% sepiolite exhibited zero activity. The effect of hydrothermal treatment with KCl only moderately retarding the SCR activity, although potassium is present on the catalyst, as can be evaluated by SEM-EDS images provided in appendix (Fig. C.3), though potassium could be present as lumps of potassium, not effectively bound to the active sites. However, the IWI treatment significantly

Fig. 4.14: SCR activities at 360°C of the fresh and K-doped reference catalyst, 1.7VWT, and selected composite catalysts

Fig. 4.15: Remaining activity at 360°C (k_{doped}/k_{fresh}) of reference and composite catalysts

decreased the SCR activity of all catalysts. The relative activities present after alkali-poisoning are depicted in Fig. 4.15, and show that all catalysts exhibited roughly similar loss of activity due to the KCl-treatment. The reference catalyst deactivated 21%, and 2/8 composite catalyst deactivated 16% after 384 hrs submersed in KCl.
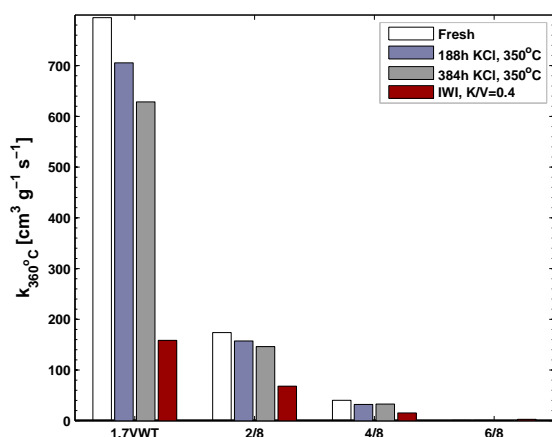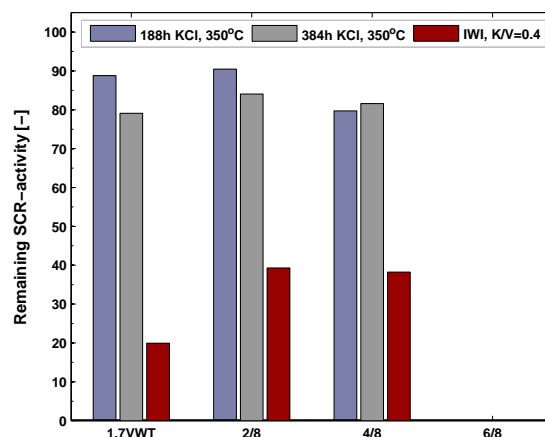
The low degree of deactivation suggests that the treatment temperature should be increased, at least to above the Hüttig temperature of KCl (422°C). At 350°C, the relative large KCl particles may never reach the majority of the active sites, e.g. due to pore blockage, where the macro pores of the catalysts (pore diameter of 1.7VWT: 298 nm, 2/8: 320 nm) could hinder the access of the KCl species. In contrast, K-depositing by IWI effectively penetrates both macro and meso pores, deactivating the reference catalyst 80% (i.e. remaining activity 20%), whereas the composite catalysts 2/8 and 4/8 only deactivates around 60%.

The reproducibility of the IWI method is confirmed by the 1.7VWT catalyst, which were earlier K-doped by IWI in a different experiment, where a deactivation of 83% were observed (cf. Tab 3.6). The relatively high deactivation of the sepiolite-containing composite catalysts is somewhat higher than previously observed for the 1.7-3.4SZ_NP catalyst, which only deactivated 38% under similar conditions. This suggests that sepiolite further reduces the alkali resistance of the catalysts, i.e. by deacidification through sulfate abstraction. However, the high vanadia content of the composite catalysts would also be more vulnerable to potassium deactivation than catalysts with lower loading[90].

4.2.3 Concise conclusion

The increasing content of sepiolite-binder in the catalyst certainly provide beneficial effects in terms of physical strength and possibility to manipulate the macro pore diameter of the extruded catalyst. On the other hand, the introduction of sepiolite also entails loss of surface acidity (damping of the α-acid site) through abstraction of sulfate from $V_2O_5 - SO_4^{2-} - ZrO_2$, forming $CaSO_4$, and thereby reducing the SCR activity of the composite catalysts.

By electrophoretic migration experiments it was show that zirconia-based catalysts containing sepiolite concentrations above 12.5 wt% are, more or less, coated by the clay fibers. Although the suggested shielding effect of the enveloping sepiolite could be affirmed here, the concept is an interesting approach in reducing the impact of potassium particles in biomass fired power plants.

The most promising candidate of the composite catalysts studied here, as a compromise between SCR activity and physical stability, is the 2/8 catalyst, comprising 75% VSZ in sepiolite. To further evaluate the performance of the optimal catalyst, the 2/8 formulation were extruded as monolith and the results are presented in the following section.

4.3   Evaluation of monolithic catalyst

The optimal catalyst, in terms of catalyst stability and SCR activity, was in section 4.2 identified as the composite catalyst comprising 75% VSZ in sepiolite, the 2/8 sample. The 2/8 formulation was extruded as cylindrically-shaped monoliths with 24 parallel channels, as presented in Fig. 4.16.

4.3.1   Catalytic performance

To ensure that the monolithic catalyst was comparable to the catalysts synthesized in connection with the series with increasing sepiolite content, the monolith were crushed to the same particle size as the 2/8 pellet catalyst from previous section. The catalytic activity of the two samples are depicted in Fig. 4.17, which reveal almost identical SCR activities. High-temperature annealing at 500°C in both cases result in significant thermal deactivation to the catalysts, as observed previously for V-based catalyst.
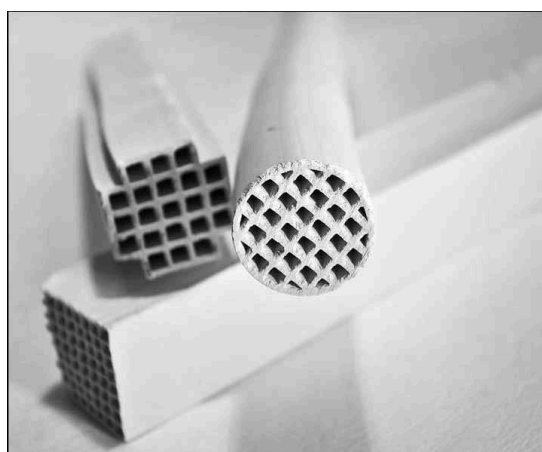

Fig. 4.16: Various shapes of the extruded monolith. Only the cylindrically shaped monolith were used for the results presented in this section
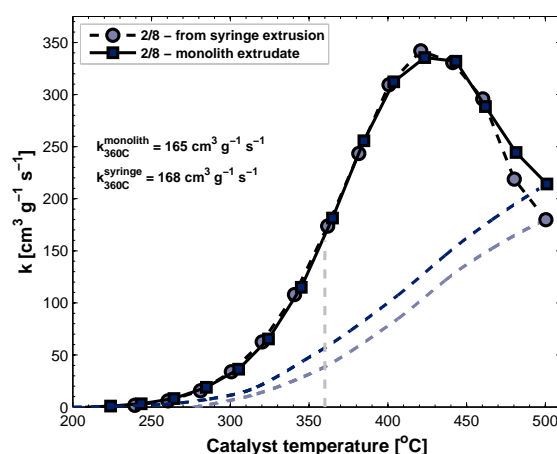

Fig. 4.17: Comparison of the SCR activity profile of mechanically and manually extruded catalysts, subsequently fractionated to 180–300μm

Interpolation of the k-values to 360°C show only an insignificant difference in activity, af-
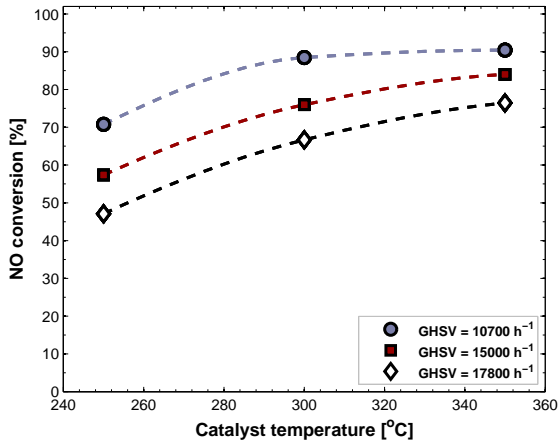
Fig. 4.18: NO conversion as function of temperature at three different space velocities
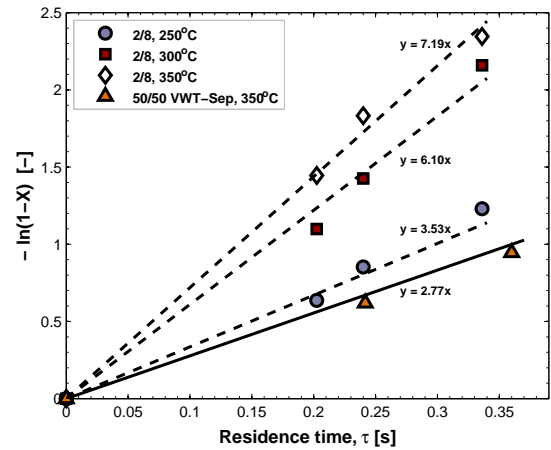
Fig. 4.19: Plot of -ln(1 − X) versus residence time. Slope equal to $k\rho_{bulk}$

firming that the monolithic catalyst produced is indeed representative of the 2/8 catalyst formulation. Considering that the catalyst synthesis has been scaled up about 50 times, it is remarkable that the SCR activities are identical to those of the catalyst manually kneaded and extruded.

The SCR activity of the extruded 2/8 monolith was tested as described in appendix, section A.2.3.3. The activity at different gas hourly space velocities (GHSV, STP) are obtained by varying the gas flows (but keeping the linear velocity above 1.2 m/s), presented in Fig. 4.18. The overall activity is naturally increased with decreasing GHSV (i.e. longer residence time). At GHSV = 10700 h^{-1} the conversion profile stagnates at temperatures above 300°C, suggesting that the SCR reaction become diffusion limited and/or mass transfer limited on the 2/8 catalyst under these circumstances. In other words, the SCR reaction is proceeding at a rate faster than the reactants can be transported to the reactive sites.

A convenient representation of the conversion is as a function of the gas residence time, τ, which can be expressed as:

$$\tau = \frac{1}{GHSV} = \frac{V_{cat}}{q} = \frac{L_{cat\,bed}}{v_L} \tag{4.1}$$

where V_{cat} is the catalyst volume, q the total gas flow, and v_L the linear velocity. Under the given test circumstances, it is not possible to reach a higher contact time due to the diffusion limitation observed at 10700 h^{-1} (τ = 0.34 s). However, based on the rate expression for the first order reaction provided in equation A.5 (page 93), is it possible to extrapolate the conversions to longer residence times. Unit analysis reveal that the rate expression of the first order rate constant, k, can be rewritten:

$$k = -\frac{F_0}{[NO]_0 W} \ln(1\text{-}X) \Rightarrow -\frac{q}{W} \ln(1\text{-}X) \tag{4.2}$$

The catalyst weight is given by its volume and bulk density ($W = \rho_{bulk} V_{cat}$). By applying equa-

tion 4.1 the residence time emerges, which can be rearranged as a function of τ:

$$k = -\frac{q}{\rho_{bulk} V_{cat}} \ln(1\text{-}X) \Leftrightarrow k = -\frac{1}{\rho_{bulk}\tau} \ln(1\text{-}X) \qquad (4.3)$$

$$-\ln(1\text{-}X) = k\rho_{bulk} \cdot \tau \qquad (4.4)$$

Thus, by plotting $-\ln(1\text{-}X)$ as a function of residence time, $k\rho_{bulk}$ can be obtained from the slope. The relationship is presented in Fig. 4.19. The first order rate constants of the monolith can be calculated since the bulk density is known, $\rho_{bulk} = 1.45$ g/cm^3. The results are outlined in Tab. 4.2, where the k-values obtained from the measurement of the fractionated monolith (k_{powder}) are also provided. The ratio between the k-values of the monolith and fractionated catalyst represents the efficiency of the monolith, under the assumption that no mass transfer limitation is occurring on the fractionated catalyst, as was the case at 350°C for the monolith (cf. Fig. 4.18). The efficiencies observed here correspond well with those found in literature [147].

Tab. 4.2: First order rate values of monolith and fractionated catalyst consisting of 25 wt% sepiolite in VSZ (2/8 catalyst)

		Catalyst temperature		
		250°C	300°C	350°C
k_{mon}	[cm^{3}g^{-1}s^{-1}]	2.4	4.2	5.0
k_{powder}	[cm^{3}g^{-1}s^{-1}]	4.7	31.8	131.7
$\eta^\dagger$	[%]	51.3	13.2	3.8

† Catalyst efficiency, $\eta = k_{mon}/k_{powder}$

By rearranging equation 4.4, the NO conversion (X) can finally be expressed as a function of τ (outlined in equation 4.5) which can be extrapolated to higher residence times, assuming absence of mass transfer limitations, as presented in Fig. 4.20.

$$X = 1 - \exp(-k\rho_{bulk}\tau) \qquad (4.5)$$

Based on the parameters found, a projection of the catalyst activity at lower space velocities can be calculated. 98% conversion is achived at $\tau = 0.6$ s in the 2/8 monolithic catalyst at 350°C, and assuming a linear gas velocity of 2 ($v_L = 1$–4 m/s [148] over honeycomb V_2O_5–WO_3–TiO_2 catalysts under industrial conditions) would require a catalyst length ($L_{cat\ bed}$) of 1.2 m to ensure total NO_x removal. As an example of industrial conditions, a 250 MW coal-fired power plant in Belgium is used. The plant is operating with a Haldor Topsøe SCR catalyst in the temperature regime 320–390°C under a total flow of 820,000 Nm^3/h with a catalyst volume 268 m^3 in two layers of 2 m in total length, and a NO_x-concentration of 1000 ppm [149], yielding a GHSV (STP) of 3060 h^{-1} ($\tau = 1.2$ s). Thus, based on the projections in Fig. 4.20, the extruded 2/8 monolith would under industrial conditions ($\tau = 1.2$ s, 350°C) remove all the NO present, and more than 98% at 250°C. Considering that the ZrO_2-based monolith exhibit somewhat higher tolerance to potassium-poisoning than the traditional V_2O_5–WO_3–TiO_2 catalyst, the lifetime of the zirconia-based catalyst may be considerably longer than the traditional catalyst in biomass-fired

installations. However, long time exposure of the sepiolite-based VSZ catalyst has not yet been carried out, and of course this would need to be addressed.
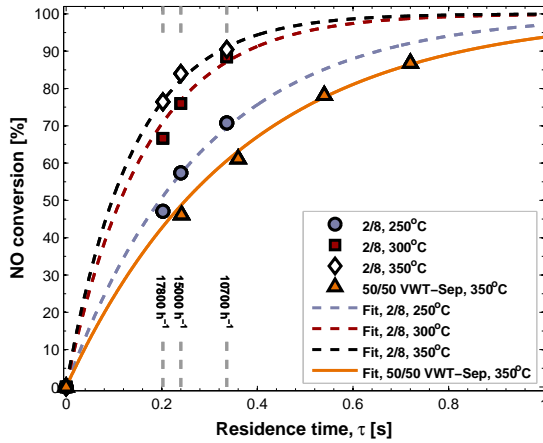
Fig. 4.20: NO conversion as a function of residence time by varying reactor temperature and space velocity
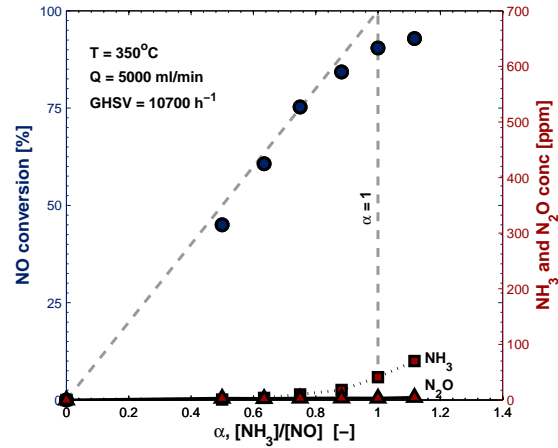
Fig. 4.21: Conversion of NO versus the ammonia/NO ratio. NH_3-slip and evolution of N_2O concentrations on right axis

4.3.2 Influence of feed ratio

The gas inlet concentration of NH_3 was varied, while fixing the NO concentration at 700 ppm in order to evaluate the experimental impact of the feed ratio α ($[NH_3]/[NO]$) on the SCR activity of the 2/8 monolith at 350°C. The NO conversion as a function of the the feed ratio is presented in Fig. 4.21, where it can be observed that the NO conversion is stoichiometrically and kinetically limited by the NH_3-concentration at substoichiometric feed ratios ($\alpha < 1$), in line with results reported by Bahamonde et al. on VWT-sepiolite monoliths[136]. Furthermore, at $\alpha < 1$, the rate expression used so far (equation A.1, page 93), $r = k[NO]^1[NH_3]^0$, fails to describe the reaction rate effectively, because it was derived assuming a NH_3-surplus. However, under these circumstances, a Rideal-type reaction rate has previously been used to describe the rate of reaction[150,151]:

$$r = k[NO]\theta_{NH_3} \tag{4.6}$$

where θ_{NH_3} is the fractional surface coverage of absorbed ammonia on the active sites, and represents the impact of ammonia on the activity.

In excess ammonia ($\alpha > 1$) the NO conversion becomes independent of the feed ratio (cf. Fig. 4.21), and the rate expression in equation A.1 holds true, where the ammonia concentration is described by zero order kinetics. Due to the 1:1 stoichiometry of the SCR reaction, an ammonia slip is observed at $\alpha > 1$. It is worth noticing that almost 90% of the NH_3-surplus at $\alpha = 1.11$ is not oxidized to NO_x, but remains on NH_3 form. However, at industrial conditions the feed ratio is operated at $\alpha = 0.8$[136,152] to avoid ammonia slip. Under these conditions (350°C, GHSV = 10700 h^{-1}), a high catalytic activity is still provided by the 2/8 monolith, removing around 80% of the initial NO, the same behavior as the titania-based catalyst[136,147].

4.3.3 Summary and conclusion

The catalyst formulation containing $V_2O_5-SO_4^{2-}-ZrO_2$ in 25% sepiolite was succesfully upscaled to a monolith. The monolithic configuration exhibited exactly the same SCR activity (when fractionated) as the manually kneaded and extruded pellet, and were thus representative of the optimal 2/8 formulation.

Catalytic characterization of the cylindric monolith at different space velocities and feed ratios revealed fairly high SCR activities, although mass transfer and/or diffusion limitations in this system commence around 350°C with the linear velocity 1.2 $^m/_s$ and GHSV = 10700 h^{-1}. However, extrapolation of the activity to lower space velocities were carried out by incorporating the residence time, τ, into the expression for the first order rate constant. Thus, the activity of the 2/8 monolith could be predicted for conditions similar to those of the industrial $V_2O_5-WO_3-TiO_2$ catalyst ($\tau = 1.2$ s, 350°C). According to these predictions, the ZrO_2-based catalyst would perform equally well, removing more than 99.9% of the incident NO_x gases. Furthermore, the advantage of the ZrO_2-based catalyst become most evident if alkali species are present in the flue gas, due to the higher potassium resistance when compared to the titania-based catalysts. Thus, in biomass-fired installations the catalyst lifetime could be considerably prolonged. However, long term exposure of the catalyst under *in situ* conditions are yet to be addressed for the 2/8 catalyst.

4.4 Conclusion

The mixing of $V_2O_5-SO_4^{2-}-ZrO_2$ with the the binding clay, sepiolite, provided physical stability to the catalyst, rendering the extrusion as monolith or pellets possible. Electrophoretic migration experiments and SEM revealed that already at small concentrations of sepiolite (above 12.5 wt%) the VSZ particles were enveloped by the clay fibers. Beyond the 'threshold' clay-concentration, other noticeable structural changes of the composite samples entailed: increased physical stability particle aggregation; decrease of surface acidity; and macro porosity. As a compromise between catalytic activity and physical stability, the formulation containing VSZ in 25% clay was selected as the optimal catalyst.
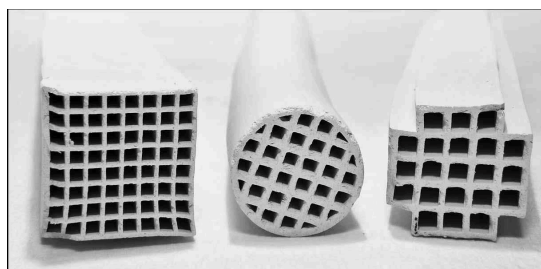
Although sepiolite was found to abstract sulfate from the VSZ particles in mixtures comprising predominantly of sepiolite (>50%), thus reducing the overall acidity and SCR activity, the presence of sepiolite on the surface of the active particles could provide some protective effect

due to its meso porosity, prohibiting larger alkali particles acces to the active sites, or simply postponing the poisoning. However, only indicative evidence for this effect was found through the slightly higher alkali-resistance of the sepiolite-based catalyst over the VWT-reference catalyst when submersed in fine particles of KCl and hydrothermally treated.

The zirconia-sepiolite formulation could be extruded in monolithic form, and contained promising SCR activity under conditions similar to industrial circumstances. This study thus opens for the possibility of further investigation into this type of SCR catalyst as a candidate, less susceptible to potassium-poisoning than the traditional titania-based catalyst.

Chapter 5

NO absorption in ionic liquids

This chapter is devoted to study NO gas removal by absorption in ionic liquids. It should be noted that absorption of gaseous NO in ionic liquids have not yet been reported in literature. Thus, due to the novelty of the field, the system is not completely understood. The removal of NO by 'wet' absorption is however not a new phenomena and some other processes are summarized in the following introduction as well as a preface to ionic liquids.

5.1 Introduction

Although the catalytic removal of NO_x from the flue gas is a very effective process, the overall high operating expenses of the SCR process and possibility of ammonia slip, have motivated a search for other methods to abate emissions of nitrogen oxides[153,154]. A promising concept is wet scrubbing systems for removal of SO_2 and NO_x. Some aqueous scrubbing systems have been developed for the simultaneous removal of NO_x and SO_2[155,156]. The wet flue gas desulfurization (FGD) typically exhibit high SO_2 removal efficiencies, but the FGD can only remove a small amount of NO_x because about 90–95% in a typical flue gas is present as insoluble NO and only the remaining 5-10% NO_2 is water soluble. Attempts to oxidize NO to water soluble NO_2 have been made by adding strong oxidizing additives, such as MnO_4^- and H_2O_2, but the treatment cost involved herein has been too high for practical utilization[155] (and references herein). Promising results of the simultaneous NO and SO_2 removal in a $Co(NH_3)_6^{2+}$ solution have been reported by Long et al.[155,157], which operates below 80°C. Another approach is complexation of NO with Fe^{2+}-chelates based on ethylenediaminetetraacetic acid (EDTA) or nitrilotriacetate (NTA)[158], as outlined in reaction R-5.1 for the case of iron-EDTA complex[154].

$$Fe^{II}(EDTA) + NO \rightleftharpoons Fe^{II}(EDTA)(NO) \qquad \text{(R-5.1)}$$

The metal-chelate can be electrochemically regenerated after absorption or reduced by sulfite ions to sulfate and nitrogen[154]. Recently a biotechnological approach were described to regenerate the iron-complex, the so-called BioDeNO$_x$ process. In this process the NO-saturated iron-chelate solution is brought in close contact with bacteria that regenerate the iron-EDTA complex and converts the bound nitrosyl to N_2[159]. The $Fe^{(II)}(EDTA)$ solution need to be somewhat diluted (<200 mM) due to the presence of microorganisms, which naturally limits the absorption capacity.

5.1.1 Ionic liquids

All of the above proposed technologies are based on liquids with a vapor pressure, which means that the solvent, to some extent, vaporizes. One promising solution to this problem could be the use of a relatively new class of solvents referred to as ionic liquids (ILs). The expression 'ionic liquid' in principle encompasses any liquid entirely composed of ions (e.g. molten salts), but within the context of this work the term will only be used to describe materials which are liquid in their pure state at room temperature. This class of solvents are often considered as 'green' solvents because of their immeasurably low vapor pressure [160] (and references herein). This feature gives the ILs an essential advantage over traditional solvents used for absorbing gases. Ionic liquids have already demonstrated promising behavior in a number of reactions where gaseous reactants enter the IL solution (such as hydrogenation, hydroformylation, and oxidations) despite low gas solubilities of the gases in the IL at ambient conditions [160,161].

Another application of the ILS is to utilize them to separate gas mixtures. Recently, a promising solid ionic cation (1,1,3,3-tetramethylguanidinium) have been identified [162] for the absorption of SO_2. Anthony et al. [160] reported of the solubilities of a number of gases (such as CO_2, CO, O_2) in imidazolium-based ILs.

Ionic liquids tend to be more viscous compared to conventional solvents [163], which can result in challenges regarding the mass transfer of gas into the IL. In the case of low-soluble gases, the mass transfer into the IL will likely be a rate limiting step, which can be minimized by increasing the interfacial gas-IL area and/or use high pressure systems [160].

So far, only little information regarding the gas solubilities in ILs is reported. Besides the reports regarding CO_2 capture [164] (and references herein) the focus of most works evolve around the reactions taking place in the IL with the gas already absorbed. Only few reports exist on gas solubilities [160,165,166], but especially Brennecke et al. have contributed with a number of seminal studies on absorption of a number of gases in imidazolium-based ILs [160,166–168].

The focus of the present work is to study the absorption and desorption behavior of NO in ILs based on the cation 1-ethyl-3-methylimidazolium (EMIM$^+$) and 1-butyl-3-methylimidazolium (BMIM$^+$).

5.2 Screening of ionic liquids

The absorption of NO in a number of different ILs were investigated in this preliminary study, all based on the cations and anions presented in Fig 5.1. Some physical properties of the pure ILs used (supplier and purity listed in Appendix, section A.4.3) are collected in Tab. 5.1, all revealing viscosities many times higher than that of water. The experimental procedure to measure the NO absorption capacity in the ILs are based on a rudimentary setup, described in section A.4.1. The absorption time was several days due to slow mass transfer from gas to IL, and the screening-experiments were therefore stopped before complete equilibrium were obtained. The resulting solubilities presented in this section are therefore based on pseudo-equilibrium
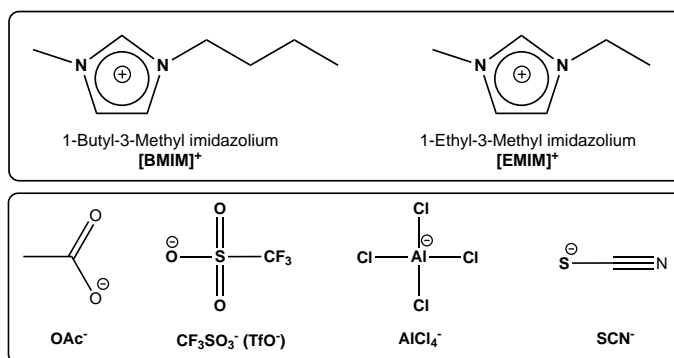
Fig. 5.1: The cations and anions used in this study. Lower box, from left to right: acetate, triflate, tetrachloroa-
luminate and thiocyanate

measurements. However, the apparent solubilities obtained here still provide sufficient infor-
mation to identify suited candidates for further studies.

Tab. 5.1: Properties of the ionic liquids used in the preliminary study. Data supplied by BASF[†]

Compound	M	Viscosity at RT	Density at RT	T_{mp}
	[g/mol]	[mPa·s]	[g/cm^3]	[°C]
[EMIM]AlCl$_4$	280.0	26	1.30	9
[BMIM]AlCl$_4$	308.0	32	1.24	-10
[EMIM]SCN	169.3	22	1.11	<-20
[BMIM]SCN	197.3	54	1.07	<-20
[EMIM]OAc	170.2	93	1.10	<-20
[BMIM]OAc	198.3	398	1.06	<-20
[EMIM]OTf	260.2	41	1.34	-11
[BMIM]OTf	288.3	84	1.30	17
[OMIM]OTf[‡]	344.4	n.a.	n.a.	n.a.
H$_2$O	18	1	1	0

[†] BASF: www.basionics.com/en/ionic-liquids/products
[‡] 1-octyl-3-methylimidazolium triflate

5.2.1 Absorption/desorption study

All the ILs presented in Tab 5.1 were evaluated with respect to their NO sorption performance.
However, not all ILs were suitable for the liquid sorption studies. The ILs based on AlCl$_4^-$ and
SCN$^-$ all formed precipitate upon contact with the NO/N$_2$ gas mixture and the absorption re-
sults were thus discarded. Although the NO-induced crystallization of the ILs observed are inter-
esting and definitely worthwhile to study further, the focus were here maintained on absorbents
which remained in their liquid state upon NO exposure. Hence, only the sorption results of
the ILs with the acetate and triflate anion are presented in Fig. 5.2 as a function of the appar-
ent mole fraction of NO absorbed (X_{NO}^{IL}). Considering the acetate-based ILs, [EMIM]OAc and
[BMIM]OAc, it is clear that significant amounts of NO can be absorbed, corresponding to about
2 moles of NO per IL molecule (equal to a NO mole fraction of 0.667). Interestingly, varying
the cation of the acetate-based ILs only seem to influence the NO solubility to a minor extent,

Fig. 5.2: Total amount of absorbed NO after pseudo-saturation at room temperature and vacuum-desorption

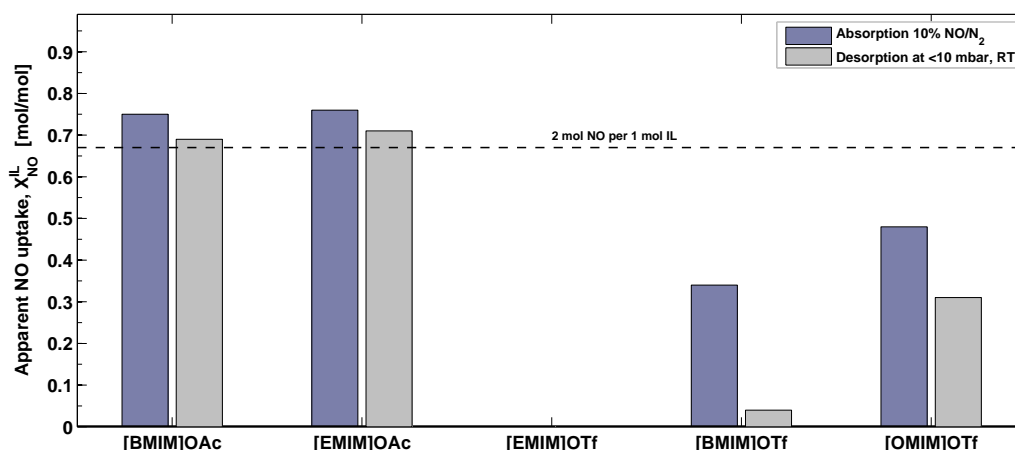in contrast to the triflate-based ILs where the absorption capacity increased with alkyl length. Thus, the [OMIM]OTf exhibit highest solubility of NO of the triflate-based ILs, absorbing about 1 mole of NO per mole of IL (mole fraction 0.5). NO absorption capacities in ionic liquids of this size have not previously been reported, to our knowledge. Only the absorption of SO_2 in the tetramethylguanidium-based ILs, [TMGHPO]Tf_2N or [TMGHPO$_2$]Tf_2N, have been reported to yield similar solubilities, i.e. mole fractions about 0.67 [162,169].

The reversibility of the gas absorption were examined by applying vacuum to the NO-absorbed IL at room temperature for at least 24 h. The remaining NO in the IL, expressed by the mole fraction of NO, is also presented in Fig. 5.2. Only a small amount of NO could be removed from the acetate-based ILs by reducing the pressure, suggesting that the NO is strongly bound in the [EMIM]OAc and [BMIM]OAc. On the other hand, the reversibility of the NO sorption in the ILs based on triflate is somewhat higher. Almost all the absorbed NO could be desorbed in the case of [BMIM]OTf, but only about 1/3 of the NO could be removed from the [OMIM]OTf under the examined conditions.

Preliminary examination of the absorption of N_2 in [BMIM]OAc were also undertaken. This did not result in any measurable weight increase, from which in can be concluded that only NO is absorbed when passing NO/N_2 through the [BMIM]OAc.

5.2.2 Influence of metal-promotion on absorption capacity

It is well known that iron can bind NO in form of the brown iron nitrosyl complex Fe(NO)$^{2+}$ [19]. The approach of incorporating a complexation or redox agent into the ionic liquid was explored in the following section where enhancing the absorption capacity of the ILs was attempted by metal promotion. Based on the preliminary sorption study (section 5.2.1), the [BMIM]OTf was selected due to its high sorption reversibility. The metal promotion was carried out by adding the triflate-salt of a metal (Fe(OTf)$_3$, Co(OTf)$_2$, and Cu(OTf)$_2$) to the [BMIM]OTf) to obtain a metal concentration of 0.5 mol/l. The absorption capacities of these metal-promoted ILs were examined, and the results are depicted in Fig. 5.3 as a function of 'time-on-stream'. The results
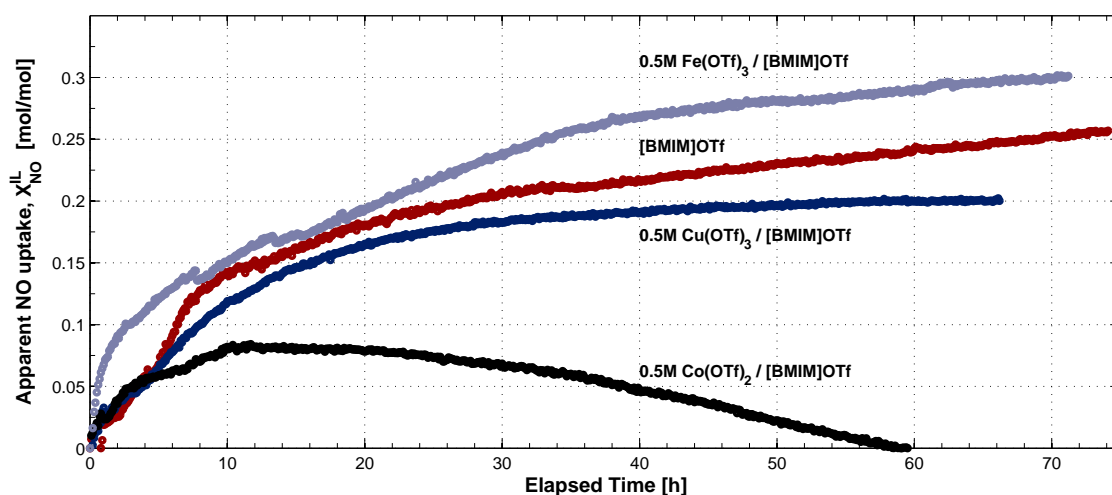
Fig. 5.3: NO absorption time-profile at 20°C for [BMIM]OTf with metals of iron, copper and cobalt dissolved. Absorption performed with 10% NO/N$_2$ on a setup similar to the one used to obtain the results presented in Fig. 5.2 (described in section A.4.1), but without a glass frit on the pipette. Thus, the time of absorption are longer due to lower gas-IL interfacial area

presented are based on continuous logging of the weight increase, which has not been corrected for buoyancy, as incited by Anthony et al.[160]. This correction is especially important for low-solubility gases where the influence of buoyancy is relatively large compared to the total weight, which is not the case here. However, this sub-study only focuses on the relative absorption trend and the influence from the buoyancy can thus be disregarded. Nonetheless, the total amount of NO absorbed in [BMIM]OTf is in the same range as in Fig. 5.2 and the influence of buoyancy is thus minimal in these experiments.

The solubility of NO in [BMIM]OTf is not further enhanced by promotion with cobalt or copper triflate. As can be can be observed in Fig. 5.3, the addition of cobalt actually decreases the solubility of NO in [BMIM]OTf significantly, although only 0.5 M cobalt was added. The weight decrease observed for the Co-doped IL, suggests that the [BMIM]OTf reacted with the NO (facilitated by Co^{2+}), resulting in the generation of a liquid with a vapor pressure, or a gradually decomposition of the IL to gaseous components.

An 20% increase in the absorption capacity was observed in the case of absorption in Fe(OTf)$_3$-/[BMIM]OTf, which together with an observed darkening of the brown-colored IL, suggests that the iron-nitrosyl complex has actually been formed.

Considering the use of the ionic liquids as NO$_x$-removing media, a reversible absorption where the IL could be reused would be essential due to presently high cost of ILs[170]. The iron nitrosyl is a rather stable complex with an equilibrium constant around 450 M^{-1} (in water)[171], which inhibits the desorption. The small increase in absorption achieved when utilizing iron-promoted ILs may thus be counterbalanced by the corresponding additional energy needed to desorb the NO. Therefore, for the remaining of the absorption study, only the pure ILs were examined.

5.2.3 Concluding remarks on preliminary sorption study

Based on the experiences from the preliminary study (section 5.2), only [BMIM]OAc and [BMIM]-OTf were selected for further examination. [BMIM]OAc was chosen based on its capability to retain large amounts of NO, and [BMIM]OTf due to its high reversibility in the absorption/desorption. Although [BMIM]OAc and [EMIM]OAc exhibited similar NO solubilities, the purity of the commercial [EMIM]OAc was only >90%, whereas [BMIM]OAc was >95% pure. Thus, to minimize the effect from any pollutants, the purest was selected for further examination.

5.3 NO sorption in [BMIM]OAc and [BMIM]OTf

The absorption of NO into [BMIM]OAc and [BMIM]OTf was measured at various temperatures at 1 bar (description of the experimental test rig and conditions is presented in section A.4.2). The absorption results presented in this section are all based on equilibrium measurements.

The NO solubilities in [BMIM]OAc and [BMIM]OTf as a function of temperature are presented in Fig. 5.4. The ILs were initially saturated at room temperature and subsequently heated stepwise under a continuous flow of 10 mol% NO/N_2 (i.e. NO partial pressure 0.1 bar). Comparing the solubilities of NO obtained here (room temperature and 0.1 bar) with e.g CO_2 absorbed in $[BMIM]BF_4$ (X_{CO2} = 0.0012, 0.1 bar) reported by Anthony et al.[168], reveal that NO sorption capacities of [BMIM]OAc and [BMIM]OTf are several magnitudes higher. A more suitable comparison with literature data could not be performed due to the lack of gas sorption data on [BMIM]OAc and [BMIM]OTf. However, gas solubilities can be predicted with a quantum chemistry method known as COSMO-RS (further description in section A.4.4), which can estimate thermophysical data, such as physisorption, in a number of ILs[172–174]. This method was applied to estimate the contribution from physisorbed NO species in [BMIM]OAc and [BMIM]OTf, the results are presented in Fig. 5.5. As can be observed, only a very small fraction of the absorption (<1%) can be ascribed to the physical binding of NO in the ILs. Thus, the NO-sorption in [BMIM]OAc and [BMIM]OTf is more of a chemical nature than physical.

The overall NO absorption capacity of the ILs at room temperature was very high (cf. Fig. 5.4). The [BMIM]OTf could host about 1.5 mol NO per mol IL (X_{NO} = 0.6), whereas [BMIM]OAc could retain about four molecules of NO per IL molecule (X_{NO} = 0.8). By heating to 70°C is was possible to remove about 3/4 of the absorbed NO molecules. In the case of [BMIM]OTf, it was possible to completely desorb all NO by heating to about 60°C, thus suggesting a weak interaction between solute and [BMIM]OTf. In contrast, the solute-solvent interaction between NO and [BMIM]OAc is stronger and not all NO could be desorbed in these experiments by increasing the temperature. This is in agreement with results from the preliminary study where NO could easily be removed from the absorbed [BMIM]OTf, as opposed to [BMIM]OAc. The solubility of NO in a liquid can be described by Henry's law[160]:

$$H_{NO}(T,P) \quad \equiv \quad \lim_{X_{NO} \to 0} \frac{f^L_{NO}}{X_{NO}} \quad \approx \quad \frac{p_{NO}}{X_{NO}} \tag{5.1}$$
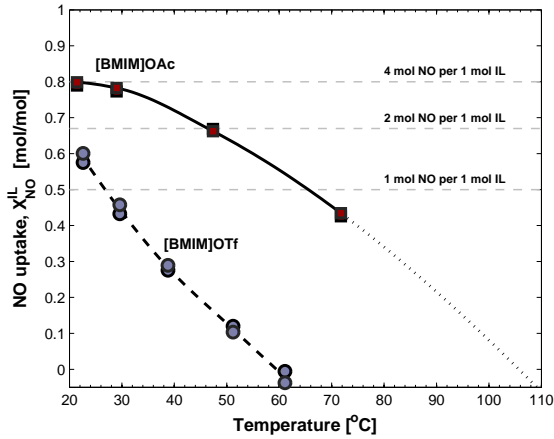
Fig. 5.4: NO absorption profile of [BMIM]OAc and [BMIM]OTf with temperature. Both experiments performed with two sorption reactors
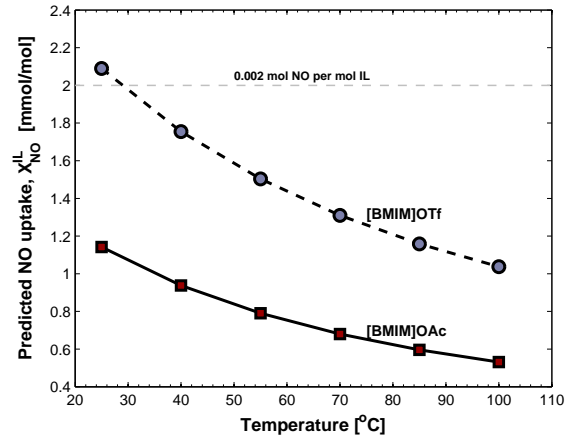
Fig. 5.5: Predicted contribution from NO physisorption in [BMIM]OAc and [BMIM]OTf

where H_{NO} is the temperature and pressure dependent Henry coefficient, f_{NO}^L is the fugacity of the vapor in the liquid, p_{NO} the partial pressure of the gas, and X_{NO} the mole fraction of NO dissolved in the liquid. Equation 5.1 thus describes a linear relationship between gas concentration and pressure, but only holds valid for solubilities approaching zero. The decrease in solubility observed with temperature (increasing NO partial pressure) in Fig. 5.4 are thus in agreement with the expected decrease with temperature.

The enthalpy (ΔH_{sol}) and entropy (ΔS_{sol}) of gas dissolution can be found by considering the effect of the temperature on the solubility. Information on the strength of interaction between the IL and solute can be found in the enthalpy, and the entropy indicates the level of order present in the NO/IL mixture. The change in enthalpy and entropy upon dissolution can be determined from the solubility data with the following thermodynamic van't Hoff relations in equation 5.2 and 5.3.

$$\Delta H_{sol} = R \left(\frac{\partial \ln H_{NO}}{\partial (1/T)} \right)_P = -R \left(\frac{\partial \ln X_{NO}}{\partial (1/T)} \right)_P \tag{5.2}$$

$$\Delta S_{sol} = -R \left(\frac{\partial \ln H_{NO}}{\partial \ln T} \right)_P = R \left(\frac{\partial \ln X_{NO}}{\partial \ln T} \right)_P \tag{5.3}$$

The equations hold valid in the Henry's law regime at infinite dilution, where the activity coefficient of the gas is independent of the amount of dissolved gas (X_{NO})[167]. The calculated enthalpies and entropies, based on measurements at highest temperatures (i.e. lowest gas solubility), are collected in Tab. 5.2. The values are based on a linear regression of the data, suggested by the van't Hoff relationships in equation 5.2 and 5.3. However, the values obtained from the linear regression are only based on solubilities at three temperatures, and the uncertainty may thus be somewhat larger than suggested here.

By applying the van't Hoff equations, a negative enthalpy change upon dissolution of NO in [BMIM]OTf was found together with an increase in the order of the system. The observed decrease in entropy suggests that NO is more ordered within the IL than in the gas. Compared to the average bond energy of the NO bond of 631 kJ/mol[175], the energy released upon sorption

is thus only about 8% of the intramolecular energy.

The magnitude of the enthalpy observed in Tab. 5.2 are in the same range as those typically observed upon absorption of gases in ILs[160,162,168]. However, the solubility data available for NO in [BMIM]OAc (cf. Fig. 5.4) are far from the conditions where the van't Hoff equations apply (Henry regime), and the resulting enthalpy and entropy can not be calculated without an considerable margin of error. However, based on the sorption results, the NO is more strongly bound in [BMIM]OAc than in [BMIM]OTf, which should result in a more negative enthalpy of absorption (more exothermic).

Tab. 5.2: Standard enthalpy and entropy of NO dissolution in [BMIM]-based ILs

	ΔH_{sol} [kJ/mol]	ΔS_{sol} [J/mol·K]
[BMIM]OTf	-53 ± 4	-167 ± 12
[BMIM]OAc[†]	n.a.	n.a.

[†] Values are based on NO solubilities obtained at $X_{NO} = 0.43–0.78$, and thus far from infinite dilution where ΔH_{sol} and ΔS_{sol} can be calculated

Based on the results obtained here and in the screening, the effect of cation and anion on the NO-solubility can be evaluated. Although similar amounts of NO can be absorbed in [BMIM]OAc and [BMIM]OTf, the reversibility is only characteristic of the triflate anion, suggesting that NO is stabilized in the solution by the acetate ion. On the other hand, in the preliminary study of the triflate-based ILs the cation was also shown to have a significant effect on the overall NO sorption and reversibility. Consequently, it can not be determined whether the anion or cation is responsible for the absorption, based on the ILs studies here. Anthony et al. suggested that the IL-anions are accountable for the gas sorption properties[168], whereas Huang et al. implied that the cations were responsible[162]. As a result, no consensus seem to exist at present about which ion to attribute for the sorption capacity, and the answer may lie within the individuality of ionic liquid and/or gas.

5.3.1 Characterization of pure and NO-saturated ionic liquids

The dissolution of NO in the ionic liquids resulted in a number of changes in the physical properties. The viscosity of the fresh and NO-saturated ILs were evaluated and the results presented in Fig. 5.6. Saturating [BMIM]OAc with NO results in a dramatic decrease in viscosity from 517±5.2 mPa·s to 29.2±0.2 mPa·s, a 94% reduction. Meanwhile, the density increased from 1.053 g/cm³ to 1.134 g/cm³. A similar trend was observed upon saturation of the [BMIM]OTf, although the initial viscosity was somewhat lower than [BMIM]OAc. The fresh [BMIM]OTf revealed a viscosity of 84±2.5 g/cm³, which decreased about 70% to 25.1±0.1 g/cm³, together with a small density increase from 1.298 g/cm³ to 1.315 g/cm³. Although the density of the ILs increased upon saturation with NO, i.e. higher compactness, an inflation of the volume (about 20–30% increase) could be observed, as shown in Fig. 5.8, confirming the presence of a large fraction of solute in the IL.

The viscosities of the ILs presented here are several tens to hundred times higher than that of water at room temperature. Bonhote et al.[163] pointed out that the high IL-viscosities are
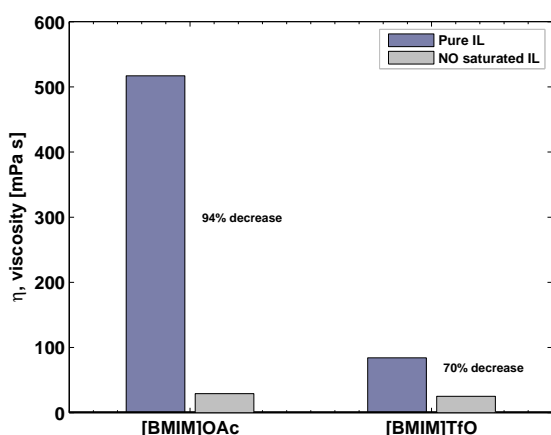
Fig. 5.6: Viscosity before and after NO saturation
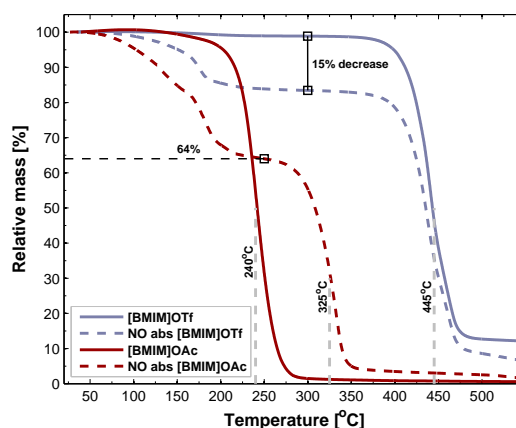
Fig. 5.7: TGA of fresh and NO-saturated [BMIM]OTf and [BMIM]OAc

largely governed by the anion-cation hydrogen bonding and van der Waals forces[1]. The significant decrease in viscosity observed upon gas sorption suggests that NO acts as a dispersive agent, decreasing the van der Waals interaction or by suppressing the $CH_3COO^-\cdots H$ bonding, known to exist in [BMIM]OAc[163]. This would be in agreement with the significant reduction in viscosity observed in Fig. 5.6.
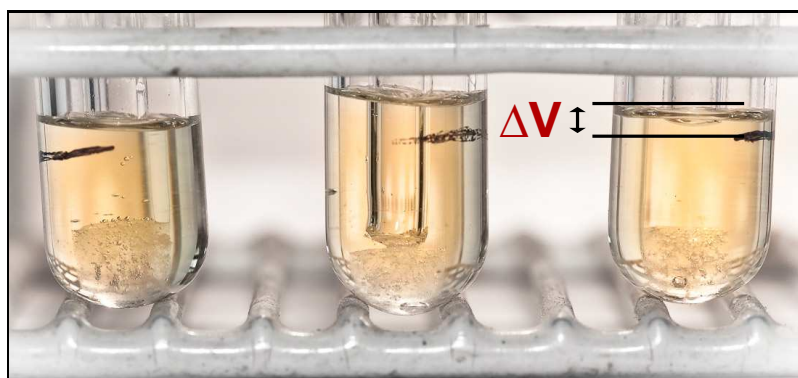
Fig. 5.8: Three glass reactors with [BMIM]OAc after NO saturation at 21°C. Black marker indicate height of IL before sorption

The thermal profile of the fresh and NO-dissolved ILs were examined with TGA. The results are presented in Fig. 5.7 (experimental description given in section A.1.8). Considering the [BMIM]OTf, a decrease in mass of 15 wt% was observed at about 200°C, implying the desorption of NO taking place. This is in agreement with the absorption results (cf. Fig 5.4) where a weight increase of 15 wt% was observed at room temperature for [BMIM]OTf. It can thus be concluded that the NO absorbed in the IL desorbs readily. Furthermore, the high degree of sorption-reversibility observed previously for [BMIM]OTf, was confirmed by the almost identical temperature of decomposition around 445°C. In other words, the molecular configuration of NO-saturated [BMIM]OTf after NO desorption is roughly identical to the fresh sample, thus

---

[1]The attractive or repulsive interaction between closed-shell molecules, such as permanent and induced dipole forces, dipole-dipole interactions

decomposing at similar temperature.

The TGA-profile of the NO-absorbed [BMIM]OAc in Fig. 5.7 is composed of two apparent NO desorption steps around 125°C and 180°C. Around 250°C the desorption stagnate, at which point the weight had decreased 36 wt%. This agrees well with the absorption results (cf. Fig. 5.4), where the weight of the IL increased 40% upon saturation. Thus, about 4 wt% NO is still trapped in the [BMIM]OAc at 250°C. The residual NO bound in the IL is likely to be responsible for the increase in decomposition temperature from about 240°C of the commercial [BMIM]OAc to ca. 325°C. A small fraction of the NO thus remain bound in the IL, suggesting formation of stronger bonds of covalent character between the solute and solvent, which confirms the irreversibility of the NO absorption in [BMIM]OAc observed.

Finally, some additional results from the characterization of the two ILs with ^{1}H-NMR and Raman spectroscopy are collected in section C.4.

5.4 Concluding remarks

Although some 'dots' still need to be connected regarding the understanding of the exact nature of the NO absorption in [BMIM]OAc and [BMIM]OTf, the system shows promising behavior. Some issues that need to be addressed involves: a) selectivity measurements of gases present in flue gas stream, e.g. N_2, O_2, CO_2, SO_2, H_2O, N_2O, NO_2; b) reversibility tests during temperature-swing (absorption/desorption); c) mass-transfer limitation need to be minimized through absorption design or by depositing the IL on an inert supporting material to increase the interfacial gas-IL area, d) effect of contaminants reaching the IL, such as alkali species, chlorine volatile organic compounds (VOCs).

The challenges of the mass-transfer limitation could be overcome by increasing the 'surface area' of the IL. The concept of the supported ionic liquid phase (SILP) system was first suggested by Riisager et al.[176] and is schematically outlined in Fig. 5.9. The method have already been
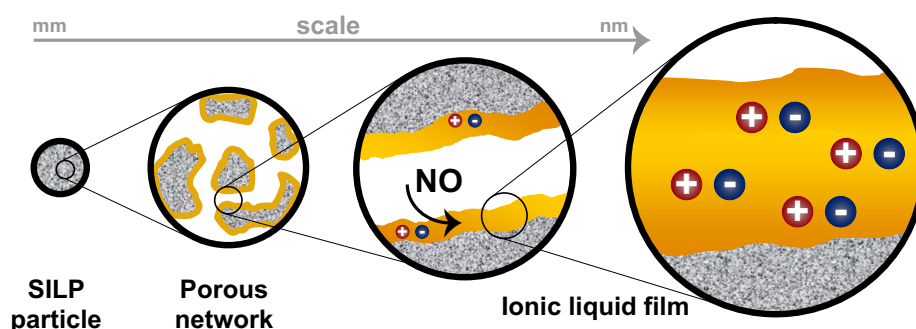
Fig. 5.9: Illustration of the SILP concept for NO absorption, where the IL is immobilized on a porous support

applied to the system studied here, where 20 wt% of [BMIM]OAc and [BMIM]OTf have been distributed on high-surface area SiO_2 particles (180–355 μm), but the evaluation of the NO-absorption capacities of the SILPs will be further investigated. By applying the SILP concept, the dynamics of the absorption/desorption should be significantly enhanced due to the shorter

diffusion distances and the increased absorption area generated[177]. Furthermore, even though a large amount of IL have been distributed onto SiO_2, the apparent properties of the SILP particles on a macroscopic scale are hereby similar to those of 'dry' particles, which significantly simplifies the handling as well as increasing the surface of the IL.

The absorption capacities of NO in IL reported here reveal a promising system for NO-scrubbing of dust-free tail-end gases, not requiring the addition of reductant such as ammonia or urea. Since no additive is needed to reduce the NO in the gas stream, the complexity of the NO removal system is somewhat reduced compared to the NH_3-SCR process. Assuming that the selectivity toward NO sorption is sufficiently high, it opens new possibilities of NO removal. The captured NO could easily be removed by increasing the temperature (temperature swing), as observed previously, where only a small increase in temperature was required to remove the NO from [BMIM]OTf. Transport of the NO-saturated IL (i.e. by exploiting the differences in viscosity) or the SILP particles to another container or location followed by desorption of NO would render possible to concentrate the NO gas. Thereby the NO could subsequently be used in e.g. the Ostwald process for the production of HNO_3 in a 'from waste to value' concept.

The conditions at the previously discussed Electrabel's Langerlo Power Station in Belgium[149] can be used as an example for considering the implementation of an IL scrubber based on the reversible [BMIM]OTf system. Here, the removal of 1000 ppm NO under a total flow of 820,000 Nm^3/h would only require an effective IL volume of around 4.2 m^3/h to remove all the incident NO. Even though the mass-transfer issue is not considered here (which is expected to be minimized by using the SILP technology), the IL-volume is considerably less than the SCR catalyst volume of 268 m^3.

For comparison of solubilities, the absorption capacities of CO_2 in ILs are considered. CO_2 capture is an area which has attracted a considerable interest over the latest years. The best IL-candidates present solubilities which are in the range of 0.5–1 mol CO_2 per mol ionic liquid (although a high partial pressure typically is required). A challenge concerning the ILs typically used is that CO_2 is strongly bound in the IL (typically $\Delta H_{sol} \approx$ -80 kJ/mol), requiring a significant amount of energy to release the CO_2[116,178,179]. Thus, the absorption capacities of the two ILs presented here, [BMIM]OAc and [BMIM]OTf, represent considerably higher absorption capacities, being able to retain 1.5 and 4 NO molecules of NO per IL molecule at room temperature, respectively. Particularly the high sorption reversibility of [BMIM]OTf (and to some extent also [BMIM]OAc) represent a novel technology for the stripping of NO. Although the results presented here are slightly fragmented, and the nature of NO absorption still somewhat unknown, the first steps in the potential use of ILs for NO_x-sorption have been taken.

Concluding remarks and outlook

The objective of the present thesis has been to contribute to the knowledge about alternative alkali-resistant technologies for the removal of NO, with focus on zirconia-based catalysts. The attention has been on alternative methods and catalysts to eliminate or harvest the nitrogen oxide from the gas stream in e.g. power plants. During this work, a number of different zirconia-based catalysts have been evaluated based on their performance in the SCR reaction before and after deactivation with potassium. In general, the resistance toward potassium found in vanadia-based catalysts supported on high-acidity sulfated zirconia were somewhat higher than that of the traditionally used SCR catalyst, which typically is based on a formulation of V_2O_5-WO_3-TiO_2. The most promising candidate, based on highest potassium resistance (the vanadia-based sulfated zirconia with high crystallinity and low content of monoclinic ZrO_2), have successfully been upscaled to a monolith, stabilized with sepiolite clay material. The monolith exhibited sufficiently high activity to perform well under industrially relevant conditions.

A different approach for the removal of gaseous NO was undertaken by employing ionic liquids as NO-absorbing liquids. Although gas-sorption in ionic liquids is not a new phenomena, it has never been reported with NO. In the present work, the two ILs, [BMIM]OAc and [BMIM]OTf were selected, based on a preliminary absorption study. These two liquids exhibited very promising behavior in the absorption of NO, being able to retain considerable amounts of nitric oxide, about 1.5–4 molecules of NO per molecule of IL. The reversibility demonstrated by [BMIM]OTf is especially notable, where almost all absorbed NO can be desorbed by a small increase in temperature (to about 60°C). This can potentially establish a new platform technology of NO sequestration, i.e. for the synthesis of nitric acid.

Although the examples for the removal of NO presented here, will not in any way solve the major challenges we face, they are small contributions to the environmental field, and hopefully this thesis will inspire other engineers and scientists in the continuous development of technologies for the removal of nitric oxide.

Chapter 7

References

[1] V. I. Pârvulescu, P. Grange, and B. Delmon, "Catalytic removal of NO," *Catalysis Today*, vol. 46, no. 4, pp. 233–316, 1998.

[2] J. H. Seinfeld, "Urban Air-pollution - State of the Science," *Science*, vol. 243, no. 4892, pp. 745–752, 1989.

[3] H. Bosch and F. Janssen, "Formation and control of nitrogen oxides," *Catalysis Today*, vol. 2, no. 4, pp. 369–379, 1988.

[4] S. Roy, M. Hegde, and G. Madras, "Catalysis for NO_x abatement," *Applied Energy*, vol. 86, no. 11, pp. 2283–2297, 2009.

[5] G. Busca, L. Lietti, G. Ramis, and F. Berti, "Chemical and mechanistic aspects of the selective catalytic reduction of NO_x by ammonia over oxide catalysts: A review," *Applied Catalysis B: Environmental*, vol. 18, no. 1-2, pp. 1–36, 1998.

[6] M. Calatayud, B. Mguig, and C. Minot, "Modeling catalytic reduction of NO by ammonia over V_2O_5," *Surface Science Reports*, vol. 55, no. 6-8, pp. 169–236, 2004.

[7] A. D. McNaught and A. Wilkinson, *Compendium of Chemical Terminology - IUPAC recommendations*. Blackwell Science, 2 ed., 1997.

[8] J. J. Berzelius *Edinburgh New Philosophical Journal*, vol. XXI, p. 223, 1836.

[9] J. M. Thomas and W. J. Thomas, eds., *Principles and Practice of Heterogeneous Catalysis*. VCH, Weinheim, Germany, 1997.

[10] D. R. Lide, ed., *CRC Handbook of Chemistry and Physics*. CRC Press/Taylor and Francis, Boca Raton, FL, 90th ed., 2010.

[11] F. Garin, "Mechanism of NO_x decomposition," *Applied Catalysis A: General*, vol. 222, no. 1-2, pp. 183–219, 2001.

[12] G. Olofsson, W. Wang, Z. Ye, I. Bjerle, and A. Andersson, "Repressing NO_x and N_2O Emissions in a Fluidized Bed Biomass Combustor," *Energy & Fuels*, vol. 16, no. 4, pp. 915–919, 2002.

[13] S. Naha and S. K. Aggarwal, "Fuel effects on NO_x emissions in partially premixed flames," *Combustion and Flame*, vol. 139, no. 1-2, pp. 90–105, 2004.

[14] G. Busca, M. A. Larrubia, L. Arrighi, and G. Ramis, "Catalytic abatement of NO_x: Chemical and mechanistic aspects," *Catalysis Today*, vol. 107-108, pp. 139–148, 2005.

[15] L. A. Ruth, "Energy from municipal solid waste: A comparison with coal combustion technology," *Progress in Energy and Combustion Science*, vol. 24, no. 6, pp. 545–564, 1998.

[16] J. Due-Hansen, A. L. Kustov, C. H. Christensen, and R. Fehrmann, "Impact of support and potassium-poisoning on the $V_2O_5-WO_3/ZrO_2$ catalyst performance in ammonia oxidation," *Catalysis Communications*, vol. 10, no. 6, pp. 803–806, 2009.

[17] N. I. Il'chenko and G. I. Golodets, "Catalytic oxidation of ammonia: I. Reaction kinetics and mechanism," *Journal of Catalysis*, vol. 39, no. 1, pp. 57–72, 1975.

[18] N. I. Il'chenko and G. I. Golodets, "Catalytic oxidation of ammonia: II. Relationship between catalytic properties of substances and surface oxygen bond energy. General regularities in catalytic oxidation of ammonia and organic substances," *Journal of Catalysis*, vol. 39, no. 1, pp. 73–86, 1975.

[19] P. Kofstad, *En innføring i grunnstoffenes kjemi*. Tano A/S, 3rd ed., 1998.

[20] H. Falsig, T. Bligaard, C. H. Christensen, and J. K. Nørskov, "Direct NO decomposition over stepped transition-metal surfaces," *Pure and Applied Chemistry*, vol. 79, no. 11, pp. 1895–1903, 2007.

[21] H. Yahiro and M. Iwamoto, "Copper ion-exchanged zeolite catalysts in $deNO_x$ reaction," *Applied Catalysis A: General*, vol. 222, no. 1-2, pp. 163–181, 2001.

[22] R. da Silveira, A. de Oliveira, S. Pergher, V. da Silva, and I. Baibich, "Palladium and Molybdenum Mono and Bimetallic Catalysts on Modernite for Direct NO Decomposition Reaction," *Catalysis Letters*, vol. 129, no. 3, pp. 259–265, 2009.

[23] S. Brandenberger, O. Kröcher, A. Tissler, and R. Althoff, "The State of the Art in Selective Catalytic Reduction of NO_x by Ammonia Using Metal-Exchanged Zeolite Catalysts," *Catalysis Reviews: Science and Engineering*, vol. 50, no. 4, pp. 492–531, 2008.

[24] M. Koebel, G. Madia, and M. Elsener, "Selective catalytic reduction of NO and NO_2 at low temperatures," *Catalysis Today*, vol. 73, no. 3-4, pp. 239–247, 2002.

[25] A. Kato, S. Matsuda, T. Kamo, F. Nakajima, H. Kuroda, and T. Narita, "Reaction between nitrogen oxide (NO_x) and ammonia on iron oxide-titanium oxide catalyst," *The Journal of Physical Chemistry*, vol. 85, no. 26, pp. 4099–4102, 1981.

[26] G. Madia, M. Koebel, M. Elsener, and A. Wokaun, "Side reactions in the selective catalytic reduction of NO_x with various NO_2 fractions," *Industrial & Engineering Chemistry Research*, vol. 41, no. 16, pp. 4008–4015, 2002.

[27] J. Kaspar, P. Fornasiero, and N. Hickey, "Automotive catalytic converters: current status and some perspectives," *Catalysis Today*, vol. 77, no. 4, pp. 419–449, 2003.

[28] P. Forzatti and L. Lietti, "The reduction of NO_x stored on LNT and combined LNT-SCR systems," *Catalysis Today*, vol. In Press, Corrected Proof, 2009.

[29] P. Balle, B. Geiger, and S. Kureti, "Selective catalytic reduction of NO_x by NH_3 on Fe/HBEA zeolite catalysts in oxygen-rich exhaust," *Applied Catalysis B: Environmental*, vol. 85, no. 3-4, pp. 109–119, 2009.

[30] P. Forzatti, "Present status and perspectives in de-NOx SCR catalysis," *Applied Catalysis A: General*, vol. 222, no. 1-2, pp. 221–236, 2001.

[31] O. Kröcher and M. Elsener, "Materials for thermohydrolysis of urea in a fluidized bed," *Chemical Engineering Journal*, vol. 152, no. 1, pp. 167–176, 2009.

[32] E. Childers, C. W. Ellis, and D. J. Ryan, "Process for catalytically reducing nitrogen oxides in industrial stack gases," 1959. 2910343.

[33] J. P. Dunn, P. R. Koppula, H. G. Stenger, and I. E. Wachs, "Oxidation of sulfur dioxide to sulfur trioxide over supported vanadia catalysts," *Applied Catalysis B: Environmental*, vol. 19, no. 2, pp. 103–117, 1998.

[34] Y. Habuta, N. Narishige, K. Okumura, N. Katada, and M. Niwa, "Catalytic activity and solid acidity of vanadium oxide thin layer loaded on TiO_2, ZrO_2, and SnO_2," *Catalysis Today*, vol. 78, no. 1-4, pp. 131–138, 2003.

[35] H. Bosch, F. J. Janssen, F. M. van den Kerkhof, J. Oldenziel, J. G. van Ommen, and J. R. Ross, "The activity of supported vanadium oxide catalysts for the selective reduction of no with ammonia," *Applied Catalysis*, vol. 25, no. 1-2, pp. 239–248, 1986.

[36] M. Iwamoto, H. Yahiro, S. Shundo, Y. Yu-u, and N. Mizuno, "Influence of sulfur dioxide on catalytic removal of nitric oxide over copper ion-exchanged ZSM-5 zeolite," *Applied Catalysis*, vol. 69, no. 1, pp. L15–L19, 1991.

[37] G. T. Went, L.-j. Leu, and A. T. Bell, "Quantitative structural analysis of dispersed vanadia species in TiO_2 (anatase)-supported V_2O_5," *Journal of Catalysis*, vol. 134, no. 2, pp. 479–491, 1992.

[38] G. Ramis, G. Busca, V. Lorenzelli, and P. Forzatti, "Fourier transform infrared study of the adsorption and coadsorption of nitric oxide, nitrogen dioxide and ammonia on TiO_2 anatase," *Applied Catalysis*, vol. 64, pp. 243–257, 1990.

[39] G. Busca, H. Saussey, O. Saur, J. C. Lavalley, and V. Lorenzelli, "FT-IR characterization of the surface acidity of different titanium dioxide anatase preparations," *Applied Catalysis*, vol. 14, pp. 245–260, 1985.

[40] M. Takagi, T. Kawai, M. Soma, T. Onishi, and K. Tamaru, "The mechanism of the reaction between NO_x and NH_3 on V_2O_5 in the presence of oxygen," *Journal of Catalysis*, vol. 50, no. 3, pp. 441–446, 1977.

[41] M. Inomata, A. Miyamoto, and Y. Murakami, "Determination of the number of V=O species on the surface of vanadium oxide catalysts. 2. V_2O_5/TiO_2 catalysts," *The Journal of Physical Chemistry*, vol. 85, no. 16, pp. 2372–2377, 1981.

[42] M. Inomata, A. Miyamoto, and Y. Murakami, "Mechanism of the reaction of NO and NH_3 on vanadium oxide catalyst in the presence of oxygen under the dilute gas condition," *Journal of Catalysis*, vol. 62, no. 1, pp. 140–148, 1980.

[43] F. J. J. G. Janssen, F. M. G. Van den Kerkhof, H. Bosch, and J. R. H. Ross, "Mechanism of the reaction of nitric oxide, ammonia, and oxygen over vanadia catalysts. I. The role of oxygen studied by way of isotopic transients under dilute conditions," *The Journal of Physical Chemistry*, vol. 91, no. 23, pp. 5921–5927, 1987.

[44] F. J. J. G. Janssen, F. M. G. Van den Kerkhof, H. Bosch, and J. R. H. Ross, "Mechanism of the reaction of nitric oxide, ammonia, and oxygen over vanadia catalysts. 2. Isotopic transient studies with oxygen-18 and nitrogen-15," *The Journal of Physical Chemistry*, vol. 91, no. 27, pp. 6633–6638, 1987.

[45] N. Y. Topsøe, J. A. Dumesic, and H. Topsøe, "Vanadia-Titania Catalysts for Selective Catalytic Reduction of Nitric-Oxide by Ammonia: II. Studies of Active Sites and Formulation of Catalytic Cycles," *Journal of Catalysis*, vol. 151, no. 1, pp. 241–252, 1995.

[46] N. Y. Topsøe, H. Topsøe, and J. A. Dumesic, "Vanadia/Titania Catalysts for Selective Catalytic Reduction (SCR) of Nitric-Oxide by Ammonia: I. Combined Temperature-Programmed in-Situ FTIR and On-line Mass-Spectroscopy Studies," *Journal of Catalysis*, vol. 151, no. 1, pp. 226–240, 1995.

[47] N.-Y. Topsøe, "Characterization of the nature of surface sites on vanadia-titania catalysts by FTIR," *Journal of Catalysis*, vol. 128, no. 2, pp. 499–511, 1991.

[48] M. Gasior, J. Haber, T. Machej, and T. Czeppe, "Mechanism of the reaction NO + NH_3 on V_2O_5 catalysts," *Journal of Molecular Catalysis*, vol. 43, no. 3, pp. 359–369, 1988.

[49] U. S. Ozkan, Y. P. Cai, and M. W. Kumthekar, "Investigation of the Mechanism of Ammonia Oxidation and Oxygen Exchange over Vanadia Catalysts Using N-15 and O-18 Tracer Studies," *Journal of Catalysis*, vol. 149, no. 2, pp. 375–389, 1994.

[50] U. S. Ozkan, Y. P. Cai, and M. W. Kumthekar, "Investigation of the Reaction Pathways in Selective Catalytic Reduction of NO with NH_3 over V_2O_5 Catalysts: Isotopic Labeling Studies Using $^{18}O_2$, $^{15}NH_3$, ^{15}NO, and ^{15}N ^{18}O," *Journal of Catalysis*, vol. 149, no. 2, pp. 390–403, 1994.

[51] G. Ramis, L. Yi, G. Busca, M. Turco, E. Kotur, and R. J. Willey, "Adsorption, Activation, and Oxidation of Ammonia over SCR Catalysts," *Journal of Catalysis*, vol. 157, no. 2, pp. 523–535, 1995.

[52] G. Ramis, L. Yi, and G. Busca, "Ammonia activation over catalysts for the selective catalytic reduction of NO_x and the selective catalytic oxidation of NH_3. An FT-IR study," *Catalysis Today*, vol. 28, no. 4, pp. 373–380, 1996.

[53] S. Soyer, A. Uzun, S. Senkan, and I. Onal, "A quantum chemical study of nitric oxide reduction by ammonia (SCR reaction) on V_2O_5 catalyst surface," *Catalysis Today*, vol. 118, no. 3-4, pp. 268–278, 2006.

[54] M. Anstrom, N.-Y. Topsøe, and J. A. Dumesic, "Density functional theory studies of mechanistic aspects of the SCR reaction on vanadium oxide catalysts," *Journal of Catalysis*, vol. 213, no. 2, pp. 115–125, 2003.

[55] J. Chen and R. Yang, "Role of WO_3 in mixed $V_2O_5-WO_3/TiO_2$ catalysts for selective catalytic reduction of nitric oxide with ammonia," *Applied Catalysis A: General*, vol. 80, no. 1, pp. 135–148, 1992.

[56] E. Broclawik, A. Góra, and M. Najbar, "The role of tungsten in formation of active sites for no SCR on the V-W-O catalyst surface – quantum chemical modeling (DFT)," *Journal of Molecular Catalysis A: Chemical*, vol. 166, no. 1, pp. 31–38, 2001.

[57] L. Lietti, I. Nova, and P. Forzatti, "Selective catalytic reduction (SCR) of NO by NH_3 over TiO_2-supported $V_2O_5-WO_3$ and $V_2O_5-MoO_3$ catalysts," *Topics in Catalysis*, vol. 11-12, no. 1, pp. 111–122, 2000.

[58] M. Kobayashi and M. Hagi, "V_2O_5-WO_3/TiO_2-SiO_2-SO_4^{2-} catalysts: Influence of active components and supports on activities in the selective catalytic reduction of NO by NH_3 and in the oxidation of SO_2," *Applied Catalysis B: Environmental*, vol. 63, no. 1-2, pp. 104–113, 2006.

[59] L. J. Alemany, F. Berti, G. Busca, G. Ramis, D. Robba, G. P. Toledo, and M. Trombetta, "Characterization and composition of commercial $V_2O_5-WO_3-TiO_2$ SCR catalysts," *Applied Catalysis B: Environmental*, vol. 10, no. 4, pp. 299–311, 1996.

[60] R. Khodayari and C. U. I. Odenbrand, "Regeneration of commercial SCR catalysts by washing and sulphation: effect of sulphate groups on the activity," *Applied Catalysis B: Environmental*, vol. 33, no. 4, pp. 277–291, 2001.

[61] S. T. Choo, S. D. Yim, I.-S. Nam, S.-W. Ham, and J.-B. Lee, "Effect of promoters including WO_3 and BaO on the activity and durability of V_2O_5/sulfated TiO_2 catalyst for NO reduction by NH_3," *Applied Catalysis B: Environmental*, vol. 44, no. 3, pp. 237–252, 2003.

[62] J. P. Chen and R. T. Yang, "Selective Catalytic Reduction of NO with NH_3 on SO_4^{-2}/TiO_2 Superacid Catalyst," *Journal of Catalysis*, vol. 139, no. 1, pp. 277–288, 1993.

[63] H. Hamada, Y. Kintaichi, M. Tabata, M. Sasaki, and T. Ito, "Sulfate-promoted Metal-oxide Catalysts For the Selective Reduction of Nitrogen Monoxide By Propane In Oxygen-rich Atmosphere," *Chemistry Letters*, no. 12, pp. 2179–2182, 1991.

[64] D. Pietrogiacomi, D. Sannino, S. Tuti, P. Ciambelli, V. Indovina, M. Occhiuzzi, and F. Pepe, "The catalytic activity of CuO_x/ZrO_2 for the abatement of NO with propene or ammonia in the presence of O_2," *Applied Catalysis B: Environmental*, vol. 21, no. 2, pp. 141–150, 1999.

[65] J. Pasel, V. Speer, C. Albrecht, F. Richter, and H. Papp, "Metal doped sulfated ZrO_2 as catalyst for the selective catalytic reduction (SCR) of NO with propane," *Applied Catalysis B: Environmental*, vol. 25, no. 2-3, pp. 105–113, 2000.

[66] G. Delahay, E. Ensuque, B. Coq, and F. Figuéras, "Selective Catalytic Reduction of Nitric Oxide by n-Decane on Cu/Sulfated-Zirconia Catalysts in Oxygen Rich Atmosphere: Effect of Sulfur and Copper Contents," *Journal of Catalysis*, vol. 175, no. 1, pp. 7–15, 1998.

[67] M. Hino and K. Arata, "Synthesis of solid superacid catalyst with acid strength of H_0<-16.04," *Journal of the Chemical Society, Chemical Communications*, vol. 851–852, 1980.

[68] J. Sohn, "Recent advances in solid superacids," *Journal of Industrial and Engineering Chemistry*, vol. 10, no. 1, pp. 1–15, 2004.

[69] M. Risch and E. E. Wolf, "Effect of the preparation of a mesoporous sulfated zirconia catalyst in n-butane isomerization activity," *Applied Catalysis A: General*, vol. 206, no. 2, pp. 283–293, 2001.

[70] C. Morterra, G. Cerrato, F. Pinna, and M. Signoretto, "Crystal phase, spectral features, and catalytic activity of sulfate-doped zirconia systems," *Journal of Catalysis*, vol. 157, no. 1, pp. 109–123, 1995.

[71] B. Li and R. D. Gonzalez, "Sol–Gel Synthesis and Catalytic Properties of Sulfated Zirconia Catalysts," *Industrial & Engineering Chemistry Research*, vol. 35, no. 9, pp. 3141–3148, 1996.

[72] J. Due-Hansen, S. Boghosian, A. Kustov, P. Fristrup, G. Tsilomelekis, K. Ståhl, C. H. Christensen, and R. Fehrmann, "Vanadia-based SCR catalysts supported on tungstated and sulfated zirconia: Influence of doping with potassium," *Journal of Catalysis*, vol. 251, no. 2, pp. 459–473, 2007.

[73] P. Moles, "Sulfated Zirconia - A Catalyst for Isomerisation reactions," *Reprinted from Speciality Chemicals*, Nov/Dec 1992.

[74] T. Yamaguchi, "Recent progress in solid superacid," *Applied Catalysis*, vol. 61, no. 1, pp. 1–25, 1990.

[75] T. Jin, T. Yamaguchi, and K. Tanabe, "Mechanism of acidity generation on sulfur-promoted metal oxides," *The Journal of Physical Chemistry*, vol. 90, no. 20, pp. 4794–4796, 1986.

[76] K. Arata and M. Hino, "Preparation of superacids by metal oxides and their catalytic action," *Materials Chemistry and Physics*, vol. 26, no. 3-4, pp. 213–237, 1990.

[77] J. P. Dunn, J.-M. Jehng, D. S. Kim, L. E. Briand, H. G. Stenger, and I. E. Wachs, "Interactions between Surface Vanadate and Surface Sulfate Species on Metal Oxide Catalysts," *The Journal of Physical Chemistry B*, vol. 102, no. 32, pp. 6212–6218, 1998.

[78] T. Kanougi, T. Atoguchi, and S. Yao, "Periodic density functional study of superacidity of sulfated zirconia," *Journal of Molecular Catalysis A: Chemical*, vol. 177, no. 2, pp. 289–298, 2002.

[79] M. Niwa, Y. Habuta, K. Okumura, and N. Katada, "Solid acidity of metal oxide monolayer and its role in catalytic reactions," *Catalysis Today*, vol. 87, no. 1-4, pp. 213–218, 2003.

[80] F. R. Chen, G. Coudurier, J. F. Joly, and J. C. Vedrine, "Superacid and Catalytic Properties of Sulfated Zirconia," *Journal of Catalysis*, vol. 143, no. 2, pp. 616–626, 1993.

[81] J. R. Sohn and M. Y. Park, "Characterization of Zirconia-Supported Tungsten Oxide Catalyst," *Langmuir*, vol. 14, no. 21, pp. 6140–6145, 1998.

[82] W. Zhou, E. I. Ross-Medgaarden, W. V. Knowles, M. S. Wong, I. E. Wachs, and C. J. Kiely, "Identification of active Zr-WO_x clusters on a ZrO_2 support for solid acid catalysts," *Nature Chemistry*, vol. 1, no. 9, pp. 722–728, 2009.

[83] G. Rodriguez-Gattorno, A. Galano, and E. Torres-García, "Surface acid-basic properties of WO_x-ZrO_2 and catalytic efficiency in oxidative desulfurization," *Applied Catalysis B: Environmental*, vol. 92, no. 1-2, pp. 1–8, 2009.

[84] I. E. Wachs, "Raman and IR studies of surface metal oxide species on oxide supports: Supported metal oxide catalysts," *Catalysis Today*, vol. 27, no. 3-4, pp. 437–455, 1996.

[85] Y. Zheng, A. D. Jensen, and J. E. Johnsson, "Deactivation of $V_2O_5-WO_3-TiO_2$ SCR catalyst at a biomass-fired combined heat and power plant," *Applied Catalysis B: Environmental*, vol. 60, no. 3-4, pp. 253–264, 2005.

[86] Å. Kling, C. Andersson, Å. Myringer, D. Eskilsson, and S. G. Järås, "Alkali deactivation of high-dust SCR catalysts used for NO_x reduction exposed to flue gas from 100 MW-scale biofuel and peat fired boilers: Influence of flue gas composition," *Applied Catalysis B: Environmental*, vol. 69, no. 3-4, pp. 240–251, 2007.

[87] Y. Zheng, P. A. Jensen, A. D. Jensen, B. Sander, and H. Junker, "Ash transformation during co-firing coal and straw," *Fuel*, vol. 86, no. 7-8, pp. 1008–1020, 2007.

[88] Jensen-Holm, J. R. Thøgersen, and P. Lindenhoff, "Impact of biomass co-combustion on SCR $DeNO_x$ operation," *Presented at Power-Gen Europe, Germany*, 2009.

[89] J. P. Chen and R. T. Yang, "Mechanism of poisoning of the V_2O_5/TiO_2 catalyst for the reduction of NO by NH_3," *Journal of Catalysis*, vol. 125, no. 2, pp. 411–420, 1990.

[90] L. Lietti, P. Forzatti, G. Ramis, G. Busca, and F. Bregani, "Potassium doping of vanadia/titania de-NO_xing catalysts: Surface characterisation and reactivity study," *Applied Catalysis B: Environmental*, vol. 3, no. 1, pp. 13–35, 1993.

[91] H. Kamata, K. Takahashi, and C. U. I. Odenbrand, "The role of K_2O in the selective reduction of NO with NH_3 over a $V_2O_5(WO_3)/TiO_2$ commercial selective catalytic reduction catalyst," *Journal of Molecular Catalysis A: Chemical*, vol. 139, no. 2-3, pp. 189–198, 1999.

[92] L. Lisi, G. Lasorella, S. Malloggi, and G. Russo, "Single and combined deactivating effect of alkali metals and HCl on commercial SCR catalysts," *Applied Catalysis B: Environmental*, vol. 50, no. 4, pp. 251–258, 2004.

[93] A. Kustov, S. Rasmussen, R. Fehrmann, and P. Simonsen, "Activity and deactivation of sulphated TiO_2 and ZrO_2-based V, Cu, and Fe oxide catalysts for NO abatement in alkali containing flue gases," *Applied Catalysis B: Environmental*, vol. 76, no. 1-2, pp. 9–14, 2007.

[94] O. Kröcher and M. Elsener, "Chemical deactivation of V_2O_5/WO_3-TiO_2 SCR catalysts by additives and impurities from fuels, lubrication oils, and urea solution. I. Catalytic studies," *Applied Catalysis B: Environmental*, vol. 77, no. 3-4, pp. 215–227, 2008.

[95] Y. Zheng, A. D. Jensen, J. E. Johnsson, and J. R. Thøgersen, "Deactivation of $V_2O_5-WO_3-TiO_2$ SCR catalyst at biomass fired power plants: Elucidation of mechanisms by lab- and pilot-scale experiments," *Applied Catalysis B: Environmental*, vol. 83, no. 3-4, pp. 186–194, 2008.

[96] F. Castellino, A. Jensen, J. Johnsson, and R. Fehrmann, "Influence of reaction products of K-getter fuel additives on commercial vanadia-based SCR catalysts. Part I. Potassium phosphate," *Applied Catalysis B: Environmental*, vol. 86, no. 3-4, pp. 196–205, 2009.

[97] F. Castellino, A. D. Jensen, J. E. Johnsson, and R. Fehrmann, "Influence of reaction products of K-getter fuel additives on commercial vanadia-based SCR catalysts: Part II. Simultaneous addition of KCl, $Ca(OH)_2$, H_3PO_4 and H_2SO_4 in a hot flue gas at a SCR pilot-scale setup," *Applied Catalysis B: Environmental*, vol. 86, pp. 206–215, Feb. 2009.

[98] M. Klimczak, P. Kern, T. Heinzelmann, M. Lucas, and P. Claus, "High-throughput study of the effects of inorganic additives and poisons on NH_3-SCR catalysts-Part I: $V_2O_5-WO_3/TiO_2$ catalysts," *Applied Catalysis B: Environmental*, vol. 95, no. 1-2, pp. 39–47, 2010.

[99] D. Nicosia, I. Czekaj, and O. Kröcher, "Chemical deactivation of V_2O_5/WO_3-TiO_2 SCR catalysts by additives and impurities from fuels, lubrication oils and urea solution: Part II. Characterization study of the effect of alkali and alkaline earth metals," *Applied Catalysis B: Environmental*, vol. 77, no. 3-4, pp. 228–236, 2008.

[100] J. Muscat, N. M. Harrison, and G. Thornton, "First-principles study of potassium adsorption on TiO_2 surfaces," *Phys. Rev. B*, vol. 59, no. 23, pp. 15457–15463, 1999.

[101] M. A. San Miguel, C. J. Calzado, and J. F. Sanz, "Modeling Alkali Atoms Deposition on TiO_2 (110) Surface," *The Journal of Physical Chemistry B*, vol. 105, no. 9, pp. 1794–1798, 2001.

[102] M. Witko, R. Grybos, and R. Tokarz-Sobieraj, "Heterogeneity of V_2O_5(010) surfaces - the role of alkali metal dopants," *Topics in Catalysis*, vol. 38, no. 1, pp. 105–115, 2006.

[103] M. Calatayud and C. Minot, "Effect of Alkali Doping on a V_2O_5/TiO_2 Catalyst from Periodic DFT Calculations," *The Journal of Physical Chemistry C*, vol. 111, no. 17, pp. 6411–6417, 2007.

[104] A. E. Lewandowska, M. Calatayud, E. Lozano-Diz, C. Minot, and M. A. Bañares, "Combining theoretical description with experimental in situ studies on the effect of alkali additives on the structure and reactivity of vanadium oxide supported catalysts," *Catalysis Today*, vol. 139, no. 3, pp. 209–213, 2008.

[105] Y. Zheng, A. D. Jensen, and J. E. Johnsson, "Laboratory Investigation of Selective Catalytic Reduction Catalysts: Deactivation by Potassium Compounds and Catalyst Regeneration," *Industrial & Engineering Chemistry Research*, vol. 43, no. 4, pp. 941–947, 2004.

[106] L. Kiwi-Minsker, D. A. Bulushev, F. Rainone, and A. Renken, "Implication of the acid-base properties of V/Ti-oxide catalyst in toluene partial oxidation," *Journal of Molecular Catalysis A: Chemical*, vol. 184, no. 1-2, pp. 223–235, 2002.

[107] G. G. Cortez, J. L. G. Fierro, and M. A. Bañares, "Role of potassium on the structure and activity of alumina-supported vanadium oxide catalysts for propane oxidative dehydrogenation," *Catalysis Today*, vol. 78, no. 1-4, pp. 219–228, 2003.

[108] M. Calatayud, F. Tielens, and F. De Proft, "Reactivity of gas-phase, crystal and supported V_2O_5 systems studied using density functional theory based reactivity indices," *Chemical Physics Letters*, vol. 456, no. 1-3, pp. 59–63, 2008.

[109] A. J. Pedersen, J. Zeuthen, F. Frandsen, H. Livbjerg, and J. Hansen, "Characterization of flue gas, fly ash, aerosol and deposit compositions as a function of waste composition and grate operation," IT3'07 Conference, Phoenix, AZ, May 14–18 2007.

[110] K. Wieck-Hansen, P. Overgaard, and O. H. Larsen, "Cofiring coal and straw in a 150 MWe power boiler experiences," *Biomass and Bioenergy*, vol. 19, no. 6, pp. 395–409, 2000.

[111] I. Gulyurtlu, T. Crujeira, M. H. Lopes, P. Abelha, D. Boavida, J. Seabra, R. Goncalves, C. Sargaco, and I. Cabrita, "The Study of Combustion of Municipal Waste in a Fluidized Bed Combustor," *Journal of Energy Resources Technology*, vol. 128, no. 2, pp. 123–128, 2006.

[112] B. B. Miller, D. R. Dugwell, and R. Kandiyoti, "Partitioning of trace elements during the combustion of coal and biomass in a suspension-firing reactor," *Fuel*, vol. 81, no. 2, pp. 159–171, 2002.

[113] A. Wierzbicka, L. Lillieblad, J. Pagels, M. Strand, A. Gudmundsson, A. Gharibi, E. Swietlicki, M. Sanati, and M. Bohgard, "Particle emissions from district heating units operating on three commonly used biofuels," *Atmospheric Environment*, vol. 39, no. 1, pp. 139–150, 2005.

[114] S. B. Rasmussen, A. Kustov, R. Fehrmann, and J. Due-Hansen, "Alkali resistant catalyst," September 2007, WO/2008/037255.

[115] J. Due-Hansen, A. L. Kustov, S. B. Rasmussen, R. Fehrmann, and C. H. Christensen, "Tungstated zirconia as promising carrier for $DeNO_x$ catalysts with improved resistance towards alkali poisoning," *Applied Catalysis B: Environmental*, vol. 66, no. 3-4, pp. 161–167, 2006.

[116] J. E. Bara, D. E. Camper, D. L. Gin, and R. D. Noble, "Room-Temperature Ionic Liquids and Composite Materials: Platform Technologies for CO_2 Capture," *Accounts of Chemical Research*, vol. 43, no. 1, pp. 152–159, 2010.

[117] M. A. Cortes-Jacome, J. A. Toledo, C. Angeles-Chavez, M. Aguilar, and J. A. Wang, "Influence of synthesis methods on tungsten dispersion, structural deformation, and surface acidity in binary $WO_3 - ZrO_2$ system," *The Journal of Physical Chemistry B*, vol. 109, no. 48, pp. 22730–22739, 2005.

[118] L. D'Souza, A. Suchopar, K. Zhu, D. Balyozova, M. Devadas, and R. M. Richards, "Preparation of thermally stable high surface area mesoporous tetragonal ZrO_2 and Pt/ZrO_2: An active hydrogenation catalyst," *Microporous and Mesoporous Materials*, vol. 88, no. 1-3, pp. 22–30, 2006.

[119] B. H. Davis, R. A. Keogh, and R. Srinivasan, "Sulfated zirconia as a hydrocarbon conversion catalyst," *Catalysis Today*, vol. 20, no. 2, pp. 219–256, 1994.

[120] V. Ramaswamy, M. Bhagwat, D. Srinivas, and A. V. Ramaswamy, "Structural and spectral features of nanocrystalline copper-stabilized zirconia," *Catalysis Today*, vol. 97, no. 1, pp. 63–70, 2004.

[121] C. J. Howard and R. J. Hill, "The polymorphs of zirconia: phase abundance and crystal structure by Rietveld analysis of neutron and X-ray diffraction data," *Journal of Materials Science*, vol. 26, no. 1, pp. 127–134, 1991.

[122] R. Barthos, F. Lónyi, G. Onyestyák, and J. Valyon, "An NH_3-TPD and -FR study on the acidity of sulfated zirconia," *Solid State Ionics*, vol. 141-142, pp. 253–258, 2001.

[123] L. V. Rees and D. Shen, "Characterization of microporous sorbents by frequency-response methods," *Gas Separation & Purification*, vol. 7, no. 2, pp. 83–89, 1993.

[124] N. Katada, T. Tsubaki, and M. Niwa, "Measurements of number and strength distribution of Brønsted and Lewis acid sites on sulfated zirconia by ammonia IRMS-TPD method," *Applied Catalysis A: General*, vol. 340, no. 1, pp. 76–86, 2008.

[125] F. Lónyi and J. Valyon, "Thermally effected structural and surface transformations of sulfated TiO_2, ZrO_2 and $TiO_2 - ZrO_2$ catalysts," *Journal of Thermal Analysis and Calorimetry*, vol. 46, no. 1, pp. 211–218, 1996.

[126] R. W. Stevens, S. S. C. Chuang, and B. H. Davis, "Temperature-programmed desorption/decomposition with simultaneous DRIFTS analysis: adsorbed pyridine on sulfated ZrO_2 and Pt-promoted sulfated ZrO_2," *Thermochimica Acta*, vol. 407, no. 1-2, pp. 61–71, 2003.

[127] J. F. Haw, J. Zhang, K. Shimizu, T. N. Venkatraman, D.-P. Luigi, W. Song, D. H. Barich, and J. B. Nicholas, "NMR and Theoretical Study of Acidity Probes on Sulfated Zirconia Catalysts," *Journal of the American Chemical Society*, vol. 122, no. 50, pp. 12561–12570, 2000.

[128] I. E. Wachs and B. M. Weckhuysen, "Structure and reactivity of surface vanadium oxide species on oxide supports," *Applied Catalysis A: General*, vol. 157, no. 1-2, pp. 67–90, 1997.

[129] A. Kustov, M. Kustova, R. Fehrmann, and P. Simonsen, "Vanadia on sulphated-ZrO_2, a promising catalyst for NO abatement with ammonia in alkali containing flue gases," *Applied Catalysis B: Environmental*, vol. 58, no. 1-2, pp. 97–104, 2005.

[130] J. A. Moulijn, A. E. van Diepen, and F. Kapteijn, "Catalyst deactivation: is it predictable? What to do?," *Applied Catalysis A: General*, vol. 212, no. 1-2, pp. 3–16, 2001.

[131] G. Centi, C. Nigro, S. Perathoner, and G. Stella, "Role of the support and of adsorbed species on the behavior of Cu-based catalysts for NO conversion," *Catalysis Today*, vol. 17, no. 1-2, pp. 159–166, 1993.

[132] G. Centi and S. Perathoner, "Nature of active species in copper-based catalysts and their chemistry of transformation of nitrogen oxides," *Applied Catalysis A: General*, vol. 132, no. 2, pp. 179–259, 1995.

[133] N. Apostolescu, B. Geiger, K. Hizbullah, M. Jan, S. Kureti, D. Reichert, F. Schott, and W. Weisweiler, "Selective catalytic reduction of nitrogen oxides by ammonia on iron oxide catalysts," *Applied Catalysis B: Environmental*, vol. 62, no. 1-2, pp. 104–114, 2006.

[134] V. Indovina, M. C. Campa, F. Pepe, D. Pietrogiacomi, and S. Tuti, "The catalytic activity of FeO_x/ZrO_2 and FeO_x/sulphated-ZrO_2 for the NO abatement with C_3H_6 in the presence of excess O_2," *Applied Catalysis B: Environmental*, vol. 60, no. 1-2, pp. 23–31, 2005.

[135] A. Bahamonde, S. Campuzano, M. Yates, P. Salerno, and S. Mendioroz, "Influence of zirconia raw materials on the development of DeNO$_x$ monolithic catalysts," *Applied Catalysis B: Environmental*, vol. 44, no. 4, pp. 333 – 346, 2003.

[136] A. Bahamonde, A. Beretta, P. Avila, and E. Tronconi, "An Experimental and Theoretical Investigation of the Behavior of a Monolithic Ti-V-W-Sepiolite Catalyst in the Reduction of NO$_x$ with NH_3," *Industrial & Engineering Chemistry Research*, vol. 35, no. 8, pp. 2516–2521, 1996.

[137] C. Knapp, F. J. Gil-Llambías, M. Gulppi-Cabra, P. Avila, and J. Blanco, "Phase distribution in titania-sepiolite catalyst supports prepared by different methods," *Journal of Materials Chemistry*, vol. 7, no. 8, pp. 1641–1645, 1997.

[138] C. U. I. Odenbrand, A. Bahamonde, P. Avila, and J. Blanco, "Kinetic study of the selective reduction of nitric oxide

over vanadia–tungsta–titania/sepiolite catalyst," *Applied Catalysis B: Environmental*, vol. 5, no. 1-2, pp. 117–131, 1994.

[139] A. Santos, A. Bahamonde, P. Avila, and F. García-Ochoa, "Measurement of the effective diffusivity for a vanadia-tungsta-titania/sepiolite catalyst for SCR of NO_x," *Applied Catalysis B: Environmental*, vol. 8, no. 3, pp. 299–314, 1996.

[140] S. Suárez, M. Yates, P. Avila, and J. Blanco, "New TiO_2 monolithic supports based on the improvement of the porosity," *Catalysis Today*, vol. 105, no. 3-4, pp. 499 – 506, 2005. 2nd International Conference on Structured Catalysts and Reactors ICOSCAR-2.

[141] J. E. Post, D. L. Bish, and P. J. Heaney, "Synchrotron powder X-ray diffraction study of the structure and dehydration behavior of sepiolite," *American Mineralogist*, vol. 92, no. 1, pp. 91–97, 2007.

[142] K. Brauner and A. Preisinger, "Struktur und Entstehung des Sepioliths," *Mineralogy and Petrology*, vol. 6, no. 1, pp. 120–140, 1956.

[143] R. Ruiz, J. C. del Moral, C. Pesquera, I. Benito, and F. González, "Reversible folding in sepiolite: study by thermal and textural analysis," *Thermochimica Acta*, vol. 279, pp. 103 – 110, 1996.

[144] R. Frost, J. Kristóf, and E. Horváth, "Controlled rate thermal analysis of sepiolite," *Journal of Thermal Analysis and Calorimetry*, vol. 98, no. 3, pp. 749–755, 2009.

[145] J. Blanco, M. Yates, P. Avila, and A. Bahamonde, "Characterization of alumina:sepiolite monoliths for use as industrial catalyst supports," *Journal of Materials Science*, vol. 29, no. 22, pp. 5927–5933, 1994.

[146] P. Avila, J. Blanco, A. Bahamonde, J. M. Palacios, and C. Barthelemy, "Influence of the binder on the properties of catalysts based on titanium-vanadium oxides," *Journal of Materials Science*, vol. 28, no. 15, pp. 4113–4118, 1993.

[147] A. Santos, A. Bahamonde, M. Schmid, P. Avila, and F. García-Ochoa, "Mass transfer influences on the design of selective catalytic reduction (SCR) monolithic reactors," *Chemical Engineering and Processing*, vol. 37, no. 2, pp. 117 – 124, 1998.

[148] S. Zurcher, M. Hackel, and G. Schaub, "Kinetics of Selective Catalytic NO_x Reduction in a Novel Gas-Particle Filter Reactor (Catalytic Filter Element and Sponge Insert)," *Industrial & Engineering Chemistry Research*, vol. 47, no. 5, pp. 1435–1442, 2008.

[149] J. J. van Ormelingen, H. Jensen-Holm, and S. L. Hvid, "Experience from erection and operation of two SCR denitrification units at Electrabels Langerlo Power Station, Genk, Belgium," in *Combined Power Plant Air Pollutant Control MEGA Symposium, May 19-22, 2003, Washington, DC, USA*, 2003.

[150] E. Tronconi and P. Forzatti, "Adequacy of lumped parameter models for SCR reactors with monolith structure," *AIChE Journal*, vol. 38, no. 2, pp. 201–210, 1992.

[151] J. W. Beeckman and L. L. Hegedus, "Design of monolith catalysts for power plant NO_x emission control," *Industrial & Engineering Chemistry Research*, vol. 30, no. 5, pp. 969–978, 1991.

[152] E. Tronconi, L. Lietti, P. Forzatti, and S. Malloggi, "Experimental and theoretical investigation of the dynamics of the SCR - $DeNO_x$ reaction," *Chemical Engineering Science*, vol. 51, no. 11, pp. 2965 – 2970, 1996.

[153] Y. peng Mao, H. Chen, X. li Long, W. de Xiao, W. Li, and W. kang Yuan, "Experimental determination of equilibrium constant for the complexing reaction of nitric oxide with hexamminecobalt(II) in aqueous solution," *Journal of Hazardous Materials*, vol. 162, no. 1, pp. 99 – 102, 2009.

[154] F. Gambardella, M. S. Alberts, J. G. M. Winkelman, and E. J. Heeres, "Experimental and modeling studies on the absorption of NO in aqueous ferrous EDTA solutions," *Industrial & Engineering Chemistry Research*, vol. 44, no. 12, pp. 4234–4242, 2005.

[155] X.-l. Long, Z.-l. Xin, M.-b. Chen, W. Li, W.-d. Xiao, and W.-k. Yuan, "Kinetics for the simultaneous removal of NO and SO_2 with cobalt ethylenediamine solution," *Separation and Purification Technology*, vol. 58, no. 3, pp. 328–334, 2008.

[156] C.-L. Yang and H. Shaw, "Aqueous absorption of nitric oxide induced by sodium chlorite oxidation in the presence of sulfur dioxide," *Environmental Progress*, vol. 17, no. 2, pp. 80–85, 1998.

[157] X.-l. Long, W.-d. Xiao, and W.-k. Yuan, "Removal of Nitric Oxide and Sulfur Dioxide from Flue Gas Using a Hexamminecobalt(II)/Iodide Solution," *Industrial & Engineering Chemistry Research*, vol. 43, no. 15, pp. 4048–4053, 2004.

[158] F. Roncaroli, M. Videla, L. D. Slep, and J. A. Olabe, "New features in the redox coordination chemistry of metal nitrosyls $M-NO^+$; M-NO; $M-NO^-$ (HNO)," *Coordination Chemistry Reviews*, vol. 251, no. 13-14, pp. 1903 – 1930, 2007.

[159] C. J. N. Buisman, H. Dijkman, P. L. Verbraak, and A. J. Den, Hartog, "Apparatus for purifying flue gas containing nitrogen oxides," May 2001.

[160] J. L. Anthony, E. J. Maginn, and J. F. Brennecke, "Solubilities and Thermodynamic Properties of Gases in the Ionic Liquid 1-n-Butyl-3-methylimidazolium Hexafluorophosphate," *The Journal of Physical Chemistry B*, vol. 106, no. 29, pp. 7315–7320, 2002.

[161] V. I. Pârvulescu and C. Hardacre, "Catalysis in ionic liquids," *Chemical Reviews*, vol. 107, no. 6, pp. 2615–2665, 2007.

[162] J. Huang, A. Riisager, R. W. Berg, and R. Fehrmann, "Tuning ionic liquids for high gas solubility and reversible gas sorption," *Journal of Molecular Catalysis A: Chemical*, vol. 279, no. 2, pp. 170 – 176, 2008.

[163] P. Bonhote, A.-P. Dias, N. Papageorgiou, K. Kalyanasundaram, and M. Gratzel, "Hydrophobic, Highly Conductive Ambient-Temperature Molten Salts," *Inorganic Chemistry*, vol. 35, no. 5, pp. 1168–1178, 1996.

[164] J. E. Bara, D. E. Camper, D. L. Gin, and R. D. Noble, "Room-Temperature Ionic Liquids and Composite Materials: Platform Technologies for CO_2 Capture," *Accounts of Chemical Research*, vol. 43, no. 1, pp. 152–159, 2010.

[165] A. Berger, R. F. de Souza, M. R. Delgado, and J. Dupont, "Ionic liquid-phase asymmetric catalytic hydrogenation: hydrogen concentration effects on enantioselectivity," *Tetrahedron: Asymmetry*, vol. 12, no. 13, pp. 1825 – 1828, 2001.

[166] J. L. Anderson, J. K. Dixon, and J. F. Brennecke, "Solubility of CO_2, CH_4, C_2H_6, C_2H_4, O_2, and N_2 in 1-Hexyl-3-methylpyridinium Bis(trifluoromethylsulfonyl)imide: Comparison to Other Ionic Liquids," *Accounts of Chemical Research*, vol. 40, no. 11, pp. 1208–1216, 2007.

[167] J. L. Anthony, E. J. Maginn, and J. F. Brennecke, "Solution Thermodynamics of Imidazolium-Based Ionic Liquids and Water," *The Journal of Physical Chemistry B*, vol. 105, no. 44, pp. 10942–10949, 2001.

[168] J. L. Anthony, J. L. Anderson, E. J. Maginn, and J. F. Brennecke, "Anion Effects on Gas Solubility in Ionic Liquids," *The Journal of Physical Chemistry B*, vol. 109, no. 13, pp. 6366–6374, 2005.

[169] S. B. Rasmussen, J. Huang, A. Riisager, H. Hamma, J. Rogez, J. Winnick, P. Wassserscheid, and R. Fehrmann, "Flue Gas Cleaning With Alternative Processes and Reaction Media," *ECS Transactions*, vol. 3, no. 35, pp. 49–59, 2007.

[170] J. D. Figueroa, T. Fout, S. Plasynski, H. McIlvried, and R. D. Srivastava, "Advances in CO_2 capture technology–The U.S. Department of Energy's Carbon Sequestration Program," *International Journal of Greenhouse Gas Control*, vol. 2, no. 1, pp. 9 – 20, 2008.

[171] A. Wanat, T. Schneppensieper, G. Stochel, R. van Eldik, E. Bill, and K. Wieghardt, "Kinetics, Mechanism, and Spectroscopy of the Reversible Binding of Nitric Oxide to Aquated Iron(II). An Undergraduate Text Book Reaction Revisited," *Inorganic Chemistry*, vol. 41, no. 1, pp. 4–10, 2002.

[172] N. A. Manan, C. Hardacre, J. Jacquemin, D. W. Rooney, and T. G. A. Youngs, "Evaluation of Gas Solubility Prediction in Ionic Liquids using COSMOthermX," *Journal of Chemical & Engineering Data*, vol. 54, no. 7, pp. 2005–2022, 2009.

[173] A. Klamt, F. Eckert, and W. Arlt, "COSMO-RS: An Alternative to Simulation for Calculating Thermodynamic Properties of Liquid Mixtures," *Annual Review of Chemical and Biomolecular Engineering*, vol. 1, pp. 101–122, 2010.

[174] A. Klamt and F. Eckert, "COSMO-RS: a novel and efficient method for the a priori prediction of thermophysical data of liquids," *Fluid Phase Equilibria*, vol. 172, no. 1, pp. 43 – 72, 2000.

[175] C. Glidewell, "Bond energy terms in oxides and oxoanions," *Inorganica Chimica Acta*, vol. 24, pp. 149–157, 1977.

[176] A. Riisager, P. Wasserscheid, R. van Hal, and R. Fehrmann, "Continuous fixed-bed gas-phase hydroformylation using supported ionic liquid-phase (SILP) Rh catalysts," *Journal of Catalysis*, vol. 219, no. 2, pp. 452 – 455, 2003.

[177] A. Riisager, R. Fehrmann, M. Haumann, B. S. K. Gorle, and P. Wasserscheid, "Stability and Kinetic Studies of Supported Ionic Liquid Phase Catalysts for Hydroformylation of Propene," *Industrial & Engineering Chemistry Research*, vol. 44, no. 26, pp. 9853–9859, 2005.

[178] Y. Zhang, S. Zhang, X. Lu, Q. Zhou, W. Fan, and X. Zhang, "Dual Amino-Functionalised Phosphonium Ionic Liquids for CO_2 Capture," *Chemistry - A European Journal*, vol. 15, no. 12, pp. 3003–3011, 2009.

[179] D. Wappel, G. Gronald, R. Kalb, and J. Draxler, "Ionic liquids for post-combustion CO_2 absorption," *International Journal of Greenhouse Gas Control*, vol. 4, no. 3, pp. 486 – 494, 2010.

[180] F. J. Gil-Llambías, A. M. Escudey, J. L. G. Fierro, and A. L. Agudo, "Determination of the active surface area of vanadia by electrophoretic migration and XPS measurements," *Journal of Catalysis*, vol. 95, no. 2, pp. 520–526, 1985.

[181] G. Ghiotti, E. Garrone, and F. Boccuzzi, "Infrared study of physical adsorption. 2. Nitric oxide on silica aerosil surfaces," *The Journal of Physical Chemistry*, vol. 91, no. 22, pp. 5640–5645, 1987.

[182] M. Moreno, F. Castiglione, A. Mele, C. Pasqui, and G. Raos, "Interaction of Water with the Model Ionic Liquid [bmim][BF_4]: Molecular Dynamics Simulations and Comparison with NMR Data," *The Journal of Physical Chemistry B*, vol. 112, no. 26, pp. 7826–7836, 2008.

Chapter A

Experimental

A.1 Characterization techniques

A.1.1 X-ray diffraction

Powder diffraction data was collected on a Huber G670 Guinier camera using $CuK_{\alpha 1}$ radiation, $\lambda = 1.5406$ Å. The sample was placed in a thin layer on scotch tape and rotated during data collection. Data were collected in the range of 3-100° in steps of 0.005^o in 2θ. Time of exposure was varied from 20–60 min. In case of data collection for Rietveld refinement, exposure was a minimum of 60 min. Rietveld refinement was done with WINPOW (Software by Kenny Ståhl), where crystallographic information files (CIF) from Fachinformationszentrum Karlsruhe are fitted against experimental XRD data, yielding information about the phase distribution and unit cell parameters.

The CIF files used for Rietveld refinement are listed by their identification code in the Inorganic Crystal Structure Database:

t$-ZrO_2$: 93030, m$-ZrO_2$: 94886, c$-ZrO_2$: 92094,

$Mg_8(Si_{12}O_{30}(OH)_4) \cdot (H_2O)_2$ (Sepiolite 2H_2O)[141]: 156200,

$Mg_8(Si_{12}O_{30}(OH)_4) \cdot (H_2O)_{12}$ (Sepiolite 12H_2O)[141]: 156199,

SiO_2: 174, $CaCO_3$: 16710, $CaSO_4$: 68592, $(V_{0.12}Zr_{0.88})O_2$: 96542.

A.1.2 Scanning electron microscopy

The morphology and particle size of the catalysts were investigated by SEM using a FEI Inspect 'S' with tungsten filament. Images were typically obtained with acceleration voltages of 2 to 10 kV. The specimens were prepared by dry dispersing the catalyst powder on carbon tape with subsequently carbon coated to avoid charging.

A.1.3 Temperature programmed desorption

To compare the strength and the number of active sites for samples, the surface acidity of the catalysts was measured with a Micromeritics AutoChem II 2920. Approximately 100 mg of sample was initially pretreated at 200°C in helium for 30 min to remove any physisorbed species and subsequently saturated with 50 $^{ml}/min$ dry 1% NH_3/He at 100°C for 60 min. Loosely bound ammonia was hereafter removed by purging with 50 $^{ml}/min$ He for 60 min, before performing temperature programmed desorption (TPD) at a heating rate of 10$^{°C}/min$ in the range 100-1000°C in a He flow of 25 $^{ml}/min$.

A.1.4 Nitrogen physisorption

Determination of the BET surface area was done by nitrogen physisorption. N_2 adsorption and desorption were performed at liquid nitrogen temperature on a Micromeritics ASAP 2020. Prior to measurement, the samples were degassed at 200°C under vacuum for 6 h

A.1.5 Mercury intrusion porosimetry

The porosity was determined by mercury intrusion porosimetry (MIP) on a CE Instruments Pascal 140/240 porosimeter on samples dried overnight at 150°C.

A.1.6 Electrophoretic migration

The zero point charges (ZPC) of the composite materials were determined by measuring the zeta potential as a function of the solution pH. The zeta potentials were calculated by the Helmholtz-Smoluchowski equation: $\bar{V} = \frac{\epsilon \xi}{4\pi\eta}$, where $\bar{V}$ is the electrophoretic mobility, ϵ the permittivity, ξ the zeta-potential and η the dynamic viscosity. The electrophoretic migration rate was measured on a Zeta-Meter Inc. Instrument model 3.0+, provided with an automatic sample transfer unit to avoid sample sedimentation problems [180]. Experiments were carried out using 30 mg of <2 μm powder samples suspended in 200 mL of mM KCl, adjusting the pH with 0.2 M KOH and HCl solutions. Each curve was recorded at least three times to ensure the reproducibility of the results.

A.1.7 NMR spectroscopy

The ionic liquids were characterized with ^{1}H-NMR, recorded on a Varian Unity Inova-500 MHz spectrometer. To avoid mixing of the samples with the solvent, pure samples were placed in closed glass capillaries. The close ampule containing the sample was placed in NMR tubes together with the solvent $CDCl_3$, which also was used as an internal standard.

A.1.8 TGA-DSC

TGA-DSC curves were obtained from measurements on a Mettler Toledo TGA/DSC 1 SF instrument equipped with a SDTA (single differential thermal analysis) sensor. The about 25 mg of sample were placed in 70 μl alumina crucibles and heated from room temperature up to 600°C with a heating rate of 10 °C/min under a N_2 flow of 20 ml/min.

A.2 Catalyst synthesis

A number of catalysts were synthesized for this study. The synthesis details are listed in the following.

Reference catalysts

Two reference catalysts have been used for this study. The first was a commercial vanadia-tungsta-titania monolith, with a vanadia loading 3 wt% V_2O_5 (1.7 wt% vanadium) on 7 wt% WO_3-TiO_2 anatase. The active catalyst, which is distributed on glass fiber surface (Fig. A.1), was crushed to particles (including the supporting fiber). The powder was pressed at 2 tons (Ø = 13mm) and fractionated to a particle size of 180-300 μm before any measurements. This catalyst is denoted throughout the study as *1.7VWT_ref*.
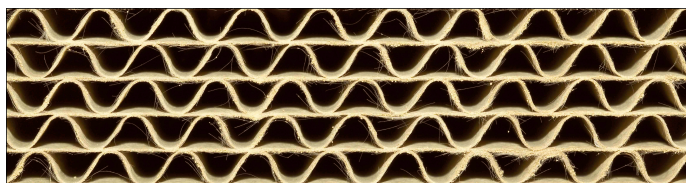

Fig. A.1: Close-up of commercial SCR catalyst monolith

The second reference catalyst is very similar in composition to the commercial reference sample, but is stabilized by small amounts of clay. 1.72 g $VOSO_4 \cdot 5\,H_2O$ was dissolved in small amount of water and 20 g of 10 wt% WO_3-TiO_2 anatase (DT-52, Millennium, particle size < 25 nm), was added to produce a slurry that was allowed to settle for an hour with stirring. Thereafter, 1 g of Bentonite (Tolsa, >95%) and 1 g of Hymod Excelsior (Imerys Minerals Ltd) is added to the slurry, whereupon water was added to obtain an homogeneous paste with a suitable viscosity for extrusion from a 20 ml syringe with a 2 mm orifice. The extruded material was sealed in a wet atmosphere for 48 hours for slow drying, and then dried overnight at 150°C in air. Calcination was carried out at 500°C for 4 hours (ramp 3.25°C/min) in air. Finally the extruded material was broken into 3–5 mm cylindrical pellets, with a total vanadia concentration of 3 wt% on WO_3-TiO_2, denoted *1.7VWT*.

Catalysts based on commercial zirconia

Vanadium-based catalysts

Vanadia-based catalysts were synthesized by incipient wet impregnation (IWI) of vanadyl solution on fractionated zirconia (180-300 μm), to obtain an vanadium concentration of 1.7 wt% (3.0 wt% V_2O_5) unless otherwise stated. The vanadyl solution were obtained from ammonium meta vanadate (Sigma-Aldrich, >99%) and oxalic acid (Merck, p.a.), where the ammonium meta vanadate is slowly added to a heated solution (50-70°C) of oxalic acid with a small amount of water. After impregnation, the sample was allowed to settle for an hour before drying at 100°C followed by calcination at 400°C in air for at least 2 hrs.

Iron-copper mixed oxide catalysts

Synthesis of iron-copper mixed oxide catalysts were carried out by sequential IWI of the aqueous nitrate precursor [$Cu(NO_3)_2$, $Fe(NO_3)_2$] on particles of 3.4SZ_NP (180-300 μm). The total molar concentration of metal species was kept constant at 364 μmol/g (equivalent to a CuO loading of

3.5 wt%), but the Cu-Fe ratio was varied, producing Fe-Cu metal oxide catalysts with the iron molar fraction, X_{Fe}, 0.00, 0.20, 0.33, 0.50, 0.67, 0.80, 1.00. After drying at 100°C, the catalysts were calcined at 450°C, 4 hrs (3.5°C/min), resulting in the catalysts presented in Fig. A.2.

Fig. A.2: Fe-Cu mixed oxide catalysts supported on 3.4SZ_NP. From left to right decreasing copper oxide loading, increasing iron oxide loading

A.2.3 Catalysts mixed with sepiolite

A.2.3.1 Catalysts for optimization of VSZ-sepiolite ratio

The sulphated zirconia was prepared by impregnating 101.6 g of the zirconia hydroxide (Melcat) with 8.3 g $(NH_4)_2SO_4$ (Panreac, >99%) by the incipient wetness method. After overnight standing in ambient conditions, the samples were dried at 150°C for 3 hours. Calcination of the samples at 500°C for 4 hours in air was performed by placing the material directly into a pre-heated furnace, in order to facilitate the preferred formation of metastable tetragonal phases. Subsequent chemical analysis (ICP-MS) revealed a sulfate loading of 5.3 wt% (measured at wt% SO_3). The catalysts were prepared by wet impregnation of $VOSO_4$ onto the sulphated zirconia, to produce a slurry that was allowed to settle for an hour with stirring. Thereafter sepiolite, α-sepiolite (Pansil 100, Tolsa S.A., 60%) and water were added in the desired amounts to obtain a homogeneous paste with an adequate viscosity for extrusion from a 20 ml syringe with a 2 mm orifice. The extrudates were slowly dried, sealed in a wet atmosphere for 48 hours then dried overnight at 150°C in air, resulting in the extrudates presented in Fig. A.3. Calcination was carried out at 500°C for 4 hours in air. Finally the extruded material was broken into 3–5 mm cylindrical pellets.

A.2.3.2 Sepiolite-based catalysts for optimization of sulfate content

A series of nine catalysts were synthesized by kneading 0–9 g $(NH_3)_2SO_4$ (Panreac, >99%) in water with the sulfated zirconia from the same batch prepared above, and 0.745 g $VOSO_4 \cdot 5\,H_2O$. After the settling of the slurry, 1.67 g sepiolite (Pansil 100, Tolsa S.A., 60%) was added and after homogeneising the slurry extruded and calcined as described above. The resulting catalysts thereby contained a total sepiolite concentration of 25 wt%, a sulfate loading of 4.1–8.2 wt%, measured at SO_3, and a total V_2O_5 loading of 4 wt%.

A.2.3.3 Monolith extrusion and activity measurements

Monolithic catalysts were made of the 2/8 formulation, with composition, drying, and calcination procedure as described above. The extruded monoliths were cylindrically shaped with 24
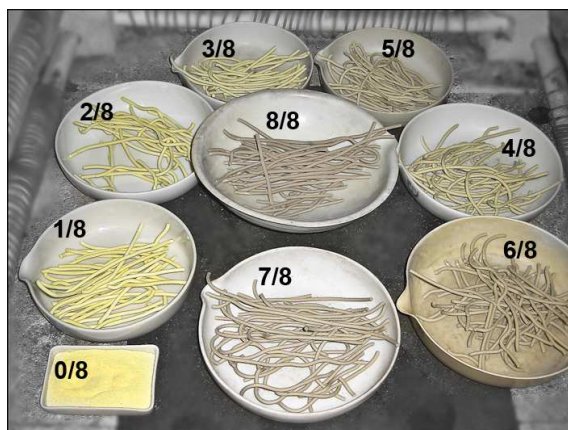
Fig. A.3: Sepiolite-VSZ catalyst series with increasing weight fraction of sepiolite from 0/8 to 8/8, the latter being sepiolite without VSZ. Notice that the $V_2O_5-SO_4^{2-}-ZrO_2$ (0/8) catalyst is on powder form due to the lack of sepiolite binder

parallel channels, with the geometric dimensions: monolith length 15–30 cm, square cell size 1.6 mm, wall thickness 0.92 mm, geometric surface 9.91 cm^2/cm^3, cell density 14.57 $cell/cm^2$ and bulk density 1.45 g/cm^3.

The SCR activity of the monolith were evaluated in a reactor system, illustrated in Fig. A.4, consisting of a pyrex tube with three electrically heat zones to ensure isothermal conditions. The catalyst temperature was monitored with two thermocouples inserted above and below the catalyst bed. Furthermore, the temperature at the entrance point of NH_3 was constantly monitored, in order to be sure that no precipitation of $(NH_4)_2NO_2$ took place. Free space surrounding the monolith and the reactor wall were filled with inert material to prevent bypass flow. Reactant gases were regulated with mass-flow controllers providing the typical inlet concentrations: NO 700 ppm, NH_3 700 ppm (except when stated otherwise), O_2 3.5 vol%, H_2O 1.8 vol%, balanced in N_2. The inlet and outlet NO and NO_2 concentrations were determined by chemiluminescence
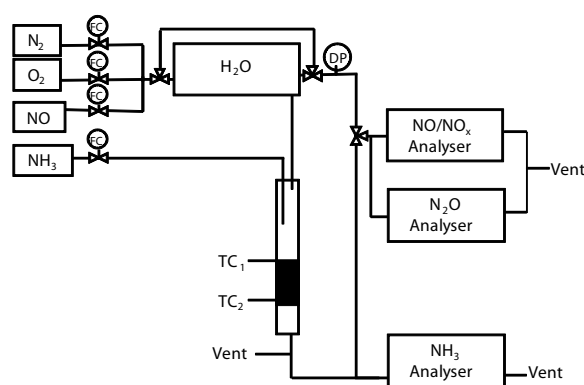

Fig. A.4: Schematic test rig for evaluation of monolith and pellet sample SCR activities

with a Signal NO + O_2 analyzer (Series 4000). Analysis of N_2O and NH_3 was carried out by IR spectroscopy with a Signal 7000FT GFC Analyzer and with an A.D.C. Double Beam Luft Type Infrared Gas Analyzer, respectively. Stable data was acquired under steady-state conditions after approximately 90 min of stabilization for each point after changing the space velocities. Before

the analyzers, a peltier element is inserted. Only one temperature per day was measured, in order to ensure complete steady state equilibrium of NH_3 on the catalyst surface.

A.2.4 Catalyst poisoning

Doping with potassium was done by IWI with a solution of KNO_3 (Merck, >99%) on the fractionated catalysts to obtain a potassium loading, relative to the active metal, of 0.4 $^{mol}/_{mol}$, unless otherwise noted. After settling and drying at 100°C, the sample were calcined at 400°C for 2 hrs.

A.3 Catalyst testing

The experimental setup used in the examination of catalytic activity is schematically illustrated in Fig. A.5 and the actual test rig is shown in Fig. A.6. SCR activities were measured with a Thermo Environmental chemiluminescence analyzer, model 17C, NH_3-analyzer.
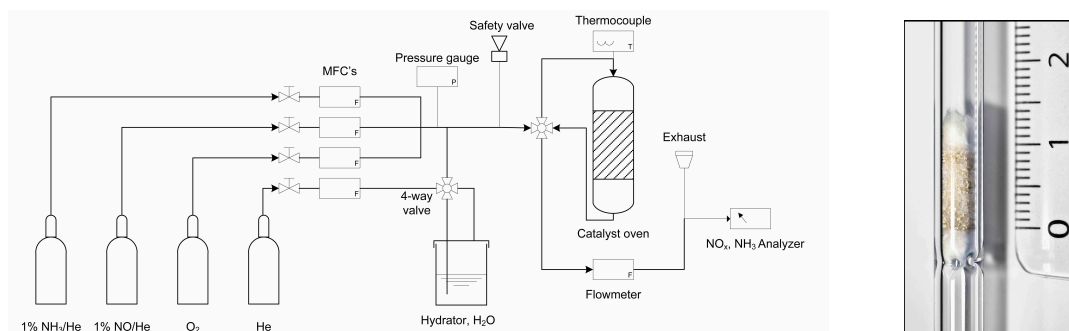

Fig. A.5: Left: Schematic drawing of the continuous flow experimental setup for catalytic measurements. **Right**: Quartz reactor with loaded sample diluted in SiO_2, fixed between two layers of quartz wool. Gas direction from top to bottom. Scale 1 cm

About 10 mg of catalyst (if catalyst was synthesized in powder form, it was pressed at 2 tons, Ø = 13 mm before fractionation) fractionated to 180-300 µm, were fixed in a quartz plug flow reactor with a total ambient flow of 300 $^{ml}/_{min}$ containing 1000 ppm NO, 1100 ppm NH_3, 3.5% O_2, 2.3% H_2O in He. The catalysts were diluted with about 125 mg quartz (Merck, 99.95%, BET surface area <0.1$^{m^2}/_g$) to ensure a cylindrical shaped catalyst bed, see Fig. A.5, right.

The catalyst testing was performed with a specially designed feed-back controlled Labview program, monitoring the total flow, NO-, NO_2-, NH_3- and total NO_x-signals, and controlling mass flow controllers and temperature. Catalyst temperature was measured directly above the catalyst bed (thermocouple not shown in Fig. A.5). A typical program was initiated by activation in the SCR gas at 200°C for minimum 60 min, followed by cooling to room temperature. From ambient conditions the temperature was stepwise increased from 25 to 500°C in steps of 20°C. Steady-state conversion was obtained at each temperature (ensured with PID feed-back controller embedded in Labview) and data collected for 5 min (frequency 10 sec) before sequential temperature increase. After the maximum temperature, the catalyst was cooled stepwise and data collected every 50°C.

Fig. A.6: Setup for testing the catalytic SCR activity at various temperatures. NH_3-NO_x-analyzer located below table along with gas diluting unit

A.3.1 Rate expression

A convenient method of representing the catalysts activity is by its rate constant, r, which is first order with respect to NO [42,89] (and references therein):

$$r = -\frac{1}{W}\frac{d[NO]}{dt} = k[NO]^1[NH_3]^0 \tag{A.1}$$

where W is the amount of catalyst, and k the first-order rate constant. Expression A.1 can be rearranged and solved:

$$\frac{d[NO]}{[NO]} = -kW\,dt \Rightarrow$$

$$\int_{[NO]_0}^{[NO]}\frac{1}{[NO]}d[NO] = -kW\int_{t=0}^{t}dt \Leftrightarrow$$

$$\ln\frac{[NO]}{[NO]_0} = -kWt \Leftrightarrow$$

$$k = -\frac{1}{Wt}\ln\frac{[NO]}{[NO]_0} \tag{A.2}$$

Introducing the fractional conversion X, of NO, which is expressed as:

$$X = \frac{[NO]_0 - [NO]}{[NO]_0} \Leftrightarrow \frac{[NO]}{[NO]_0} = 1 - X \tag{A.3}$$

Upon substitution of $\frac{[NO]}{[NO]_0}$ from equation A.3 into equation A.2, we obtain the following:

$$k = -\frac{1}{Wt}\ln(1\text{-}X) \tag{A.4}$$

By assuming plug flow in the reactor, i.e. time is proportional to a volume flux through the reactor, we can introduce the inlet NO molar concentration, $[NO]_0$ (mol/l), which is unit-counterbalanced by the molar inflow rate of NO, F_0 (mol/s). This is collected in the expression of the first order rate constant, k:

$$k = -\frac{F_0}{[NO]_0 W}\ln(1\text{-}X) \tag{A.5}$$

Thereby we obtain a rate expression wherein the catalyst weight is incorporated, in contrast to the *conversion* of NO, which is often used in the literature, but difficult to compare at different space velocities.

A.4 NO gas absorption in ionic liquids

A.4.1 Preliminary screening

Preliminary gas absorption was carried out in a ca. 5 ml test tube with 1 ml ionic liquid (IL) at room temperature (22–23°C). The 10% NO/N_2 were introduced into the IL through a glass pasteur pipette retrofitted with a glass frit to reduce the bubble size and increase the gas-liquid contact area (interfacial area). The flow was maintained at around 5 ml/min to contain the bubbles formed within the test tube. The acetate-based ILs were exposed to the NO gas for about 100 h, whereas the triflate-based only were subjected to the gas for about 43 h. The absorption of NO was monitored in real time by logging the weight increase with with a PC interfaced with the microbalance (accuracy 0.1 mg). However, to avoid balance drifting, the absorption results are supplied by measuring the total weight of the test tube with IL and pipette before and after NO absorption. Any increase in weight of the sample after NO exposure were attributed solely to the absorption of NO. The weight increase are in all cases given as the fraction molar increase, defined in equation A.6.

$$X_{NO}^{IL} = \frac{n_{NO}}{n_{NO} + n_{IL}} \tag{A.6}$$

Subsequent to the absorption procedure, the NO-absorbed ionic liquids were subjected to vacuum in order to estimate the reversibility of the bound NO. The samples were desorbed at pressures below 10 mbar for minimum 24 h at room temperature.

A.4.2 Equilibrium gas absorption-desorption

The absorption of 10% NO/N_2 were performed at 1 bar at room temperature, by passing the gas stream (ca. 10 ml/min under ambient conditions) via a glass frit (diameter 6 mm) through 1000 µl of ionic liquid. The ionic liquid were loaded in individual cylindric glass tubes (length 105 mm, inner diameter 10 mm) with inlet and outlet valves. The exit of the glass frit were located just above the bottom of the cylinder so the gas bubbles would supply 'stirring' of the solution during absorption. The absorption experiments were performed with three glass reactors with the same ionic liquid, for reproducibility. All reactors were placed in a glass tube rack in an oven where temperature could be varied to an certainty of ± 0.5°C, as outlined in Fig. A.7. The ionic liquid were saturated at room temperature before the temperature were increased in a step wise manner, where the solubility of the NO were determined at each step. The gas flow to each reactor were supplied by Bronkhorst flow controllers. The temperature were monitored continuously via Labview with a thermocouple located close to the ionic liquids in the oven.

The mass increase of the IL phase were determined by weighing the reactors with IL on a microbalance (accuracy 0.1 mg) on a regular basis. Before removal from the oven for weighing, the gas inlet and outlet valves were closed to avoid gas desorption due to changes in pressure. To ensure that the thermodynamic equilibrium were obtained, the weighing procedure were repeated until the weight were constant within 6 h between consecutive measurements.
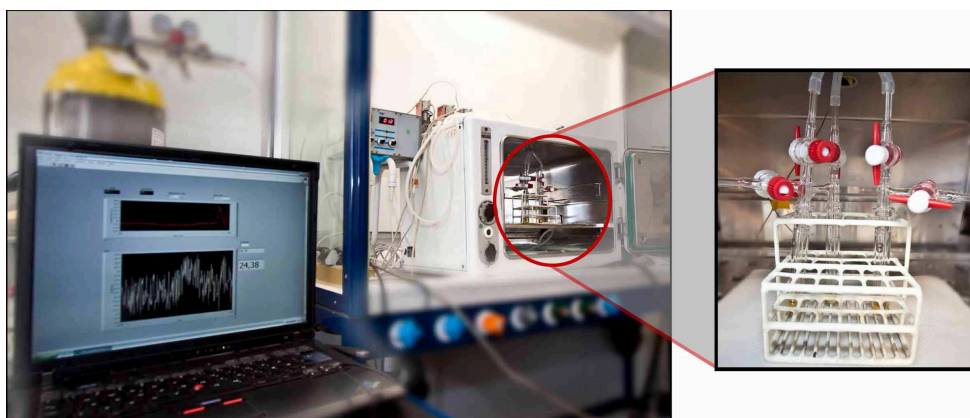
Fig. A.7: Setup for equilibrium absorption experiments. The ionic liquid are placed in glass reactors and placed in oven

A.4.3 Chemicals

The ILs used in the preliminary study were all commercial grade and were used without any further purification. The ILs were: 1-ethyl-3-methylimidazolium tetrachloroaluminat (>95%, Fluka/BASF), 1-ethyl-3-methylimidazolium thiocyanate (>95%, Fluka/BASF), 1-ethyl-3-methyl-imidazolium acetate (>90%, Fluka/BASF), 1-ethyl-3-methylimidazolium triflate (99%, Io-li-tec), 1-butyl-3-methylimidazolium tetrachloroaluminat (>95%, Aldrich/BASF), 1-butyl-3-methylimi-dazolium thiocyanate (>95%, Fluka/BASF), 1-butyl-3-methylimidazolium acetate (>95%, Aldrich/-BASF), 1-butyl-3-methylimidazolium triflate (>98%, Solchemar), 1-octyl-3-methylimidazolium triflate (99%, Io-li-tec).

A.4.4 NO gas solubility predictions with COSMO-RS

Theoretical calculations of NO gas solubility in ionic liquids were performed using the software COSMO*thermX* Version C21_0110. The program predicts thermophysical data for mixtures and is based on a method called COSMO-RS (Conductor-like Screening Model for Real Solvents) which combines quantum chemical calculations with statistical thermodynamics[174]. The COSMO files used for the calculations were obtained from the TZVP database in the program. These files contain results of quantum chemical calculations, including the optimized geometries of the molecules, performed with the DFT method using TZVP basis sets.

Chapter B

Standard thermodynamic properties

Tab. B.1: CRC standard thermodynamic properties of gases at 298.15K and 1 bar. Values from [10]

Molecular formula	Name	$\Delta_f H^o_{298K}$ [kJ/mol]	$\Delta_f G^o_{298K}$ [kJ/mol]	ΔS^o_{298K} [J/mol K]
O_2	Oxygen	0		205.2
O_3	Ozone	142.7	163.2	238.9
N_2	Nitrogen	0		191.6
N_2O	Nitrous oxide	81.6	103.7	220
NO	Nitric oxide	91.3	87.6	210.8
N_2O_3	Nitrogen trioxide	86.6	142.4	314.7
NO_2	Nitrogen dioxide	33.2	51.3	240.1
N_2O_4	Nitrogen tetroxide	11.1	99.8	304.4
N_2O_5	Nitrogen pentoxide	13.3	117.1	355.7
NH_3	Ammonia	-45.9	-16.4	192.8
CO_2	Carbon dioxide	-393.5	-394.4	213.8
CH_4	Methane	-74.6	-50.5	186.3
H_2	Hydrogen	0		130.7
CO	Carbon monoxide	-110.5	-137.2	197.7
H_2O	Water	-241.8	-228.6	118.8

Appendix B. Standard thermodynamic properties

Tab. B.2: Thermodynamic calculations based on data reported in Tab. B.1

Reaction		ΔH^o_{298K} [kJ/mol]	ΔS^o_{298K} [J/mol K]	ΔG^o_{298K} [kJ/mol]	Eq. const., K_{298K}[†]		$T_{\Delta G^o=0}$[‡] [K]
NO_X removal							
$4\,NO + 4\,NH_3 + O_2$	$\longrightarrow$ $4\,N_2 + 6\,H_2O$	-1632	-340	-1531	1.6E+268	bar^1	4796
$6\,NO + 4\,NH_3$	$\longrightarrow$ $5\,N_2 + 6\,H_2O$	-1815	-365	-1706	7.9E+298	bar^1	4970
NO	$\longrightarrow$ $\frac{1}{2}N_2 + \frac{1}{2}O_2$	-91	-12	-88	2.2E+15	bar^0	7363
$2\,NO + 2\,NO_2 + 4\,NH_3$	$\longrightarrow$ $4\,N_2 + 6\,H_2O$	-1516	-194	-1458	3.2E+255	bar^{-2}	7824
NO removal with different reductants							
$NO + CO$	$\longrightarrow$ $\frac{1}{2}N_2 + CO_2$	-374	-99	-345	2.6E+60	$bar^{-1/2}$	3785
$4\,NO + 4\,NH_3 + O_2$	$\longrightarrow$ $4\,N_2 + 6\,H_2O$	-1632	-340	-1531	1.6E+268	bar^1	4796
$NO + CH_4 + \frac{3}{2}O_2$	$\longrightarrow$ $\frac{1}{2}N_2 + CO_2 + 2\,H_2O$	-894	-158	-847	2.2E+148	bar^0	5668
$NO + H_2$	$\longrightarrow$ $\frac{1}{2}N_2 + H_2O$	-333	-127	-295	5.3E+51	$bar^{-1/2}$	2625
NO_X formation							
$O_2 + N_2$	$\longrightarrow$ $2\,NO$	183	25	175	2.0E-31	bar^0	7363
$2\,NO + O_2$	$\longrightarrow$ $2\,NO_2$	-116	-147	-72	5.0E+12	bar^{-1}	793
$2\,NO$	$\longrightarrow$ $N_2O + \frac{1}{2}O_2$	-101	-99	-71	3.3E+12	$bar^{-1/2}$	1020
$3\,NO$	$\longrightarrow$ $N_2O + NO_2$	-159	-172	-108	7.5E+18	bar^{-1}	923
$4\,NH_3 + 4\,NO + 3\,O_2$	$\longrightarrow$ $4\,N_2O + 6\,H_2O$	-1306	-637	-1116	3.3E+195	bar^{-1}	2050
$NO + O_3$	$\longrightarrow$ $NO_2 + O_2$	-201	-4	-199	8.9E+34	bar^0	45636
$2\,N_2O$	$\longrightarrow$ $2\,NO + N_2$	19	365	-89	4,5E+15	bar^1	53
N_2O_3	$\longrightarrow$ $NO + NO_2$	38	136	-3	3.0E+00	bar^1	278
NO_X formation from air							
$N_2 + \frac{1}{2}O_2$	$\longrightarrow$ N_2O	82	-74	104	6.7E-19	$bar^{-1/2}$	-1100
$\frac{1}{2}N_2 + \frac{1}{2}O_2$	$\longrightarrow$ NO	91	12	88	4.5E-16	bar^0	7363
$N_2 + \frac{3}{2}O_2$	$\longrightarrow$ N_2O_3	87	-185	142	1.5E-25	$bar^{-3/2}$	-469
$\frac{1}{2}N_2 + O_2$	$\longrightarrow$ NO_2	33	-61	51	1.0E-09	$bar^{-1/2}$	-545
$N_2 + 2\,O_2$	$\longrightarrow$ N_2O_4	11	-298	100	3.2E-18	bar^{-2}	-37
NH_3 oxidation							
$4\,NH_3 + 3\,O_2$	$\longrightarrow$ $2\,N_2 + 6\,H_2O$	-1267	-291	-1180	6.5E+206	bar^1	4358
$4\,NH_3 + 4\,O_2$	$\longrightarrow$ $2\,N_2O + 6\,H_2O$	-1104	-439	-973	3.0E+170	bar^0	2514
$4\,NH_3 + 5\,O_2$	$\longrightarrow$ $4\,NO + 6\,H_2O$	-902	-241	-830	2.7E+145	bar^{-1}	3740
$4\,NH_3 + 6\,O_2$	$\longrightarrow$ $2\,N_2O_3 + 6\,H_2O$	-1094	-660	-897	1,5E+157	bar^{-2}	1657
$4\,NH_3 + 7\,O_2$	$\longrightarrow$ $4\,NO_2 + 6\,H_2O$	-1134	-534	-957	1.3E+25	bar^{-1}	2123
$2\,NH_3 + 8\,NO$	$\longrightarrow$ $5\,N_2O + 3\,H_2O$	-956	-616	-772	2.1E+135	bar^{-2}	1553
$4\,NH_3 + 4\,NO + 3\,O_2$	$\longrightarrow$ $4\,N_2O + 6\,H_2O$	-1306	-637	-1116	3.3E+195	bar^{-1}	2050
Various NO_2 reactions							
$6\,NO_2 + 8\,NH_3$	$\longrightarrow$ $7\,N_2 + 12\,H_2O$	-2734	-216	-2669	∞	bar^5	12644
$2\,NO_2 + 4\,NH_3 + O_2$	$\longrightarrow$ $3\,N_2 + 6\,H_2O$	-1334	-169	-1283	6.4E+224	bar^2	7891
$8\,NO_2 + 6\,NH_3$	$\longrightarrow$ $7\,N_2O + 9\,H_2O$	-1595	-468	-1456	1.0E+255	bar^{-2}	3406
$4\,NO_2 + 4\,NH_3 + O_2$	$\longrightarrow$ $4\,N_2O + 6\,H_2O$	-1074	-344	-971	1.3E+170	bar^{-1}	3121

[†] Calculated with $K = \exp\left[-\frac{\Delta G^o_{298K}}{RT}\right]$

[‡] Temperature where spontaneous reaction takes place under the coarse assumption that ΔH^o and ΔS^o are temperature independent. $\Delta G^o = 0$, thus $\Delta G^o = \Delta H^o - T\Delta S^o \Rightarrow$ $0 = \Delta H^o - T\Delta S^o \Leftrightarrow T = \frac{\Delta H^o}{\Delta S^o}$

Chapter C

Supplementary figures

C.1   Optimization of sepiolite-VSZ ratio

Fig. C.1 show the paramagnetic species, such as V^{4+} and Fe^{3+}, that are present in the composite catalyst. With increasing sepiolite content, the strong signal from Fe(III) develops around 1500 Gauss, confirming the presence of impurities in the sepiolite. Simultaneous, the signal from vanadyl species is gradually displaced. At highest sepiolite loadings, the presence of Mn^{2+} species in the sepiolite is also confirmed.
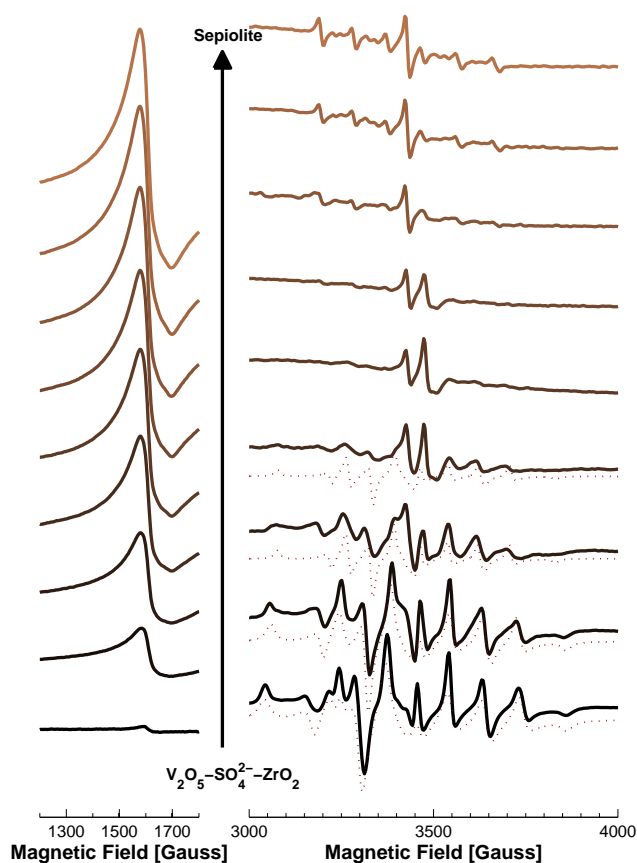
Fig. C.1: Room temperature electron resonance spectroscopy (EPR) profiles of the sepiolite/$V_2O_5-SO_4^{2-}-ZrO_2$ composite catalysts with increasing weight fraction of sepiolite. **Left:** EPR signal due to the presence of Fe^{3+}-species in sepiolite. **Right:** Signal originating from V^{4+}. Dotted red curve: simulated EPR signal of V^{4+}. At highest sepiolite concentrations, the samples display signal from a Mn^{2+}-impurity

---
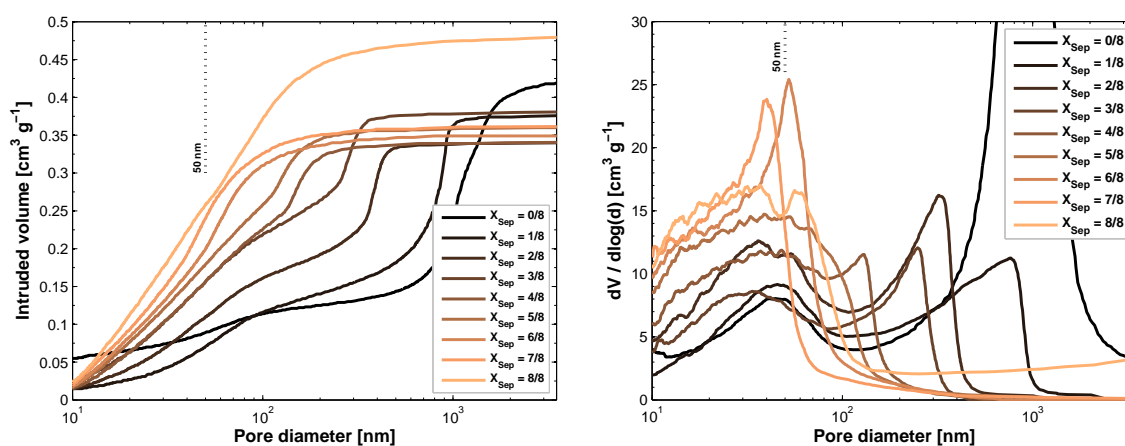
Fig. C.2: Cumulative pore volume curves (**left**) and pore size distribution (**right**) obtained by MIP of extruded catalysts, prepared with different $V_2O_5-SO_4^{2-}-ZrO_2$ / sepiolite weight ratio

The porosity of the manually extruded composite catalysts can be determined based on Fig. C.2. The $V_2O_5-SO_4^{2-}-ZrO_2$ sample (0/8) display large interparticular pores of around 1 µm due to its powder configuration. However, the large macro pores of the mixed catalyst are gradually reduced in diameter with increasing sepiolite content. Thus, the porosity can be designed, based on the content of sepiolite.

C.2   SEM-EDS of 2/8 catalyst after KCl hydrothermal treatment
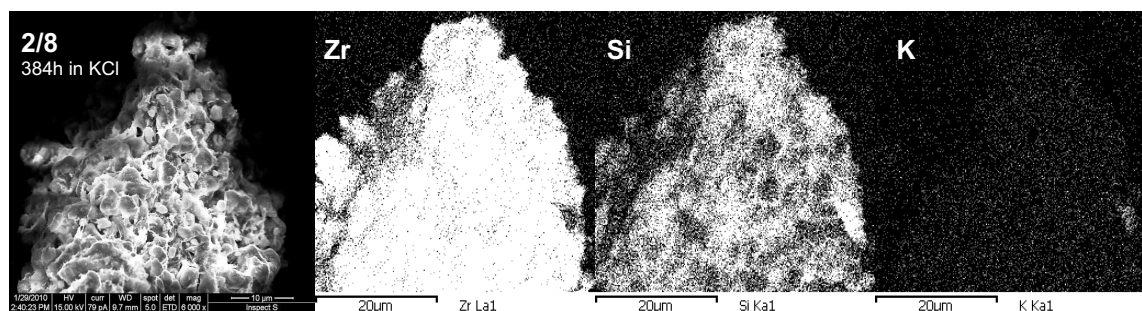
Fig. C.3: SEM-EDS (energy dispersive X-ray spectroscopy) of the 2/8 composite catalyst after hydrothermal treatment at 350°C in humid air, submersed in KCl for 384 hrs

The distribution of KCl on the catalysts were performed subsequent to hydrothermal treatment to evaluate the distribution of potassium. According to the results obtained with EDS, the potassium 'density' seem to be almost homogeneously distributed over the particle surface. However, whether potassium is actually reaching the active vanadia sites or blocked by sepiolite (that is partly covering the surface) can not be determined here.

C.3 Optimization of sulfate content

With increasing sulfate content, the catalytic activity proceeds through a maximum sulfate concentration around 6.3 wt% (as SO_3), at where the sepiolite probably is neutralized. However, the overall impact on the SCR activity with increased sulfate loading is moderate. This stresses the importance of sulfating the $Zr(OH)_2$ for obtaining high acidity, in contrast to sulfation of ZrO_2 [73], as were done here.
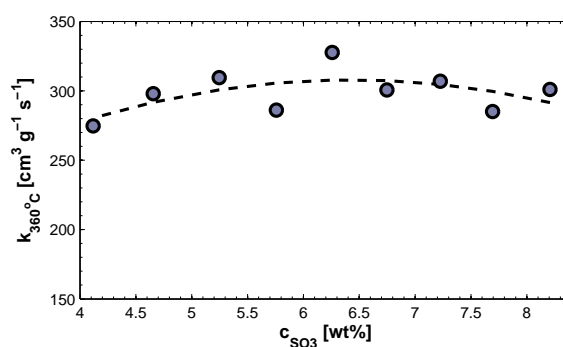

Fig. C.4: SCR activity at 360°C of the extruded 2/8 catalyst pellets with additional ammonium sulfate added

C.4 Characterization of ionic liquids for NO absorption

The pure and NO-saturated [BMIM]OAc and [BMIM]OTf were evaluated with Raman spectroscopy. NO exhibit a stretching frequency around 1870 cm^{-1} [181], which could not be observed in any of the obtained spectra (cf. Fig C.5 and C.6). However, in case of [BMIM]OAc a peak developed after NO saturation in the OH stretching region at 2965 cm^{-1}, implying the presence of water in the IL. The water 'contamination' could originate from the gas mixture.
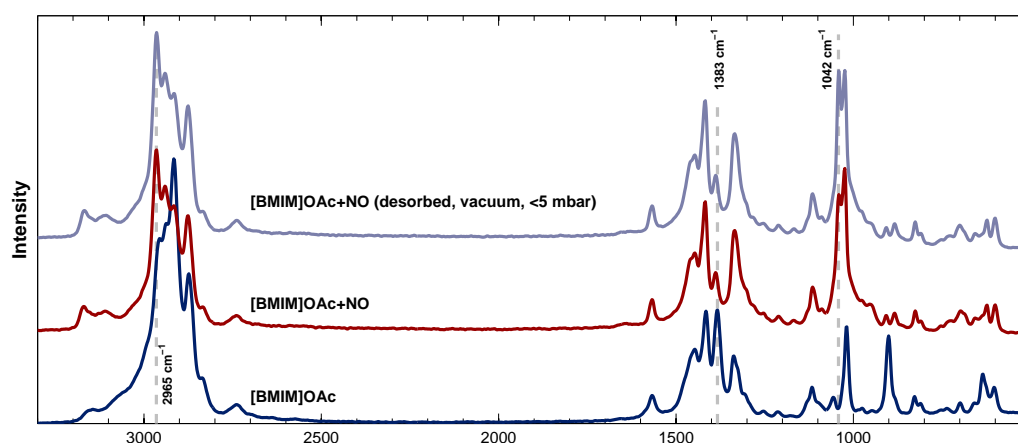

Fig. C.5: Raman spectroscopy of the fresh and NO saturated [BMIM]OAc. NO from the saturated [BMIM]OAc was attempted removed by reducing the pressure at room temperature

In case of the [BMIM]OTf, only one band suggest that the IL has been altered, which confirms that NO is only weakly bound to the IL. The band at 1312 cm^{-1} disappears subsequent to

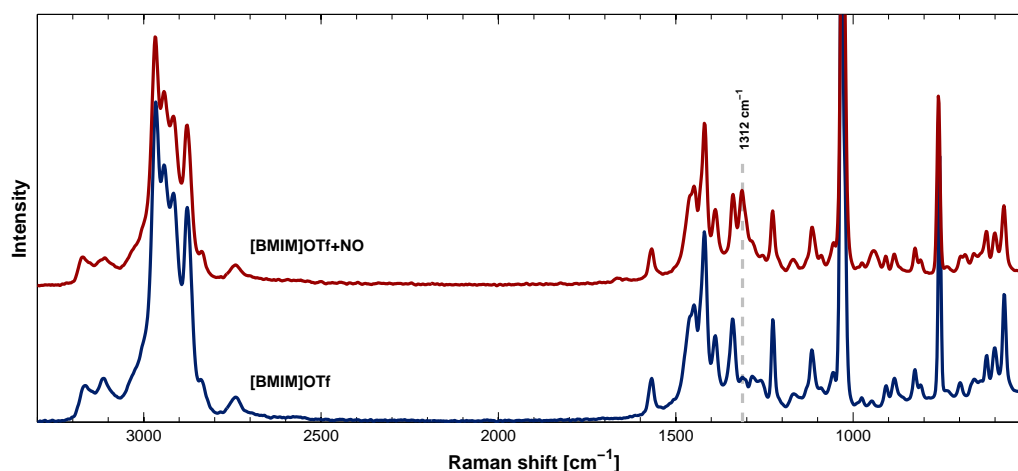saturation. Further investigation is being undertaken to identify the remaining bands.

Fig. C.6: Raman spectroscopy of the fresh and NO saturated [BMIM]OTf

^{1}H-NMR were performed on the pure and NO-saturated ILs, the chemical shifts of the protons are presented in Fig. C.7. The protons of the [BMIM]OTf are only involved in minor low-field shifts of around 0.2 ppm. Apparently, only the alkyl chains are affected by the absorption of NO, suggesting that the imidazolium-part is not or only weakly involved in the 'coordination' of NO. The overall small proton shifts observed here are in agreement with the weak interaction previously between NO and [BMIM]OTf, e.g. in the reversible absorption experiments and Raman spectroscopy.
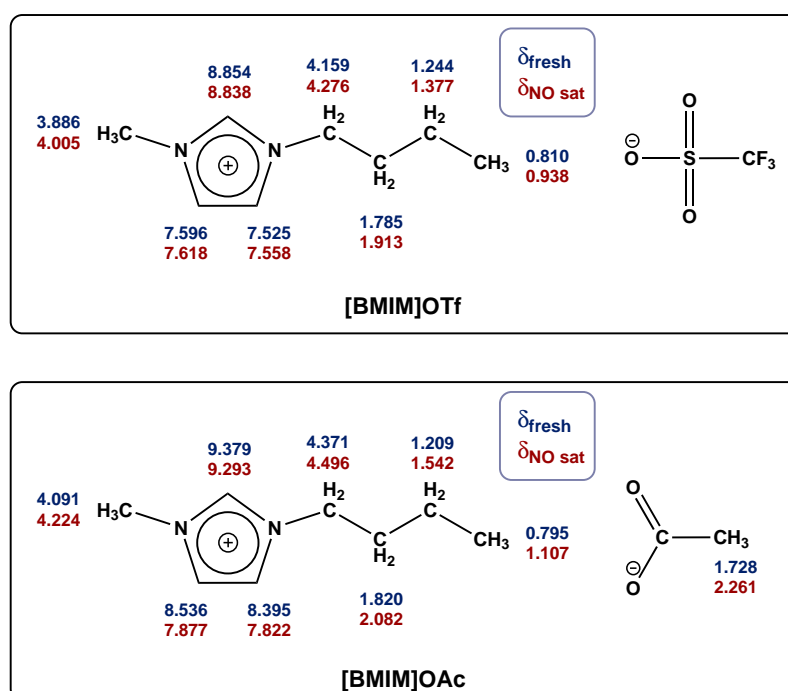

Fig. C.7: ^{1}H-NMR chemical shifts before and after NO-absorption. Experimental description in section A.1.7

In contrast, saturating the [BMIM]OAc with NO results in somewhat larger proton shifts of the both the acetate anion and the cation, implying that both ions are involved in the strong

sorption of nitric oxide. Moreno et al. [182] performed a NMR study on the effect of water on the [BMIM]BF$_4$. Even at high water loadings (mole fraction 0.36) they report of almost unaltered chemical shifts. Only in the case of the singlet imidazolium proton, a small shift was observed of around 0.2 ppm. Thus, even if small amounts of water is present in the IL (as implied by Raman spectroscopy), it would not induce such a significant shift as observed in the case of NO-saturated [BMIM]OAc. Hence, the dramatic impact on the protons can only be due to the presence of NO in the IL.

After saturation in NO, a new low-field peak was observed in the proton NMR spectra for both ILs. In the case of the NO-saturated [BMIM]OAC, the singlet was located at $\delta = 14.489$ ppm, and for the [BMIM]OTf at $\delta = 11.951$ ppm. The two singlets could be attributed to a weakly bound proton, maybe involving a NO molecule ("HNO").

List of publications

D

List of included publications

Paper 1 • *Structural characterization of 1,1,3,3-tetramethylguanidinium dichromate*
Johannes Due-Hansen, Kenny Ståhl, Soghomon Boghosian, Anders Riisager, Rasmus Fehrmann, *Dalton Transactions*, **2010** (submitted)

Paper 2 • *Pore design of pelletised VO_x/ZrO_2-SO_4/Sepiolite composite catalysts*
Søren B. Rasmussen, Johannes Due-Hansen, Malcolm Yates, Mirza Villaroel, F. Javier Gil Llambías, Rasmus Fehrmann, Pedro Ávila, *Studies in Surface Science and Catalysis*, **2010** (accepted)

Paper 3 • *SCR activity of conformed CuO_x/ZrO_2-SO_4 catalysts*
Søren B. Rasmussen, Malcolm Yates, Johannes Due-Hansen, Pedro Ávila, Rasmus Fehrmann, *Studies in Surface Science and Catalysis*, **2010** (accepted)

Paper 4 • *Multidisciplinary Determination of the Phase Distribution in the $VO_X-ZrO_2-SO_4$-Sepiolite Catalytic System (Distribución de las Fases en el Sistema $VO_X-ZrO_2-SO_4$-Sepiolita Determinada Por Varios Metódos)*
Søren B. Rasmussen, Johannes Due-Hansen, Mirza Villaroel, F. Javier Gil-Llambías, Rasmus Fehrmann, Pedro Ávila, *XXII CICAT*, **2010** (accepted for oral + paper)

Paper 5 • *Impact of support and potassium-poisoning on the V_2O_5-WO_3/ZrO_2 catalyst performance in ammonia oxidation*
Johannes Due-Hansen, Arkady L. Kustov, Claus Hviid Christensen, Rasmus Fehrmann, *Catalysis Communications*, 10, **2009**, 803–806

Miscellaneous publications

- *Vanadia-based SCR catalysts supported on tungstated and sulfated zirconia: Influence of doping with potassium*
  Johannes Due-Hansen, Soghomon Boghosian, Arkady Kustov, Peter Fristrup, George Tsilomelekis, Kenny Ståhl, Claus Hviid Christensen, Rasmus Fehrmann *Journal of Catalysis*, 251, **2007**, 459–473

- *Fe-BEA Zeolite Catalysts for NH_3-SCR of NO_X*
  Anne Mette Frey, Selcuk Mert, Johannes Due-Hansen, Rasmus Fehrmann, Claus Hviid Christensen, *Catalysis Letters*, 130, **2009**, 1–8

- *On the redox behaviour of the V_2O_5-WO_3/TiO_2 SCR at moderate temperatures: Influence of Hydrogen-Oxygen Treatment as observed by Operando & in-situ Spectroscopy at 250°C*
  Johannes Due-Hansen, Søren Birk Rasmussen, Ewelina Mikolajska, Miguel Angel Bañares, Pedor Ávila, Rasmus Fehrmann, (manuscript)

- *Biobrændsel - et varmt alternativ*
  Anne Mette Frey, Asbjørn Klerke, Johannes Due-Hansen, Claus Hviid Christensen, Nye Kemiske Horisonter, DTU, Litotryk Svendborg A/S, **2007**

- *Alkali Resistant Catalyst*
  Søren Birk Rasmussen, Arkady Kustov, Rasmus Fehrmann, Johannes Due-Hansen, Patent (WO/2008/037255), September **2007**

Structural characterization of 1,1,3,3-tetramethylguanidinium dichromate

Johannes Due-Hansen, Kenny Ståhl, Soghomon Boghosian,
Anders Riisager, Rasmus Fehrmann

Paper

1

Structural characterization and catalytic properties of 1,1,3,3-tetramethylguanidinium dichromate

Johannes Due-Hansen[*],[a], Kenny Ståhl[a], Soghomon Boghosian[b], Anders Riisager[a], Rasmus Fehrmann[*],[a]

[a] Department of Chemistry, Centre for Catalysis and Sustainable Chemistry, Technical University of Denmark, 2800 Lyngby, Denmark

[b] Department of Chemical Engineering, University of Patras and FORTH/ICE-HT, GR-26500 Patras, Greece

[*] Corresponding authors

e-mail jdh@kemi.dtu.dk, tel +45-4525-2363 (J. Due-Hansen),

e-mail rf@kemi.dtu.dk, tel +45-4525-2389 (R. Fehrmann)

Abstract

The structure of 1,1,3,3-tetramethylguanidinium dichromate was determined from powder X-ray diffraction data. The compound crystallizes in the monoclinic system (space group $P2_1/n$) with a = 10.79679 (19) Å, b = 11.7580 (2) Å, c = 8.15076 (14) Å, β = 109.5247 (6)°. The structure consists of dichromate anions ($Cr_2O_7^{2-}$) stabilized by tetramethylguanidinium cations ($NH_2C(N(CH_3)_2)_2^+$ or $TMGH^+$). Phase transitions of $[TMGH]_2Cr_2O_7$ were determined by differential scanning calorimetry, thermal gravimetric analysis and *in situ* Raman spectroscopy, where the decomposition of the matrix into CrO_x was found at 171–172°C. Further heat treatment to above 400°C resulted in formation of the thermodynamically stable Cr_2O_3, most likely with the $TMGH^+$ cation as reductant. The catalytic activity of $[TMGH]_2Cr_2O_7$ supported on TiO_2 anatase in the selective catalytic reduction (SCR) of nitrogen oxide was also investigated, however only moderate activity was observed in the temperature range 100–400°C compared to the activity of e.g. vanadia supported on titania.

1. Introduction

Selective catalytic reduction (SCR) plays an important role in the removal of nitrogen oxides from flue gases generated by fuel combustion in stationary sources. The traditional, and widely commercialized, catalyst for the SCR reaction is composed of V_2O_5 and WO_3 or MoO_3 supported on TiO_2 which is operated in the temperature window of 300–400°C [1]. Due to the relatively high operating temperatures the catalyst unit is often placed upstream of cleaning units (e.g. desulfurizer, electrostatic particle remover) to avoid costly reheating of the flue gas. This environment, however, promotes deactivation of the catalyst because of high concentrations of dust. Plac-

ing the SCR unit downstream of the desulfurization and dust removal units would thus solve the deactivation, but also lower the temperature of the flue gas and consequently the activity of the catalyst, since the low-temperature activity of the traditional SCR catalysts is negligible. Accordingly, efforts have been made to develop catalysts operating in the range 80-280°C [2–8], which would render placement of the SCR unit possible in the tail end after the desulfurizer and particulate control installations.

Recent studies have shown that chromium and/or manganese oxides, such as MnO_x [9], MnO_x/TiO_2 [10], Fe-Mn-TiO$_x$ [8], MnO_x-CeO_2 [11], exhibit good low-temperature SCR potential, but their N_2-selectivity and sulfur resistance need to be improved. Sreekanth et al. [12] investigated the NO conversion over a range of mono and bimetallic transitions metals, namely Cr, Mn, Cu, Mn-Cu and Mn-Cr, and found that the monometallic catalysts, Cr, Mn and Cu yielded better SCR performance than the mixed oxides, especially at low-temperature (100°C). Schneider et al. [13] reported higher selectivity to N_2 (>90%) for a range of titania-supported chromia catalysts (i.e. CrO_2, Cr_2O_3, CrOOH), but the catalytic performance, such as N_2O selectivity, was very sensitive to the phase of the chromium oxide.

In this paper we have examined the low-temperature SCR activity of a newly characterized compound of chromium, tetramethylguanidinium dichromate, which was first reported by Kim et al. [14] for oxidation of alcohols. The physiochemical properties of 1,1,3,3-tetramethylguanidine are well documented, e.g. by Anderson and Hammer [15], but the 1,1,3,3-tetramethylguanidinium dichromate salt has not been structurally characterized. The crystal structure of the resembling guanidinium dichromate has been reported by Wajsman et al. [16]. However, addition of four methyl groups to the arrangement changes the structure and there are therefore some differences in the matrix.

2. Experimental section

2.1 Synthesis

$[TMGH]_2Cr_2O_7$ was synthesized by mixing 1,1,3,3-tetramethylguanidine, TMG (Aldrich, 99%) with absolute ethanol in the molar ratio 1:5 (slightly exothermic). Equimolar amounts of ammonium chromate (Fluka, 99%) were added to the solution under stirring, resulting in evolution of ammonia gas due to the reaction(1)

$$2\,TMG + 2\,(NH_4)_2CrO_4 \longrightarrow [TMGH]_2Cr_2O_7 + 4\,NH_3(g) + H_2O \tag{1}$$
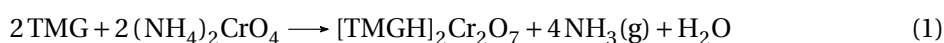
whereby the solution changed color from yellow to orange within about 30 minutes indicative of transformation of the chromate to dichromate. To ensure complete reaction the slurry was stirred overnight before the ethanol and water was subsequently removed under reduced pressure with a rotary evaporator. Finally the residue was dried in a vacuum oven at 60°C.

The preparation of 20 wt% $[TMGH]_2Cr_2O_7$ supported on titania (8.2 mol% Cr/TiO$_2$) was performed by initial mixing of TMG, $(NH_4)_2CrO_4$ and absolute ethanol in a molar ratio of 1:1:35. To the resulting slurry, TiO$_2$ (Aldrich, nanopowder, 99.7% anatase) was then added and the mixture

stirred overnight before solvent and water were removed under reduced pressure in a rotary evaporator.

2.2 Characterization

FTIR spectra were obtained at room temperature in KBr on a Perkin Elmer 1710 FTIR spectrometer. All samples, in the KBr tablet, were dried overnight at 100°C before recording of the spectra. 32 consecutive scans in the range 4000–400 cm^{-1} were performed at 2 cm^{-1} resolution.

Powder diffraction data was collected on a Huber G670 Guinier camera using $CuK\alpha_1$ radiation. The sample were placed in a thin layer on scotch tape and rotated during data collection. Data were collected for 4h in the range 3-100° in steps of 0.005° in 2θ. The pattern were indexed by the program ITO [17] and the crystal structure solved by EXPO [18,19]. The structure was refined by WINPOW (a local variation of LHMP) [20]. Hydrogen positions were added in calculated positions and the methyl group hydrogens were given large thermal parameters to mimic rotational disorder. Moreover, as the dichromate part was found disordered the bridging O4 was split in two positions (the average position would give a 180° Cr-O4-Cr angle). The individual disordered positions of O1, O2 and O3 could not be resolved, but showed increased thermal parameters. The methyl groups were found rotated out of the central plane to minimize the H-H interactions in agreement with related tetramethylguanidinium structures [21].

Thermal stability of the samples was determined by thermogravimetry (simultaneous TGA-DSC, Netzsch, model STA 409) with a heating rate of 20°C/min under a nitrogen atmosphere. The decomposition gases were further analyzed with mass spectrometry.

For recording of the Raman spectra of $[TMGH]_2Cr_2O_7/TiO_2$, approximately 100 mg of the sample was pressed into a wafer and mounted on the sample holder of an *in situ* Raman CSTR-like optical cell. The spectra were recorded at various temperatures in the range 25–400°C under flowing O_2 using the 488.0 nm line of a Spectra Physics Stabilite 2017 Ar^+ laser operated at a power of 40 mW, collected on the sample by a slightly defocused cylindrical lens in order to reduce sample irradiance. The scattered light was collected at 90°, analyzed with a 0.85 Spex 1403 double monochromator and detected by a -20°C cooled RCA PMT equipped with EG&G photon counting electronics [22].

SCR activities were measured with a Thermo Environmental chemiluminescence NO_x and NH_3-analyzer, model 17C. About 40 mg of catalyst (pressed at 2 tons, Ø = 13mm, fractionated to 180-300 µm) were fixed in a quarts plug flow reactor with a total ambient flow of 300 ml/min containing 1000 ppm NO, 1100 ppm NH_3, 3.5% O_2, 2.3% H_2O in He. The gas hourly space velocity (GHSV) was 70,000 h^{-1}. The catalysts were diluted with 125 mg quartz 180-300 µm particles (Merck, 99.95%) to ensure a cylindrical shaped catalyst bed with plug-flow conditions. The catalytic activity was reported as the first-order rate constant k, in the first order removal of NO using the definition reported previously [22].

3. Results and Discussion

3.1 Characterization

The synthesized $[TMGH]_2Cr_2O_7$ was characterized by various techniques, such as XRD, DSC, TGA and FTIR, to support the structure determination.
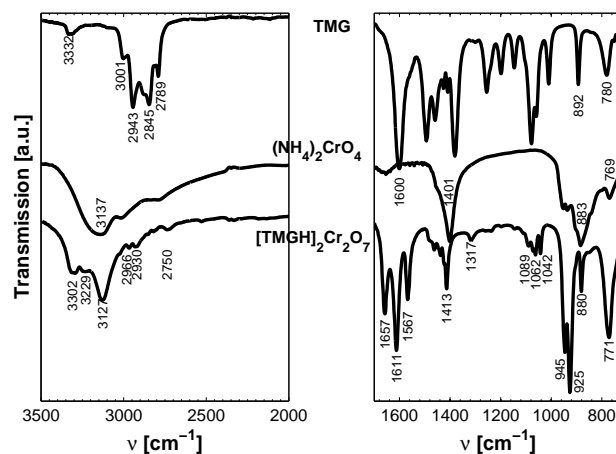

Figure 1. FTIR spectra of $[TMGH]_2Cr_2O_7$ and the synthesis-precursors

The infrared spectral data of $[TMGH]_2Cr_2O_7$ in Figure 1 showed that the chromate bands of the precursor $(NH_4)_2CrO_4$ at 951, 936, 883 and 769 cm^{-1} were replaced with characteristic bands for dichromate, i.e. 945, 925, 880, 771 cm^{-1} [23] in the product, as expected. The same bands (except the band at 771 cm^{-1}) were also determined by Kim et al. [14]. The elimination of the >N-H stretch vibration around 3330 cm^{-1} of TMG and the broad N-H bands around 3140 cm^{-1} of NH_4^+ in ammonium chromate further confirmed full protonation of TMG occurred during synthesis of $[TMGH]_2Cr_2O_7$.

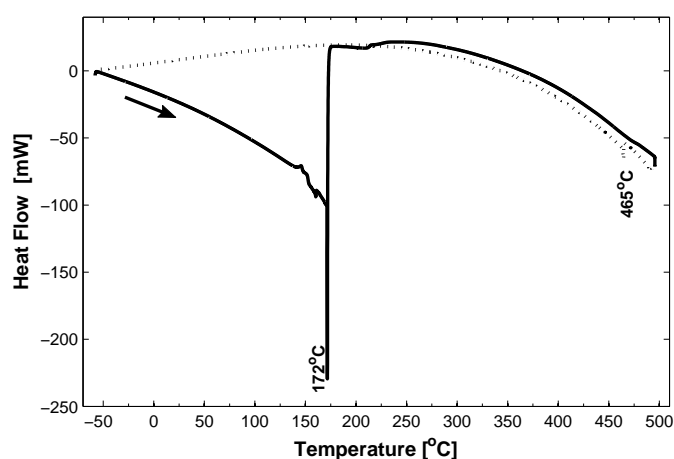Figure 2. DSC of $[TMGH]_2Cr_2O_7$. Heating rate 5°C/min in Ar

Besides the bands from dichromate, the $[TMGH]_2Cr_2O_7$ spectra also contained an additional imine (C=N-R$_2$) band at 1657 cm^{-1} [24]. This suggests the electrons to be delocalized between all three nitrogen atoms and the sp^2 carbon instead of being confined to one nitrogen atom as

in pure TMG.

[TMGH]$_2$Cr$_2$O$_7$ was investigated by DSC analysis, as presented in Figure 2. When heating from -60°C to 172°C a continuous endothermic heat flow was found, suggesting a slow phase transformation or crystal reorganization. At 172°C a distinctive energy uptake was observed for the crystal due to decomposition of the salt into organic residues and CrO$_x$. The irreversible decomposition of the [TMGH]$_2$Cr$_2$O$_7$ was confirmed by the DSC profile upon cooling from 500°C to -60°C , since no phase transitions occurred here.
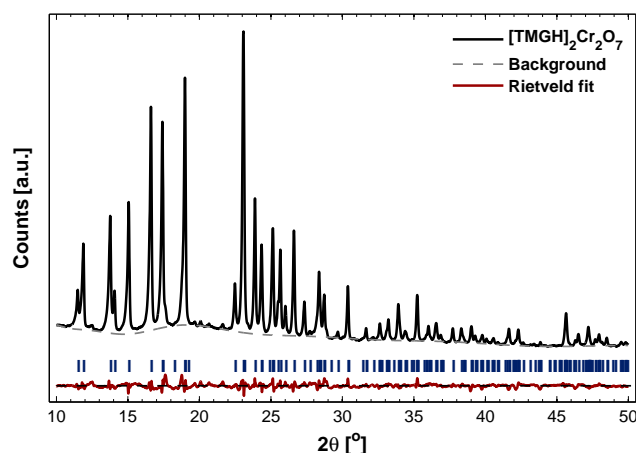

Figure 3. XRD diffractogram of [TMGH]$_2$Cr$_2$O$_7$ and the difference pattern from the Rietveld refinement. Markers indicate Kα_1 Bragg positions

The results of the Rietveld refinement of the powder diffraction data of [TMGH]$_2$Cr$_2$O$_7$ are displayed in Figure 3 (2θ = 10-50°). Here a good agreement between the experimental and fitted data was found for the monoclinic cell. The cell dimensions found through refinement are collected in Table 1.

Table 1. Crystal data

Chemical Formula	(C$_5$H$_{14}$N$_3$)$_2$Cr$_2$O$_7$
Formula mass	448.372 g/mol
Crystal system	Monoclinic
Space group	P2$_1$/n
Z	2
a	10.79679 (19) Å
b	11.7580 (2) Å
c	8.15076 (14) Å
α,γ	90°
β	109.5247 (6)°
V	975.23 (3) Å3

The determined crystal structure of [TMGH]$_2$Cr$_2$O$_7$ is presented in Figure 4 with both of the two possible O4 positions depicted (more projections of the structure are collected in Supplementary Material). Note that the anion therefore is not depicted correctly from a stoichiometric point of view, but should be viewed as two different configurations, presented simultaneously. Thus, the average position of the bridging oxygen in the Cr1-O4-Cr1 is the 180° configuration.

The guanidine part of the tetramethylguanidinium cation group had a planar configuration due to the C1=N3 double bond. However, the terminal C1-N3 bond distance appeared rather long (1.595 (11) Å), which is probably due to the delocalization of the π-electrons over the C-N bonds, in accordance with observations from FTIR spectra. Single-crystal XRD studies (i.e. higher resolution) of [TMGH]$_3$Sb$_2$Br$_9$ done by Bujak and Zaleski [21], report of a double bond length of 1.330 (7) Å.
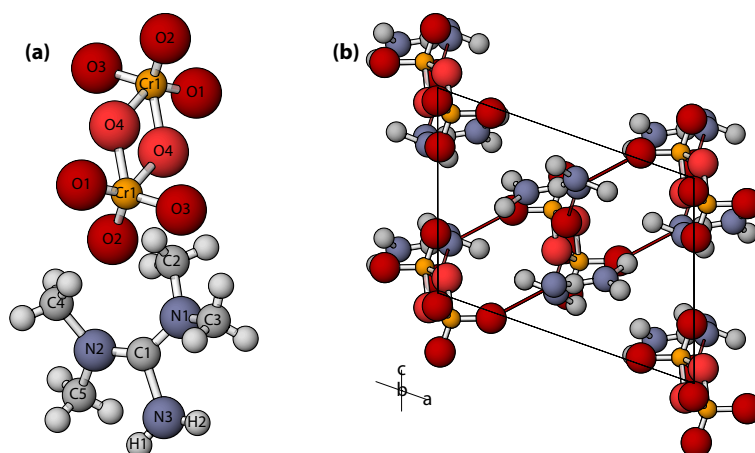

Figure 4. (a) The atom labels of Cr$_2$O$_7^{2-}$ anion displayed with the bridging O4 atom in two possible positions and the tetramethylguanidinium cation with calculated hydrogen atoms. (b) Crystal structure and hydrogen bonds of [TMGH]$_2$Cr$_2$O$_7$ (without hydrogen atoms) viewed along the b-axis projection

For the Cr$_2$O$_7^{2-}$ group, the length of the Cr-O bond with the bridging O4 atom was 1.725 (9) Å and thus longer than the terminal Cr-O bonds which were in the range 1.414-1.581 Å. Hence, the dichromate group configuration was comparable with the monoclinic β-K$_2$Cr$_2$O$_7$ system, where the length of the bridging oxygen atom in Cr-O has been reported to be 1.7819 Å and the cornering oxygens to be somewhat shorter in the range of 1.605-1.624 Å [25]. The reason for the shorter bond length from chromium to a cornering oxygen atom could be a result of displacement of charge from the dichromate polyhedra to [TMGH]$^+$ through hydrogen bonds.

The hydrogen bonds H1···O2 and H2···O3 cross-linked the iminium-part of [TMGH]$^+$ with dichromate ions in the (101) plane, thus forming layers connected by ionic and van der Waal's bonds (Figure 4b). A similar cation-anion linkage was previously reported for [TMGH]$_3$Sb$_2$Br$_9$ [21]. The hydrogen bond lengths were 1.998 Å (N3-H1···O2 angle: 150.5°) and 2.018 Å (N3-H2···O3 angle: 153.8°), respectively. The hydrogen bonds were thus of same strength as those found in liquid water. This agrees well with FTIR spectra of [TMGH]Cr$_2$O$_7$ in Figure 1, where a splitting of the N-H bonds was observed at 3302 and 3229 cm^{-1}.

The weight loss curves (TGA) for the [TMGH]$_2$Cr$_2$O$_7$, TiO$_2$-supported [TMGH]$_2$Cr$_2$O$_7$ and reference materials are shown in Figure 5. The corresponding DSC results are presented in Supplementary Material. The thermal decomposition of [TMGH]$_2$Cr$_2$O$_7$ took place in two steps. The first decomposition occurred at 171°C , as also observed in Figure 2, where the dichromate possibly formed intermediate CrO$_3$ [26]. During the second weight reduction from 171-400°C , the remaining organic residues was decomposed and CrO$_3$ reduced to Cr$_2$O$_3$.
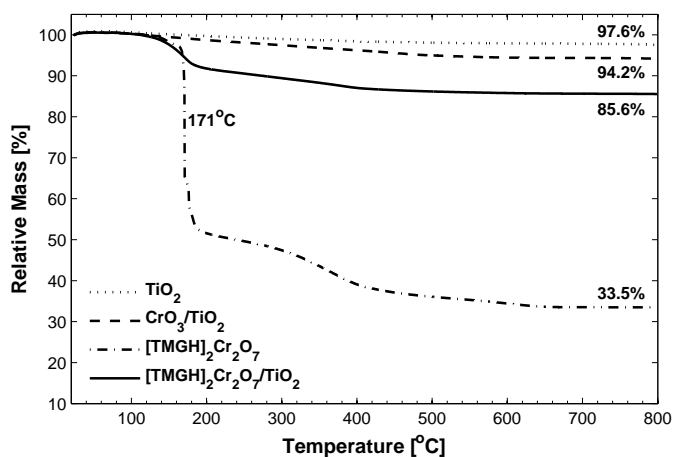
Figure 5. Relative TGA profiles and the remaining weight at 800°C

Assuming that the final product after thermal treatment of $[TMGH]_2Cr_2O_7$ is the thermodynamically most stable Cr_2O_3, then the mass loss would result in a final weight of 33.9 wt% (M_{Cr2O3} x $\frac{m_{[TMGH]2Cr2O7}}{M_{[TMGH]2Cr2O7}}$) which complies very vell with the observed 33.5 wt%. Hence, a redox reaction took place with the reduction of chromium and a resulting oxidation of the organic material. Similar argument for the other samples, and exploiting that the weight loss of TiO_2 was known, namely 2.4 wt%, results in the calculated yields a) CrO_3/TiO_2: 93.7 wt%, b) $[TMGH]_2Cr_2O_7/TiO_2$: 84.9 wt%. Thus, all TGA-results were within about 1% of the expected values.

The first decomposition of $[TMGH]_2Cr_2O_7$ at 171°C was accompanied by the mass spectroscopy signales m/z = 28, 30, 44, 72, suggesting liberation of some TMG synthons ($C=NH_2^+$, m/z = 28, $N(CH_3)_2$, m/z = 44, $[NH_2CN(CH_3)_2]$, m/z = 72) as expected. Possibly CO_2 (m/z = 44) was also formed in connection with the reduction of Cr(VI) to Cr(III).

Figure 6 shows sequential in situ Raman spectra obtained with increasing temperature for a fresh $[TMGH]_2Cr_2O_7/TiO_2$ catalyst sample under flowing O_2 gas. At temperatures up to 150°C (i.e. below the decomposition temperature of 171°C only the 638 cm^{-1} (E_g) band due to TiO_2-anatase is seen in the recorded region of the Raman spectra (550–1100 cm^{-1}). Starting from 200°C the Raman spectra are gradually being transformed and new bands emerge in the Cr-O stretching region (i.e. a broad band at 850 cm^{-1} and a band at 1000 cm^{-1}), which are reminiscent of the respective spectral features of the deposited chromia phase of chromia/titania catalysts. Thus, a progressive deconstruction of the organic framework of $[TMGH]_2Cr_2O_7$ and liberation of a deposited $(CrO_x)_n$ phase take place. The Raman "snapshots" obtained at higher temperatures show that the bands due to the deposited chromia phase gain intensity relative to e.g. the 635 cm^{-1} (E_g) anatase band that undergoes (as expected) a slight red shift with increasing temperature. At 400°C the organic matrix is almost completely decomposed (see Figure 5), leaving a chromia phase deposited on titania corresponding to a loading of 8.2 mol% Cr/TiO_2 (5.5 wt% Cr/TiO_2). The final spectrum obtained at 400°C (after in situ calcination in the Raman cell) exhibits a band due to Cr=O stretching at 999 cm^{-1} (with a shoulder at 1020 cm^{-1}) and a much broader band at 850 cm^{-1} due to Cr-O-Cr functionalities [27,28]. Although the occur-
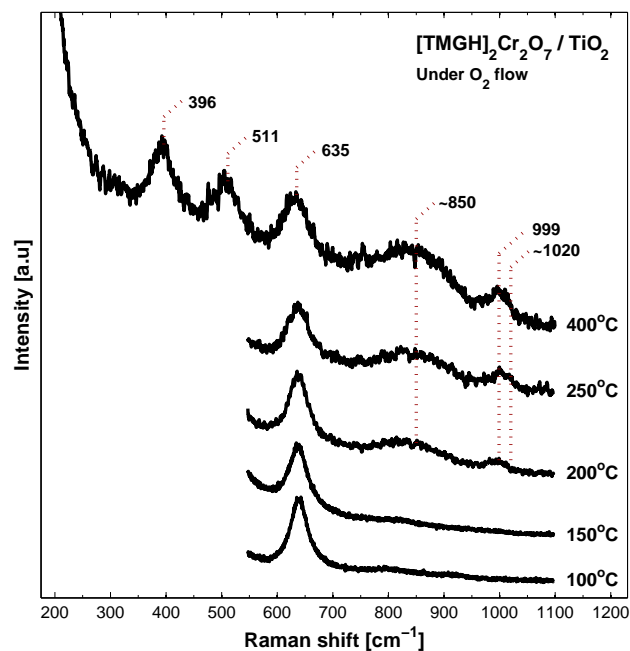
Figure 6. Sequential *in situ* Raman spectra of $[TMGH]_2Cr_2O_7/TiO_2$ obtained under flowing O_2 at temperatures as indicated. Laser wavelength, $\lambda_0 = 488.0$ nm; time constant, $\tau = 4$ s; laser power, w = 40 mW; resolution, $7\ cm^{-1}$

rence of two bands in the Cr=O stretching region (separated by 20 cm^{-1}) may indicate a di-oxo $Cr(=O)_2$ configuration [29], it has been shown that the Raman data combined with $^{18}O/^{16}O$ vibrational isotope effects are consistent with a mono-oxo configuration and an existence of two types of mono-oxo species [30]. Thus, the deposited chromia phase consists of two distinct mono-oxo species, namely a monochromate and associated (polymeric) chromates (bands at 999 cm^{-1} and at 1020 cm^{-1} due to Cr=O and at 850 cm^{-1} due to Cr-O-Cr functionalities of the polychromates). Although, by general consensus the high frequency Cr=O band is assigned to the monochromate [27,30] there have been also cases in which the high frequency Cr=O band has been ascribed to the polychromates [28]. Bands observed at 396 and 511 cm^{-1} originate from the TiO_2 anatase support, corresponding to the Raman vibrating modes B_{1g} and A_{1g}, respectively [31].

3.2 SCR reactions

The performance of $[TMGH]_2Cr_2O_7/TiO_2$ (8.2 mol% Cr/TiO_2) in conversion of NO by reduction with ammonia is depicted in Figure 7 along with a CrO_3/TiO_2 (4.3 mol% Cr/TiO_2) reference catalyst. Above 200°C both samples exhibited increased NO conversion until 300°C, whereas the degree of conversion decreased at temperatures from about 325°C. The achieved low-temperature activity was considerably higher than reported by Schneider et at. [13] for various chromium oxides on titania (10 wt% chromium oxide content), where no conversion of NO were detected below 350°C, even with a relatively low GHSV at 28,000 h^{-1}.
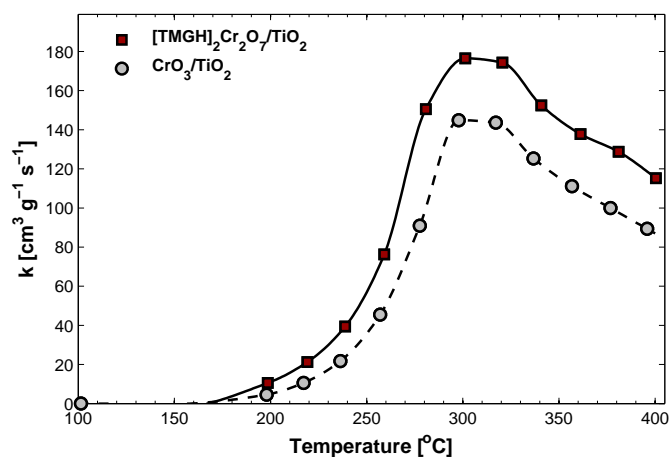
Figure 7. The SCR performance as first-order rate constant, k, versus temperature

At all temperatures $[TMGH]_2Cr_2O_7/TiO_2$ displayed higher SCR activity than CrO_3/TiO_2, which partly can be explained by the higher loading of chromium. Furthermore, it is noteworthy that no SCR activity of $[TMGH]_2Cr_2O_7/TiO_2$ was detected at temperatures below the decomposition temperature at 171°C, thereby making the $[TMGH]_2Cr_2O_7/TiO_2$ unsuitable for SCR catalysis, although a dispersive effect of the chromium species due to the $[TMGH]_2Cr_2O_7$ can be imagined. However, after decomposition the sample exhibited activity in the reduction of NO with fairly high selectivity, resulting in formation of less than 2% NO_2 at temperatures below 325°C. At higher temperatures the chromium-based catalysts exhibited though considerable oxidation of both NO and NH_3 ($\Delta[NH3]/\Delta[NO]$ ratio presented in supplementary material), and seems thus to be more promising candidates for oxidation reactions under normal SCR operation conditions.

4. Conclusion

The crystal structure of 1,1,3,3-tetramethylguanidinium dichromate was found to consist of chromate dimers charge counter-balanced by tetramethylguanidinium cations. The matrix decomposed at 171–172°C into chromium oxides, whereas further thermal treatment at temperatures up to 700°C resulted in formation of Cr2O3.

The activity in the SCR process was investigated by supporting 20 wt% of $[TMGH]_2Cr_2O_7$ on TiO_2. Minor conversion of NO was found only at temperatures above ≈170°C (after decomposition of the salt) and thus attributed to the activity of formed chromium oxides. Furthermore, above ≈325°C the $[TMGH]_2Cr_2O_7/TiO_2$ functioned as an oxidation catalyst which oxidized the NH_3 to nitrogen oxides, thus making it unsuited as SCR catalyst at normal operation conditions.

Acknowledgments

References

1. G. Busca, L. Lietti, G. Ramis, F. Berti, Appl. Catal. B: Environ., 1998, **18**, 1-36

2. M. Inomata, A. Miyamoto, Y. Murikami, J. Catal., 1980, **62**, 140-148

3. F.J.J.G. Janssen, F.M.G. van den Kerkhof, H. Bosch, J.R.H. Roos, J. Phys, Chem., 1987, **91**, 5921-5927

4. L. Singoredjo, R. Korver, F. Kapeijn, J. Moulijn, Appl. Catal. B: Environ., 1992, **1**, 297-316

5. S.C. Wood, Chem. Eng. Prog., 1994, 9**0**, 32-38

6. J.A. Dumesic, N.-Y. Topsøe, H. Topsøe, T. Slabiak, J. Catal., 1996, **163**, 409-417

7. Z. Zhu, Z. Liu, S. Liu, H. Niu Appl. Catal. B: Environ., 1999, **23**, L229-L233

8. F. Liu, H. He, Y. Ding, C. Zhang, Appl. Catal. B: Environ., 2009, **93**, 194-204

9. M. Kang, E.D. Park, J.M. Kim, J.E. Yie, Appl. Catal. A: General, 2007, **327**, 261-269

10. J. Li, J. Chen, R. Ke, C. Luo, J. Hao, Catal. Commun., 2007, **8**, 1896-1900

11. M. Casapu , O. Kröcher , M. Elsener, Appl. Catal. B: Environ., 2009, **88**, 413-419

12. P.M. Sreekanth, D.A. Peña, P.G. Smirniotis, Ind. Eng. Chem. Res., 2006, **45**, 6444-6449

13. H. Schneider, M. Maciejewski, K. Köhler, A. Wokaun, A. Baiker, J. Catal., 1995, **157**, 312-320

14. S. Kim, D.C. Lhim, P.H. Lee, Bull. Korean Chem. Soc., 1986, **7**, 86-87

15. M.L. Anderson, R.N. Hammer, J. Chem. Eng. Data, 1967, **12**, 442-447

16. E. Wajsman, M. Cygler, M.J. Grabowsko, A. Stepien, Roczniki Chemii, Ann. Soc. Chim. Polonorum, 1976, **50**, 1587-1592

17. J.W. Visser, J. Appl. Cryst., 1969, **2**, 89-95

18. A. Altomare, G. Cascarano, C. Giacovazzo, M.C. Burla, G. Polodori, G. Camalli, J. Appl. Crystallogr., 1994, **27**, 435-436

19. A. Altomare, M.C. Burla, G. Cascarano, C. Giacovazzo, A. Guagliardi, A.G.G. Moliterni, G. Polodori, J. Appl. Crystallogr., 1995, **28**, 842-846

20. C.J. Howard, R.J. Hill, AAEC (now ANSTO) Report M112, Lucas Heights Research Laboratory, Australia (1986)

21. M. Bujak, J. Zaleski, J. Acta Crystallogr., 2007, **E63**, m102-m104

22. J. Due-Hansen, S. Boghosian, A. Kustov , P. Fristrup, G. Tsilomelekis, K. Ståhl, C.H. Christensen, R. Fehrmann, J. Catal., 2007, **251**, 449-473

23. G. Socrates, Infrared and Raman Characteristic Group Frequencies, 3rd edition, John Wiley & Sons 2001

24. M. Hesse, H. Meier, B. Zeeh, Spectroscopic Methods in Organic Chemistry, Geirg Thieme Verlag Stuttgart, New York, 1997

25. S.V. Krivovichev, E.V. Kir'yanova, S.K. Filatov, P.C. Burns, Acta Cryst., 2000, **C56**, 629-630

26. D. de Wall, A.M. Heyns, J. Alloy and Compounds, 1992, **187**, 171-180

27. B. M. Weckhuysen, I. E. Wachs, J. Phys. Chem., 1996, **100**, 14437-14442

28. B. M. Weckhuysen, I. E. Wachs, R.A. Schoonheydt, Chem. Rev., 1996, **96**, 3327-3349

29. K. Nakamoto, Infrared and Raman Spectra of Inorganic and Coordination Compounds, 6th ed., Wiley, New York, 2009

30. B. M. Weckhuysen, I. E. Wachs, J. Phys. Chem. B, 1997, **101**, 2793- 2796

31. T. Ohsaka, F. Izumi, Y. Fujiki, J. Raman Spec., 1978, **7**, 321-324

Structural characterization and catalytic properties of 1,1,3,3-tetramethylguanidinium dichromate

Johannes Due-Hansen[1]**, Kenny Ståhl**[2]**, Soghomon Boghosian**[3]**, Anders Riisager**[4]**, Rasmus Fehrmann**[5]

April 24, 2010

Abstract

In the following is the supplementary results collected from the study of $[TMGH]_2Cr_2O_7$: Projections of the crystal structure along the a and c axis, the NO_2 selectivity and NH_3/NO ratio from the activity experiment, and the heat flow from the TGA-DSC experiment.
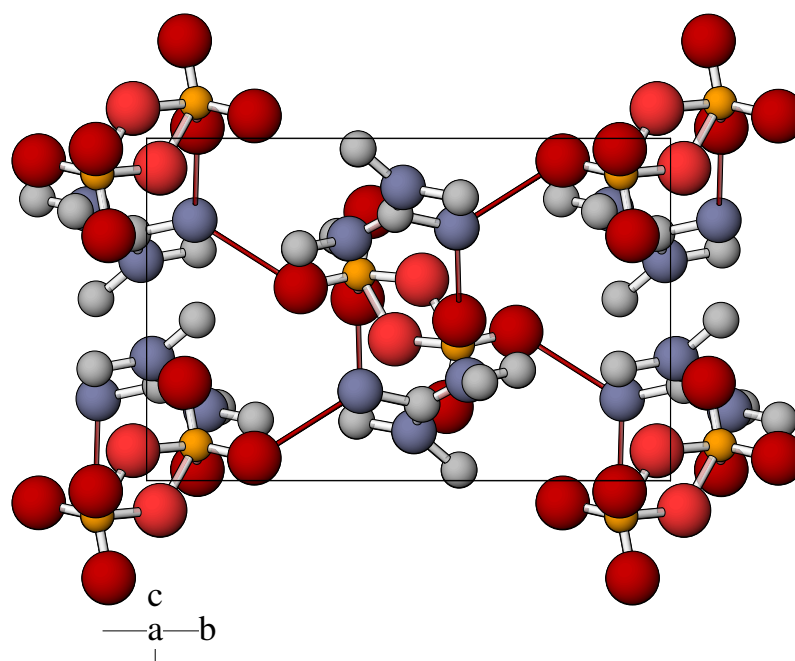
1. Crystal structure

Figure 1. Crystal structure and hydrogen bonds of $[TMGH]_2Cr_2O_7$ (without hydrogen atoms) viewed along the a-axis projection

---

[1] Department of Chemistry, Centre for Catalysis and Sustainable Chemistry, Technical University of Denmark, 2800 Lyngby, Denmark, Email:

[2] Department of Chemistry, Centre for Catalysis and Sustainable Chemistry, Technical University of Denmark, 2800 Lyngby, Denmark

[3] Department of Chemical Engineering, University of Patras and FORTH/ICE-HT, GR-26500 Patras, Greece

[4] Department of Chemistry, Centre for Catalysis and Sustainable Chemistry, Technical University of Denmark, 2800 Lyngby, Denmark

[5] Department of Chemistry, Centre for Catalysis and Sustainable Chemistry, Technical University of Denmark, 2800 Lyngby, Denmark, Email:
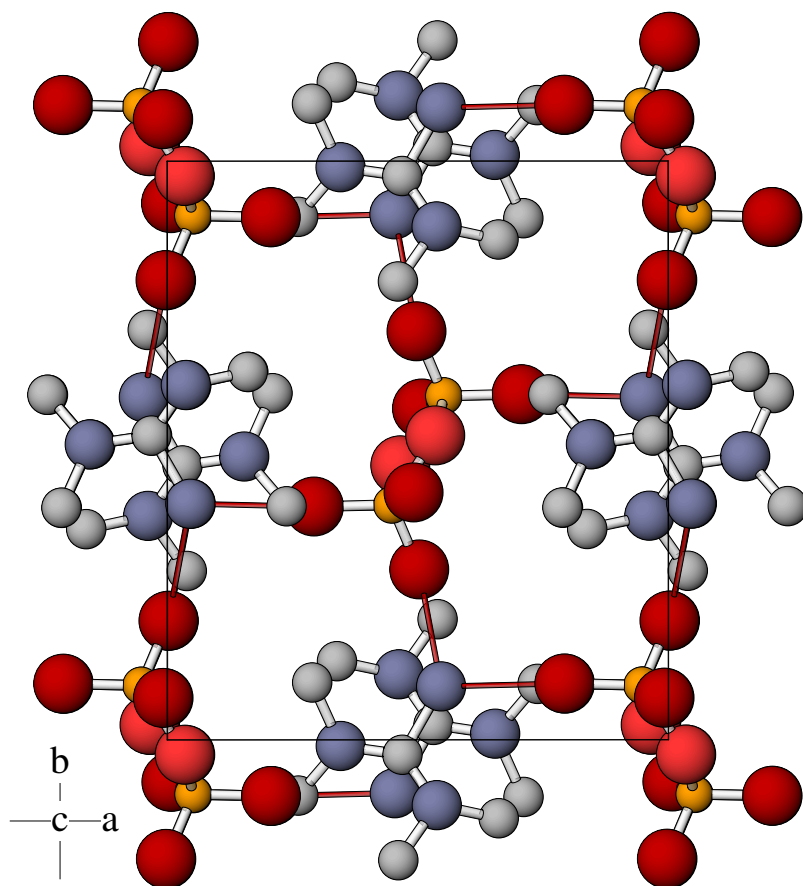
Figure 2. Crystal structure and hydrogen bonds of $[TMGH]_2Cr_2O_7$ (without hydrogen atoms) viewed along the c-axis projection
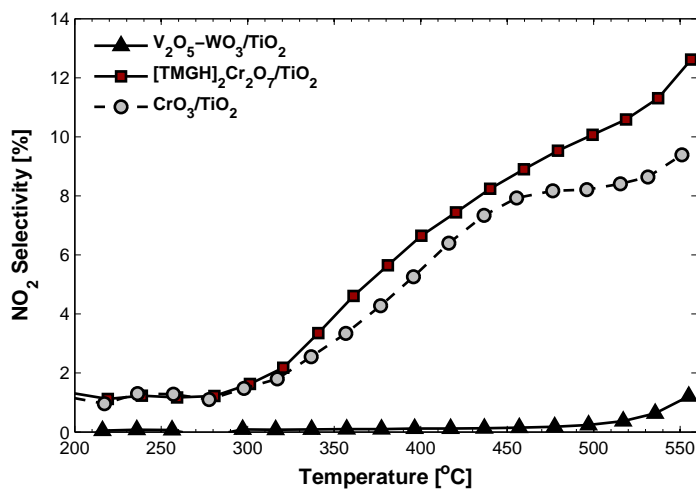
2. NO$_2$ selectivity and NH$_3$/NO ratio

Figure 3. NO$_2$ selectivity of CrO_3/TiO_2, $[TMGH]_2Cr_2O_7/TiO_2$. As reference a 3wt% $V_2O_5-WO_3/TiO_2$ is used
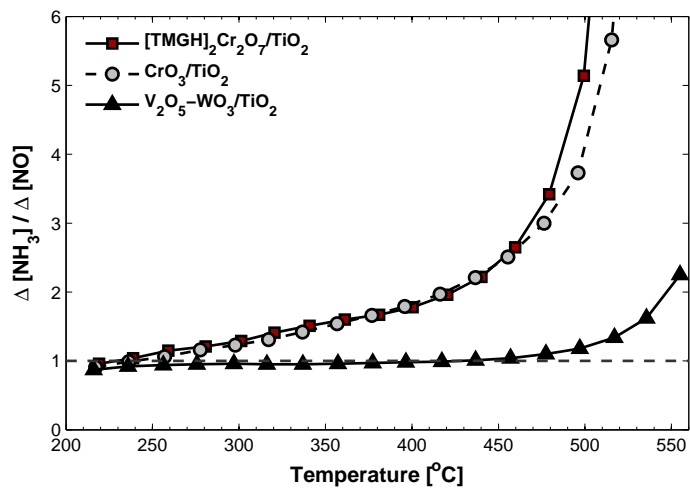
Figure 4. $\Delta[NH_3]/\Delta[NO]$ ratio of CrO_3/TiO_2, $[TMGH]_2Cr_2O_7/TiO_2$. As reference a 3wt% $V_2O_5-WO_3/TiO_2$ is used. A $\Delta[NH_3]/\Delta[NO]$ ratio above unity suggests catalytic oxidation of ammonia

3. DSC results from TGA-DSC experiment

Figure 5. Heat flow during TGA run

Pore design of pelletised VOx/ZrO2-SO4/Sepiolite composite catalysts

Søren B. Rasmussen, Johannes Due-Hansen,
Malcolm Yates, Mirza Villaroel, F. Javier Gil Llambías,
Rasmus Fehrmann, Pedro Ávila

Paper

2

Pore design of pelletised VO_X/ZrO_2-SO_4/Sepiolite composite catalysts

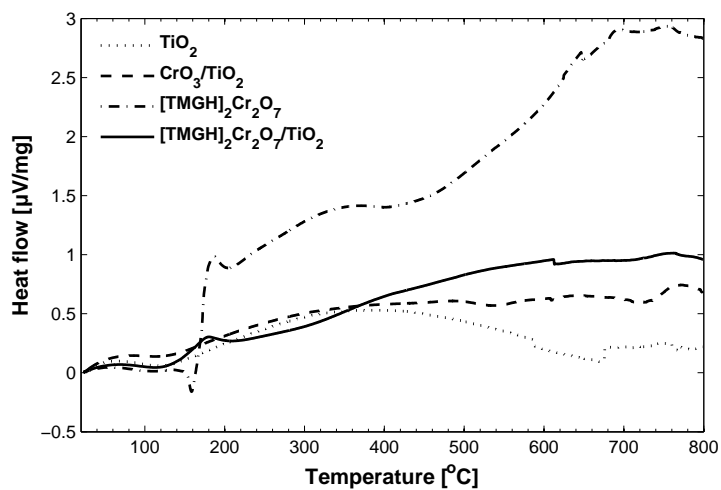Søren B. Rasmussen[a], Johannes Due-Hansen[b], Malcolm Yates[a*], Mirza Villaroel[c], F. Javier Gil Llambías[c], Rasmus Fehrmann[b], Pedro Ávila[a]

[a]*Instituto de Catálisis y Petroleoquímica (ICP), Consejo Superior de Investigaciones Científicas (CSIC), Calle Marie Curie 2, Cantoblanco, 28049 Madrid, Spain*
[b] *Centre for Catalysis and Sustainable Chemistry (CSC), Department of Chemistry, Technical University of Denmark (DTU), Bygn. 207, Kemitorvet, 2800 Kgs. Lyngby, Denmark*
[c] *Facultad de Química y Biología, Universidad de Santiago de Chile (USACH), Casilla 40, Correo 33, Santiago, Chile .*

Abstract

The NH_3-SCR activities of a series of extruded and calcined VO_X/ZrO_2-SO_4 - sepiolite catalysts were determined. The pore structures were heavily influenced by the clay content with macropore sizes ranging from 50 to >1000 nm. Mechanical strength and SCR activity measurements suggested that 25% w/w sepiolite is the optimal catalyst composition.

Keywords: Composite, extrusion, biomass, NH_3-SCR, ZrO_2-SO_4, sepiolite.

1. Introduction

The NH_3-SCR process is established as a robust and useful technique for the elimination of NO_X from off-gases. Commercially used V_2O_5-WO_3/TiO_2 catalysts reduce NO selectively to N_2 and H_2O by the following reaction:

$$O_2 + 4NO + 4NH_3 \rightarrow 4N_2 + 6H_2O \qquad (1)$$

The reaction involves two cycles, an acid cycle and a redox cycle [1,2]. Thus, the redox capacity of V(V) and V(IV) is of key importance, but also it is crucial to have sufficient acidic surface sites in order to chemisorb and administer NH_3 for the SCR reaction [3]. To comply with the Kyoto protocol, substitution of fossil fuels with biomass constitutes a practical, economical and environmentally viable solution, as biomass (straw, wood chips, saw dust *etc*.) attains its carbon from air during photosynthesis. Thus, biomass can be regarded as a CO_2 neutral fuel, and making attempts to increase the biomass content in energy production is of great interest. Though biomass combustion technology is relatively easy to implement in coal and oil-fired power plants, there are drawbacks. Among others, potassium fly ash particles, originating from the firing of biomass, poison the traditional SCR catalysts [4]. Thus, there is an urgent need for alternative potassium fly ash resistant catalysts. We report herein some special features of composite VO_X-ZrO_2-SO_4/sepiolite catalysts. The catalyst exhibit increased surface acidity as well as a shielding effect of the working catalyst, induced by the sepiolite clay enhancing the durability of the SCR catalyst while working under exposure to fly ash that contains potassium.
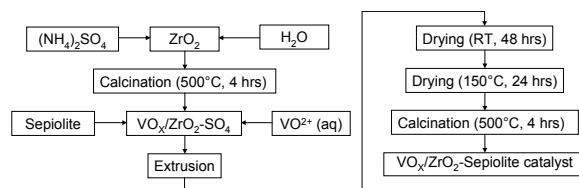
Figure 1: Synthesis route employed to produce scalable pelletised catalysts.

2. Experimental

2.1. Catalyst preparation

Melcat $Zr(OH)_4$ with a particle size $d_{50} = 15\mu m$ was used as the zirconia source and the ammonium sulphate was from Panreac (> 99%). The sulphated zirconia was prepared by impregnating 101.6 g of the zirconia hydroxide with 8.3 g $(NH_4)_2SO_4$ by the incipient wetness method. After digestion/drying in ambient conditions for 2 hours the samples were dried at 150°C for 3 hours. Calcination of the samples at 500°C for 4 hours in air was then performed by placing the material directly into a pre-heated furnace, in order to facilitate the preferred formation of metastable tetragonal phases. The catalysts were prepared by wet impregnation of $VOSO_4$ onto the sulphated zirconia, to produce a slurry that was allowed to settle for an hour under stirring. Thereafter sepiolite, α-sepiolite Pansil 100 supplied by Tolsa S.A. and water were added in the desired amounts to obtain a homogeneous paste with an adequate viscosity for extrusion from a 20 ml syringe with a 2 mm orifice. The extrudates were allowed to dry slowly, sealed in a wet atmosphere for 48 hours then dried overnight at 150°C in air. Calcination was carried out at 500°C for 4 hours in air. Finally the extruded material was broken into 3-5mm cylindrical pellets. The synthesis procedure is outlined in Figure 1.

2.2. Catalyst characterisation

The specific surface areas (S_{BET}), were obtained from the corresponding nitrogen adsorption isotherms at $-196°$ C using a Micromeritics Tristar apparatus, after application of the BET equation in the relative pressure range 0.05–0.35 $p/p°$. Prior to N_2 adsorption, the samples were outgassed overnight at 150°C to a vacuum of $<10^{-4}$ Pa to ensure a dry clean surface, free from any loosely held adsorbed species. The determination of the surface area of the external (A_{extern}), the cumulative pore volumes (V_P), and the macropore porediameters (D_{macro}) were complemented by mercury intrusion porosimetry (MIP) using a CE Instruments Pascal 140/240 and applying the Washburn equation for cylindrical pores [5], with the values recommended by the IUPAC of 141° and 484 mNm^{-1}, for the contact angle and surface tension of mercury.

Table 1: Textural characteristic of conformed catalysts.

Sample	8/8	7/8	6/8	5/8	4/8	3/8	2/8	1/8	0/8
Sepiolite (%)	100	87.5	75	62.5	50	37.5	25	12.5	0
A_{extern} (m^2/g)	118	128	140	146	146	144	143	143	152
S_{BET} (m^2/g)	130	136	140	145	148	147	146	145	156
V_p (cm^3/g)	0.325	0.305	0.291	0.278	0.260	0.234	0.215	0.195	0.201
D_{macro} (nm)	26	40	52	82	130	248	320	767	911

2.3. NO SCR with ammonia

The SCR activity measurements were carried out on crushed samples sieved to obtain fractions of 0.18–0.300 mm. These measurements were carried out in a fixed-bed reactor, with 10 mg of the catalyst loaded between two layers of inert quartz wool. The reactant gas composition was 1000 ppm NO, 1100 ppm NH$_3$, 3.5% O$_2$, 2.3% H$_2$O and He balance. The total flow rate was 300 mL/min (ambient conditions), with a continuous monitoring of the NO and NH$_3$ concentration with a Thermo Electron model 17C chemiluminescent NO–NOx gas analyser. The catalytic activity, represented as a first-order rate constant (k), can be calculated from the NO conversion, X, as Eq. 2:

$$k = -\frac{F_0}{[NO]_0 V_{cat}} \ln(1 - X) \tag{2}$$

where F$_0$ is the molar inflow of NO, [NO]$_0$ is the initial molar concentration of NO, and V$_{cat}$ is the catalyst bed volume.

2.4. KCl poisoning

To simulate poisoning by potassium in the flue gas stream, the sample pellets were submerged in fine particles of KCl (<200 nm) and placed in a furnace for 248 hrs at 350°C in a water saturated air flow. Hereby the temperature is above the Tamman temperature for KCl (m.p. = 771ºC, T$_{Tamman}$ = 258.5ºC). Thus, the salt is surface mobile, and will diffuse into the catalyst pores deactivating any accessible active sites

3. Results & Discussion

3.1. Catalyst pore system

The characteristic data from the pore analyses are collated in Table 1. The S$_{BET}$ areas were maintained close to 150 m^{2}g^{-1} for samples with a sepiolite content below 62.5% w/w, whereupon the surface area gradually reduces to a minimum of 130 m^2/g - the surface area of pure sepiolite. Since the catalysts were treated at 500°C, little microporosity remained although all exhibited high external surface areas, useful for a catalytic system. The N$_2$ adsorption-desorption isotherms (V$_{N2}$ versus P/P^0) and MIP cumulative pore volumes (V$_P$) are shown in Figure 2 for samples with 0-50% w/w sepiolite content.
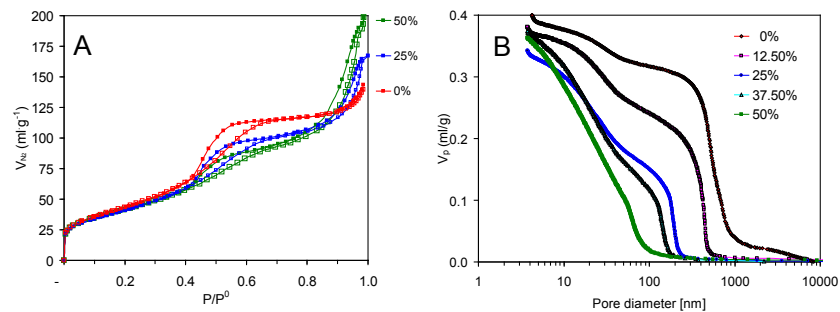

Figure 2: A) Nitrogen adsorption-desorption isotherms of composite catalysts with 0, 25, 50% w/w sepiolite content measured as the volume of N$_2$ (V$_{N2}$) versus the relative pressure (P/P^0). B) MIP cumulative pore volumes (V$_P$) for 0, 12.5, 25, 37.5 and 50% w/w sepiolite.
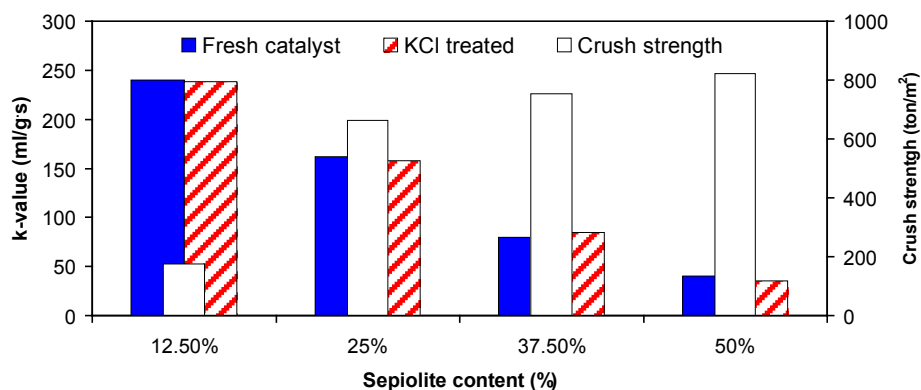
Figure 3: SCR activities of composite catalysts before and after 248 hours of hydrothermal treatment at 350°C in the presence of potassium chloride (left axis). On the right axis the crush strength measurements are shown.

Varying the sepiolite content of the VO_X/ZrO-SO_4/sepiolite composites has a marked effect on the observed pore volumes and macropore diameter. For instance, by introducing 25% w/w of sepiolite the characteristic interparticular macropore diameter decreased from 911 nm (0/8, pure VO_X-ZrO_2-SO_4) to 320 nm.

3.2. Catalytic activity and relation to the pore system and crushing strength

Comparing the activity data in Figure 3, before and after KCl exposure, it may be appreciated that almost no deactivation was observed. An extruded reference catalyst (3% w/w) V_2O_5-WO_3/TiO_2) under the same conditions suffered an 11% deactivation. It therefore seems that the sepiolite provides a protective effect of the catalytically active centres, or at least delays the deactivation by potassium salts. Furthermore, the effect is present even for the sample with only 12.5% w/w sepiolite, suggesting that the sulfated zirconia itself might have some chemical affinity for the potassium species, which enhance the resistance to deactivation. The crush strengths of the catalysts are also provided in Figure 3. The optimal composition of the composite system, regarding both activity and crushing strength is deduced to be a catalyst consisting of 25% w/w sepiolite.

References

1. H. Bosch, F.J.J.G. Janssen, 1988, Catalytic Reduction of Nitrogen Oxides, Catal. Today, 2, 4, 369-529.
2. G. Busca, L. Lietti, G. Ramis, F. Berti, 1998, Chemical and mechanistic aspects of the selective catalytic reduction of NOx by ammonia over oxide catalysts: A review, Appl. Catal. B: Environ., 18, 1-2, 1-26.
3. Q. Liu, Z. Liu, C. Li, 2006, Adsorption and Activation of NH_3 during Selective Catalytic Reduction of NO by NH_3, Chin. J. Catal., 27, 636-646.
4. Y. Zheng, A.D. Jensen, J.E. Johansson, J.R. Thøgersen, 2008, Deactivation of V_2O_5-WO_3-TiO_2 SCR catalyst at biomass fired power plants: Elucidation of mechanisms by lab- and pilot-scale experiments, Appl. Catal. B: Environ., 83,186-194.
5. E.W. Washburn, 1921, The Dynamics of Capillary Flow, Physical Review, 17, 3, 273 - 283.

SCR activity of conformed CuO$_x$/ZrO$_2$-SO$_4$ catalysts

Søren B. Rasmussen, Malcolm Yates, Johannes Due-Hansen, Pedro Ávila, Rasmus Fehrmann

Paper

3

SCR activity of conformed CuO_X/ZrO_2-SO_4 catalysts

S.B. Rasmussen,[a*] M. Yates[a], J. Due-Hansen[b], P. Ávila[a] R. Fehrmann[b]

[a]*Instituto de Catálisis y Petroleoquímica (ICP), Consejo Superior de Investigaciones Científicas (CSIC), Calle Marie Curie 2, Cantoblanco, 28049 Madrid, Spain*
[b] *Centre for Catalysis and Sustainable Chemistry (CSC), Department of Chemistry, Technical University of Denmark (DTU), Bygn. 207, Kemitorvet, DK-2800 Kgs. Lyngby, Denmark*

Abstract

CuO_X/ZrO_2-SO_4 catalysts have been synthesised as conformed materials with the use of sepiolite as agglomerant and the performance in the NH_3-SCR reaction with relation to biomass fired boiler units have been studied. The optimal Cu-loading of the catalysts is 3 wt.% CuO, both in terms of activity and selectivity. This catalyst constitutes a possible solution for NO removal in biomass-related applications, since it posses mainly Lewis acid sites, and therefore might be less subjected to deactivation by potassium containing fly ash particle produced during biomass combustion

Keywords: CuO_X, sepiolite, biomass, NH_3-SCR, ZrO_2-SO_4.

1. Introduction

The use of biomass in fossil fuel based power plants is of increasing interest, since it is considered as a CO_2 neutral fuel, having zero human impact on the carbon release to the atmosphere. Simultaneously, continuous efficient selective catalytic reduction of NO with ammonia (NH_3-SCR) remains a very important condition for the implementation of biomass fuel as a sustainable alternative for energy production. However, the NH_3-SCR catalyst suffers from a number of deactivation phenomena when installed in boiler units based on biomass combustion, due to exposure to potassium containing fly ash[1]. The active V=O and V-OH sites on the commercially used V_2O_5-WO_3/TiO_2 based catalyst reacts with the potassium salts and form inactive alkali vanadates, which are unable to adsorb ammonia.

Therefore new NH_3-SCR catalysts more resistant to deactivation by potassium salts metals are needed. One of the possible ways to increase catalyst resistance to alkaline poisons is the use of supports revealing high or super-acidic properties, which would interact more strongly with potassium than vanadium species. Potassium oxide affects the Brønsted acid sites of the catalyst to a much larger extent than Lewis sites. Therefore, another possible solution for NO removal in biomass-related applications is the use of other metal oxides as active components, which posses mainly Lewis acidity [2,3]. In this context we have synthesised and studied CuO_X/ZrO_2-SO_4 catalysts with respect to the performance of NH_3-SCR in biomass fired boiler units.

| CuO | Sepiolite | ZrO_2 | Starch | H_2O | $(NH_4)_2SO_4$ |

IWI
Extrusion
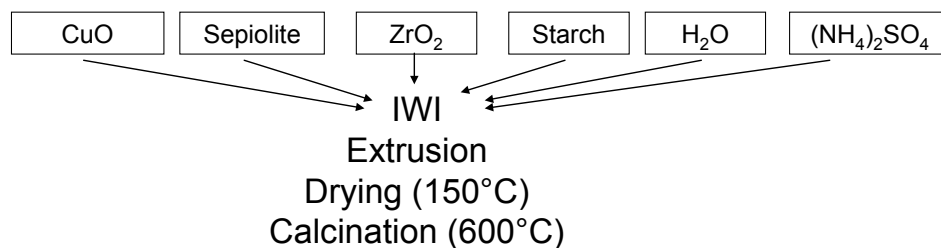Drying (150°C)
Calcination (600°C)

Figure 1: "One pot" synthesis route used for the synthesis of sepiolite supported CuO_X-applied for the production of scalable pelletised catalysts.

2. Experimental

2.1. Catalyst preparation

The zirconia source was freshly precipitated $Zr(OH)_4$ from Mel Chemicals. The α-sepiolite employed (Pansil 100) was supplied by Tolsa S.A. Ammonium sulphate and the Cu-precursor, $Cu(NO_3)_2$ were from Panreac, (> 99%).

The sulphated zirconia was prepared by dissolving $(NH_4)_2SO_4$, and $Cu(NO_3)_2$ into a part of the water. Thereafter the solution was mixed with the homogenised powder blend of the oxides and pore generating agent (PGA, starch), and extra water was added in order to obtain a paste of adequate rheology. After digestion/drying in ambient atmosphere for 2 hours with occasional kneading, the paste was extruded from 20 ml plastic syringes with 2 mm orifices. The samples were then dried at 150°C for overnight. Calcination of the samples was performed at 600°C for 4 hours in air. Finally the extruded materials were chopped into 3-5mm cylindrical pellets. The synthesis procedure is outlined in Figure 1.

2.2. Catalyst characterisation

The thermal gravimetric analysis of the samples were carried out on a Netzsch 409 EP Simultaneous Thermal Analysis device. The DSC curves were measured using approximately 20-30 mg of powered sample which were heated in an air flow of 75 ml·min^{-1} at a rate of 5 ºC·min^{-1} from room temperature to 1000 ºC, using α-alumina as reference. The specific surface areas, S_{BET}, were obtained from nitrogen adsorption at −196 ∘C using a Micromeritics Tri-Star apparatus, after application of the BET equation at relative pressures in the range 0.05–0.35 p/p∘.

Table 1. Textural characteristic of conformed catalysts

Sample	S_{BET} (m^2g^{-1})	S_{Extern} (m^2g^{-1})	V_{meso} (cm^3g^{-1})	V_{macro} (cm^3g^{-1})
1% CuO	110	104	0.20	0.71
2% CuO	80	68	0.19	0.68
3% CuO	79	70	0.20	0.73
5% CuO	84	77	0.19	0.74

Prior to N$_2$ adsorption the samples were outgassed overnight at 150 ∘C to a vacuum of <10^{-4} Pa to ensure a dry clean surface, free from loosely held adsorbed species.

2.3. NO SCR with ammonia

Activity measurements of the cylindrical pellet shaped catalysts were carried out in a continuous tubular glass reactor that operated at an integral regimen close to an isothermal axial profile. The reactor was 75 cm long and had an internal diameter of 2.54 cm. Ammonia was fed directly into the reactor bed to avoid the formation of ammonia salts [4]. Pellet beds 10 cm long were used. The inlet and outlet NO and NO$_2$ concentrations were determined by chemiluminescence with a Signal NO + NO$_2$ analyser (Series 4000). Analysis of N$_2$O and NH$_3$ was carried out by IR spectroscopy with a Signal 7000FT GFC Analyser and with an A.D.C. Double Beam Luft Type Infrared Gas Analyser, respectively.

3. Results & Discussion

3.1. Characterisation

The characteristic data from the pore analyses of the CuO$_X$/ZrO$_2$-SO$_4$ catalysts are collated in Table 1. The BET surface areas are around 84 m^{2}g^{-1}, except for the 1% CuO$_X$, which exhibits 110 m^{2}g^{-1}. The samples exhibit high external surface areas, close to the BET surface areas, which suggests that no micro porosity remains. A thermo gravimetric analysis was carried out in order to determine how the sepiolite, copper oxide, PGA and sulphation modify the phase transitions of the zirconia hydroxide gel (Fig. 2). The phase change from amorphous zirconia to the monoclinic phase was observed to occur at around 440°C for pure zirconia hydroxide gel. By introducing the sulphate as stabilizer for zirconia instead the transformation into the tetragonal phase is achieved at around 580°C, which appeared to be unaltered by the presence of the binder, and thus treatment at 600∘C was valid to ensure its formation. Furthermore we tested if the PGA and the introduction of Copper salts had influence on the transformations. It was observed that introduction of CuO$_X$ lead to lower combustion temperatures for the starch, but the transition temperature for formation of the tetragonal zirconia phase remained constant. Based on these data 600°C was chosen as the temperature for calcinations.
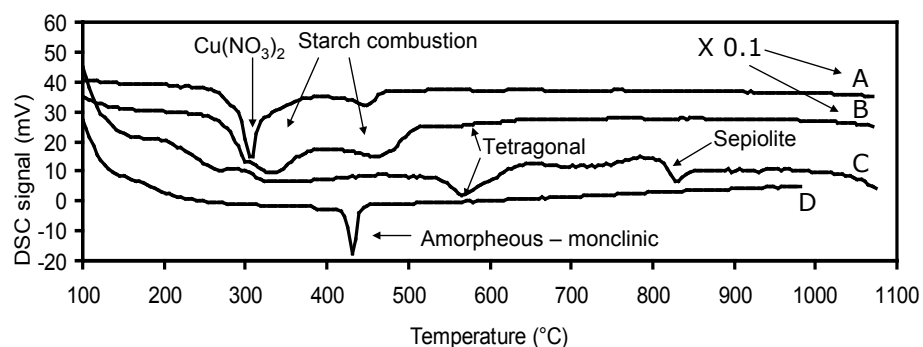

Figure 2: A) CuO$_X$/ZrO$_2$-SO$_4$ sepiolite catalyst B) ZrO$_2$-SO$_4$ sepiolite carrier material with PGA. C) ZrO$_2$-SO$_4$ sepiolite carrier material without PGA. D) Pure ZrO$_2$.
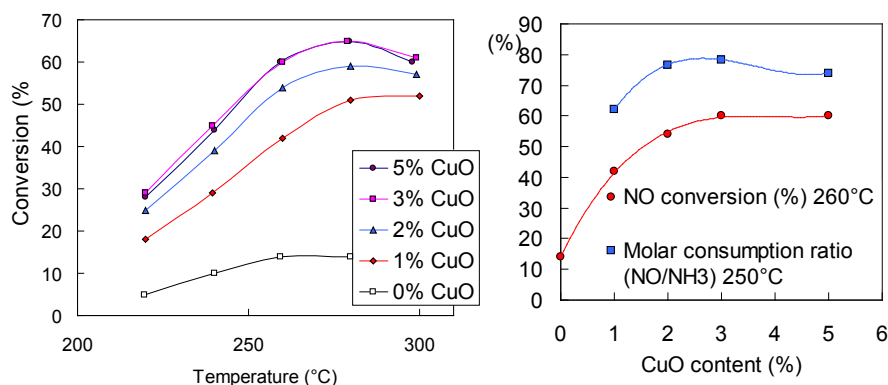
Figure 3: SCR activity of composite catalyst before and after 248 hours of potassium-exposure at 350°C.

3.2. Catalytic activity

Varying the CuO_X content on the CuO_X/ZrO-SO_4/sepiolite catalysts has some effects on the catalytic activities and selectivities. The NH_3-SCR activity is steadily increasing with the CuO content until the catalyst contains 3% CuO. Thereafter formation of crystalline CuO sets in according to complementary powder XRD data. Thereafter, any additional copper is deposited as crystalline CuO, which doesn't contribute to the catalytic activity, since the conversion remains stable. However, this also implies that the crystalline copper formed is merely a spectator species- hence there is no significant decline in activity nor in selectivity. However, the slight decrease in NO/NH_3 consumption ratio observed for the catalysts with 3% compared to 5% CuO could be interpreted as a slight loss in selectivity suggesting that for this catalytic system 3% CuO provides the optimal loading of the active species.

References

[1] H. Zhou, A.D. Jensen, P. Glarborg, A. Kavaliauskas, 2006, "Formation and reduction of nitric oxide in fixed-bed combustion of straw Fuel", 85, 5-6, 705-716.

[2] A.L. Kustov, S.B. Rasmussen, R. Fehrmann, P. Simonsen, 2007, "Activity and deactivation of sulphated TiO_2- and ZrO_2-based V, Cu, and Fe oxide catalysts for NO abatement in alkali containing flue gases", Appl. Catal. B: Environmental, 76, 1-2, 9-14.

[3] D. Pietrogiacomi, A. Magliano, D. Sannino, M.C. Campa, P. Ciambelli, V. Indovina, 2005, "In situ sulphated CuO_X/ZrO_2 and CuO_X/sulphated-ZrO_2 as catalysts for the reduction of NO_X with NH_3 in the presence of excess O_2", Appl. Catal. B: Environmental, 60, 1-2, 83-92.

[4] J. Blanco, P. Avila, C. Barthelemy, A. Bahamonde, J.A. Odriozola, J.F. Garcia de la Banda, 1989, "Influence of phosphorus in vanadium-containing catalysts for NOx removal", Appl. Catal. 55, 1, 151-164.

Multidisciplinary Determination of the Phase Distribution in the VO$_x$-ZrO$_2$-SO$_4$-Sepiolite Catalytic System

Søren B. Rasmussen, Johannes Due-Hansen, Mirza Villaroel,
F. Javier Gil-Llambías, Rasmus Fehrmann, Pedro Ávila

Paper

4

Distribución de las fases en el Catalizador VO_X-ZrO_2-SO_4-Sepiolita determinada por varios métodos.

S.B. Rasmussen[a,*], J. Due-Hansen[b], M. Villarroel[c], F.J. Gil-Llambias[c], R. Fehrmann[b], P. Ávila[a]

[a] *Instituto de Catálisis y Petroleoquímica, C.S.I.C. 28049-Madrid, Spain*
[b] *Centre for Catalysis and Sustainable Chemistry (CSC), DTU Chemistry, Tecnical University of Denmark, 2800 Kgs. Lyngby, Denmark*
[c] *Departamento de Química, Universidad de Santiago de Chile, Chile*
*S.B. Rasmussen: Fax: *34 91 585 4760, sbrasmussen@icp.csic.es*

Resumen

Se ha preparado y caracterizado una serie de catalizadores V_2O_5/ZrO_2/SO_4 – sepiolita, cuya actividad catalítica en la reacción NH_3-SCR se ha relacionado con el contenido de la fase activa VO_XSO_4 en ZrO_2. La distribución de la sepiolita y óxido de zirconio en la superficie de la mezcla mecánica fue estudiada por la técnica de migración electroforética. Las muestras se caracterizaron además por adsorción de nitrógeno, difracción de rayos X y por microscopía electrónica de barrido. Los resultados de migración electroforética mostraron que la adición de cantidades crecientes de sepiolita, la cual se amasa en agua junto con la zirconia, tiene un efecto dramático sobre el sistema, porque produce una sensible disminución de la fracción molar de zirconia en la superficie, y se alteran las propiedades electroforéticas de las mezclas.

Las microfotografías SEM, los patrones de difracción de rayos X y las medidas de la actividad de las muestras estudiadas concuerdan con los resultados de migración electroforética, verificándose que hasta una composición del 75% en VO_X-ZrO_2-SO_4, las fibras de sepiolita cubren las partículas de zirconia. Esto tiene una influencia ligeramente negativa sobre la actividad del catalizador global de estos catalizadores; sin embargo, se considera que puede ser una excelente propiedad que permitiría mejorar la vida de los catalizadores De-NO_x, expuestos a partículas de cenizas volantes, que contienen sales de potasio malignos.

Palabras clave: NH_3-SCR; sepiolita; zirconia sulfatada; potencial zeta

Abstract

A series of V_2O_5/ZrO_2/SO_4 - sepiolite mixtures were extruded, calcined and characterized. NH_3-SCR activity was found to be related to the content of the active VO_X-ZrO_2-SO_4 phase. The distribution of sepiolite and zirconia at the surface of the mechanical mixtures was studied by the electrophoretic migration technique. The samples were further characterised by nitrogen adsorption, XRD and scanning electron micrography techniques. The electrophoretic migration results showed that the addition of sepiolite to zirconia, kneaded in water, had a dramatic effect on the quantity of zirconia present at the support's surface, both strongly decreasing the molar fraction of zirconia at the surface, and altering the electrophoretic properties of the mixtures.

The SEM micrographs, XRD patterns and activity measurements of the water-kneaded samples agreed with the electroforetic migration results. Furthermore, it was verified by electrophoretic migration experiments that up until a composition of 75% VO_X-ZrO_2-SO_4, the sepiolite fibres coats the zirconia particles. This has a slightly negative influence on overall catalyst activity of fresh catalysts. However, it is believed that this can enhance lifetime of DeNOx catalysts exposed to fly ash particles, which contain malignant potassium salts.

Keywords: NH_3-SCR; sepiolite; sulfated zirconia; zeta potential

Distribución de las Fases en el Sistema VO_X-ZrO_2-SO_4-Sepiolita Determinada Por Varios Metódos

S.B. Rasmussen[a,*], J. Due-Hansen[b], M. Villarroel[c], F.J. Gil-Llambias[c], R. Fehrmann[b], P. Ávila
[a] *Instituto de Catálisis y Petroleoquímica, C.S.I.C. 28049-Madrid, Spain*
[b] *Centre for Catalysis and Sustainable Chemistry (CSC), DTU Chemistry, Tecnical University of Denmark, 2800 Kgs. Lyngby, Denmark*
[c] *Departamento de Quıímica, Universidad de Santiago de Chile, Chile*
**S.B. Rasmussen: Fax: +34 915 85 4760, sbrasmussen@icp.csic.es*

Resumen

Se ha preparado y caracterizado una serie de catalizadores V_2O_5/ZrO_2/SO_4 – sepiolita, cuya actividad catalítica en la reacción NH_3-SCR se ha relacionado con el contenido de la fase activa VO_xSO_4 en ZrO_2. La distribución de la sepiolita y óxido de zirconio en la superficie de la mezcla mecánica fue estudiada por la técnica de migración electroforética. Las muestras se caracterizaron además por adsorción de nitrógeno, difracción de rayos X y por microscopía electrónica de barrido. Los resultados de migración electroforética mostraron que la adición de cantidades crecientes de sepiolita, la cual se amasa en agua junto con la zirconia, tiene un efecto dramático sobre el sistema, porque produce una sensible disminución de la fracción molar de zirconia en la superficie, y se alteran las propiedades electroforéticas de las mezclas.

Las microfotografías SEM, los patrones de difracción de rayos X y las medidas de la actividad de las muestras estudiadas concuerdan con los resultados de migración electroforética, verificándose que hasta una composición del 75% en VO_x-ZrO_2-SO_4, las fibras de sepiolita cubren las partículas de zirconia. Esto tiene una influencia ligeramente negativa sobre la actividad del catalizador global de estos catalizadores; sin embargo, se considera que puede ser una excelente propiedad que permitiría mejorar la vida de los catalizadores De-NO_x, expuestos a partículas de cenizas volantes, que contienen sales de potasio malignos.

Palabras clave: NH_3-SCR; sepiolita; zirconia sulfatada; potencial zeta

Introducción

El catalizador comercial generalmente usado para la Reducción Catalítica Selectiva de NOx con amoniaco, NH_3-SCR, está basado en V_2O_5/TiO_2 y reduce selectivamente al NO en presencia de aire, según la siguiente reacción:

$$O_2 + 4NO + 4NH_3 \rightarrow 4N_2 + 6H_2O \qquad (1)$$
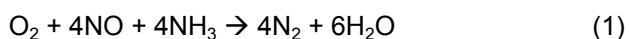
Esta reacción consta de dos ciclos, un ciclo de ácido y un ciclo redox [1- 9]. Para el ciclo de oxidación-reducción, la capacidad redox de V (V) y V (IV) es de importancia clave, mientras que para el ciclo ácido, el elemento clave es contar con suficientes centros ácidos superficiales para quimisorber y distribuir el NH_3 en la superficie del catalizador V_2O_5/TiO_2.

En un intento por cumplir con el Protocolo de Kyoto, la sustitución de combustibles fósiles con biomasa constituye una solución viable, práctica, económica y ambiental, ya que la biomasa (en forma de paja, virutas de madera, polvo, etc.) conserva su carbono del aire durante la fotosíntesis. Así, la biomasa, en este sentido puede ser considerada como un combustible neutro de CO_2, y actualmente en Dinamarca DONG Energy A / S está intentando aumentar el contenido de biomasa en la producción de energía hasta un 20%.

Aunque la tecnología de combustión de biomasa es relativamente fácil de implementar en las centrales eléctricas de carbón y petróleo, existen algunos inconvenientes que deben ser resueltos. Por un lado, el potasio de las partículas de cenizas volantes es muy agresivo a altas temperaturas, e induce problemas a los materiales, como la corrosión y el deterioro de las baldosas cerámicas en el quemador. Por otra parte, también es

extremadamente venenoso para los catalizadores de la reacción NH$_3$-SCR mencionados.

Experimental

Preparación de la muestra: Como fuente de zirconio se utilizó hidróxido de zirconio Zr(OH)$_4$ Melcat, con un tamaño de partícula d$_{50}$ = 15μm y el sulfato amónico de Panreac (> 99%). La zirconia sulfatada fue preparada por impregnación de 101,6 g de hidróxido de zirconio, con 8,3 g de (NH$_4$)$_2$SO$_4$ por el método de humedad incipiente. Después de la digestión y secado en condiciones ambientales durante 2 horas, las muestras se secaron a 150°C durante 3 horas. Se llevó a cabo la calcinación de las muestras a 500°C durante 4 horas en aire colocando el material directamente en un horno precalentado, a fin de facilitar la formación preferente de las fases cúbica metaestable y tetragonal.

Los catalizadores fueron preparados por impregnación húmeda de VOSO$_4$ en la zirconia sulfatada, para producir una pasta que se deja durante una hora en agitación. Posteriormente, se añaden la sepiolita, α-sepiolita Pansil 100 suministrada por Tolsa SA y el agua en los niveles deseados para obtener una pasta homogénea con una viscosidad adecuada para la extrusión de una jeringa de 20 ml con un orificio de 2 mm. Se dejan secar lentamente los extruídos, manteniéndolos en un ambiente húmedo durante 48 horas y luego se secan a 150°C durante toda la noche en aire. La calcinación se realizó a 500°C durante 4 horas en atmósfera de aire. Por último, el material resultante fue dividido en piezas cilíndricas 3-5mm de largo.

Actividad catalítica (Reducción Catalítica Selectiva de NO con NH$_3$): Las medidas de la actividad SCR se llevaron a cabo en un reactor de lecho fijo, con 10 mg de catalizador, colocado entre dos capas de lana de cuarzo inerte. La composición de los gases de reacción fue de 1000 ppm de NO, 1100 ppm de NH$_3$, 3,5% de O$_2$, 2,3% de H$_2$O y He hasta balance. El caudal total fue de 300 ml/min. (en condiciones normales), con un seguimiento continuo de la concentración de NO por quimioluminiscencia con un analizador de gases Thermo Environmental, modelo 17C. La actividad catalítica, representada como una constante de velocidad de orden 1(k), puede calcularse a partir de la conversión de NO, X, a partir de la ecuación 2:

$$k = -\frac{F_0}{[NO]_0 V_{cat}} \ln(1 - X)$$

(2)

donde F$_0$ es el flujo molar de entrada de NO, [NO]$_0$ es la concentración molar de entrada de NO, y V$_{cat}$ es el volumen de lecho catalítico.

Textura: Se determinaron los valores de área especifica (BET) mediante isotermas de adsorcion/desorcion de nitrogeno con un Micromeritics TriStar 3000 y la distribución de volumenes de micro, meso y macro poros combinando los resultados de esta técnica con los obtenidos mediante porosimetría de intrusión de mercurio.

Migración Electroforética: El Punto de Carga cero (ZPC) de los materiales composites fue determinado midiendo el potencial zeta en función del pH de la solución. Los potenciales zeta fueron obtenidos usando la ecuación de Helmholtz-Smoluchowski midiendo la velocidad de migración electroforética de las partículas en un Zeta-Meter Inc. Instrument, modelo 3.0+, provisto de una unidad de transferencia de muestra automática (bomba peristáltica y pinzas eléctricas especiales) para evitar los problemas de sedimentación de muestra.

Los experimentos se realizaron usando 30 mg de muestras de polvo (<2 μm) suspendidas en 200 ml de KCl 10^{-3} M, ajustando el pH con disoluciones 0,2 M de KOH y HCl. En cada muestra no se detectó más de un tipo de particula, excepto para la que contenía 12,5% de sepiolita. Cada curva fue repetida al menos dos veces para confirmar la reproducibilidad de los resultados.

Se ha calculado la fracción molar de cada componente en la superficie de la muestra de acuerdo al método previamente descrito [10], que se basa en el hecho de que el punto de carga cero (ZPC) de una mezcla cae entre los puntos isoeléctricos (IEP) de los materiales individuales (A y B). Según este principio se desarrollaron las ecuaciones (3) y (4).

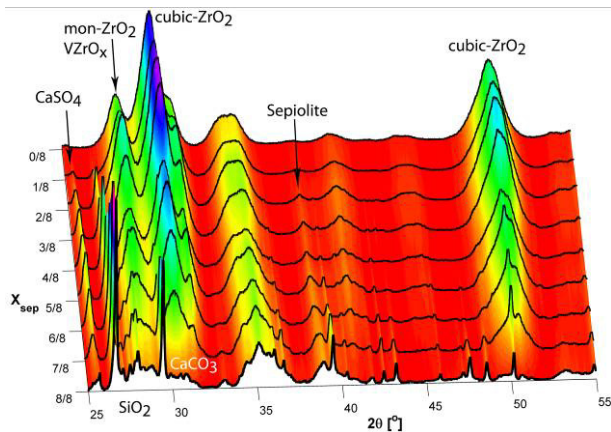$$ZPC = X_A (IEP)_A + X_B (IEP)_B$$

(3)

$$X_A + X_B = 1$$

(4)

Figura 1: Difractogramas de Rayos-X de los composites VO_X-ZrO_2-SO_4/sepiolita después de la extrusión, secado y calcinación a 500°C.

Esto permite determinar la fracción molar de cada componente expuesta en la superficie, relacionando dicho valor con la composición total de la muestra. No se realizaron cálculos posteriores para obtener el grado de cubrimiento aparente (% en peso en la superficie) como se han realizado en estudios previos, debido a la dificultad de asignar una masa molecular a la sepiolita, cuya fórmula estructural es $Si_{12}Mg_8O_{30}(OH)_4(H_2O)_4 \cdot 8H_2O$ [11].

Micoscopía Electrónica de Barrido (SEM): La morfología y el tamaño de las partículas de los catalizadores fueron investigados por SEM, utilizando un FEI Inspect 'S' con filamento de tungsteno. Las imágenes fueron obtenidas con voltajes de aceleración de 5 a 10 kV. sobre las muestras previamente grafitizadas.

Difracción de rayos-X (XRD): Se obtuvieron los difractogramas de polvo de cada muestra usando un difractómetro Huber G670 Guinier analizando el rango de 2θ: 3-100° en etapas de 0,005°, durante un tiempo de 120 min a temperatura ambiente y longitud de onda λ= 1,54051Å. La muestra se coloca en una capa fina de cinta adhesiva y se gira durante la recolección de datos.

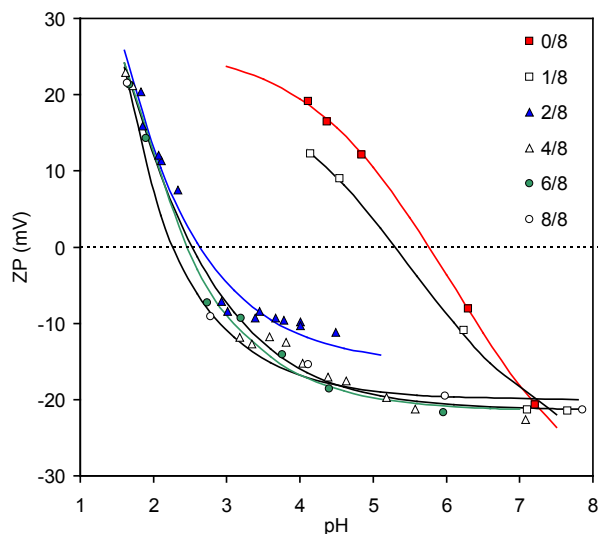**Figura 2:** Potenciales Zetas a 25ºC K en función del pH obtenidos con suspensiones de sepiolita, VO_X-ZrO_2-SO_4 y sus mezclas, amasados en agua y tratados a 773 K durante 4 h en aire.

Resultados y Discusión

En la Figura 1 se muestran los difractogramas de rayos X de los composites VO_X-ZrO_2-SO_4/sepiolite después de la extrusión, secado y calcinación a 500°C. En ella se aprecian los picos de difracción de ZrO_2 a 2θ = 28-32º. En las muestras se aprecia la formación de la fase monoclínica, pero la fase dominante es la fase cúbica. Esta última fase cristalina se parece mucho a la tetragonal de ZrO_2 (2θ = 31,586), que se ha sugerido que es necesario para la generación de la alta acidez en la zirconia sulfatada. Por lo tanto, esta reflexión se asigna muy a menudo a esta fase. Sin embargo, en un análisis previo de Rietveld, se concluyó que dicha reflexión corresponde de hecho a la fase cúbica, la cual probablemente presenta propiedades similares.

Por otra parte, con el aumento del contenido de sepiolita se observa la aparición progresiva de sepiolita cristalina, $CaCO_3$, SiO_2 y $CaSO_4$ (Ca^{2+} de la fase de sepiolita que reacciona con sulfato de la fase de zirconia). La formación de $CaSO_4$ podría sugerir que la acidez de la fase de zirconia puede disminuir, y debería añadirse sulfato extra para compensar este efecto. Esta observación puede ser importante para la actividad catalítica del catalizador, pero no modifica el alcance de este trabajo, ya que aquí se concentra la atención en la distribución de fases entre VO_X-ZrO_2-SO_4 y sepiolita.
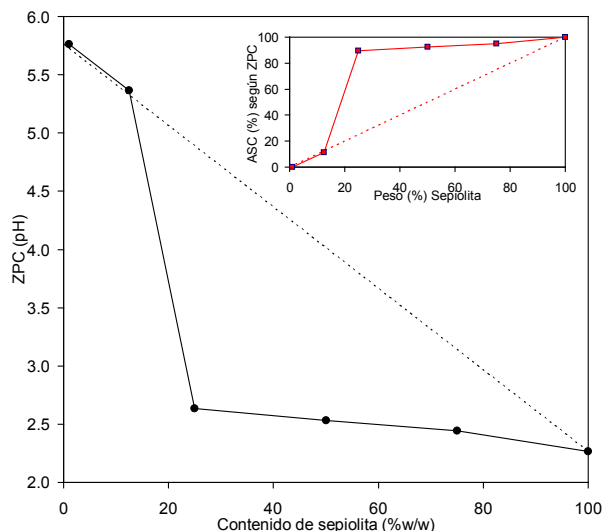
4

Figura 3: Variación de los puntos de carga cero ZPC y del recubrimiento superficial aparente (ASC en gráfica insertada), en función del contenido en sepiolita.

Figura 4: Microfotografías SEM de la serie de $VO_x ZrO_2$-SO_4/sepiolite.

En la Figura 2 se muestran las curvas del potencial zeta en function del pH del sistema VO_X-ZrO_2-SO_4, la sepiolita y sus meclas amasadas con agua, todas ellas tratadas a 500ºC durante 4 h. Los Puntos isoeléctricos (IEPs) de la sepiolita, el ZPC del sistema VO_X-ZrO_2-SO_4 y de sus mezclas, así como los recubrimientos superficiales aparentes resultantes, se muestran en la Figura 3. Estos valores del ZPC se calcularon por interpolación de la curva de potencial Zeta.

El valor de ZPC= 5,8 del sistema VO_X-ZrO_2-SO_4, es función del IEP de la fase pura de zirconia [12], el V_2O_5, y el efecto del sulfato. El IEP de la sepiolita, 2,2, ha sido previamente reportado [13]. El efecto de la adición de sepiolita a la zirconia que se muestra en la Figura 2, indica que la presencia de sepiolita provoca un gran desplazamiento del ZPC a valores bajos, incluso con bajos contenidos del silicato. Este efecto fue menos pronunciado para contenidos altos de sepiolita.

El ZPC alcanza un valor muy cercano al de la sepiolita pura con sólo el 25% (w/w) de este silicato en la composición global. Este efecto se muestra en la Figura 3, donde se representa el ZPC en función del contenido de sepiolita. Las fracciones molares de sepiolita en la superficie, calculadas mediante la aplicación de la ecuación 3 y 4 a los resultados (véase la sección experimental) se presentan en la Figura 3 (gráfica insertada), expresados como porcentajes.
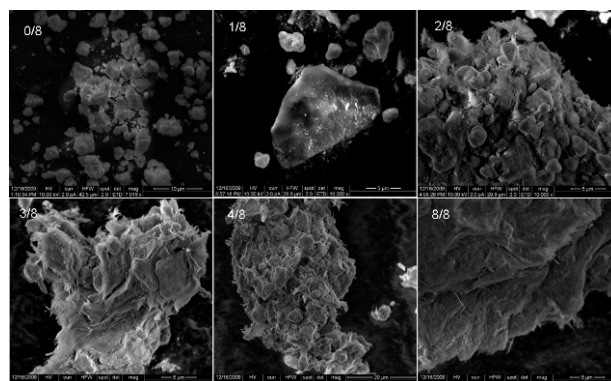
No es de extrañar que el porcentaje de zirconia en la superficie se redujera en gran medida por la adición de pequeñas cantidades de sepiolita.

Este efecto de fuerte enmascaramiento de la sepiolita a un óxido (zirconia) en la superficie se ha demostrado antes para titanio [14], si bien en este caso de la fase VO_X-ZrO_2-SO_4 es mucho más pronunciado que en el caso de la titania. El porcentaje de zirconia necesario para alcanzar fracciones molares de 50% de zirconia en la superficie fue de más del 75% en peso.

Dado que la fase activa de la reacción estudiada es el sistema VO_X-ZrO_2-SO_4, sería importante conseguir una protección parcial de los sitios activos optimizando la composición de este tipo de catalizadores con el fin de aumentar la vida útil del catalizador. De esta forma se ha considerado que la sepiolita podría ejercer esta función protectora siempre que se mantenga una buena accesibilidad del zirconio presente en la superficie.

El comportamiento de la mezcla de los dos sólidos podría explicarse a partir de la termodinámica y las fuerzas motrices que operan en la interacción de los dos componentes y la morfología del sistema durante el proceso de amasado. Esto ha sido investigado por este grupo en un estudio anterior [14] para el caso de un catalizador SCR sobre la base de titania-sepiolita. La sepiolita tratada a 500ºC se compone de partículas con tamaños que van desde 100 a 250 μm. Estas partículas están compuestas, a su vez, por haces de fibras, que varían en tamaño desde 0,2 hasta 1μm de longitud y 10-100 nm de ancho. Las partículas de titanio (0,05-0,1μm) están formadas por agregados de 0,3-1 μm, en el que las partículas originales mantienen su identidad.
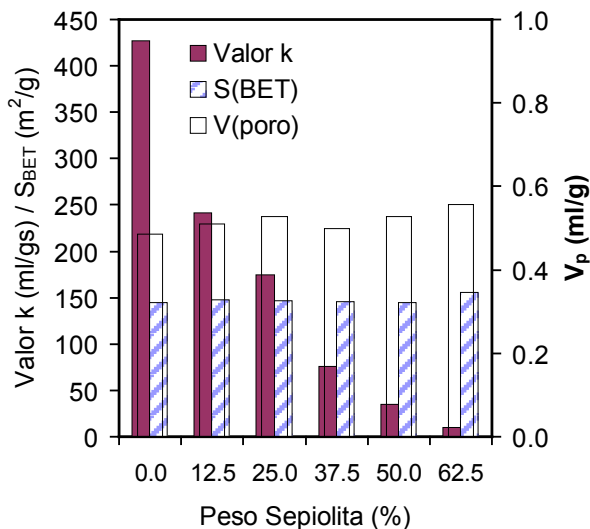
5

Figura 5: Variación de la actividad NH_3-SCR a 360ºC en función del contenido en sepiolita de los catalizadores VO_X-ZrO_2-SO_4/sepiolita.

El objetivo de este trabajo es utilizar estos fenómenos para incorporar parcialmente la fase activa de zirconia dentro de los haces de fibras de sepiolita y proteger así a los centros de óxido de vanadio de los compuestos de potasio básicos presentes en los gases de combustión de biomasa.

El recubrimiento físico de la fase de zirconia por la sepiolita puesto de manifiesto por las medidas del potencial zeta ha sido confirmado por análisis SEM de los catalizadores calcinados (Figura 4). A partir de estas micrografías se puede ver que la superficie de la muestra 1/8 (12,5% sepiolita), básicamente, presenta una morfología similar a la de la muestra 0/8 (sistema VO_X-ZrO_2-SO_4). Algunas fibras de la sepiolita se puede ver adjunto a las partículas de óxido de zirconio, lo cual explica plenamente por qué el punto de carga cero de la muestra de 1/8 es un promedio simple entre la composición y los potenciales de carga cero de las fases puras.

Sin embargo, desde la muestra 2/8 (25% en sepiolita), se observa un cambio morfológico espectacular. El material compuesto se observa como cristales de zirconio rodeados de haces de fibras de sepiolita con un aspecto externo muy similar al de la sepiolita pura (muestra 8/8). Esto concuerda totalmente con la variación de los valores de ZPC observada en las Figuras 2 y 3. En ellas se aprecia que todas las muestras con un porcentaje de sepiolita igual o superior al 25% en peso (muestras 2/8 - 8/8) tienen el punto de carga cero muy cerca del valor del PIE de la sepiolita pura.

En la Figura 5, se muestran los valores de actividad en el proceso NH_3-SCR a 360°C para los catalizadores estudiados, en función del contenido de sepiolita. Como es bien sabido que las especies activas en este proceso son los VO_X distribuidos sobre óxidos de metales de transición (TiO_2, Al_2O_3, o ZrO_2), la tendencia general observada en la Figura 5 es la lógica. En general, al aumentar el contenido de sepiolita se observa una disminución de la actividad. Sin embargo, la tendencia no parece seguir completamente una relación lineal entre el contenido de fase activa (VO_X/ZrO_2-SO_4) y la actividad. La disminución de la actividad parece más fuerte de lo esperado al aumentar el contenido de sepiolita.

Esta pérdida de linearidad podría deberse a un bloqueo severo de los centros activos por parte de la sepiolita que dificulte el acceso de los gases, lo cual no parece muy probable teniendo en cuenta los espacios interfibrilares observados por SEM. En la Figura 5 también se puede confirmar que no hay cambios drásticos con respecto a los volúmenes de poros o áreas específicas, y parece que la caída de la actividad es debida a una desactivación química de la fase activa de la sepiolita. Esta segunda opción está en concordancia con la formación de las fases $CaSO_4$ observadas por difracción de rayos X en la Figura 1.

Conclusiones

La serie de catalizadores híbridos de V_2O_5-ZrO_4-SO_4/sepiolita obtenidos por extrusión de sus mezclas, secados y calcinados a 500ºC, demostraron ser activos para el proceso NH_3-SCR. La velocidad de reacción de cada catalizador está directamente relacionada con la cantidad de fase activa de VO_X-ZrO_2-SO_4 presente, pero se observó la existencia de cierta desactivación debida a la formación de $CaSO_4$ confirmada por los resultados de DRX. Se ha verificado, por experimentos de migración electroforética, que las fibras de sepiolita recubren externamente las partículas de ZrO_2-SO_4 hasta una composición de 75% de ZrO_2-SO_4.

La influencia negativa de la adición de sepiolita sobre la actividad del catalizador global probablemente puede ser compensada mediante la adición de sulfato extra durante la síntesis o el uso de sepiolita de alta pureza, con bajo contenido en Ca. Por otra parte, es especialmente interesante la posible mejora de la vida de catalizador, debido al efecto inducido por el recubrimiento de la fase activa por una capa de sepiolita, que sería especialmente efectiva en plantas térmicas de biomasa, en las que los catalizadores se ven sometidos a una fuerte desactivación causada por el potasio que contienen las partículas de cenizas volantes.

6

Referencias

[1] G. Busca, L. Lietti, G. Ramis, F. Berti, *Appl. Catal. B*, 18 (1998).

[2] V.I. Pârvulescu, P. Grange, B. Delmon, *Catal. Today* 46 (1998) 233.

[3] N.-Y. Topsøe, H. Topsøe, J.A. Dumesic, *J. Catal.* 151 (1995) 226.

[4] F. J. Gil-Llambıas A. Lopez-Agudo, *J. Catal.*,95 (1985) 520.

[5] N.-Y. Topsøe, J.A. Dumesic, H. Topsøe, *J. Catal.* 151 (1995) XXX.

[6] Y. Topsøe, *Science* 265 (1994) 1217.

[7] I.E. Wachs, G. Deo, B.M. Weckhuysen, A. Andreini, M.A. Vuurman, M. de Boer, M.D. Amiridis, *J. Catal.* 161 (1996) 211.

[8] J.A. Dumesic, N. Topsøe, H. Topsøe, Y. Chen, T. Slabiak, *J. Catal.* 163 (1996) 409.

[9] M. Anstrom, J.A. Dumesic, N.-Y. Topsøe, *Catal. Lett.* 78 (2002) 281.

[10] F. J. Gil-Llambías and A. M. Escudey-Castro, *J. Chem. Soc., Chem. Commun.*, (1982) 478.

[11] K. Brunauer and A. Preisinger, *Tschermaks Mineral. Petrogr. Mitt.*, 6 (1956) 120.

[12] G. A. Parks, *Adv. Chem. Ser.*, 67 (1967) 121; *Chem.* Rev., 65 (1965) 177.

[13] C. Knapp, F.J. Gil-Llambias, M. Gulppi-Cabra, P. Avila, J. Blanco, *J. Mater. Chem.*, 7 (1997) 1641.

[14] P. Avila, J. Blanco, A. Bahamonde, J. M. Palacios and C. Barthelemy, *J.Mater. Sci*., 28 (1993) 4113.

Impact of support and potassium-poisoning on the V₂O₅-WO₃/ZrO₂ catalyst performance in ammonia oxidation

Johannes Due-Hansen, Arkady L. Kustov,
Claus Hviid Christensen, Rasmus Fehrmann

Paper

5

Impact of support and potassium-poisoning on the V_2O_5–WO_3/ZrO_2 catalyst performance in ammonia oxidation

Johannes Due-Hansen *, Arkady L. Kustov, Claus Hviid Christensen [1], Rasmus Fehrmann *

Department of Chemistry and Center for Sustainable and Green Chemistry, Technical University of Denmark, Kemitorvet 207, DK-2800 Lyngby, Denmark

ARTICLE INFO

ABSTRACT

A series of WO_3-promoted zirconia supports were synthesized and calcined between 400 and 800 °C. Subsequently vanadium oxide was introduced to obtain 3.5 wt% V_2O_5. The influence of the calcination temperature and potassium-poisoning (K/V = 0.2, molar ratio) on the catalytic activity in the selective catalytic reduction (SCR) of NO with NH_3 was previously studied. Here, we focus on the influence of these parameters on the catalytic activity for the undesirable oxidation of ammonia, which decrease the N_2 selectivity of the SCR process. It is found that potassium doping of the catalysts results in a considerable decrease in the overall ammonia conversion while selectivity to NO increases.

© 2008 Elsevier B.V. All rights reserved.

1. Introduction

The selective catalytic reduction (SCR) of NO_x by NH_3 in the presence of O_2 remains the state of the art technology for controlling NO_x emissions from stationary sources. Transition metal oxides (most commonly vanadia) promoted with tungsten or molybdenum oxides supported on anatase are among the most active SCR catalysts used in industrial scale at temperatures 300–450 °C. It is generally agreed by most researchers that the SCR reaction proceeds through an Eley–Rideal mechanism with activation of ammonia by adsorption and NO reacting directly from the gas phase or from a weakly adsorbed state. However, the selectivity of the SCR reaction can be compromised by the undesired oxidation of ammonia to N_2, N_2O, NO, and NO_2.

$$4NH_3 + 3O_2 \rightarrow 2N_2 + 6H_2O \qquad (1)$$
$$2NH_3 + 2O_2 \rightarrow N_2O + 3H_2O \qquad (2)$$
$$4NH_3 + 5O_2 \rightarrow 4NO + 6H_2O \qquad (3)$$
$$4NH_3 + 7O_2 \rightarrow 4NO_2 + 6H_2O \qquad (4)$$

A significant work on the catalytic oxidation of ammonia over various metal oxides, including V_2O_5, WO_3 and TiO_2, was undertaken already in the 1970's by Il'chenko and Golodets [1]. They discussed the correlation between the selectivity of the NH_3 oxidation and the binding energy of lattice oxygen in metal oxides, since a higher binding energy of oxygen would cause a poorer oxidation ability of the metal oxide. The study showed that high lattice oxygen binding energy induces a low NH_3 oxidation rate, but high N_2 selectivity. The formation of nitrous oxides during ammonia oxidation has recently been described over V_2O_5–WO_3/TiO_2 catalysts at high temperatures [2]. The authors observed that the selectivity towards N_2O increased with temperature and vanadia loading. Ozkan et al. [3,4] suggests three combinational sites responsible for the ammonia adsorption, by isotopic labeling studies, namely the following neighboring sites: (a) two V=O, responsible for NO formation from ammonia, (b) V=O and V–OH, responsible for oxidative formation of N_2 and N_2O from ammonia, and (c) two V–OH, accountable for formation of N_2 from ammonia. The authors therefore concluded that the V=O sites are responsible for the oxidation of ammonia to NO and N_2O. Jung and Grange [5] showed by DRIFT spectroscopy of V_2O_5, that above 400 °C almost all vanadium is fully oxidized, in other words, all V–OH sites are oxidized to V=O sites at temperatures higher than 400 °C. This implies that both increased rate of NO formation during the ammonia oxidation and decreased selectivity to N_2 in the SCR reaction can be explained by the increased number of V=O sites above 400 °C. Thus,

---

* Corresponding authors. Tel.: +45 4525 2363 (J. Due-Hansen), tel.: +45 4525 2389 (R. Fehrmann).

E-mail addresses: jdh@kemi.dtu.dk (J. Due-Hansen), rf@kemi.dtu.dk (R. Fehrmann).

[1] Present address: Haldor Topsøe A/S, Nymøllevej 55, DK-2800 Lyngby, Denmark.

the oxidation state of vanadium, i.e. the distribution between the dual active V–OH and V=O sites, is an essential factor for controlling the reactivity and ammonia oxidation.

Although the adsorption, activation and oxidation of ammonia over vanadia-based catalysts have been investigated to a certain degree, the literature of the potassium influence on the reaction is only scarcely covered. The effect of alkaline metals on the SCR activity of V_2O_5/TiO_2 catalysts has been reported by some authors [6–9]. Most of them conclude that the poisons are affecting the Brønsted acid sites (V–OH), thus decreasing both their number and activity in NO reduction. Chen and Yang [10] reported on the alkali influence on the NO conversion of V_2O_5/TiO_2 and V_2O_5–WO_3/TiO_2 catalysts and found that doping with 0.3–2.2 wt% K_2O resulted in an overall "negative nitrogen monooxide conversion" in the NH_3 SCR reaction at temperatures above ~450 °C, i.e. additional NO was produced by the competitive reaction of ammonia oxidation than consumed by SCR reaction. The authors thus claimed that K_2O additive was an effective promoter for ammonia oxidation. However, they only measured the actual ammonia oxidation at 500 °C on V_2O_5/TiO_2, WO_3/TiO_2 and V_2O_5–WO_3/TiO_2 samples, and thus not on potassium-doped samples.

Recent studies have shown that the catalysts supported on tungstated zirconia have improved resistance towards alkali poisoning in the reaction of NH_3 SCR with ammonia [11]. Especially the crystallinity of the zirconia-supported catalyst was found to be an important parameter accounting for NO_x reduction activity. Nevertheless, the catalyst doping with potassium in all cases lead to a considerable decrease of their catalytic activity. It was suggested that potassium adsorbs to the same sites as ammonia, thus blocking a fraction of the sites necessary for the SCR reaction. Therefore, a support with a high surface acidity is required, to host the basic potassium, leaving the active vanadia sites available for reaction. The traditional support used for SCR catalysts is titania, promoted with tungsten or molybdenum oxides. This system reveals only moderate surface acidity. On the contrary, tungstated zirconia is known to display high surface acidity and its surface properties, e.g. acidity, specific surface area, and crystallinity can be tuned in a wide range by varying preparation procedure, WO_x content and calcination temperature [12,13].

To our knowledge, there are no studies of the ammonia oxidation over vanadia-loaded zirconia-based catalysts and their corresponding potassium-doped samples. In the present paper, we report on the activity of fresh and potassium-doped vanadia–zirconia-based catalysts for the oxidation of ammonia.

2. Experimental

2.1. Catalyst preparation

Tungstated zirconia (WZ) was synthesized by coprecipitation of ammonium metatungstate and zirconyl nitrate hydrate and calcined at different temperatures ranging from 400 (WZ_400) to 800 °C (WZ_800). The resulting supports, containing 20 wt% WO_3, were pressed at 10 tons (Ø = 13 mm) and crushed into 0.180–0.295 mm particles and consequently impregnated to obtain 2.0 wt% vanadium (VWZ). Doping with potassium was performed using incipient wetness impregnation with a KNO_3 solution to obtain samples with a K/V molar ratio of 0.2, resulting in the poisoned catalyst K_2O–V_2O_5–WO_3/ZrO_2 (KVWZ). After doping, the samples were dried at 100 °C for 2 h. For further synthesis details, see [11].

The commercial reference catalyst shaped as fiber-reinforced monolith system, consists of a 3 wt% V_2O_5 and 7 wt% WO_3 supported on TiO_2, anatase (1.7VWT_ref). The active material on the monolith-surface was separated from the fiber material and pressed into tablets at 5 tons, Ø = 13 mm and crushed into 0.180–0.295 mm particles.

2.2. Catalyst characterization

Room-temperature X-ray powder diffraction (XRD) measurements were recorded on a Huber G670 powder diffractometer using Ni-filtered Cu Kα radiation (λ = 1.5406 Å) with 2θ scan range 10–65° in steps of 0.02°. The XRD-patterns of the crystalline structures were refined with the Rietveld technique using WINPOW software [14]. The crystalline peak profiles were represented by a pseudo-Voigt profile function and a five-coefficient Chebyshev polynomial background fitting.

2.3. Catalytic activity measurements

The ammonia oxidation reaction was carried out in a continuous flow fixed bed vertical quartz reactor, operating at atmospheric pressure.

In the ammonia oxidation experiments, the ammonia concentration were measured with a Jasco V-570 UV/VIS/NIR spectrophotometer, using the characteristic ammonia absorption band around λ = 201 nm. Thermo Electron's Model 10A Rack-Mounted Chemiluminescent NO–NO_x Gas Analyzer was used to detect NO concentrations. The operating gas composition for the ammonia oxidation was: 1100 ppm NH_3, 3.5% O_2, 2.3% H_2O and balance N_2. The total flow rate was maintained at 300 ml/min (ambient conditions).

3. Results and discussion

3.1. Surface area and structural characterization

The morphological characteristics of the WO_3/ZrO_2 supports calcined at different temperatures and the results of the BET surface area measurements are outlined in Table 1 and show the effect of calcination temperature on the surface area, crystallinity and phase composition of the support. After synthesis, the samples were annealed in air between 400 and 800 °C. Calcination at 400 and 500 °C resulted in essentially amorphous samples, whereas calcination at 600–800 °C yielded more crystalline samples. With increasing calcination temperature, there is a significant increase in sample crystallinity from 37.1% to 54.7% when going from 500 to 600 °C, respectively. Further increase in calcination temperature leads to increased crystallinity, resulting in highest crystallinity (67.5%) for the sample calcined at 800 °C (cf. Supplementary material Fig. 1).

The crystalline samples are composed of three ZrO_2 crystal phases with different zirconium/oxygen atom positions and interatomic distances. X,Y,Z coordinates of the space groups are avail-

Table 1
Textural support characteristics of the WO_3/ZrO_2 samples calcined at 400–800 °C. Crystallinity and the calculated volumetric distribution of the crystalline ZrO_2 and WO_3 phases are determined by Rietveld analysis. Standard deviation is given in parentheses.

	BET area (m^2/g)	Crystallinity[a] (%)	V_{WO_3} (vol%)	V_{cubic}	V_{mon}	V_{tet}
WZ_400	226.8	35.2	–	–	–	–
WZ_500	167.3	37.1	–	–	–	–
WZ_600	136.6	54.7	0.06 (0.00)	8.69 (0.78)	0.01 (0.00)	91.25 (1.50)
WZ_700	99.5	64.9	0.07 (0.00)	23.94 (1.17)	0.01 (0.00)	75.99 (1.79)
WZ_800	58.5	67.5	7.06 (0.19)	22.74 (0.99)	9.66 (0.40)	60.55 (1.44)
1.7VWT_ref	60.5	–	–	–	–	–

[a] Calculated with the diffraction pattern program 'Winprep' 2006-01-17 from 2θ 10–65°.
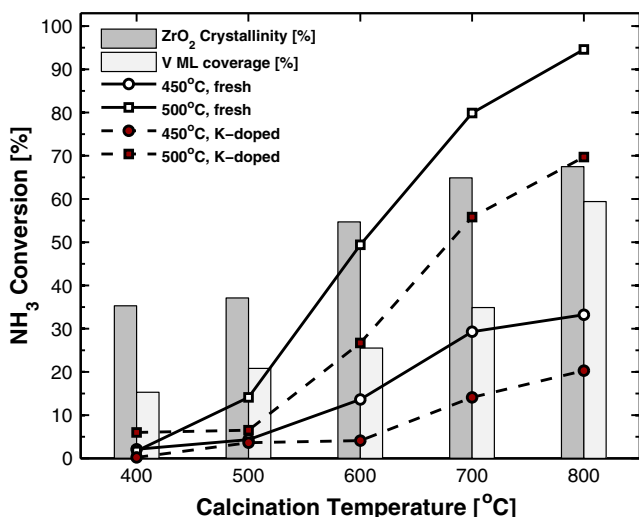
Fig. 1. NH_3 conversion, vanadium monolayer surface coverage and crystallinity for fresh $V_2O_5–WO_3/ZrO_2$ and corresponding K-doped catalysts calcined from 400 to 800 °C at two operating temperatures (450 and 500 °C). Experimental conditions: 50 mg sample, 1100 ppm NH_3, 3.5% O_2, 2.3% H_2O and balance N_2 to 300 ml/min.

able in Supplementary material, Table 1. The volumetric amount of crystalline phase of monoclinic WO_3 and the three zirconia phases (tetragonal, monoclinic and cubic) are calculated with the Rietveld method for WO_3/ZrO_2 samples calcined at temperatures between 600 and 800 °C and presented in Table 1.

Cortés-Jacome et al. [15] have also performed Rietveld analysis of WO_3/ZrO_2 samples, synthesized according to similar recipe. The authors tried to fit the XRD results with a model, first based on tetragonal and cubic zirconia, which resulted in a poor fit. Better results were obtained when fitting with two combined tetragonal phases, by varying the oxygen position (corresponding to the z-position of t-ZrO_2). In this study, however, the cubic and monoclinic phases of ZrO_2 are included in the model in order to describe the possible influence of different crystal phases on the catalytic behavior in the NH_3 SCR reaction.

For the sample calcined at 600 °C, the majority of the crystalline zirconia is present in the tetragonal form, 91.25 vol%, whereas only 8.69 vol% exists as cubic ZrO_2, with hardly any monoclinic impurities in the matrix. As a function of the calcination temperature, the relative phase composition of the polymorph mixture changes. Increasing the calcination temperature results in a decrease in tetragonal ZrO_2, compensated by increased amount of cubic and monoclinic ZrO_2 along with appearance of monoclinic tungsten oxide phase. The latter can be related to the decrease of the surface area with increasing calcination temperature and therefore higher surface concentration of WO_x species, far exceeding monolayer coverage. The observed results are in good correlation with previous studies of the temperature effect on the crystalline zirconia [13,16]. The authors found that zirconia was present in mainly tetragonal form at lower temperatures and transformed to monoclinic phase above 600 °C. It was found that sintering of zirconia crystallites at elevated temperatures leads to the stabilization of ZrO_2 in the monoclinic phase.

3.2. NH_3 oxidation measurements

The ammonia oxidation on the fresh and poisoned catalyst samples has been measured between room temperature and 550 °C. Below 400 °C, only negligible NH_3 oxidation was observed for all catalysts tested. Both NH_3 conversion and selectivity towards NO formation are increasing with calcination temperature. The ammo-

Table 2
The NH_3 SCR activity at 450 °C and surface acidity for the fresh vanadia-based catalyst and the corresponding potassium-doped [11].

	SCR activity (s^{-1})		Ammonia desorbed (μmol/g)	
	Fresh	K-doped	Fresh	K-doped
2.0VWZ_600	367	198	460	416
2.0VWZ_700	348	160	363	404
2.0VWZ_800	385	79	211	180
1.7VWT_ref	451	92	–	–

nia conversion for different catalysts along with the crystallinity and fractional vanadium monolayer (ML) coverage of the corresponding tungstated zirconia support are presented in Fig. 1 at 450 and 500 °C as function of the support calcination temperature. Vanadium monolayer coverage on ZrO_2 is reported at 6.8 V/nm^2 [17], which can be recalculated to 15–59% vanadium ML coverage for the 2.0VWZ_400 and 2.0VWZ_800 samples respectively (1.0–4.0 V/nm^2). All fresh catalysts show noticeable activity in ammonia oxidation reaction, which increases parallel with the calcination temperature of the support (WZ). The crystallinity of the support and vanadium surface density seems to influence the NH_3 oxidation ability to a much larger extent than surface acidity (see Table 2). Amorphous samples (VWZ_400, VWZ_500), even though they possess high specific surface area, show quite low ammonia conversion.

Poisoning of the $V_2O_5–WO_3/ZrO_2$ system with K_2O leads to a decline of the overall NH_3 oxidation activity. Previously, a similar decrease of the activity in NH_3 SCR reaction was observed after potassium-poisoning [11]. This indicates that potassium is either deactivating both types of the sites used for the NH_3 SCR reaction and the NH_3 oxidation or both reactions proceed in parallel on the same type of active sites which are sensitive towards poisoning with potassium.

In order to compare selectivities of different catalysts at the same levels of NH_3 conversion the selectivity is plotted versus the conversion (Fig. 2), where the main products of NH_3 oxidation are N_2 and NO. Commercial SCR catalyst consisting of 3 wt% V_2O_5–7 wt% WO_3/TiO_2 (denoted as 1.7VWT_ref) is used as reference. It is clearly seen that all crystalline unpoisoned catalysts, including the anatase-based reference catalyst, fit into almost identical selectivity vs. conversion curves. This indicates that the conversion of
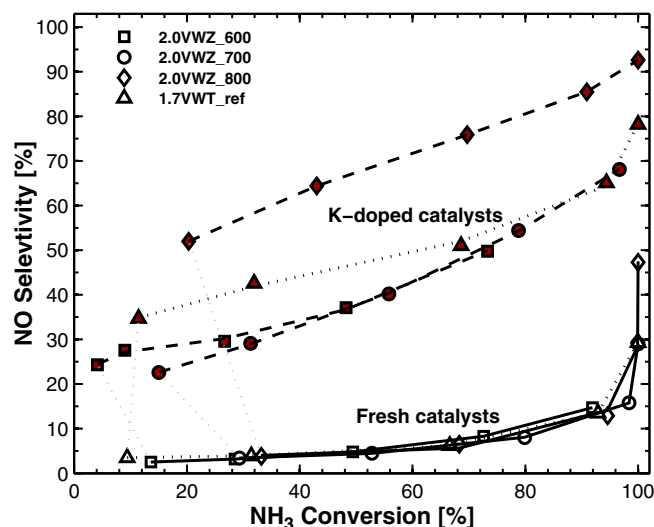

Fig. 2. NO Selectivity versus the NH_3 conversion for fresh and K-doped catalysts measured in the temperature range 450–550 °C. Open symbols represent fresh catalysts, solid symbols denote the corresponding K-doped samples.

ammonia is proceeding by a similar mechanism over all fresh catalysts and that the selectivity to NO is determined by similar factors. Two amorphous catalysts, VWZ_400 and VWZ_500, display negligible ammonia conversion and are therefore not shown here. Although all the fresh catalysts show low selectivity to NO at temperatures below 525 °C, a significant increase in the selectivity is observed at higher temperatures and consequently higher NH_3 conversions. For example, the VWZ_800 catalyst converts almost 100% of the ammonia already at 525 °C with high selectivity to NO, particularly 47% at 550 °C.

Doping the zirconia-based catalysts with potassium to K/V = 0.2 results in an increased selectivity to NO for all catalysts, while the conversion of ammonia decreases significantly, as indicated by the gray dotted lines in Fig. 2, representing the data recorded at 450 °C. The increase in NO selectivity with reaction temperature (i.e. with increasing NH_3 conversion in Fig. 2) is associated with the expected decrease in N_2 selectivity at elevated reaction temperatures. Madia et al. [18] also reported this trend for V_2O_5–WO_3/TiO_2 catalysts in the ammonia oxidation reaction. The increase in the NO selectivity due to K-doping is highest for the reference V_2O_5–WO_3/TiO_2 and VWZ_800 catalysts, which both has highest vanadium surface concentration of all the samples tested, 3.3 and 4.0 V/nm^2, respectively. This complies well with the results of Nova et al. [2], who reported of decreasing N_2 selectivity for samples with high surface vanadium density. Surprisingly, the overall conversion of NH_3 on the reference catalyst is almost unaffected by the potassium doping in contrast to the more vulnerable SCR reaction, where the catalyst deactivates almost completely. According to Ozkan et al. [3,4], the results suggest that only V=O sites are available on the catalyst surface and responsible for the increase in NO selectivity, meaning that all the V–OH sites have been deactivated by potassium.

Apparent activation energies for the ammonia oxidation to NO have been calculated and are presented in Table 3. The reaction is assumed first-order in NH_3, due to the high concentration of oxygen compared to ammonia. For the fresh zirconia-based catalysts, all calculated activation energies are in the range of 114–160 kJ/mol, and 217 kJ/mol for the reference catalyst. For the comparison, apparent activation energy of the NH_3 SCR reaction on the $3V_2O_5$–$7WO_3$/TiO_2 reference catalyst is calculated to be 64 kJ/mol, which correlate well with those reported in the literature for V_2O_5/TiO_2 catalysts, which are in the range 69–82 kJ/mol for a V_2O_5–MoO_3/TiO_2 catalyst [19]. The large difference between activation energies for SCR reaction and ammonia oxidation explains why the SCR reaction is prevailing at temperatures below 400 °C. Doping the catalyst with potassium (K/V = 0.2) leads to an increase in the corresponding apparent activation energy of about 30% in average, i.e. a decrease in ammonia oxidation rate, as observed in Fig. 2. However, care must be taken in the interpretation of the activation energies since the calculated apparent activation energies in the present work are based on relative high ammonia conversions (up to ~10%) and therefore not entirely in the kinetic region. For example, a slight increase in activation energy is calculated for the reference catalyst, from 217 to 227 kJ/mol when doping with potassium despite slightly higher NH_3 conversion is detected after being poisoned with potassium.

4. Conclusion

The Rietveld refinement of the tungstated zirconia calcined from 400 to 800 °C confirm that the majority of the crystalline phase is present as tetragonal ZrO_2. Phase transformation of the tetragonal zirconia into cubic and monoclinic forms occurs with increasing calcination temperature, as well as formation of monoclinic WO_3 at temperatures above 700 °C.

All samples tested for ammonia oxidation exhibited negligible NH_3 oxidation at operating temperatures below 400 °C. At temperatures above 450 °C a noticeable increase in ammonia oxidation rate is observed.

The activity of the catalysts in NH_3 oxidation correlate well with the vanadium surface density and the crystallinity of the support, which implies that the support is either involved in the NH_3 oxidation mechanism or facilitates the formation of specific active sites responsible for ammonia oxidation. For the same NH_3 conversion levels, selectivity towards NO is similar for all fresh zirconia- and anatase-based catalysts indicating that the conversion of ammonia is proceeding by a similar mechanism over all fresh catalysts and that the selectivity to NO is determined by similar factors.

Doping of the catalysts with potassium (K/V = 0.2) results in reduction in the NH_3 conversion for all samples, which correlate well with the calculated apparent activation energies. Since poisoning with potassium also induces a decrease in the overall SCR activity, this could indicate that potassium is affecting the sites used for both the NH_3 SCR and ammonia oxidation reaction. Although doping with potassium decreases the overall activity in ammonia oxidation, a significant increase in the selectivity towards NO is observed for the potassium-poisoned samples.

Acknowledgements

Appendix A. Supplementary data

Supplementary data associated with this article can be found, in the online version, at doi:10.1016/j.catcom.2008.12.002.

References

[1] (a) N.I. Il'chenko, G.I. Golodets, J. Catal. 39 (1975) 57;
(b) N.I. Il'chenko, G.I. Golodets, J. Catal. 39 (1975) 73.
[2] I. Nova, L. dall'Acqua, L. Lietti, E. Giamello, P. Forzatti, Appl. Catal. B 35 (2001) 31.
[3] U.S. Ozkan, Y. Cai, M.W. Kumthekar, J. Catal. 149 (1994) 375.
[4] U.S. Ozkan, Y. Cai, M.W. Kumthekar, J. Catal. 149 (1994) 390.
[5] S.M. Jung, P. Grange, Appl. Catal. B 36 (2002) 325.
[6] J.P. Chen, R.T. Yang, J. Catal. 125 (1990) 411.
[7] H. Kamata, K. Takahashi, C.U.I. Odenbrand, J. Mol. Catal. A 139 (1999) 189.
[8] I.E. Wachs, B.M. Weckhuysen, Appl. Catal. A 157 (1997) 67.
[9] D.A. Bulushev, F. Rainone, L. Kiwi-Minsker, A. Renken, Langmuir 17 (2001) 5276.
[10] J.P. Chen, R.T. Yang, Appl. Catal. A 80 (1992) 135.
[11] J. Due-Hansen, A.L. Kustov, S.B. Rasmussen, R. Fehrmann, C.H. Christensen, Appl. Catal. B 66 (2006) 160.
[12] J.G. Santiesteban, J.C. Vartuli, S. Han, R.D. Bastian, C.D. Chang, J. Catal. 168 (1997) 431.
[13] J.C. Sohn, M.Y. Park, Langmuir 14 (1998) 6140.
[14] WINPOW 2005-12-30, Rietveld refinement framework by Kenny Ståhl, Department of Chemistry, Technical University of Denmark.
[15] M.A. Cortés-Jacome, J.A. Toledo-Antonio, H. Armendáriz, I. Hernández, X. Bokhimi, J. Solid State Chem. 164 (2002) 339.
[16] M. Bhagwat, V. Ramaswamy, Mater. Res. Bull. 39 (2004) 1627.
[17] I.E. Wachs, Catal. Today 27 (1996) 437.
[18] G. Madia, M. Koebel, M. Elsener, A. Wokaun, Ind. Eng. Chem. Res. 41 (2002) 4008.
[19] L. Lietti, I. Nova, G. Ramis, L. Dall'Acqua, G. Busca, E. Giamello, P. Forzatti, F. Bregani, J. Catal. 187 (1999) 419.

Table 3
Apparent activation energies[*] for the apparent first-order NH_3 oxidation to NO.

	E_a [kJ/mol]	
	Fresh	K-doped
2.0VWZ_600	114	155
2.0VWZ_700	123	174
2.0VWZ_800	160	199
1.7VWT_ref	217	227

[*] Calculated for temperature interval 400–450 °C.